Development and Validation of a Mathematical Model for Surge in Radial Compressors (Alternative Format Thesis)

Powers, Kate

Award date:
2021

Awarding institution:
University of Bath

Development and Validation of a Mathematical Model for Surge in Radial Compressors (Alternate Format Thesis)

Powers, Kate

Award date:
2021

Awarding institution:
University of Bath

Development and Validation of a Mathematical Model for Surge in Radial Compressors

submitted by

Katherine Powers

for the degree of *Doctor of Philosophy*

at the

University of Bath

Department of Mathematical Sciences

May 2021

COPYRIGHT NOTICE

DECLARATION OF ANY PREVIOUS SUBMISSION OF THE WORK

The material presented here for examination for the award of a higher degree by research has not been incorporated into a submission for another degree.

Signature of Author .....  .....

Katherine Powers

DECLARATION OF AUTHORSHIP

I am the author of this thesis, and the work described therein was carried out by myself personally in collaboration with my supervisors Paul Milewski, Chris Brace, Colin Copeland and Chris Budd.

Signature of Author .....  .....

Katherine Powers

ABSTRACT

Radial compressors are found in many systems including automotive engines, air-conditioning systems, and aircraft axillary power units. The work in this thesis focuses on the application of automotive turbochargers but the methodology is applicable for all uses.

Turbocharger compressors increase the power output of an engine. They are limited at low flow rates by compressor surge. Surge is characterised by low frequency oscillations in mass flow and pressure, and is often damaging to the compressor.

There have been many attempts to model and predict the point of surge onset, usually via map-based models. Many of these rely on calibration to experimental or CFD data. This has two main disadvantages: (i) the model requires calibrating each time a change in the compressor geometry occurs, and (ii) there is no way to gain insight into the physical causes of surge.

The work in this thesis aims to address these problems by developing a new model for surge starting from the fundamental equations of fluid motion, and only including a minimal number of fitted parameters. All models are developed using mathematical averaging techniques and validated by conducting experiments of a compressor operating in stable, surge and reverse flow regimes.

The resulting surge model has been able to capture both mild surge, where oscillations occur without any full flow reversal, and deep surge, where flow is observed travelling in the reverse direction through the compressor. This is the first time any model has been able to capture and explain the existence of both types of surge.

During model development, it was discovered that incidence losses at the impeller inlet and diffuser recirculation were the main factors that determine the location of surge onset. Also, explanations were found for observed phenomena like the quiet period that is sometimes observed during surge.

Finally, stability analysis was performed on the reduced order surge model, and the existence of both supercritical and subcritical Hopf bifurcations were discovered. This analysis reinforced and explained the behaviour of the model simulations.

ACKNOWLEDGEMENTS

There are so many people who have helped me along my PhD journey and I am so grateful to all of you. I do not have space here to do justice to the guidance, support, and kindness you have given or shown me.

First and foremost, I would like to thank my supervisors Paul Milewski, Chris Brace, Colin Copeland and Chris Budd. Especially, Paul and Chris (Brace) who have been with me from the beginning to the very end. Your guidance and support has been invaluable. No matter how stuck I became, between you, you always managed to help me find a new way of thinking about the problem. I am very grateful for your patience, understanding, kindness, and willingness to help, both with the research and during personally difficult times. I shall miss working with you.

Next, I would like to thank the SAMBa CDT as a whole. Not only did you provide the funding for this research (EPSRC: EP/L015684/1), you provided a social and supportive environment. I am grateful to the management team for their guidance and support, and to the many friends and colleagues (in SAMBa or the wider maths department) who have discussed research, shared in the highs and lows of a PhD, and made this entire journey more enjoyable.

I also wish to thank those office mates and colleagues in Mechanical Engineering who were willing to discuss my work, answer my questions, or help with the more practical side of engineering. Coming into engineering from a different discipline was a steep learning curve, so I am very grateful for your patience and support.

Likewise, I am grateful to the people at Cummins Turbo Technologies. I am so glad that you took interest in my research, and am very grateful for all the support you have provided since, including hosting me on site, providing data and equipment, and for your time, enthusiasm and encouragement.

I would also like to thank all those I have worked with through student services throughout my time at the university. Your continued support and advice has helped me navigate various issues whether big or small. I could not have done this without your help.

On a personal level, I wish to thank my family and friends. Thank you for always sticking by me, through the good and bad. Your unwavering support and encouragement has helped keep me motivated through the hard times, and the fun and laughter we share makes the good times even better.

In particular, I would like to thank my Dad who not only supported me as a parent but often as my unofficial fifth supervisor. Whether as a sounding board, a mentor, a problem solver, an image editor or a supportive listener - thank you for always being there.

Finally, I wish to dedicate this thesis in memory of my Grandma, Nadine Powers (1937-2020), who I know will always be proud of me.

Contents

List of Figures

List of Tables

Nomenclature

a	Speed of sound
$\hat{a}$	Impeller inlet stall parameter
a_H	Hopf bifurcation stability parameter
A	Cross-sectional area
$\hat{b}$	Diffuser stall parameter
B	Greitzer's parameter
c_v	Specific heat at constant volume
d_H	Hopf bifurcation parameter
E	Specific total energy
f	Friction factor
F	Friction function
$\tilde{\mathbf{F}}$	Force per unit volume
$\mathbf{g}$	Acceleration due to gravity
h	Height
J	Jacobian
L	Length
m	Mass
$\dot{m}$	Mass flow rate
Ma	Mach number
n_b	Number of blades
p	Pressure
q	Mass flow per radian
Q	Heat energy
r	Radius
r_a	Rayleigh number
R	Specific gas constant
S	Surface area
t	Time
T	Temperature, or period of oscillation
$\mathbf{u}, u$	Velocity
U	Internal energy
V	Volume
W	Work
x	Distance
α	Flow angle into the diffuser
α^*	Critical angle for diffuser stall
β	Flow angle into the impeller
β_B	Blade angle at impeller inlet
γ	Specific heat ratio
Δx	Grid spacing
η	Diffuser stall function
κ	Isentropic constant
λ	Eigenvalue
λ_s	GAM smoothing parameter
μ	Throttle parameter
ν	Shear loss parameter
ξ	Impeller stall function
Π	Stress
ρ	Density
σ_p	Prandtl number
τ	Non-dimensional time
$\boldsymbol{\tau}$	Deviatoric stress
ϕ	Basis functions
Φ	Non-dimensional mass flow
Ψ	Non-dimensional pressure
ω_H	Helmholtz frequency
$\boldsymbol{\Omega}, \Omega$	Impeller rotational speed

Subscripts/superscripts:

amb Ambient	ss Steady state
c Compressor	S Stationary frame
D Diffuser	tip Impeller tip
I Impeller	T Throttle
p Plenum	x Axial or x direction
r Radial	θ Tangential
R Rotating frame	$*$ Critical or equilibrium value

Chapter 1

Introduction

1.1 Thesis Motivation

Turbochargers are a vital component for aiding engine manufacturers to meet the latest emissions standards. However, turbocharger operation is limited by surge for low mass flow rates. Surge often comprises of violent pressure oscillations that cause damage to the turbocharger and its installation. Therefore, for every application, turbochargers need to be matched in a way that ensures they won't be required to operate in surge. Thus, in this thesis, we aim to improve current methods for predicting the onset of surge.

1.1.1 Overview of Turbochargers

Turbochargers are a boosting mechanism that increases the power output of an engine. Figure 1-1 shows a schematic of a turbocharged engine. A turbocharger consists of a compressor and a turbine that are connected via by a common shaft [1]. Exhaust gases are used to drive the turbine, which in turn drives the compressor. The compressor raises the pressure and density of inlet air and feeds it to the inlet of the engine [1]. This supplies the engine cylinders with more oxygen per unit volume, meaning more fuel can be burnt for the same size of engine, which results in a higher power output [2].

Turbochargers were first developed by Dr. Alfred J. Büchi of Switzerland between 1909 and 1912 [3]. However, his ideas gained little acceptance at the time and it

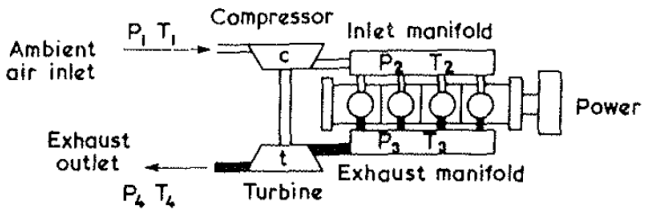

Figure 1-1: Typical arrangement of a turbocharged engine [1]. P_i denotes the pressure and T_i denotes the temperature at each stage of the cycle.

took until 1925 for the first successful turbocharger application to appear, where two German ships were fitted with 2000 hp turbocharged diesel engines. Following this, and throughout the 1930s, turbochargers with axial turbines were used in marine, railway, and large stationary applications [3].

In the 1940s radial turbines were developed, meaning that radial flow turbochargers were developed for use on small automotive diesel engines. By the 1950s, major engine producers such as Cummins, Volvo and Scania began experimenting with turbocharged engines for trucks [3]. Initially, these early designs were unsuccessful due to the large size of the turbocharger, but by 1954 German engineer Kurt Beirer developed the first compact turbo compressor, making turbocharged engines more viable for smaller applications [4].

Nowadays, both axial and radial (also known as centrifugal) turbochargers are still used. Typically, axial turbochargers are used in aircraft or marine applications where large volumes of air need to be compressed [1]. However, centrifugal turbochargers are common in automotive engines because they maintain relatively high efficiency when reduced to small sizes, they have a larger operating range, and they are cheaper to

Figure 1-2: Slice through an axial turbocharger [5] (left) and centrifugal turbocharger [6] (right).

Figure 1-3: Left: Turbocharger for Wärtsilä RT-flex96C engine for a cargo ship [9]. Right: Garrett GT0632SZ turbocharger suited for use with 1L engines [11].

manufacture [1]. Fig. 1-2 shows the differences between the two types.

As the name suggests, the flow through axial compressors is purely axial. They consist of pairs of rotating fans and stationary aerofoils. The rotating fans accelerate the flow and the stationary aerofoils diffuse the flow in order to convert the increased rotational kinetic energy into pressure [7].

Centrifugal compressors are similar but they turn the flow during the compression. The axial flow is directed onto a rotating impeller, which imparts kinetic energy to the flow and changes its direction so that it exits radially [1]. The flow then passes through a diffuser to slow down the air and increase its pressure, before being collected by a volute [1, 8].

Turbochargers can come in a huge range of sizes. The left image in Fig. 1-3 shows the turbocharger for the Wärtsilä RT-flex96C engine, which is currently the worlds largest and most powerful engine. In 2006, it was installed on the Emma Mærsk cargo ship that can carry 11000 20ft shipping containers at 31 knots [9]. However, the right image in Fig. 1-3 shows a Garrett micro turbo. This turbo is ideally suited to two and three-cylinder diesel engines and petrol engines less that 1L [10].

In the 1970s, turbochargers started being used in Formula 1, which made turbocharged passenger car engines very popular [12]. However, the real breakthrough in passenger car turbocharging was achieved in 1978 with the introduction of the first turbocharged diesel engine passenger car. This resulted in increasing the efficiency of diesel engines so they were comparable to petrol engines [12].

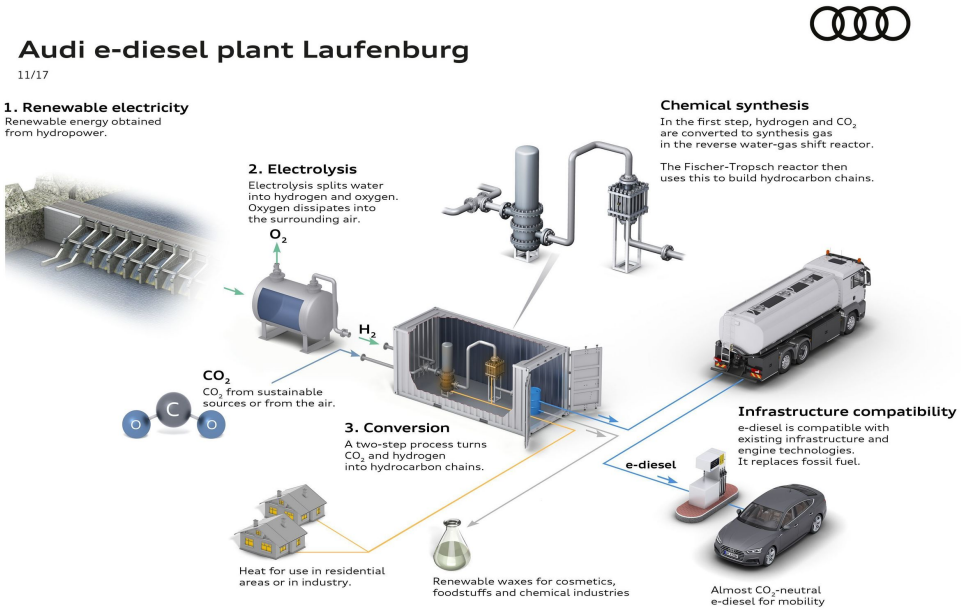

Figure 1-4: Schematic by Audi on how synthetic e-fuels are generated and used [14].

Nowadays, the turbocharging of petrol and diesel engines is primarily viewed as a means of reducing fuel consumption and therefore environmental pollution [12]. Smaller engines are more efficient because they are lighter and have fewer frictional losses. Therefore, seeing as turbochargers increase the power output of an engine, it is possible to use a downsized engine alongside a turbocharger to improve efficiency without reducing power.

We can see this shift towards environmentally-conscious thinking by looking at the types of new vehicles being bought and registered: from early 2018 to early 2019, there was a 20% decrease in diesel, 6% increase in petrol and 18% increase in alternative fuel registrations [13]. Also, during Jan-Mar 2019, 1.9% of all new registrations were for ultra low emission vehicles (ULEVs), which emit less than 75g of CO_2 per kilometre travelled [13].

Looking further into the future, synthetic e-fuels are a viable possibility to reduce emissions without the need for significant modification to the design of the internal combustion engine. Figure 1-4 shows how e-fuels can be used with our existing infrastructure. The idea is that renewable energy sources, such as wind, solar, or hydropower, provide electrical power to break water into hydrogen and oxygen via electrolysis [14]. This

can then be combined with carbon dioxide to obtain e-methane, e-diesel, or e-kerosene. Therefore, these fuels are having a net-zero carbon impact as they utilise carbon that is already in the atmosphere, rather than adding carbon to the atmosphere that is currently stored in the ground, e.g. through fossil fuels [14].

The fact that this would allow the internal combustion engine to remain relatively the same, also means that turbochargers will still be useful in the future for improving efficiency or power from an engine.

For this thesis, we will focus on automotive turbochargers. The automotive industry is large and has been continually growing since the end of WWII. At the end of March 2019, there were 38.4 million vehicles licensed in Great Britain: 82.5% were cars, 10.6% were LGVs, 1.3% were HGVs, and 3.3% were motorcycles [13]. Therefore, focusing on improvements for automotive applications, particularly cars, has the potential for a large impact.

Since the majority of cars use relatively small radial turbochargers, we will focus our attention on these. However, the methodology discussed within this thesis can be used for larger turbochargers and adapted for other applications.

1.1.2 Operation of Radial Compressors

Figure 1-5 shows the four components of a radial compressor: the inlet pipe, the impeller, the diffuser and the volute.

The inlet is a simple pipe which directs the flow from above onto the impeller eye. Some inlets have guide vanes in order to gain some control over the flow behaviour [1].

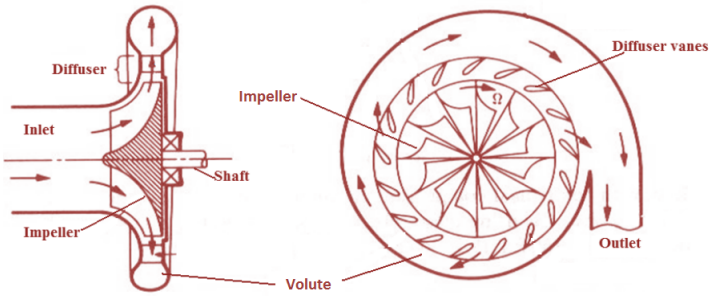

Figure 1-5: Components of a radial compressor from side and plan view points [15].

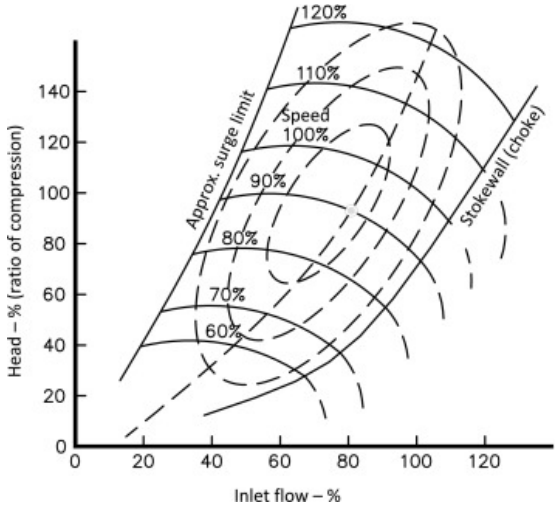

Figure 1-6: Example compressor map showing the surge and choke limits [16].

The impeller is a rotating set of blades that raise the kinetic energy, and hence velocity, of the flow. The blades in Fig. 1-5 are straight radial blades, however, it is more common for blades to be backswept, i.e. curved against rotation. This is because backswept blades reduce the amount of flow distortion transmitted from the impeller to the diffuser [1]. It is also common practice to use splitter blades. These are blades that extend from part way down the impeller to the impeller tip. They still help to control the air flow, but they reduce the risk of blockage at the impeller eye caused by having too many blades [1].

The job of the diffuser is to convert the high velocity of the air leaving the impeller into pressure. The diffuser is a thin gap surrounding the impeller that can be vaned (as in Fig. 1-5), or vaneless. Even though vaned diffusers have a better peak efficiency, vaneless diffusers are more commonly used in automotive turbochargers because they have a larger range of operation [1].

The volute collects air from around the circumference of the diffuser and delivers it to the exit pipe. The volute is designed in a way to maintain the flow properties from the diffuser. The spiral shape occurs because the volute will collect more air as it wraps around the diffuser, so the area increases to accommodate this.

The operating range of a compressor is typically displayed on a compressor map, where we plot the flow through the compressor against the pressure ratio across it. Figure 1-6 shows an example.

There are essentially three regions on the map: stable, choke and surge. The central

stable area is the region of normal operation of the compressor. It is bounded on the left by the surge line and on the right by a choking region.

The choking region is where the air velocity at some location within the compressor approaches sonic conditions and so the compressor can't accept any higher mass flow rate. In this scenario, the compressor speed is likely to rise substantially with little change to the mass flow rate [1].

The surge region is where flow instabilities are observed. The dividing line between stable operation and surge is often difficult to predict as it depends on the whole compression system, not just the compressor itself.

1.1.3 Surge and its Problems

Surge is an aerodynamic instability that exists when operating a compressor at low mass flow rates. Normally air flows from regions of high pressure to regions of low pressure. The compressor generates pressure in the outlet pipe and so the air is travelling against the pressure gradient.

When operating with a small mass flow, it is possible for flow reversal to occur as the force applied to the fluid by the pressure gradient is large enough to overcome the fluid momentum. Once flow reversal occurs, the pressure drops in the outlet pipe and the air resumes its forward directional flow. This oscillation in mass flow and pressure is termed surge [1].

Surge is a large amplitude, low frequency oscillation of the averaged flow through the compressor [17]. However, there are different classifications of surge.

When the oscillations in mass flow are large enough that actual flow reversal is seen, this is called deep surge [18]. Alternatively, when mass flow and pressure oscillations are observed but the flow always remains travelling in the forward direction, this is classed as mild or incipient surge [18].

It is also possible to see a combination of behaviours. For example, Fig. 1-7 illustrates an observable limit cycle for surge behaviour. It has four operating regimes: (1) The speed of the flow at the impeller tip increases and the mass flow rate decreases; (2) The compressor operates in mild surge, so fluctuations in pressure and mass flow grow; (3) The mass flow reverses and the pressure drastically decreases; (4) The flow recovers rapidly to the forward direction and the cycle repeats from (1) [19].

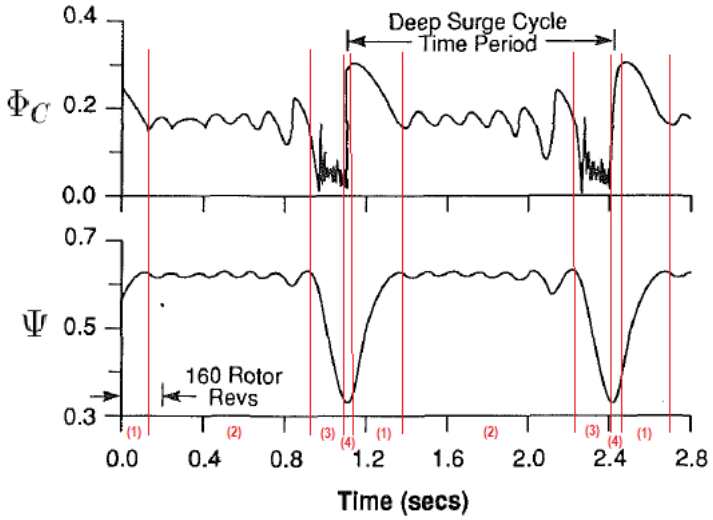

Figure 1-7: Time-resolved behaviour during a surge limit cycle, where Φ_C denotes dimensionless mass flow in the compressor, and Ψ denotes dimensionless pressure [19].

Surge is commonly found to be triggered by some form of stall. There are two main types of stall.

The first can occur at the inlet to the impeller or a vaned diffuser and is caused by incidence. This means that, as mass flow decreases, the inlet flow angle increases and causes a separation of the flow at the blade or vane wall [1].

The second type is often seen in a vaneless diffuser and is caused by recirculation. This is where friction reduces the radial velocity of the flow near the shroud-side wall of the diffuser, reducing its spiral angle so that it is swept back into the impeller [1].

It has been discovered that a compressor operating at high impeller speed is more likely to surge due to stall in the diffuser, and a compressor operating at low impeller speed is more likely to surge due to stall in the impeller inducer [20].

Operation in deep surge often damages the compressor and surrounding installation, which can be costly to repair [1]. Surge causes vibrations that can unbalance the machinery, which can result in contact between the impeller blades and the housing. This leads to bending or fracture of the impeller blades. Operation in surge also results in excessive internal temperatures due to extra friction between the components and energy losses in the air as it recirculates. This rise in temperature can damage the installation, for example through the melting of plastic connectors [17].

The mild form of surge is less damaging, but is still very noisy. This causes problems with customer acceptance because the sound would be off-putting to any driver.

Since surge limits the amount of boost provided at low engine speeds, it is desirable to operate close to surge without entering it for prolonged periods of time. Therefore, it is important for designers and manufacturers to create models that can predict the location of the surge region, as well as aid understanding of the flow dynamics near that region.

However, due to the unstable nature of surge, and the fact that it depends on the system pipework, this limit is often difficult to predict. Motivated by this, the work undertaken in this thesis looks into new approaches for modelling and predicting surge in radial compressors.

1.2 Literature Review

1.2.1 Existing Models

Models Requiring Turbochargers

There are many reasons why simulating an engine is useful. It allows for the prediction of performance under different operating conditions, as well as optimisation and development of designs of specific components. Therefore, even when turbochargers are not the main focus of research, it is often important to have a model of them so the entire engine performance can be studied.

There are many industrially-focused engine simulation software packages available, including GT-POWER, Ricardo Wave, and LESoft [21, 22]. GT-POWER is part of the GT-SUITE by Gamma Technologies. It is able to predict engine performance quantities, like power and torque, and includes physical models for wave dynamics, combustion and after-treatment [22].

Most of the systems being analysed are highly complex. For example, Fig. 1-8 shows schematic of a 4-cylinder turbocharged engine modelled in GT-POWER. Each component has its own model, so it is important that individual models are computationally fast because running the whole system will call on each component multiple times.

This means that the current models for turbochargers in these engine systems are very

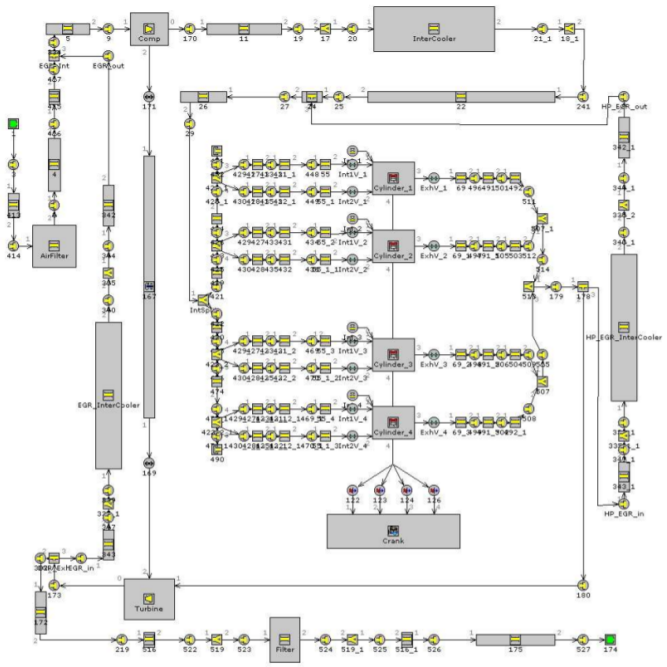

Figure 1-8: Example GT-POWER model for a 4-cylinder turbocharged engine [23].

simplistic. For example, the component model for the turbocharger compressor in GT-POWER requires the specification of a compressor map [24], which is then extrapolated into surge and choke regions.

Often, a fictitious compressor is created with no surge or choke limits, resulting in monotonically decreasing characteristics [23]. Simulations are then run with this hypothetical compressor and compared to actual compressor maps afterwards in order to select the operating range, i.e. the surge and choke limits [23].

It is possible to specify the surge line into the software and use this as a constraint when performing calculations like geometry optimisation [25]. This would discount any simulated point that occurred within the surge region and so the final optimisation would lie in the correct domain of operation.

Reduced Order Surge Models

When looking directly for compressor surge properties, reduced order surge models are commonly used. Such models have been around since the 1950s [26]. However, nearly all models are based on the work by Greitzer in 1976 [17].

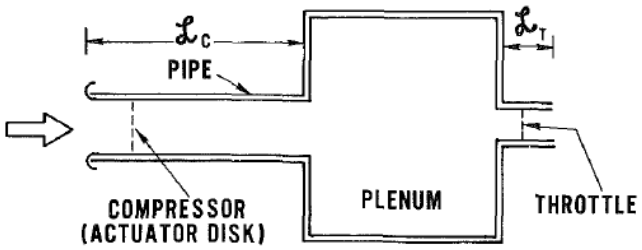

Figure 1-9: Compression system used in Greitzer's model [17]. The pipes containing the compressor and throttle have much smaller diameters than the plenum, and have lengths L_c and L_T respectively.

Greitzer simplifies an axial compression system to the model shown in Fig. 1-9. Here, the compressor (modelled via an actuator disk) is connected to a large exit plenum, and the air discharges through a throttle (also represented by an actuator disk) [17].

Greitzer considered flows of low inlet Mach number, so the associated pressure rise is small in comparison to ambient pressure. This, combined with the relatively low oscillation frequency of surge, meant Greitzer could assume the flow in the compressor and throttle pipes was incompressible. The one dimensional incompressible momentum equation is given by

$$\rho \frac{du}{dt} = -\frac{\partial p}{\partial x}. \tag{1.2.1}$$

Integrating this with respect to x in the compressor and throttle pipes gives

$$\frac{L_c}{A_c}\frac{d\dot{m}_c}{dt} = \rho_c L_c \frac{du_c}{dt} = p_c - p_p, \tag{1.2.2}$$

$$\frac{L_T}{A_T}\frac{d\dot{m}_T}{dt} = \rho_T L_T \frac{du_T}{dt} = p_p - p_T, \tag{1.2.3}$$

where subscripts p, c and T denote the plenum, compressor and throttle respectively, and $\dot{m} = A\rho u$ is the mass flow rate with cross-sectional area, A. [17]

Greitzer assumed the plenum is large enough so that fluid velocities are negligible, but still smaller than the wavelength of an acoustic wave oscillating at a typical surge frequency. The latter assumption allowed Greitzer to also assume the pressure is constant in space throughout the plenum at any instant in time. Applying conservation of mass in the plenum gives us

$$\dot{m}_c - \dot{m}_T = V_p \frac{d\rho_p}{dt} = \frac{\rho_{amb} V_p}{\gamma p_{amb}} \frac{dp_p}{dt}, \tag{1.2.4}$$

by assuming the fluid is isentropic and that temperature in the plenum $T_p = \frac{p_p}{R\rho_p}$ is ambient. Here V_p denotes the volume of the plenum and γ is the specific heat ratio. [17]

Therefore, Greitzer is assuming that all of the kinetic energy of the flow is associated with the motion of the fluid in the compressor and throttle pipes, and all of the potential energy is associated with the compression of the gas in the plenum [17].

To close the system we need to know p_c and p_T. Greitzer decided to use

$$\hat{t}\frac{dp_c}{dt} = p_{c_{ss}} - p_c \tag{1.2.5}$$

to determine p_c, where $p_{c_{ss}}$ denotes a steady-state compressor characteristic, and $\hat{t}$ is a time constant that describes the growth of stall cells (usually obtained via experiment). Using this ODE instead of directly assuming $p_c \approx p_{c_{ss}}$ allows the model to simulate the lag in compressor response, which can cause a lag between reaching the stall limit and observing rotating stall cells or surge. [17]

For p_T Greitzer assumed that we have either a variable area nozzle or a valve, so that the orifice equation

$$p_T = \frac{1}{2}\rho_{amb}u_T^2 = \frac{\dot{m}_T^2}{2\rho_{amb}A_T^2} \tag{1.2.6}$$

holds [17].

Greitzer then nondimensionalised the mass flows with $\rho_{amb}\Omega A_c$, the pressures with $\frac{1}{2}\rho_{amb}\Omega^2$ and the time variables with $\frac{1}{\omega_H}$, where $\omega_H = a\sqrt{\frac{A_c}{V_p L_c}}$ is the Helmholtz frequency, Ω is the mean rotor velocity, and a is the speed of sound.

Denoting the dimensionless mass flows by Φ, the dimensionless pressure differences by Ψ, and dimensionless time variables by τ, leads to the system

$$\frac{d\Phi_c}{d\tau} = B(\Psi_c - \Psi) \tag{1.2.7}$$
$$\frac{d\Phi_T}{d\tau} = \frac{B}{G}(\Psi - \Psi_T) \tag{1.2.8}$$
$$\frac{d\Psi}{d\tau} = \frac{1}{B}(\Phi_c - \Phi_T) \tag{1.2.9}$$
$$\frac{d\Psi_c}{d\tau} = \frac{1}{\hat{\tau}}(\Psi_{c_{ss}} - \Psi_c) \tag{1.2.10}$$

where $G = \frac{L_T A_c}{L_c A_T}$, and $B = \frac{\Omega}{2a}\sqrt{\frac{V_p}{A_c L_c}}$ [17]. B is often referred to as Greitzer's parameter

and can be regarded as the ratio of pressure forces and inertial forces acting in the compressor pipe [27].

Often, this system of ODEs is simplified further by assuming (i) $\hat{\tau} = 0$, so the compressor acts in a quasi-steady manor, and (ii) that the pressure at the throttle is set instantaneously by the pressure in the plenum so we can use

$$\dot{m}_T = \sqrt{2\rho_{amb} A_T^2 p_p} \tag{1.2.11}$$

as a direct function instead of the ODE (see, for example, [28], [19], [29]). This would reduce the above system to just two ODEs, namely:

$$\frac{d\Phi_c}{d\tau} = B(\Psi_{c_{ss}} - \Psi) \tag{1.2.12}$$

$$\frac{d\Psi}{d\tau} = \frac{1}{B}(\Phi_c - \Phi_T) \tag{1.2.13}$$

where Φ_T is the nondimensional form of the throttle equation. This system is often referred to as the Moore-Greitzer equations.

Despite the fact Greitzer's model was derived for axial compressors, this model has also been used for radial compressors. For example, Arnulfi et al. [27] used a model derived from Greitzer's in order to simulate an industrial low-pressure multistage centrifugal compressor with vaned diffusers. The main difference in Arnulfi's model was the use of a discontinuous parameter for $\hat{\tau}$ so that a significant time lag was only introduced when stalling occurred because this matched observed experiments [27].

Similarly, Elder et al. [20] and Fink et al. [19] used models based on Greitzer's for vaned and vaneless radial compressors respectively. However, instead of using experiments to determine the compressor characteristic, they used meanline or lumped parameter modelling approaches. Furthermore, Fink et al. extended Greitzer's work to take into account the effect of impeller inertia and speed variation, but this required the additional specification of a torque characteristic [19].

There are many examples of these quasi-steady compressor models in literature, however, the main variation in the work seems to be how the compressor characteristic is specified. The steady-state behaviour of the compressor is far more complex than that of the throttle and so a characteristic is more complicated to determine. There have been three main approaches for obtaining the compressor characteristics.

The first is through complex experimental studies. In 1984, Koff and Greitzer [30]

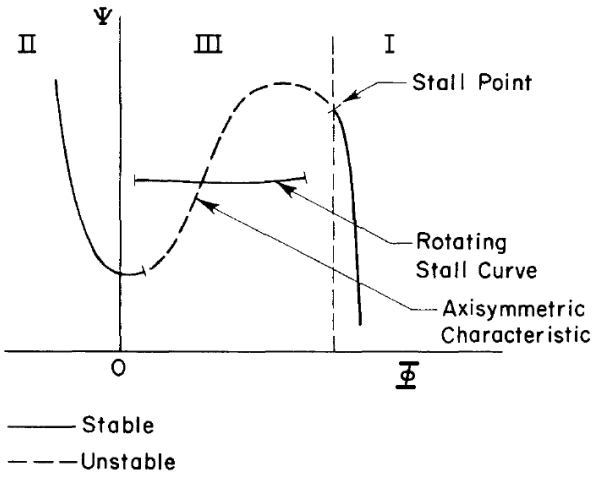

Figure 1-10: Axisymmetric compressor characteristic partitioned into three regions: I - unstalled forward flow, II - reversed flow, and III- low forward flow [30].

developed a technique for estimating the axisymmetric compressor characteristic for an axial compressor. Figure 1-10 shows the general shape they proposed.

The curve in the reversed flow and unstalled forward flow regimes was found by direct measurements taken on a test rig because axisymmetric flow is the stable operating mode in both of these regions. However, when rotating stall appeared the shape was more difficult to determine, and so transients were analysed and an argument was made for having a smoothly varying characteristic based on the behaviour of diffuser stall.

This has been done more recently for small centrifugal compressors by Galindo et al. [31]. In order to take measurements in the low forward flow regime to the left of the usual surge limit, they used a very small volume downstream of the compressor. Doing so increases the Helmholtz frequency ω_H of the system and hence reduces Greitzer's parameter B. According to Fink et al. [19], if B is smaller than a critical value, the compression system will maintain itself at an overall steady equilibrium point. Therefore, by keeping the downstream volume small, Galindo et al. were able to avoid deep surge and take direct measurements of the equilibrium point [31].

In order to measure the compressor map in the reversed flow regime, Galindo et al. forced compressed air into the outlet of the compressor while maintaining the correct rotational direction of the impeller [31]. Figure 1-11 shows the resulting characteristics.

The second approach is via curve fitting and extrapolation. The most common tech-

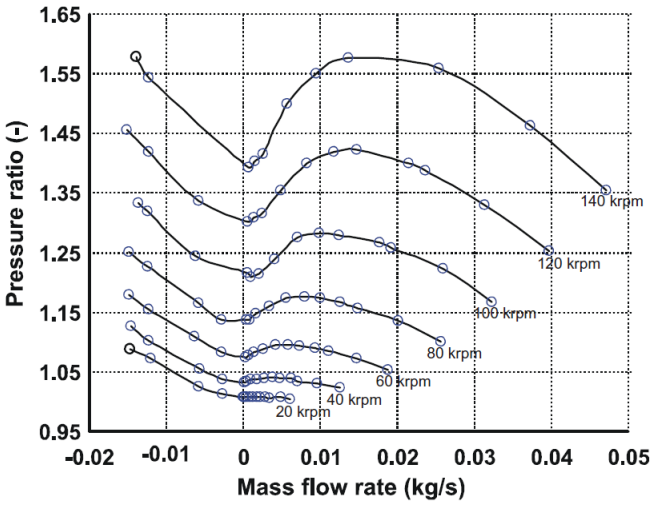

Figure 1-11: Measured steady-state compressor map extended into the surge and negative flow zones experimentally [31].

nique is to use the cubic relation proposed by Moore and Greitzer in 1986 [32], i.e.

$$\Psi_{c_{ss}} = \psi_{c_0} + H\left[1 + \frac{2}{3}\left(\frac{\Phi}{W} - 1\right) - \frac{1}{2}\left(\frac{\Phi}{W} - 1\right)^3\right] \tag{1.2.14}$$

with parameters ψ_{c_0}, H and W found through fitting to experimental compressor map data. However other curve fitting techniques have been proposed, including ones involving Chebyshev polynomials in order to capture more features of the characteristics [33], and ones involving elliptic equations in order to adjust the characteristic for different settings on a variable-geometry diffuser [34].

The third is via meanline modelling. In a mean-line model the compressor is divided into sections over which the equations of motion and loss models are evaluated. Most of the mean-line models follow the meridional path of the compressor and typically split it into sections for the inlet, impeller, diffuser and volute [20, 35]. However, there are two-zone models that have primary and secondary flow sections within the impeller in order to account for slip [36].

The majority of these mean-line models apply empirical loss models to the sections. Typical collections of loss models for compressors can be found in [37, 38, 39]. These loss models usually have loss coefficients that need to be tuned to the particular compressor that is being studied, which makes meanline modelling still partially reliant on experimental data or CFD simulation.

Computational Fluid Dynamics

When more detailed modelling of a turbocharger is required, engineers typically turn to numerical simulation software like Ansys-CFX to perform computational fluid dynamics (CFD). With the advancement in computing power, this has been a growing area of interest.

In a CFD model, a 3D domain is built in the computer and a mesh is constructed over it. This mesh divides the domain into millions of control volumes, or cells, within which the conservation of mass, momentum and energy equations can be solved numerically using finite differences (FDs) or finite element methods (FEMs) [40].

FEM uses the weak form of the equations of motion. To exemplify this, consider the 1D Poisson's equation

$$-\frac{d^2w}{dx^2} = g, \qquad w(\pm 1) = 0. \tag{1.2.15}$$

The weak form is found by multiplying by an arbitrary function v such that $v(\pm 1) = 0$ and integrating [41]. So we get

$$\int_{-1}^{1} vg dx = -\int_{-1}^{1} v\frac{d^2w}{dx^2}dx = \cancelto{0}{-v\frac{dw}{dx}\Big|_{-1}^{1}} + \int_{-1}^{1} \frac{dv}{dx}\frac{dw}{dx}dx. \tag{1.2.16}$$

From here, we define a finite dimensional basis, $\{\phi_1, \phi_2, ..., \phi_n\}$, where each function satisfies the boundary condition $\phi_i(\pm 1) = 0, \forall i$. We can then find an approximate solution to w via $w \approx \sum_{i=1}^{n} w_i\phi_i$, which will converge to the exact solution as $n \to \infty$ [41]. Writing $v = \sum_{j=1}^{n} v_j\phi_j$ we get

$$\sum_{j=1}^{n} v_j \int_{-1}^{1} \phi_j g dx = \sum_{j=1}^{n}\sum_{i=1}^{n} v_j \left(\int_{-1}^{1} \frac{d\phi_j}{dx}\frac{d\phi_i}{dx}dx\right) w_i, \tag{1.2.17}$$

which in vector notation becomes $\mathbf{v}^T\mathbf{c} = \mathbf{v}^T K\mathbf{w}$ where

$$c_j = \int_{-1}^{1} \phi_j g dx \qquad \text{and} \qquad K_{ji} = \int_{-1}^{1} \frac{d\phi_j}{dx}\frac{d\phi_i}{dx}dx. \tag{1.2.18}$$

Therefore, this just reduces to the matrix solve of $K\mathbf{w} = \mathbf{c}$ to find the vector of coefficients for the approximate solution $\mathbf{w}$.

The simplest basis for FEM are piecewise linear functions $\phi_i(x_j) = \delta_{ij}$ where δ_{ij} is the

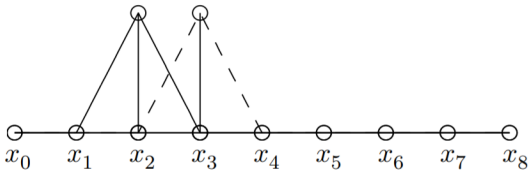

Figure 1-12: Example FEM basis with piecewise linear functions $\phi_2(x)$ and $\phi_3(x)$ shown with solid and dashed lines respectively [41]. Each function ϕ_i will only interact with its two neighbours.

Kronecker delta (see Fig. 1-12). This means that

$$c_j = \int_{-1}^{1} \phi_j g dx \approx \sum_{i=1}^{n} \delta_{ij} g(x_i) = g(x_j) \tag{1.2.19}$$

so the function only needs to be known at the grid points, $x_1, x_2, ...$, and we have a summation over evaluated function points.

This basis has the advantage that K will be tridiagonal, hence the system $K\mathbf{w} = \mathbf{c}$ can be solved very quickly, however convergence to the true solution can be slow and so often a large n is required for accuracy [41].

Automatic, CFD based geometric optimisations are commonly used by centrifugal compressor designers. However, one major issue that remains unresolved is how to determine the surge margin of these compressors [42].

Conducting a detailed, fully-unsteady, 3D flow analysis through a compressible large-eddy simulation would be the most appropriate method for determining the surge limit. However, since the impeller runs at speeds requiring thousands of revolutions per second and surge has a period of approximately 0.1 seconds, many iterations of the CFD model are needed to simulate a single surge cycle. Furthermore, a fine mesh would be required in order to capture the small scale flow dynamics, like impeller stall, that influence surge, so this is far too computationally expensive for manufacturing needs [42].

Therefore, a common method is to run a steady-state CFD simulation iteratively along a speed line, and define the surge limit as the last converged CFD calculation [42]. This is not ideal as there could be other reasons why a simulation did not converge, and the need for multiple iterations still makes this method costly in terms of computation.

Furthermore, running a complex CFD model often doesn't have the ability to identify

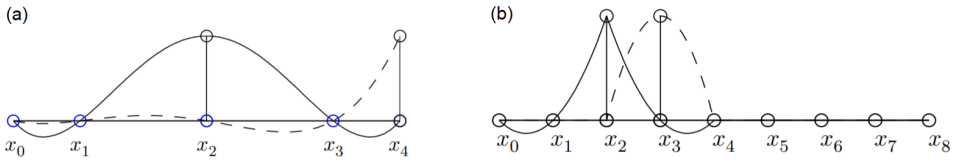

Figure 1-13: Lagrange polynomial basis [41]. (a) Global basis for SM method, with ϕ_2 (solid) and ϕ_4 (dashed). (b) Local basis for SEM method, with ϕ_2 (solid) and ϕ_3 (dashed).

key parameters of physical phenomena that lead to certain events. For example, by defining the surge limit to be the last converged CFD simulation, it is not simple to identify from previous simulations what physical phenomena are contributing to surge because there are many variables and interactions to consider.

1.2.2 Alternative Modelling Techniques

Further to the existing compressor and surge related models, there are other mathematical modelling techniques that could be helpful for analysing surge.

Advanced Numerical Approaches

Numerical methods for simulating flows are becoming increasingly common. One such area of interest are Spectral Methods (SMs) and Spectral Element Methods (SEMs).

These work in a similar way to the FEM described above. They also require a weak form of the problem, and expand the solution in terms of a basis [41]. The key difference is in the choice of basis. While FEM resulted in a summation of evaluated function values, SMs and SEMs approximate a solution as a summation of functions.

SMs are those where each function in the basis spans the entire domain (i.e. a global basis) whereas SEMs are similar to the FEM in that they are only non-zero over a small portion of the domain (i.e. a local basis) [41]. Common basis choices for SMs are trigonometric functions (see [43] for example), or Lagrange polynomials [41]. Restricting Lagrange polynomials to certain parts of the domain would result in a SEM. Figure 1-13 shows Lagrange polynomials as a global basis and a local basis.

Since SMs require a basis that is defined over the entire domain while still satisfying

the boundary conditions, these methods are only suitable when the domain comprises of simple geometries. For more complicated geometries, SEMs are needed.

The choice of the basis functions is important when considering computational cost. Not only will a large basis (i.e. $n \gg 1$) increase computational cost, but a poorly conditioned matrix K will also cause these methods to be costly [41].

SMs and SEMs have been used for solving the Navier-Stokes fluid equations. For example, Lomtev and Karniadakis [44] develop a discontinuous spectral method with a hierarchical basis formed from Jacobi polynomials. This formulation sees good convergence even on a highly distorted mesh, and high computational efficiency [44]. Therefore, it would be possible to extend works like this to improve the efficiency of CFD codes used for simulating compressor surge.

Statistical Approaches

Another mathematical approach to consider is statistical regression modelling. This is where experimental data is used to predict how a variable is dependent on other known parameters. So, in the context of surge, we could find a statistical model for the location of the surge limit by considering geometric dimensions of the compressor and test rig, and operating parameters like impeller speed. This approach could also be used to create a function for the compressor characteristic that depends on known geometry.

One such approach is to fit a Generalised Additive Model (GAM). Suppose that we want to estimate a formula for the random variable W_i and we have a set of observed data w_i along with known parameters $v_{1i}, v_{2i}, v_{3i}, ...$ then a GAM takes the form

$$g_0(\mathbb{E}(W_i)) = g_1(v_{1i}) + g_2(v_{2i}) + g_3(v_{3i}) + ... \tag{1.2.20}$$

for functions g_i, where $\mathbb{E}$ is the expectation over many realisations of the variable at fixed parameter values [45]. We can find the best fit for the functions g_i by expanding them in terms of a basis. For example, suppose we wish to understand how the wear of a car engine depends on its size. Labelling w_i = wear and v_i = size, means we wish to fit the GAM:

$$w_i = g(v_i) + \epsilon_i, \tag{1.2.21}$$

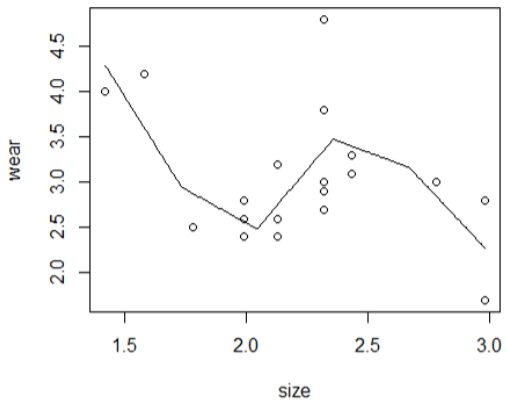

Figure 1-14: GAM fit of engine wear vs size for a basis of size $k = 6$ [45].

where ϵ represents noise in the observed data. To find g we can write

$$g(x) = \sum_{j-1}^{k} \phi_j(x)\vartheta_j, \tag{1.2.22}$$

where ϕ_j are basis functions, and ϑ_j are unknown parameters that we can find via a least squares fit to the observed data [45]. For this example with a piecewise linear basis for size $k = 6$ we get the resulting function in Fig. 1-14.

Choosing the basis size k automatically from the data is difficult, so instead k is usually set to equal the number of data points and

$$||w - V\vartheta|| + \lambda_s \vartheta^T S \vartheta \tag{1.2.23}$$

is minimised to penalise the sinuousness of the fitting [45]. Here, $\vartheta^T S \vartheta$ are the squared differences and λ_s is referred to as the smoothing parameter. This is determined by minimising the Generalised Cross Validation (GCV), which is a measure of how well the fitted function approximates each data point in turn [45]. The resulting GAM fit for this is shown in Fig. 1-15

As can be seen, even simple piecewise linear GAM fits can produce reasonable models for estimating a variable. The main downside to statistical approaches is the requirement of a large amount of data that spans the parameters of interest. For example, for surge we would need test data for different types and sizes of turbochargers, as well as different rigs and operating conditions.

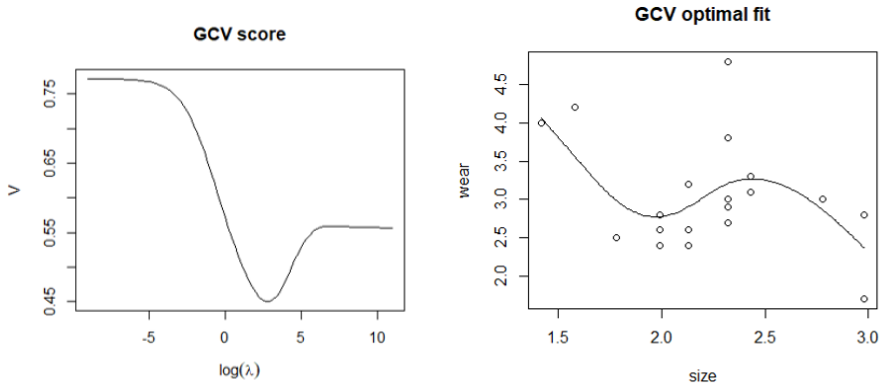

Figure 1-15: Left: Generalised Cross Validation score used to identify smoothing parameter $\lambda \equiv \lambda_s$ [45]. Right: GAM fit of engine wear vs size for this smoothing parameter [45].

Reduced Modelling

Finally, we will discuss reduced modelling approaches. These are techniques where we reduce the complexity (usually via reduction in the dimension) of the problem but still retain the dominant behaviours in the solution. There are numerous approaches that fit in this category; some follow formal procedures and others have a more flexible, ad-hoc method.

One approach is called averaging. As the name suggests, this is where we replace the original functions of the system with the average over one or more dimensions.

Averaging over time is commonly used in dynamical systems to give asymptotic approximations to the original time-dependent system [46]. For example, suppose we have a periodic system dependent on some small parameter ϵ,

$$\dot{x} = \epsilon g(x, t, \epsilon), \quad g(x, t, \epsilon) = g(x, t + T, \epsilon). \tag{1.2.24}$$

Since ϵ is small, the change in x with time is slow in comparison to the period of oscillation T. Often we are interested in the overall dynamic behaviour and less interested in the small fluctuations with time. Therefore, we can compute the time average of the function g by

$$\bar{g}(x) = \frac{1}{T} \int_0^T g(x, s, 0) \ ds. \tag{1.2.25}$$

It has been shown that the solution w to $\dot{w} = \epsilon \bar{g}(w)$ will be within $\mathcal{O}(\epsilon)$ of the true

solution $x(t)$ for $t < \frac{1}{\epsilon}$, so we can use w to give us insight to the overall dynamic behaviour of the system [46].

It is possible to use averaging with systematic asymptotic methods in order to capture more of the solution complexity. For example, suppose we have flow down a straight pipe in the x direction, then the average flows in the y and z directions would be zero. We could write the flow velocity as

$$\mathbf{u}(t,x,y,z) = \bar{u}(t,x)\mathbf{e}_x + \tilde{\mathbf{u}}(t,x,y,z), \tag{1.2.26}$$

where $\tilde{\mathbf{u}}$ is the deviation of the flow from the average flow. This deviation is likely to be largest at the pipe walls, and so Boundary Layer Theory (see for example [47]) could be applied to understand more of the flow dynamics and help quantify the error of the averaging approximation.

Another reduced modelling approach is Galerkin truncations. This is where variables are expanded in terms of basis functions. That way, model reduction can be achieved by selecting the first few dominant terms.

To see this, suppose we wish to understand the behaviour of convection currents in fluids. This requires the coupled incompressible Navier-Stokes and thermal convection equations:

$$u_t + \mathbf{u}\cdot\nabla\mathbf{u} = -\nabla p + \sigma_p\Delta\mathbf{u} + r_a\sigma_p\varphi\hat{k}, \tag{1.2.27}$$

$$\nabla\cdot\mathbf{u} = 0, \tag{1.2.28}$$

$$\varphi_t + \mathbf{u}\cdot\nabla\varphi = u_3 + \Delta\varphi, \tag{1.2.29}$$

where subscript t denotes differentiation with respect to time, r_a is the Rayleigh number, and σ_p is the Prandtl number, and $\mathbf{u} = u_1\hat{i} + u_2\hat{j} + u_3\hat{k}$ with unit vectors $\hat{i},\hat{j},\hat{k}$ [48].

The incompressibility condition (Eq. 1.2.28) allows us to define a stream function ψ where $u_1 = 0$,

$$u_2 = \frac{\partial\psi}{\partial z}, \quad \text{and} \quad u_3 = -\frac{\partial\psi}{\partial y}. \tag{1.2.30}$$

This transforms the system into

$$\zeta_t + J = \sigma_p \Delta\zeta + r_a \sigma_p \varphi_y, \tag{1.2.31}$$

$$\varphi_t + J = \Delta\varphi - \psi_y, \tag{1.2.32}$$

$$\zeta = -\Delta\psi, \tag{1.2.33}$$

where J is the Jacobian of (ζ, ψ) with respect to (y, z) [48].

We can now expand the stream function, ψ, and the temperature function, φ, in terms of a Fourier-Galerkin expansion to get

$$\psi(y, z, t) = \sum_{m,n \in \mathbb{C}} w_{n,m} exp(in\pi z) exp(im\pi y) \tag{1.2.34}$$

$$\varphi(y, z, t) = \sum_{m,n \in \mathbb{C}} v_{n,m} exp(in\pi z) exp(im\pi y). \tag{1.2.35}$$

where $i = \sqrt{-1}$ and $\mathbb{C}$ denotes complex numbers [48].

This is where we can choose the number of terms we wish to take in the expansion to form a reduced model. Here, we will choose to take one term in the stream function and two in the temperature function. This results in

$$\psi(y, z, t) = w(t) \sin(\pi z) \sin(k\pi y) \tag{1.2.36}$$

$$\varphi(y, z, t) = v_1(t) \sin(\pi z) \cos(k\pi y) + v_2(t) \sin(2\pi z), \tag{1.2.37}$$

where k is the wave number [48].

We can substitute these formulae into the above PDEs. This is then simplified further by multiplying by $\sin(\pi z) \sin(k\pi y)$ and integrating over the y and z directions. This leaves us with three ODEs:

$$w_t = -\sigma_p \pi (1 + k^2) w(t) - \frac{k\pi}{\pi(1 + k^2)} \sigma_p r_a v_1(t) \tag{1.2.38}$$

$$v_{1t} = -k\pi^2 w(t) v_2(t) - \pi(1 + k^2) v_1(t) - k\pi w(t) \tag{1.2.39}$$

$$v_{2t} = \frac{\pi^2}{k} w(t) v_1(t) - \pi^2 v_2(t) \tag{1.2.40}$$

[48]. This system is far simpler than the original, and is of the form of the known

Lorenz system:

$$X_t = c_1(Y - X) \tag{1.2.41}$$

$$Y_t = -Y + c_2 X - XZ \tag{1.2.42}$$

$$Z_t = -c_3 Z + XY, \tag{1.2.43}$$

for constants c_i, which has been frequently studied via dynamical systems analysis as it is known to exhibit chaotic behaviour [48]. Therefore, it is possible to gain understanding of convection currents in fluids by studying the far simpler Lorenz equations.

1.2.3 Discussion of Approaches

Numerical

The accuracy of numerical simulations of flows has increased dramatically over the past decade due to the rapid growth in high speed computing power. Spectral, or spectral element, methods may be more computationally efficient than standard CFD codes, but they are both typically run on high-performance super computers with parallel code in order to achieve maximum accuracy in the shortest amount of time.

Since surge cycles often experience local or small scale phenomena like rotating stall, recirculation, and eddy currents, full unsteady 3D simulations are required to completely capture the dynamics. CFD can struggle when modelling large scale phenomena that depend on small scale effects because it is too computationally expensive to perform this direct numerical simulation with the required fineness of mesh [40]. SM or SEM methods with a hierarchical basis are better able to deal with different scales within the simulation, so it is possible to use these methods for improvements to numerical surge simulation.

However, CFD is a well established tool and so new numerical models are unlikely to be taken up by companies. The industry is more likely to make use of less accurate but very quick models that can help give insight into the behaviour of surge during the early design stages, as they currently tend to rely heavily on experiments for this.

Experimental or Statistical

The advantage of using a predominantly experimental approach for surge studies is its simplicity because reading data or evaluating polynomial-like expressions are very quick computationally. However, surge is not always easy to measure experimentally. This is partially due to its damaging nature, which means a compressor cannot be operated in this region for long periods of time, and partially its complexity. For example, sometimes the surge limit can be recorded at different locations for the same experimental set-up, meaning it can be very sensitive to initial conditions.

Also, since surge is a system level phenomenon, the experimental results are often limited to the particular experimental set-up and not any compressor installation. This means that a large variety of tests would need to be performed in order to understand what behaviour is specific to that set-up and what can be applied universally. Conducting experiments are expensive in both equipment and time requirements; so approaches that require a large amount of experimental data are less desirable [49].

Furthermore, forming functions based mostly on experiment makes it difficult to gain intuition into why the system behaves as it does. This information is vital because if we can understand what causes the system to surge, it can help control the system to prevent it from occurring.

Reduced Modelling

Since numerical modelling would be too computationally expensive, and experimental data doesn't give us the required insight into the surge phenomenon, creating a reduced model appears to be the best way forward.

Of the methods discussed in the previous section, averaging is the approach that is easiest to compare back to the original physics. This not only makes any resulting simulations easier to understand but gives us the freedom to incorporate some empirically generated physical models into the system. Furthermore, it is possible to extend this approach at a later date to include asymptotics or Galerkin truncations on the perturbation from the average flow.

The strength of having a mathematically simple model is that it is relatively simple to perform analysis like stability analysis and bifurcation theory (see [28] for an example of this analysis applied to Greitzer's model). These are powerful tools which would

allow us to gain insight into how the dynamics of surge changes when parameters, such as geometrical dimensions, are varied.

To model surge in a compression system, we could average the Navier-Stokes equations for fluid motion in order to reduce the dimension from 3D in space to just 1D in space. Doing this in a way that minimises the number of fitted parameters, would result in a model with a high predictive ability.

Fast running, simple models that can predict the onset of surge for any turbocharger and test rig set up would hugely benefit the turbocharger industry. It would speed up the early design stages, due to less reliance on time consuming CFD, and reduce costs because of a reduced need for experimental testing.

Greitzer's model falls into this category of reduced models as it has integrated out the spatial dependence, making it only dependant on time. The use of Greitzer's model in this from has been relatively unchanged over the past 30 years. Therefore, using more analytical methods to develop a model similar to Greitzer's could provide some improvements.

Firstly, the derivation of Greitzer's model relied on the specific set up of a test rig. In particular, it required that the system contained a large exit plenum. However, a lot of systems do not include such a plenum, so using the averaging technique on the specific test rig or engine set up could improve accuracy of the model results.

Also, Greitzer's ODEs are simplified ODEs with nonlinearity only appearing through the assumed compressor and throttle characteristics. In contrast, by applying averaging methods to the nonlinear Navier Stokes equations we could systematically retain all required nonlinear terms and thus generate more accurate simulations.

Moreover, if we average to reduce the unsteady Navier Stokes equations from 3D to 1D spatially, we could evaluate the resulting PDE of time and space to simulate the pressure and mass flow waves travelling through the system pipework. How these waves interact with, say, their reflections, could provide some useful understanding of the system level surge phenomena. Also, the PDE system being only 1D in space would still run very quickly in comparison to CFD.

It is also important to note that systems like Greitzer's rely on the specification of a steady-state compressor characteristic. We could create a reduced model for this by also using the technique of averaging on the steady Navier Stokes equations to reduce the system to 1D in space. The benefit of using the same mathematical technique for

both parts of the surge model is that we would have consistency of assumptions with both models.

Also, a reduced model for the compressor characteristic that is 1D in space would provide more detail than the meanline modelling approach. It would allow for simulation of the steady-state flow throughout the compressor, rather than at the specific regions that a meanline models evaluate over. Furthermore, as it would be developed directly from the Navier Stokes equations, it can be created in a way that reduces the amount of dependence on empirical loss models which would improve its predictive capability and remove the need to tune the characteristic to a particular compressor.

1.3 Aims of Thesis

This thesis aims to:

- Create a predictive model for the onset of compressor surge.
  This model will need to balance the model accuracy with computational efficiency. Therefore, we aim to develop a model that is as simple as possible, while still capturing the main dynamics of surge.

- Gain further understanding of surge dynamics.
  This includes understanding the routes into surge, the pressure wave dynamics in the compression system, and the stability of the system. Insight will be obtained from both the development of, and the analysis of, any reduced order surge models.

1.4 Structure of Thesis

Chapter 2 describes the initial formulation for a reduced order model for surge. It begins by understanding the fundamental equations of fluid motion, and then uses averaging techniques to develop a model to capture surge in a simple compression system.

The resulting model depends on the specification of compressor and throttle characteristics. Therefore, equations for these are developed, again using averaging techniques on the fundamental fluid equations.

Special care is taken during the creation of the compressor characteristic to ensure that only the most essential dynamics are included. Thus keeping the characteristic as computationally efficient as possible, but retaining the ability to capture all relevant surge dynamics.

Chapter 3 takes a more detailed look into the dynamics of the system when the flow in the compressor is reversed. The compressor characteristic is altered to ensure it captures the reserve flow dynamics correctly, and is validated via experiments.

Chapter 4 extends the model for the compressor characteristic to allow the reduced order surge model to capture both mild and deep surge oscillations. Also, the surge model is studied in its PDE form and solved numerically in order to simulate mass flow and pressure waves travelling through the system. The generated simulations are validated through experimental surge tests.

Chapter 5 performs stability analysis on the ODE form of the reduced order surge model. Linear stability analysis is used to determine what variables influence the location of the surge limit, and bifurcation theory is used to explain some of the dynamics observed in model simulations and experimental data.

Finally, Chapter 6 summaries the work undertaken in this thesis. It highlights the key insights into the physics behind the surge phenomenon gained during the development and analysis of the surge models. Suggestions for how this research could be extended in the future are also made.

This thesis follows the alternative thesis format and so Chapters 2, 3, and 4 contain papers that are published or submitted for publication.

Chapter 2

Reduced Model for Surge with Cubic-shaped Compressor Characteristics

Following from the discussion in Chapter 1, we shall address the thesis aims via the creation of a new reduced order model for compressor surge. We shall develop this by performing averaging techniques on the fundamental equations for fluid motion. Starting from these fundamental equations allows us to keep track of any assumptions being made, and ensure they are consistent throughout the model development.

2.1 Equations of Fluid Motion

There are three fundamental fluid equations that come from conservation laws. Namely, conservation of mass, momentum and energy. In this section, we will derive these equations so that we can gain a physical understanding of the individual terms.

2.1.1 Conservation of Mass

Consider a volume $V(t)$ of fluid moving with time. The mass of this volume is given by

$$m(t) = \int_{V(t)} \rho \ dV \tag{2.1.1}$$

where ρ is the density [50]. Since $V(t)$ is a closed system and matter cannot be created or destroyed, $m(t)$ is constant in time, i.e.

$$\frac{dm}{dt} = \frac{d}{dt}\int_{V(t)} \rho \ dV = 0. \tag{2.1.2}$$

We can use the Reynolds' Transport Theorem to take the differential through the integral sign. This gives us

$$\int_{V(t)} \frac{\partial \rho}{\partial t} + \nabla \cdot (\rho \mathbf{u}) \ dV = 0. \tag{2.1.3}$$

The first term is the change in mass with time within the volume $V(t)$, and the second is the mass flux into and out of the volume.

Since $V(t)$ is a arbitrary volume of fluid, this implies that the integrand must be zero. Hence, the conservation of mass can be written as

$$\frac{\partial \rho}{\partial t} + \nabla \cdot (\rho \mathbf{u}) = 0. \tag{2.1.4}$$

2.1.2 Conservation of Momentum (in a Rotating Frame)

Suppose that we have a continuum of fluid with velocity $\mathbf{u}(\mathbf{x}, t) = (u_1(\mathbf{x}, t), u_2(\mathbf{x}, t), u_3(\mathbf{x}, t))^T$, density $\rho(\mathbf{x}, t)$ and volume $V(\mathbf{x}, t)$, where $\mathbf{x} = (x_1, x_2, x_3)^T$ denotes position. The rate of change of a quantity of interest, say $g(\mathbf{x}, t)$, as we follow the fluid is given by

$$\frac{Dg}{Dt} = \frac{\partial g}{\partial t} + \sum_{i=1}^{3} \frac{\partial g}{\partial x_i}\frac{dx_i}{dt} = \frac{\partial g}{\partial t} + (\mathbf{u} \cdot \nabla) g \tag{2.1.5}$$

where $\frac{D}{Dt}$ is termed the total derivative [51].

Now, Newton's Second Law of motion states that the total force acting on a system is equal to its mass multiplied by its acceleration. Since mass $m = \rho V$, we can divide through by volume to get

$$\rho \frac{D\mathbf{u}}{Dt} = \tilde{\mathbf{F}} \tag{2.1.6}$$

where $\tilde{\mathbf{F}}$ is the force acting on fluid per unit volume [52].

By expanding the total derivative, adding conservation of mass (Eq. 2.1.4) multiplied

by $\mathbf{u}$, and noticing

$$(\rho\mathbf{u}\cdot\nabla)\mathbf{u}+\mathbf{u}\nabla\cdot(\rho\mathbf{u})=\nabla\cdot(\rho(\mathbf{u}\otimes\mathbf{u})), \tag{2.1.7}$$

Eq. 2.1.6 becomes

$$\frac{\partial}{\partial t}(\rho\mathbf{u})+\nabla\cdot(\rho(\mathbf{u}\otimes\mathbf{u}))=\tilde{\mathbf{F}}. \tag{2.1.8}$$

This is now in a similar form to the conservation of mass, where the first term is the change of momentum within the volume V and the second is the flux of momentum.

To find $\tilde{\mathbf{F}}$, we need to consider three types of forces acting on the fluid: (i) gravitational, (ii) internal stresses, and (iii) rotational.

For (i), Newton's second law tells us the force applied to the fluid will be $m\mathbf{g}$, where $\mathbf{g}$ is acceleration due to gravity. Therefore, on division by volume, $\tilde{\mathbf{F}}_{(i)}=\rho\mathbf{g}$.

For (ii), note that the force applied to the fluid is a stress, Π, acting on an area. Using the Divergence theorem, this becomes

$$\int_A \Pi\cdot dA=\int_V \nabla\cdot\Pi\ dV, \tag{2.1.9}$$

and so the force per unit volume is $\tilde{\mathbf{F}}_{(ii)}=\nabla\cdot\Pi$. It is normal to decompose the stresses into normal stresses (i.e. pressures) and shear stresses. Hence, $\Pi_{ij}=-p\delta_{ij}+\boldsymbol{\tau}_{ij}$ where δ_{ij} is the Kronecker delta and $\boldsymbol{\tau}$ is the deviatoric stress tensor, and so $\tilde{\mathbf{F}}_{(ii)}=-\nabla p+\nabla\cdot\boldsymbol{\tau}$ [53].

Finally, for (iii), suppose that a particle of fluid is in a rotating field of angular velocity $\boldsymbol{\Omega}$. Let S denote the stationary frame and R the rotating frame of reference. Then if the particle moved in the rotating frame, an observer in stationary frame would see this motion of the particle as well as the motion of the field. So if the particle has position $\mathbf{x}$, then

$$\left(\frac{d\mathbf{x}}{dt}\right)_S=\left(\frac{d\mathbf{x}}{dt}\right)_R+\boldsymbol{\Omega}\times\mathbf{x} \tag{2.1.10}$$

[54]. Differentiating this again, and noticing $\frac{d^2\mathbf{x}}{dt^2}=\frac{D\mathbf{u}}{Dt}$, gives us

$$\left(\frac{D\mathbf{u}}{Dt}\right)_S=\left(\frac{D\mathbf{u}}{Dt}\right)_R+\frac{d\boldsymbol{\Omega}}{dt}\times\mathbf{x}+2\boldsymbol{\Omega}\times\mathbf{u}+\boldsymbol{\Omega}\times(\boldsymbol{\Omega}\times\mathbf{x}) \tag{2.1.11}$$

[50]. Therefore, assuming the angular velocity is constant, Newton's second law gives us

$$\tilde{\mathbf{F}}=\rho\left(\frac{D\mathbf{u}}{Dt}\right)_R=\rho\left(\frac{D\mathbf{u}}{Dt}\right)_S-2\rho\boldsymbol{\Omega}\times\mathbf{u}-\rho\boldsymbol{\Omega}\times(\boldsymbol{\Omega}\times\mathbf{x}). \tag{2.1.12}$$

This means that the momentum in the rotating frame has two extra forces, $\tilde{\mathbf{F}}_{(iii)} = -2\rho\boldsymbol{\Omega} \times \mathbf{u} - \rho\boldsymbol{\Omega} \times (\boldsymbol{\Omega} \times \mathbf{x})$, than if the flow field was stationary. The term $2\rho\boldsymbol{\Omega} \times \mathbf{u}$ is called the Coriolis force and $\rho\boldsymbol{\Omega} \times (\boldsymbol{\Omega} \times \mathbf{x})$ is called the centrifugal force [51].

Putting all these together, we get that

$$\tilde{\mathbf{F}} = \rho\mathbf{g} - \nabla p + \nabla \cdot \boldsymbol{\tau} - 2\rho(\boldsymbol{\Omega} \times \mathbf{u}) - \rho(\boldsymbol{\Omega} \times (\boldsymbol{\Omega} \times \mathbf{x})) \tag{2.1.13}$$

is the total force acting on fluid per unit volume. Thus, the conservation of momentum in a rotating frame becomes

$$\frac{\partial}{\partial t}(\rho\mathbf{u}) + \nabla \cdot (\rho(\mathbf{u} \otimes \mathbf{u})) + 2\rho(\boldsymbol{\Omega} \times \mathbf{u}) + \rho(\boldsymbol{\Omega} \times (\boldsymbol{\Omega} \times \mathbf{x})) = \rho\mathbf{g} - \nabla p + \nabla \cdot \boldsymbol{\tau}. \tag{2.1.14}$$

2.1.3 Conservation of Energy

The first law of thermodynamics states that

$$\frac{DQ}{Dt} = \frac{DU}{Dt} + \frac{DW}{Dt}, \tag{2.1.15}$$

where Q is the heat energy supplied, U is the internal energy and $\frac{DW}{Dt}$ is the work done by the system.

There are two ways in which work is done on the fluid. The first is pressure causing a change in volume, i.e.

$$p\frac{D}{Dt}\left(\frac{1}{\rho}\right). \tag{2.1.16}$$

This can be written as $\frac{p}{\rho}\nabla \cdot \mathbf{u}$ because conservation of mass in total derivative form gives us

$$\frac{D\rho}{Dt} = -\rho(\nabla \cdot \mathbf{u}). \tag{2.1.17}$$

The second is the work done on adjacent layers of a fluid by the action of shear forces [55], i.e.

$$\frac{1}{\rho}\boldsymbol{\tau} : \nabla\mathbf{u} = \frac{1}{\rho}\sum_{i=1}^{3}\sum_{j=1}^{3}\boldsymbol{\tau}_{ij}\frac{\partial u_i}{\partial x_j}. \tag{2.1.18}$$

Therefore, on multiplication by ρ, the equation for thermal energy is given by

$$\rho\frac{DQ}{Dt} = \rho\frac{DU}{Dt} + p\nabla \cdot \mathbf{u} - \boldsymbol{\tau} : \nabla\mathbf{u}. \tag{2.1.19}$$

Now, taking the dot product of $\mathbf{u}$ with the conservation of momentum (Eq. 2.1.6 with 2.1.13) results in

$$\rho\mathbf{u}\cdot\frac{D\mathbf{u}}{Dt}=\rho\mathbf{u}\cdot\mathbf{g}-\mathbf{u}\cdot\nabla p+\mathbf{u}\cdot(\nabla\cdot\boldsymbol{\tau})-2\rho\mathbf{u}\cdot(\boldsymbol{\Omega}\times\mathbf{u})-\rho\mathbf{u}\cdot(\boldsymbol{\Omega}\times(\boldsymbol{\Omega}\times\mathbf{x})). \quad (2.1.20)$$

Notice that, $\mathbf{u}\cdot(\boldsymbol{\Omega}\times\mathbf{u})=0$,

$$\mathbf{u}\cdot(\boldsymbol{\Omega}\times(\boldsymbol{\Omega}\times\mathbf{x}))=-(\boldsymbol{\Omega}\times\mathbf{x})\cdot(\boldsymbol{\Omega}\times\mathbf{u})=-\frac{D}{Dt}\left(\frac{|\boldsymbol{\Omega}\times\mathbf{x}|^2}{2}\right), \quad (2.1.21)$$

and

$$\mathbf{u}\cdot\mathbf{g}=-\frac{D(g\tilde{h})}{Dt}, \quad (2.1.22)$$

where $\tilde{h}$ is vertical height as $\mathbf{u}\cdot\mathbf{g}$ is the component of velocity acting in the direction of gravity [52]. Therefore, we can write Eq. 2.1.20 in terms of total derivatives by

$$\rho\frac{D}{Dt}\left(\frac{|\mathbf{u}|^2}{2}+g\tilde{h}-\frac{|\boldsymbol{\Omega}\times\mathbf{x}|^2}{2}\right)=-\mathbf{u}\cdot\nabla p+\mathbf{u}\cdot(\nabla\cdot\boldsymbol{\tau}). \quad (2.1.23)$$

Finally, since $-\mathbf{u}\cdot\nabla p=p(\nabla\cdot\mathbf{u})-\nabla\cdot(p\mathbf{u})$, we have that

$$p(\nabla\cdot\mathbf{u})=\rho\frac{D}{Dt}\left(\frac{|\mathbf{u}|^2}{2}+g\tilde{h}-\frac{|\boldsymbol{\Omega}\times\mathbf{x}|^2}{2}\right)+\nabla\cdot(p\mathbf{u})-\mathbf{u}\cdot(\nabla\cdot\boldsymbol{\tau}). \quad (2.1.24)$$

Combining this with Eq. (2.1.19), and using $\mathbf{u}\cdot(\nabla\cdot\boldsymbol{\tau})+\boldsymbol{\tau}:\nabla\mathbf{u}=\nabla\cdot(\boldsymbol{\tau}\cdot\mathbf{u})$, we get

$$\rho\frac{DQ}{Dt}=\rho\frac{D}{Dt}\left(\frac{|\mathbf{u}|^2}{2}+g\tilde{h}-\frac{|\boldsymbol{\Omega}\times\mathbf{x}|^2}{2}+U\right)+\nabla\cdot(p\mathbf{u})-\nabla\cdot(\boldsymbol{\tau}\cdot\mathbf{u}). \quad (2.1.25)$$

Define E to be the total specific energy in a rotating frame, i.e.

$$E=\frac{|\mathbf{u}|^2}{2}+g\tilde{h}+U-\frac{|\boldsymbol{\Omega}\times\mathbf{x}|^2}{2}. \quad (2.1.26)$$

Then, the conservation of energy becomes

$$\rho\frac{DE}{Dt}+\nabla\cdot(p\mathbf{u})-\nabla\cdot(\boldsymbol{\tau}\cdot\mathbf{u})=\rho\dot{Q}, \quad (2.1.27)$$

or, on expansion of the total derivative and addition of conservation of mass (Eq. 2.1.4) multiplied by E,

$$\frac{\partial}{\partial t}(\rho E)+\nabla\cdot(\rho\mathbf{u}E+p\mathbf{u})-\nabla\cdot(\boldsymbol{\tau}\cdot\mathbf{u})=\rho\dot{Q}. \quad (2.1.28)$$

2.1.4 Initial Assumptions

Since we are looking in particular at air flow, we can make some initial assumptions. Firstly, we will assume that we have a perfect gas, so $U = c_v T$ for a constant c_v, and an ideal gas so

$$p = \rho R T. \tag{2.1.29}$$

We can also assume that gravitational effects are negligible, because air density is relatively small and we are assuming our turbochargers are not too far off the ground.

Finally, for the sake of model simplicity, we will assume we have no heat transfer and no viscous dissipation, i.e. the terms $\dot{Q}$ and $\nabla \cdot (\tau \cdot \mathbf{u})$ are neglected. However, we will still consider dissipative losses like friction.

2.2 Reduced Model for Surge

The next step in modelling surge is to apply the fundamental equations of fluid motion to a situation where we know surge is observed.

In order to find the surge limit for turbochargers experimentally, they are usually installed on a gas stand where the compressor and turbine sections are independently controlled. Different amounts of hot, compressed air can be fed into the turbine section to set the rotor speed to a desired value. Figure 2-1 shows the compressor-side installation, where the compressor is connected to a valve via a simple pipe. As the valve is shut, the amount of air going through the compressor is restricted and surge can be observed.

Let us model the air in the pipe between the compressor and throttle valve. The equations of motion give us:

$$\frac{\partial \rho}{\partial t} + \nabla \cdot (\rho \mathbf{u}) = 0, \tag{2.2.1}$$

$$\frac{\partial}{\partial t}(\rho \mathbf{u}) + \nabla \cdot (\rho(\mathbf{u} \otimes \mathbf{u})) = -\nabla p + \nabla \cdot \boldsymbol{\tau}, \tag{2.2.2}$$

$$\frac{\partial}{\partial t}(\rho E) + \nabla \cdot (\rho \mathbf{u} E + p\mathbf{u}) = 0, \tag{2.2.3}$$

where

$$E = \frac{|\mathbf{u}|^2}{2} + c_v T \tag{2.2.4}$$

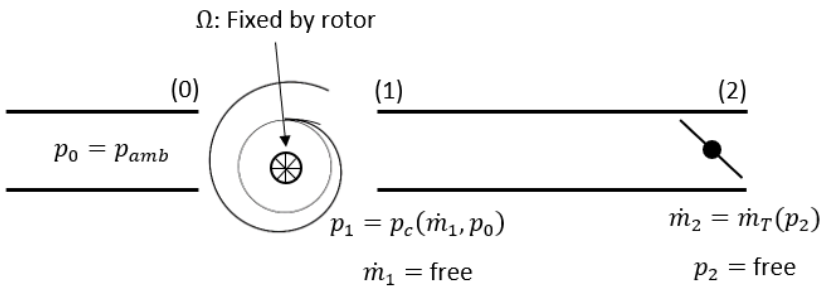

Figure 2-1: Schematic of compressor installation used for reduced order surge model. The impeller rotational speed, Ω is set by the turbine rotor. The inlet to the compressor is assumed to be ambient air. The outlet is assumed to be a constant area pipe ending in a throttle valve.

as $\mathbf{\Omega} = 0$ because we are in a stationary frame of reference. Notice that, since $p = \rho RT$, we can write

$$E = \frac{|\mathbf{u}|^2}{2} + \frac{c_v}{R}\frac{p}{\rho} = \frac{|\mathbf{u}|^2}{2} + \frac{1}{\gamma - 1}\frac{p}{\rho} \tag{2.2.5}$$

where γ is the specific heat ratio.

For simplicity, let's assume that we have no shear stress forces (including friction) acting on the flow, so $\nabla \cdot \boldsymbol{\tau} = 0$. Therefore, the energy equation in total derivative form (Eq. 2.1.27) after expanding $\nabla \cdot (p\mathbf{u})$ becomes

$$\rho \frac{D}{Dt}\left(\frac{|\mathbf{u}|^2}{2} + \frac{1}{\gamma - 1}\frac{p}{\rho}\right) = -p\nabla \cdot \mathbf{u} - \mathbf{u} \cdot \nabla p. \tag{2.2.6}$$

Similarly, the momentum equation in total derivative form (Eq. 2.1.6) becomes

$$\rho \frac{D\mathbf{u}}{Dt} = -\nabla p. \tag{2.2.7}$$

Taking the dot product of this with $\mathbf{u}$ gives us

$$\rho \frac{D}{Dt}\left(\frac{|\mathbf{u}|^2}{2}\right) = \rho \mathbf{u} \cdot \frac{D\mathbf{u}}{Dt} = -\mathbf{u} \cdot \nabla p, \tag{2.2.8}$$

so subtracting this from Eq. 2.2.6 leaves us with

$$\rho \frac{D}{Dt}\left(\frac{1}{\gamma - 1}\frac{p}{\rho}\right) = -p\nabla \cdot \mathbf{u}. \tag{2.2.9}$$

Finally, using conservation of mass (Eq. 2.1.17), we get that

$$\rho \frac{D}{Dt}\left(\frac{1}{\gamma-1}\frac{p}{\rho}\right) = \frac{p}{\rho}\frac{D\rho}{Dt}, \tag{2.2.10}$$

which reduces to

$$\frac{D}{Dt}\left(\ln\left(\frac{p}{\rho^\gamma}\right)\right) = 0. \tag{2.2.11}$$

Integrating this, and rearranging, gives $p = \kappa\rho^\gamma$ for some constant κ. When the energy equation collapses to this form, the system is called isentropic.

Suppose we are in Cartesian coordinates with the pipe sitting along the x-direction. Then, since we are primarily interested in how the dynamics change along the length of the pipe, we can average the system over the y and z-directions. Therefore, the average of a function G will be

$$\bar{G}(x) = \frac{1}{A}\iint_A G(x,y,z)\ dydz, \tag{2.2.12}$$

where A is the cross-sectional area of the pipe.

Notice that we can write the conservation of mass as

$$\frac{\partial\rho}{\partial t} + \frac{\partial\rho u_x}{\partial x} + \nabla_{yz}\cdot(\rho\mathbf{u}) = 0, \tag{2.2.13}$$

where

$$\nabla_{yz}\cdot(\rho\mathbf{u}) = \frac{\partial\rho u_y}{\partial y} + \frac{\partial\rho u_z}{\partial z} \tag{2.2.14}$$

is the divergence purely in the y and z direction. Therefore, integrating the conservation of mass gives us

$$\iint_A \frac{\partial\rho}{\partial t}\ dydz + \iint_A \frac{\partial\rho u_x}{\partial x}\ dydz + \iint_A \nabla_{yz}\cdot(\rho\mathbf{u})\ dydz = 0. \tag{2.2.15}$$

For the first two terms, the derivative can be pulled out of the integral because A does not depend on t or x and the definition of the average (Eq. 2.2.12) can be used. For the final term, we can use the Divergence theorem in the 2D y-z plane. This gives us

$$\frac{\partial}{\partial t}\left(A\bar{\rho}\right) + \frac{\partial}{\partial x}\left(A\overline{\rho u_x}\right) + \int_{\partial A}(\rho\mathbf{u})\cdot\hat{\mathbf{n}}\ dS = 0, \tag{2.2.16}$$

where $\hat{\mathbf{n}}$ is the outward pointing unit normal and S is the surface of the pipe.

The flux leaving the pipe through the walls is $\mathbf{u}\cdot\hat{\mathbf{n}}$. Therefore, we will assume $\mathbf{u}\cdot\hat{\mathbf{n}} = 0$

so no air can escape the pipe through the walls. This leaves us with

$$\frac{\partial}{\partial t}\left(A\bar{\rho}\right)+\frac{\partial}{\partial x}\left(A\overline{\rho u_x}\right)=0. \tag{2.2.17}$$

Similarly for the x-component of the conservation of momentum, we can integrate

$$\frac{\partial \rho u_x}{\partial t}+\frac{\partial \rho u_x^2}{\partial x}+\nabla_{yz}\cdot\left(\rho \mathbf{u} u_x\right)=-\frac{\partial p}{\partial x}, \tag{2.2.18}$$

and pass the integrals through the derivatives of t and x to get

$$\frac{\partial}{\partial t}\left(A\overline{\rho u_x}\right)+\frac{\partial}{\partial x}\left(A\overline{\rho u_x^2}\right)+\int_{\partial A}\rho u_x \mathbf{u}\cdot\hat{\mathbf{n}}\ dS=-\frac{\partial}{\partial x}\left(A\bar{p}\right). \tag{2.2.19}$$

Thus, using the fact that $\mathbf{u}\cdot\hat{\mathbf{n}}=0$, we have

$$\frac{\partial}{\partial t}\left(A\overline{\rho u_x}\right)+\frac{\partial}{\partial x}\left(A\overline{\rho u_x^2}\right)=-\frac{\partial}{\partial x}\left(A\bar{p}\right). \tag{2.2.20}$$

For the y and z components of the conservation of momentum write $\mathbf{u}_{yz}=(u_y,u_z)^T$. Then we have

$$\frac{\partial \rho \mathbf{u}_{yz}}{\partial t}+\frac{\partial}{\partial x}(\rho u_x \mathbf{u}_{yz})+\nabla_{yz}\cdot\left(\rho \mathbf{u}_{yz}\otimes\mathbf{u}_{yz}\right)=-\nabla_{yz}p. \tag{2.2.21}$$

Following the same procedure as above, this gives us

$$\frac{\partial}{\partial t}(A\overline{\rho \mathbf{u}_{yz}})+\frac{\partial}{\partial x}(A\overline{\rho u_x \mathbf{u}_{yz}})=-\oint_{\partial A} p\ dS \tag{2.2.22}$$

because the no-flux boundary condition means that $\int_{\partial A}\rho \mathbf{u}_{yz}\mathbf{u}_{yz}\cdot\hat{\mathbf{n}}\ dS=0$. If we assume that the pressure is the same at every point on the pipe surface, then

$$\oint_{\partial A} p\ dS=0, \tag{2.2.23}$$

and writing in component form we have

$$\frac{\partial}{\partial t}(A\overline{\rho u_y})+\frac{\partial}{\partial x}(A\overline{\rho u_x u_y})=0. \tag{2.2.24}$$

$$\frac{\partial}{\partial t}(A\overline{\rho u_z})+\frac{\partial}{\partial x}(A\overline{\rho u_x u_z})=0. \tag{2.2.25}$$

A common problem with the method of averaging is that we end up with more unknown

quantities than equations. In our case we have eight variables but only five equations because we do not have relations for $\overline{\rho u_x^2}, \overline{\rho u_x u_y}$, and $\overline{\rho u_x u_z}$. Therefore, a closure rule is required in order to find a unique solution to the PDEs.

The simplest closure rule is to say

$$\overline{ab} \approx \bar{a}\bar{b}, \quad \forall a, b. \tag{2.2.26}$$

Notice that we can write $a = \bar{a} + \epsilon\tilde{a}$ where $\bar{a}$ is the average of a and $\epsilon\tilde{a}$ is the remainder. By adding the assumption that $||\tilde{a}||_{L^2}$ is of the same order as $||\bar{a}||_{L^2}$, we enforce that ϵ is of the order of magnitude of the deviation of the variable a from its mean value $\bar{a}$.

Similarly, we can write $b = \bar{b} + \delta\tilde{b}$ for $||\tilde{b}||_{L^2} = \mathcal{O}(||\bar{b}||_{L^2})$. Therefore, taking the average of the product ab gives us

$$\overline{ab} = \overline{\bar{a}\bar{b} + \epsilon\tilde{a}\bar{b} + \delta\tilde{b}\bar{a} + \epsilon\delta\tilde{a}\tilde{b}} = \bar{a}\bar{b} + \epsilon\delta\overline{\tilde{a}\tilde{b}} \tag{2.2.27}$$

because $\overline{\tilde{a}} = \overline{\tilde{b}} = 0$. So this closure rule is a good approximation, especially if one of ϵ or δ are small which implies that a or b do not vary too much from their mean.

Other closure rules are possible that will push the approximation error to higher order. For example, to find an equation for $\overline{\rho u_x^2}$ we can multiply the x-component of the momentum equation by u_x to get

$$u_x \frac{\partial}{\partial t}(\rho u_x) + u_x \nabla \cdot (\rho u_x \mathbf{u}) = -u_x \frac{\partial p}{\partial x}. \tag{2.2.28}$$

Noticing that

$$u_x \frac{\partial}{\partial t}(\rho u_x) + u_x \nabla \cdot (\rho u_x \mathbf{u}) = \rho u_x \frac{\partial u_x}{\partial t} + \rho u_x \mathbf{u} \cdot \nabla u_x + \underbrace{u_x^2 \frac{\partial \rho}{\partial t} + u_x^2 \nabla \cdot (\rho \mathbf{u})}_{=0} \tag{2.2.29}$$

due to conservation of mass, we get

$$\left(u_x \frac{\partial}{\partial t}(\rho u_x) + u_x \nabla \cdot (\rho u_x \mathbf{u}) \right) + \left(\rho u_x \frac{\partial u_x}{\partial t} + \rho u_x \mathbf{u} \cdot \nabla u_x \right) = -2u_x \frac{\partial p}{\partial x}, \tag{2.2.30}$$

which can be simplified to

$$\frac{\partial}{\partial t}(\rho u_x^2) + \nabla \cdot (\rho u_x^2 \mathbf{u}) = -2u_x \frac{\partial p}{\partial x}. \tag{2.2.31}$$

Therefore, we can average this to get

$$\frac{\partial}{\partial t}(A\overline{\rho u_x^2}) + \frac{\partial}{\partial x}(A\overline{\rho u_x^3}) = -2A\overline{\left(u_x \frac{\partial p}{\partial x}\right)}. \tag{2.2.32}$$

This means we have an evolution equation for the $\overline{\rho u_x^2}$ and now only require a closure rule for higher order terms, for example,

$$\overline{\rho u_x^3} = \frac{\overline{\rho u_x}\,\overline{\rho u_x^2}}{\bar{\rho}} \tag{2.2.33}$$

which should give a more accurate approximation than Eq. 2.2.26.

However, the system is more complex because we have another PDE that needs solving, and we would have to include a closure rule for $\overline{u_x \frac{\partial p}{\partial x}}$ as well. Therefore, we will close our system by using Eq. 2.2.26 because we are aiming to find a mathematically simple system that captures the main surge dynamics.

This means that Eqs. 2.2.24 becomes

$$\frac{\partial}{\partial t}(A\bar{\rho}\bar{u}_y) + \frac{\partial}{\partial x}(A\bar{\rho}\bar{u}_x\bar{u}_y) = 0. \tag{2.2.34}$$

Since we expect the momentum to change down the length of the pipe, we need to allow $\bar{\rho}\bar{u}_x$ to vary with x. Therefore, the only way to satisfy this equation is to assume $\bar{u}_y = 0$. The same argument applied to Eq. 2.2.25 leads to $\bar{u}_z = 0$.

Therefore, the conservation of mass, momentum and energy for our system becomes

$$\frac{\partial}{\partial t}(A\rho) + \frac{\partial}{\partial x}(A\rho u) = 0, \tag{2.2.35}$$

$$\frac{\partial}{\partial t}(A\rho u) + \frac{\partial}{\partial x}(A\rho u^2) = -\frac{\partial}{\partial x}(Ap), \tag{2.2.36}$$

$$p = \kappa\rho^\gamma, \tag{2.2.37}$$

where we have used $u \equiv u_x$ and dropped the bars for notational ease.

Using Eq. 2.2.37 and the definition of mass flow rate $\dot{m} = A\rho u$, we can re-write this

system as

$$\frac{\partial p}{\partial t} = -\frac{\gamma \kappa^{\frac{1}{\gamma}}}{A} p^{\frac{\gamma-1}{\gamma}} \frac{\partial \dot{m}}{\partial x} \tag{2.2.38}$$

$$\frac{\partial \dot{m}}{\partial t} = -A\frac{\partial p}{\partial x} - \frac{\kappa^{\frac{1}{\gamma}}}{A}\frac{\partial}{\partial x}\left(\frac{\dot{m}^2}{p^{\frac{1}{\gamma}}}\right). \tag{2.2.39}$$

These PDEs simulate the averaged mass flow and pressure in any constant-area, frictionless pipe. It is only with the specification of boundary conditions that this becomes specific to the compression system in Fig. 2-1.

A common way to specify these is to have steady-state characteristics for the compressor and the throttle, usually $p_c(\dot{m})$ for the compressor and $\dot{m}_T(p)$ for the throttle. These functions give relations between the mass flow and pressure if the component was operating in a steady manor. Therefore, using these as boundary conditions creates a quasi-steady model which assumes the components operate in a steady manor at each instant in time.

When surge occurs, oscillations in mass flow and pressure are usually observed at all locations in the pipe. Therefore, we could simplify Eqs. 2.2.38 and 2.2.39 further by averaging over the length of the pipe and still have the ability to identify unsteady behaviour.

Let L be the length of the pipe and label quantities at $x = 0$ and $x = L$ as 1 and 2 respectively. Then integrating Eqs. 2.2.38 and 2.2.39 in x between 0 and L gives

$$\frac{\partial \bar{p}}{\partial t} = \frac{\gamma \kappa^{\frac{1}{\gamma}}}{AL} \bar{p}^{\frac{\gamma-1}{\gamma}} (\dot{m}_1 - \dot{m}_2), \tag{2.2.40}$$

$$\frac{\partial \overline{\dot{m}}}{\partial t} = \frac{A}{L}(p_1 - p_2) + \frac{\kappa^{\frac{1}{\gamma}}}{AL}\left(\frac{\dot{m}_1^2}{p_1^{\frac{1}{\gamma}}} - \frac{\dot{m}_2^2}{p_2^{\frac{1}{\gamma}}}\right). \tag{2.2.41}$$

With the equations in this form, we can directly incorporate the boundary conditions discussed above to get

$$\frac{\partial \bar{p}}{\partial t} = \frac{\gamma \kappa^{\frac{1}{\gamma}}}{AL} \bar{p}^{\frac{\gamma-1}{\gamma}} (\dot{m}_1 - \dot{m}_T(p_2)), \tag{2.2.42}$$

$$\frac{\partial \overline{\dot{m}}}{\partial t} = \frac{A}{L}(p_c(\dot{m}_1) - p_2) + \frac{\kappa^{\frac{1}{\gamma}}}{AL}\left(\frac{\dot{m}_1^2}{p_c(\dot{m}_1)^{\frac{1}{\gamma}}} - \frac{\dot{m}_T(p_2)^2}{p_2^{\frac{1}{\gamma}}}\right). \tag{2.2.43}$$

To complete this system we need to specify $\dot{m}_1$ and p_2. Since we wish them to be freely influenced by the air in the pipe, we set these to equal the average $\bar{\dot{m}}$ and $\bar{p}$ respectively.

This choice means that information travels instantaneously down the pipe, i.e. the mass flow near the compressor is instantly impacted by any change in the average flow caused by the throttle valve, rather than there being time for this information to propagate as a wave down the pipe. However, this does not impact its ability to detect unsteady behaviour, it may just reduce the accuracy of timescales (like oscillation frequency) observed in the system.

Therefore, on dropping the bars, we get the following ODEs describing the compression system:

$$\frac{dp}{dt} = \frac{\gamma\kappa^{\frac{1}{\gamma}}}{AL} p^{\frac{\gamma-1}{\gamma}} (\dot{m} - \dot{m}_T(p)), \tag{2.2.44}$$

$$\frac{d\dot{m}}{dt} = \frac{A}{L}(p_c(\dot{m}) - p) + \frac{\kappa^{\frac{1}{\gamma}}}{AL}\left(\frac{\dot{m}^2}{p_c(\dot{m})^{\frac{1}{\gamma}}} - \frac{\dot{m}_T(p)^2}{p^{\frac{1}{\gamma}}}\right). \tag{2.2.45}$$

Notice that we can obtain the Moore-Greitzer formulation by linearising this. For Eq. 2.2.44, removing the nonlinear terms simply gives

$$\frac{d\dot{m}}{dt} = \frac{A}{L}(p_c(\dot{m}) - p) \tag{2.2.46}$$

which is equivalent to Eq. 1.2.12. For Eq. 2.2.45, we can use the fact that the speed of sound a is given by

$$a^2 = \frac{dp}{d\rho} = \kappa\gamma\rho^{\gamma-1} = \gamma\kappa^{\frac{1}{\gamma}} p^{\frac{\gamma-1}{\gamma}}. \tag{2.2.47}$$

Therefore, this equation is linearised by replacing a with its average, $\bar{a}$ =const., to give

$$\frac{dp}{dt} = \frac{\bar{a}^2}{AL}(\dot{m} - \dot{m}_T(p)), \tag{2.2.48}$$

which is equivalent to Eq. 1.2.13.

This means that our model generated by averaging the fundamental equations of motion will improve on the well used Moore-Greitzer formulation by capturing some of the nonlinear dynamics of surge.

Regardless of whether we use the PDE, ODE or Moore-Greitzer form of our reduced order surge model, we require the specification of steady-state characteristics for the throttle and compressor. In the following sections, we will derive these in a similar

manor to above to ensure we have consistency across the entire model.

2.3 Throttle Characteristic

In order to model the throttle, we shall assume that in steady-state it behaves like an orifice (see Fig. 2-2) where the pipe area changes instantly from one side of the throttle valve to the other.

The fundamental equations of motion for steady flow (i.e. $\frac{\partial}{\partial t} \equiv 0$) with no shear forces (i.e. $\nabla \cdot \boldsymbol{\tau} = 0$) gives us

$$\nabla \cdot (\rho \mathbf{u}) = 0 \tag{2.3.1}$$

$$\nabla \cdot (\rho(\mathbf{u} \otimes \mathbf{u})) = -\nabla p \tag{2.3.2}$$

$$\nabla \cdot (\rho \mathbf{u} E + p\mathbf{u}) = 0. \tag{2.3.3}$$

Similarly to Section 2.2, let's suppose we are in Cartesian coordinates with the orifice sitting along the x-direction. Then we can follow exactly the same procedure as above and average over the y and z directions.

Notice that averaging Eqs. 2.3.1 and 2.3.2 are identical to Eqs. 2.2.17 and 2.2.20 respectively, without the $\frac{\partial}{\partial t}$ terms.

For Eq. 2.3.3, notice that it can be written as $\nabla \cdot ((\rho E + p)\mathbf{u}) = 0$. This is of the same form as Eq. 2.3.1, and so we can follow the same averaging argument.

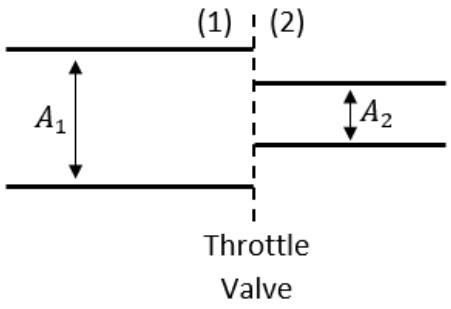

Figure 2-2: Schematic of orifice used to derive the steady-state throttle characteristic.

The resulting averaged equations, once the bars are dropped, are

$$\frac{\partial}{\partial x}\left(A\rho u_x\right) = 0 \tag{2.3.4}$$

$$\frac{\partial}{\partial x}\left(A\rho u_x^2\right) = -\frac{\partial}{\partial x}\left(Ap\right) \tag{2.3.5}$$

$$\frac{\partial}{\partial x}\left(A(\rho E + p)u_x\right) = 0, \tag{2.3.6}$$

where

$$E = \frac{u_x^2}{2} + \frac{1}{\gamma - 1}\frac{p}{\rho}. \tag{2.3.7}$$

Now, Eq. 2.3.4 tells us that $\dot{m} = A\rho u_x$ is constant. Similarly, Eq. 2.3.6 implies

$$A(\rho E + p)u_x = \text{const.}. \tag{2.3.8}$$

Dividing through by $\dot{m}$ and substituting in E transforms this into

$$\frac{u_x^2}{2} + \frac{\gamma}{\gamma - 1}\frac{p}{\rho} = \frac{\dot{m}^2}{2A^2\rho^2} + \frac{\gamma}{\gamma - 1}\frac{p}{\rho} = \text{const.}. \tag{2.3.9}$$

Therefore, labelling quantities by 1 or 2 for either side of the orifice (see Fig. 2-2), we get

$$\frac{\dot{m}_1^2}{2A_1^2\rho_1^2} + \frac{\gamma}{\gamma - 1}\frac{p_1}{\rho_1} = \frac{\dot{m}_1^2}{2A_2^2\rho_2^2} + \frac{\gamma}{\gamma - 1}\frac{p_2}{\rho_2} \tag{2.3.10}$$

because $\dot{m}_2 = \dot{m}_1$ by conservation of mass. Rearranging for $\dot{m}_1$ gives

$$\dot{m}_1 = \pm\sqrt{\frac{2\gamma}{\gamma - 1}\frac{A_1^2A_2^2\rho_1\rho_2}{|A_2^2\rho_2^2 - A_1^2\rho_1^2|}|\rho_2 p_1 - \rho_1 p_2|}, \tag{2.3.11}$$

where absolute values have been used to ensure the square-root is always real.

To determine which sign we take, let's set the positive direction of flow to be from 1 to 2. We know that air will flow from regions of high pressure to regions of low pressure. Therefore, when $\dot{m} > 0$, we have $p_1 > p_2$ and so

$$\rho_2 p_1 - \rho_1 p_2 = \rho_1\rho_2\left(\frac{p_1}{\rho_1} - \frac{p_2}{\rho_2}\right) > 0 \tag{2.3.12}$$

Similarly, when $\dot{m} < 0$ we have $(\rho_2 p_1 - \rho_1 p_2) < 0$.

Suppose also that the throttle restricts the pipe so it effectively reduces the area from

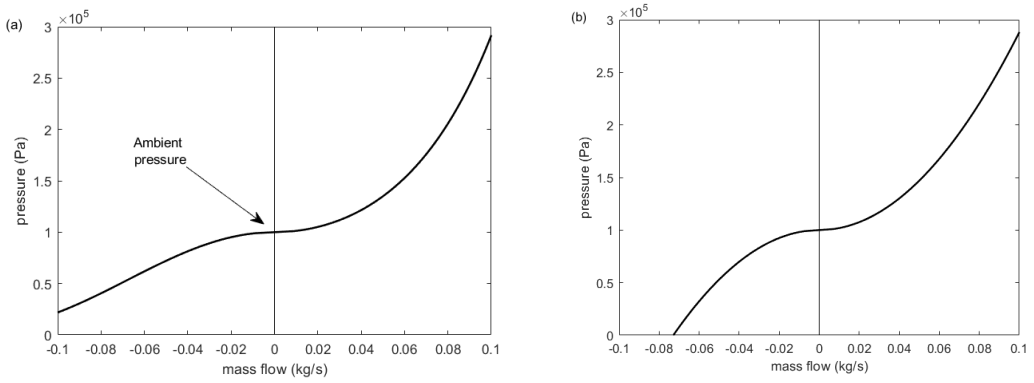

Figure 2-3: (a) Steady-state throttle characteristic to be used in reduced order surge model. The intercept occurs when the flow in the pipe has identical conditions to that on the other side of the throttle valve (in this case ambient). (b) Incompressible version of throttle characteristic commonly used in literature.

A to μA, for some fraction μ, and the air after going through the throttle is at ambient conditions.

Then, the throttle characteristic is given by

$$\dot{m}_T = \text{sgn}(p\rho_{amb} - p_{amb}\rho)\sqrt{\frac{2\gamma}{\gamma - 1}\frac{\mu^2 A^2 \rho\rho_{amb}}{|\mu^2\rho_{amb}^2 - \rho^2|}|p\rho_{amb} - p_{amb}\rho|}. \tag{2.3.13}$$

As we saw in Section 2.2, the fact that we have no stress terms means the isentropic relation holds (see Eq. 2.2.11). Hence, we can simply use that $\rho = \left(\frac{p}{\kappa}\right)^{\frac{1}{\gamma}}$, to make this a function only of p. Figure 2-3(a) shows the resulting characteristic in the mass flow - pressure plane.

Our formula for the throttle characteristic is slightly different to those typically used in literature because the orifice equation is usually derived from the incompressible form of conservation of energy. We decided to derive the compressible form of the orifice equation to ensure consistency across the model, i.e. the model for the pipes, compressor and throttle will all assume compressible flow.

As we can see from Fig. 2-3(b), the compressible throttle characteristic is different from the incompressible version because it has a horizontal asymptote at zero pressure, which makes sense because pressure is always positive and only zero if a vacuum is achieved. However, since this mainly affects the case where air is flowing backwards through the orifice, we could use the incompressible version in studies where the air is always travelling in a forward direction through the throttle.

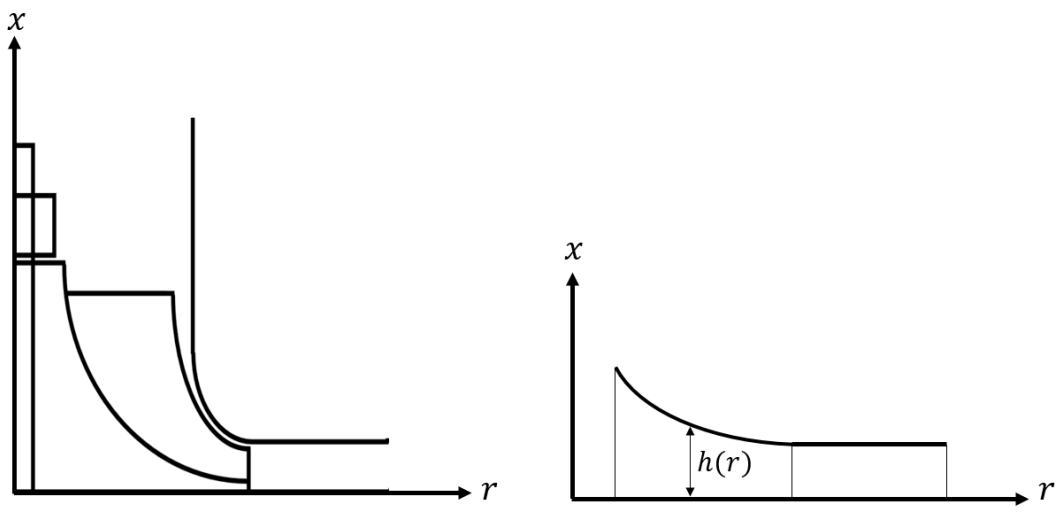

Figure 2-4: Standard impeller and diffuser geometry (left) and geometry used in model where air no longer turns from axial to radial but enters radially (right) in the cylindrical polar coordinate system.

2.4 Compressor Characteristic

Modelling the compressor in steady state is more complex than modelling the throttle valve as we are dealing with a rotating impeller and a stationary diffuser, both of which have changing cross-sectional areas.

There is also the volute to consider, but since its primary objective is to collect the air from around the diffuser and deliver it to the outlet pipework, we shall assume that this happens instantaneously and just focus on the impeller and diffuser.

Therefore, since air in a the impeller and diffuser predominately travels radially outward from the impeller eye, it makes sense to work in the cylindrical-polar coordinate system (i.e. (r, θ, x)) where the axis of rotation is in the axial, x, direction.

For simplicity, we shall also assume an impeller geometry where the air does not enter axially and turn to exit radially, but enters and exits in a purely radial direction (see Fig. 2-4).

Let Ω be the speed of rotation around the x-axis. Then, in cylindrical-polar coordinates,

the steady-state component form of the fundamental fluid equations are:

$$\frac{1}{r}\frac{\partial}{\partial r}(r\rho u_r) + \frac{1}{r}\frac{\partial}{\partial \theta}(\rho u_\theta) + \frac{\partial}{\partial x}(\rho u_x) = 0 \tag{2.4.1}$$

$$\frac{1}{r}\frac{\partial}{\partial r}(r\rho u_r^2) + \frac{1}{r}\frac{\partial}{\partial \theta}(\rho u_r u_\theta) + \frac{\partial}{\partial x}(\rho u_r u_x) - \frac{\rho u_\theta^2}{r} - 2\rho\Omega u_\theta - \rho\Omega^2 r = -\frac{\partial p}{\partial r} + [\nabla \cdot \boldsymbol{\tau}]_r \tag{2.4.2}$$

$$\frac{1}{r}\frac{\partial}{\partial r}(r\rho u_r u_\theta) + \frac{1}{r}\frac{\partial}{\partial \theta}(\rho u_\theta^2) + \frac{\partial}{\partial x}(\rho u_\theta u_x) + \frac{\rho u_r u_\theta}{r} + 2\rho\Omega u_r = -\frac{1}{r}\frac{\partial p}{\partial \theta} + [\nabla \cdot \boldsymbol{\tau}]_\theta \tag{2.4.3}$$

$$\frac{1}{r}\frac{\partial}{\partial r}(r\rho u_x u_r) + \frac{1}{r}\frac{\partial}{\partial \theta}(\rho u_\theta u_x) + \frac{\partial}{\partial x}(\rho u_x^2) = -\frac{\partial p}{\partial x} + [\nabla \cdot \boldsymbol{\tau}]_x \tag{2.4.4}$$

$$\frac{1}{r}\frac{\partial}{\partial r}(r u_r(\rho E + p)) + \frac{1}{r}\frac{\partial}{\partial \theta}(u_\theta(\rho E + p)) + \frac{\partial}{\partial x}(u_x(\rho E + p)) = 0 \tag{2.4.5}$$

where

$$E = \frac{|\mathbf{u}|^2}{2} + \frac{1}{\gamma - 1}\frac{p}{\rho} - \frac{\Omega^2 r^2}{2}. \tag{2.4.6}$$

2.4.1 Isentropic Formulation

Similarly to the previous two sections, we begin by simplifying the system by assuming there are no shear stress forces, i.e. $\nabla \cdot \tau = 0$. This means that we have isentropic flow and the relation $p = \kappa\rho^\gamma$ holds. This can be proven by a similar argument to that of Eq. 2.2.6 - 2.2.11 with the rotational terms included.

Now, since the impeller and diffuser are distinct components in the centrifugal compressor, we will consider them separately in the model formulation.

Impeller

Let us assume we have straight radial blades, so $u_\theta = 0$ in the impeller channels. This results in:

$$\frac{1}{r}\frac{\partial}{\partial r}(r\rho u_r) + \frac{\partial}{\partial x}(\rho u_x) = 0 \tag{2.4.7}$$

$$\frac{1}{r}\frac{\partial}{\partial r}(r\rho u_r^2) + \frac{\partial}{\partial x}(\rho u_r u_x) - \rho\Omega^2 r = -\frac{\partial p}{\partial r} \tag{2.4.8}$$

$$2\rho\Omega u_r = -\frac{1}{r}\frac{\partial p}{\partial \theta} \tag{2.4.9}$$

$$\frac{1}{r}\frac{\partial}{\partial r}(r\rho u_x u_r) + \frac{\partial}{\partial x}(\rho u_x^2) = -\frac{\partial p}{\partial x} \tag{2.4.10}$$

$$\frac{1}{r}\frac{\partial}{\partial r}(r u_r(\rho E + p)) + \frac{\partial}{\partial x}(u_x(\rho E + p)) = 0. \tag{2.4.11}$$

Notice that this has removed all mention of θ apart from in the second momentum equation (Eq. 2.4.9). This equation specifies that there will be a pressure gradient in the tangential direction due to the Coriolis force. We can therefore make the simplifying assumption that all variables (except p) are constant with θ and can be considered as a function of r and x only.

Using this, we can integrate Eq. 2.4.9 to get

$$p(r, \theta, x) = -2\Omega r \rho u_r(r, x)\theta + \tilde{p}(r, x) \tag{2.4.12}$$

where $\tilde{p}$ is the constant of integration chosen so that it corresponds to the pressure in the centre of a channel. This means the channel walls are at

$$\frac{(\pi + 2\pi k)}{n_b}, \qquad k = 0, .., n_b - 1 \tag{2.4.13}$$

where n_b is the number of blades. Therefore, assuming each impeller channel behaves identically, we can take the average of this over the θ direction by

$$\bar{p}(r, x) = \frac{1}{2\pi}\sum_{i=1}^{n_b}\int_{-\frac{\pi}{n_b}}^{\frac{\pi}{n_b}} p(r, \theta, x)\ d\theta. \tag{2.4.14}$$

This results in $\bar{p} = \tilde{p}(r, x)$ because

$$-\frac{\Omega r \rho u_r(r, x)}{\pi}\sum_{i=1}^{n_b}\int_{-\frac{\pi}{n_b}}^{\frac{\pi}{n_b}} \theta\ d\theta = 0. \tag{2.4.15}$$

Therefore, by approximating $p(r, \theta, x)$ by its value at the centre of the impeller channel, we no longer need Eq. 2.4.9 and we have a system that is only dependent on r and x.

Since we want to understand the dynamics as we travel through the compressor, it makes sense to average the flow over the x-direction so we end up with a 1D model for flow in the radial direction.

Define the average of a variable G by

$$\bar{G} = \frac{1}{h(r)} \int_0^{h(r)} G \ dx. \tag{2.4.16}$$

Since the integral limits are a function of r, we will need to use the Leibniz rule for differentiating integrals, i.e.

$$\frac{\partial}{\partial r} \left(\int_0^{h(r)} G \ dx \right) = \int_0^h \frac{\partial G}{\partial r} \ dx + G\Big|_h \frac{\partial h}{\partial r}. \tag{2.4.17}$$

To average conservation of mass (Eq. 2.4.7), we integrate between 0 and $h(r)$ in x. We apply the Leibniz rule to the first term and directly integrate the second to get

$$\frac{1}{r}\frac{\partial}{\partial r} \left(\int_0^h r\rho u_r \ dx \right) - \rho u_r\Big|_h \frac{\partial h}{\partial r} + \rho u_x\Big|_0^h = 0. \tag{2.4.18}$$

Using the definition of the average, and grouping the terms at the boundaries $x = 0$ and $x = h(r)$, gives us

$$\frac{1}{r}\frac{\partial}{\partial r}(rh\overline{\rho u_r}) + \left(-\rho u_r \frac{\partial h}{\partial r} + \rho u_x \right) \Big|_h - \rho u_x\Big|_0 = 0. \tag{2.4.19}$$

Notice that at $x = 0$,

$$-\rho u_x = \rho \begin{pmatrix} u_x \\ u_r \end{pmatrix} \cdot \begin{pmatrix} -1 \\ 0 \end{pmatrix} \tag{2.4.20}$$

is the flux leaving the impeller in the $-x$ direction, and so this is zero as no air can escape through the base of the impeller.

At $x = h(r)$, notice that the outward pointing unit normal $\hat{\mathbf{n}}$ is given by

$$\hat{\mathbf{n}} = \frac{1}{\sqrt{1 + (h')^2}} \begin{pmatrix} 1 \\ -h' \end{pmatrix} \tag{2.4.21}$$

because, at any given point, it is perpendicular to the tangent vector $(h', 1)^T$ as shown in Fig. 2-5. Therefore,

$$-\rho u_r \frac{\partial h}{\partial r} + \rho u_x = \rho \begin{pmatrix} u_x \\ u_r \end{pmatrix} \cdot \begin{pmatrix} 1 \\ -h' \end{pmatrix} \tag{2.4.22}$$

is the flux leaving the impeller through the casing at $h(r)$, and so is again zero.

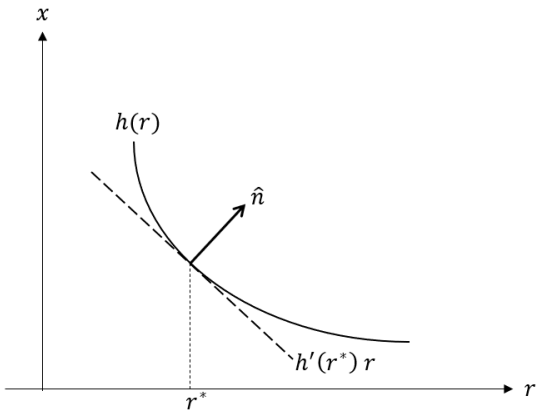

Figure 2-5: Height of impeller blade given by the function $x = h(r)$. The outward pointing unit normal, $\hat{\mathbf{n}}$, at any point r^* is perpendicular to the tangent at that point.

This means that the average of Eq. 2.4.7 is

$$\frac{1}{r}\frac{\partial}{\partial r}(rh\overline{\rho u_r}) = 0. \tag{2.4.23}$$

Following exactly the same approach for Eqs. 2.4.8, 2.4.10, and 2.4.11, gives

$$\frac{1}{r}\frac{\partial}{\partial r}(rh\overline{\rho u_r^2}) - h\bar{\rho}\Omega^2 r = -\frac{\partial}{\partial r}(h\bar{p}) + p\Big|_h \frac{\partial h}{\partial r}, \tag{2.4.24}$$

$$\frac{1}{r}\frac{\partial}{\partial r}(rh\overline{\rho u_r u_x}) = -p\Big|_0^h, \tag{2.4.25}$$

$$\frac{1}{r}\frac{\partial}{\partial r}(rh\overline{\rho u_r E} + rh\overline{u_r p}) = 0. \tag{2.4.26}$$

Similarly to the approach in Section 2.2, we assume that $\overline{ab} = \bar{a}\bar{b}, \forall a, b$.

We will also assume that the pressure is constant in the x direction, so

$$p\Big|_h = p\Big|_0 = \bar{p}. \tag{2.4.27}$$

This means that Eq. 2.4.25 reduces to

$$\frac{1}{r}\frac{\partial}{\partial r}(rh\bar{\rho}\bar{u}_r\bar{u}_x) = 0, \tag{2.4.28}$$

and so we need to assume $\bar{u}_x = 0$ so no restrictions are placed on how $\bar{\rho}\bar{u}_r$ varies with r through this equation.

Thus, on dropping bars, the averaged equations of motion for steady flow through the impeller are

$$\frac{1}{r}\frac{\partial}{\partial r}(rh\rho u_r) = 0 \tag{2.4.29}$$

$$\frac{1}{r}\frac{\partial}{\partial r}(rh\rho u_r^2) - h\rho\Omega^2 r = -h\frac{\partial p}{\partial r} \tag{2.4.30}$$

$$\frac{1}{r}\frac{\partial}{\partial r}\left(rh\rho u_r\left(\frac{u_r^2}{2} + \frac{\gamma}{\gamma-1}\frac{p}{\rho} - \frac{\Omega^2 r^2}{2}\right)\right) = 0 \tag{2.4.31}$$

where

$$E = \frac{u_r^2}{2} + \frac{1}{\gamma-1}\frac{p}{\rho} - \frac{\Omega^2 r^2}{2}. \tag{2.4.32}$$

In order to simplify this system, we can replace the energy equation (Eq. 2.4.31) with the isentropic condition $p = \kappa\rho^\gamma$, and integrate Eq. 2.4.29 to give

$$q = rh\rho u_r, \tag{2.4.33}$$

where q is a constant. Notice also that $q = \frac{\dot{m}}{2\pi}$ because the cross sectional area of the impeller is $A = 2\pi rh$.

Therefore, substituting these in Eq. 2.4.30 and dividing through by $h\rho$, gives

$$\frac{q}{rh\rho}\frac{\partial u_r}{\partial r} - \Omega^2 r = -\gamma\kappa\rho^{\gamma-2}\frac{\partial\rho}{\partial r}. \tag{2.4.34}$$

Noticing that $\frac{q}{rh\rho} = u_r$ and integrating results in

$$\frac{u_r^2}{2} - \frac{\Omega^2 r^2}{2} = -\frac{\kappa\gamma}{\gamma-1}\rho^{\gamma-1} + c_1, \tag{2.4.35}$$

which, when written entirely in terms of ρ, becomes

$$\frac{q^2}{2r^2h^2\rho^2} + \frac{\kappa\gamma}{\gamma-1}\rho^{\gamma-1} = \frac{\Omega^2 r^2}{2} + c_1, \tag{2.4.36}$$

for constant of integration c_1 that can be found by using the boundary condition that $\rho = \rho_{amb}$ at the impeller inlet.

Equation 2.4.36 can therefore be solved to find the density ρ, and hence $p = \kappa\rho^\gamma$, at each mass flow $\dot{m} = 2\pi q$ for a chosen impeller speed setting, Ω.

Diffuser

In the diffuser, we can assume that the flow is independent of θ as a vaneless diffuser is axisymmetric. Also, $\Omega = 0$ since the diffuser is not a rotating part. Therefore, the fundamental equations of motion give us

$$\frac{1}{r}\frac{\partial}{\partial r}(r\rho u_r) + \frac{\partial}{\partial x}(\rho u_x) = 0 \tag{2.4.37}$$

$$\frac{1}{r}\frac{\partial}{\partial r}(r\rho u_r^2) + \frac{\partial}{\partial x}(\rho u_r u_x) - \frac{\rho u_\theta^2}{r} = -\frac{\partial p}{\partial r} \tag{2.4.38}$$

$$\frac{1}{r}\frac{\partial}{\partial r}(r\rho u_r u_\theta) + \frac{\partial}{\partial x}(\rho u_\theta u_x) + \frac{\rho u_r u_\theta}{r} = 0 \tag{2.4.39}$$

$$\frac{1}{r}\frac{\partial}{\partial r}(r\rho u_x u_r) + \frac{\partial}{\partial x}(\rho u_x^2) = -\frac{\partial p}{\partial x} \tag{2.4.40}$$

$$\frac{1}{r}\frac{\partial}{\partial r}(r u_r(\rho E + p)) + \frac{\partial}{\partial x}(u_x(\rho E + p)) = 0 \tag{2.4.41}$$

This system is already a function of r and x only. Therefore, as before, we average over the axial height to get a 1D model for the flow in the radial direction.

In the diffuser, the channel height remains constant, so we can perform averaging without needing the Leibniz rule. Also, our no-flux boundary conditions simply become

$$u_x\big|_0 = u_x\big|_h = 0. \tag{2.4.42}$$

Therefore, the five averaged equations of motion are

$$\frac{1}{r}\frac{\partial}{\partial r}(rh\overline{\rho u_r}) = 0, \tag{2.4.43}$$

$$\frac{1}{r}\frac{\partial}{\partial r}(rh\overline{\rho u_r^2}) - \frac{h\overline{\rho u_\theta^2}}{r} = -h\frac{\partial \bar{p}}{\partial r}, \tag{2.4.44}$$

$$\frac{1}{r}\frac{\partial}{\partial r}(rh\overline{\rho u_r u_\theta}) + \frac{h\overline{\rho u_r u_\theta}}{r} = 0, \tag{2.4.45}$$

$$\frac{1}{r}\frac{\partial}{\partial r}(rh\overline{\rho u_r u_x}) = -p\Big|_0^h, \tag{2.4.46}$$

$$\frac{1}{r}\frac{\partial}{\partial r}(rh(\overline{\rho u_r E} + \overline{u_r p})) = 0, \tag{2.4.47}$$

respectively.

As with the impeller, we assume that $\overline{ab} = \bar{a}\bar{b}$ and that the pressure, p, is constant in x. Hence, Eq. 2.4.46 requires us to assume $\bar{u}_x = 0$ in order to not apply additional

restriction on $\bar{\rho}\bar{u}_r$ through this equation.

Therefore, on dropping the bars, the equations of motion in the diffuser are

$$\frac{1}{r}\frac{\partial}{\partial r}(rh\rho u_r) = 0 \tag{2.4.48}$$

$$\frac{1}{r}\frac{\partial}{\partial r}(rh\rho u_r^2) - \frac{h\rho u_\theta^2}{r} = -h\frac{\partial p}{\partial r} \tag{2.4.49}$$

$$\frac{1}{r}\frac{\partial}{\partial r}(rh\rho u_r u_\theta) + \frac{h\rho u_r u_\theta}{r} = 0 \tag{2.4.50}$$

$$\frac{1}{r}\frac{\partial}{\partial r}\left(rh\rho u_r\left(\frac{u_r^2}{2} + \frac{u_\theta^2}{2} + \frac{\gamma}{\gamma-1}\frac{p}{\rho}\right)\right) = 0 \tag{2.4.51}$$

where

$$E = \frac{u_r^2}{2} + \frac{u_\theta^2}{2} + \frac{1}{\gamma-1}\frac{p}{\rho}. \tag{2.4.52}$$

To simplify this system, we can again replace the energy equation (Eq. 2.4.51) with the isentropic relation $p = \kappa\rho^\gamma$. We can also integrate Eq. 2.4.48 to get $q = rh\rho u_r$, where q is constant.

Therefore, we can take out $q = rh\rho u_r$ from the differential in Eq. 2.4.50 and divide through by $h\rho u_r$ to get

$$\frac{\partial u_\theta}{\partial r} + \frac{u_\theta}{r} = 0. \tag{2.4.53}$$

This can be integrated to give

$$u_\theta = \frac{c}{r} \tag{2.4.54}$$

for a constant c that can be found by using the boundary condition of $u_\theta = \Omega r$ at the impeller tip, ie. $c = \Omega r_{tip}^2$.

Substituting these relations for q, u_θ, and p into Eq. 2.4.49 and dividing by $h\rho$ results in

$$u_r\frac{\partial u_r}{\partial r} - \frac{\Omega^2 r_{tip}^4}{r^3} = -\gamma\kappa\rho^{\gamma-2}\frac{\partial\rho}{\partial r} \tag{2.4.55}$$

because $u_r = \frac{q}{rh\rho}$. Therefore, integrating this and writing u_r in terms of q, gives us

$$\frac{q^2}{2r^2h^2\rho^2} + \frac{\kappa\gamma}{\gamma-1}\rho^{\gamma-1} = -\frac{\Omega^2 r_{tip}^4}{2r^2} + c_2, \tag{2.4.56}$$

where c_2 is a constant of integration that can be found by applying the boundary condition that density is continuous at the impeller - diffuser interface.

Therefore, this can be solved to find the density, ρ, through the diffuser at each mass

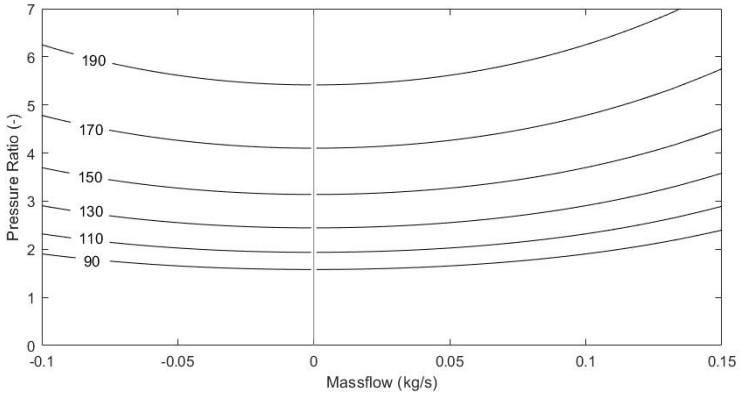

Figure 2-6: Compressor characteristics computed using isentropic formulation of equations of motion. Impeller speeds in krpm are indicated on each line.

flow, for a chosen impeller speed Ω.

Model Results

Solving Eq. 2.4.36 and Eq. 2.4.56 for multiple mass flows at six different impeller speeds gives the characteristics shown in Fig. 2-6.

This models a compressor that operates in an ideal way, i.e. the more flow we add, the more pressure we can generate. However, this is not physical. As we saw in Section 1.2.1, compressor characteristics found via experiment show that the pressure decreases with higher flow rates. Therefore, this model does not capture the main physics and so is not suitable.

To improve on this, it appears that friction is needed. Friction causes losses for higher mass flows and so should reduce the pressure at these values.

2.4.2 Addition of Friction

To include frictional losses into the compressor, we go back to the fundamental fluid equations (Eq. 2.4.1 - 2.4.5) and assume that the only effect of the stress tensor is as a result of friction. This means we can write

$$\nabla \cdot \boldsymbol{\tau} = F, \tag{2.4.57}$$

where F is a friction function. Notice that this is friction per unit volume because, during derivation of the fundamental fluid equations, all terms were divided by volume.

We will assume that F relates to skin fiction, rather than the internal friction of the fluid. This is defined as the shearing stress exerted by the fluid on the surface over which it flows [56]. Therefore,

$$F = -\boldsymbol{\tau}_w S \tag{2.4.58}$$

where $\boldsymbol{\tau}_w$ is the wall shearing stress, and S is the surface area (per unit volume). This can be written as

$$F = -\frac{1}{2} f \rho \mathbf{u}|\mathbf{u}| S \tag{2.4.59}$$

where f is the fanning friction factor [57]. Notice that $\mathbf{u}|\mathbf{u}|$ ensures that the friction always acts against the flow.

For ease of solving the system ODEs, we will simplify this further to

$$F = -\frac{1}{2} f \rho \mathbf{u}|u_r| S \tag{2.4.60}$$

and assume that the friction factor f encompasses the difference, i.e.

$$f \propto \frac{\sqrt{u_r^2 + u_\theta^2}}{u_r}. \tag{2.4.61}$$

In the impeller this f is equivalent to the fanning friction factor as $u_\theta = 0$, however it will be slightly different in the diffuser. In practice, we will fit the friction factor to experimental data in order to find an accurate value for simulations.

To generate a model for the steady state operation of the compressor we can follow exactly the same procedure as in Section 2.4.1 with the addition of F in the momentum equations to give

$$\frac{1}{r}\frac{\partial}{\partial r}(r h \rho u_r) = 0 \tag{2.4.62}$$

$$\frac{1}{r}\frac{\partial}{\partial r}(r h \rho u_r^2) - h\rho\Omega^2 r = -h\frac{\partial p}{\partial r} + hF_r \tag{2.4.63}$$

$$\frac{1}{r}\frac{\partial}{\partial r}\left(r h \rho u_r \left(\frac{u_r^2}{2} + \frac{\gamma}{\gamma - 1}\frac{p}{\rho} - \frac{\Omega^2 r^2}{2}\right)\right) = 0 \tag{2.4.64}$$

for the impeller and

$$\frac{1}{r}\frac{\partial}{\partial r}(rh\rho u_r) = 0, \tag{2.4.65}$$

$$\frac{1}{r}\frac{\partial}{\partial r}(rh\rho u_r^2) - \frac{h\rho u_\theta^2}{r} = -h\frac{\partial p}{\partial r} + hF_r, \tag{2.4.66}$$

$$\frac{1}{r}\frac{\partial}{\partial r}(rh\rho u_r u_\theta) + \frac{h\rho u_r u_\theta}{r} = hF_\theta, \tag{2.4.67}$$

$$\frac{1}{r}\frac{\partial}{\partial r}\left(rh\rho u_r\left(\frac{u_r^2}{2} + \frac{u_\theta^2}{2} + \frac{\gamma}{\gamma-1}\frac{p}{\rho}\right)\right) = 0, \tag{2.4.68}$$

for the diffuser, where the bars have been dropped for ease.

To simplify these systems of ODEs, note that we no longer satisfy the isentropic relation because of the additional frictional losses. Therefore, for the impeller, we integrate Eqs. 2.4.62 and 2.4.64 to get $q = rh\rho u_r$ and

$$\frac{u_r^2}{2} + \frac{\gamma}{\gamma-1}\frac{p}{\rho} - \frac{\Omega^2 r^2}{2} = E_I \tag{2.4.69}$$

respectively, where q and E_I are both constants. Rearranging Eq. 2.4.69 for p and substituting into Eq. 2.4.63 along with q and

$$F_r = -\frac{1}{2}f\rho|u_r|u_r S_I, \quad S_I = 2\left(\frac{n_b}{2\pi r} + \frac{1}{h}\right), \tag{2.4.70}$$

for number of impeller blades n_b, results in

$$\frac{\partial\rho}{\partial r} = \frac{-\rho q^2\left(\frac{1}{r} + \frac{1}{h}\frac{\partial h}{\partial r}\right) - \Omega^2 r^3 h^2\rho^3 + \gamma f\rho|q|q\left(\frac{n_b}{2\pi r} + \frac{1}{h}\right)}{\left(\frac{\gamma+1}{2}\right)q^2 - (\gamma-1)\left(\frac{\Omega^2 r^2}{2} + E_I\right)r^2h^2\rho^2}, \tag{2.4.71}$$

which is an ODE that can be solved quickly via numerical methods, like Runga-Kutta, for the density ρ.

Similarly, for the diffuser, we integrate Eqs. 2.4.65 and 2.4.68 to get $q = rh\rho u_r$ and

$$\frac{u_r^2}{2} + \frac{u_\theta^2}{2} + \frac{\gamma}{\gamma-1}\frac{p}{\rho} = E_D, \tag{2.4.72}$$

and substitute these along with

$$F_r = -\frac{1}{2}f\rho|u_r|u_r S_D, \quad S_D = \frac{2}{h}, \tag{2.4.73}$$

into Eq. 2.4.66 to get

$$\frac{\partial \rho}{\partial r} = \frac{-\frac{\rho q^2}{r} - r^2 h^2 \rho^3 \left(\gamma \frac{u_\theta^2}{r} + (\gamma - 1) u_\theta \frac{\partial u_\theta}{\partial r}\right) + \gamma \frac{f}{h} \rho |q| q}{\left(\frac{\gamma+1}{2}\right) q^2 + (\gamma - 1)\left(\frac{u_\theta^2}{2} - E_D\right) r^2 h^2 \rho^2}. \tag{2.4.74}$$

Finally, Eq. 2.4.67 is given by

$$\frac{1}{r}\frac{\partial}{\partial r}(r h \rho u_r u_\theta) + \frac{h \rho u_r u_\theta}{r} = -h \frac{1}{2} f \rho |u_r| u_\theta S_D \tag{2.4.75}$$

because the friction F_θ opposes the momentum of the fluid. Therefore, taking $q = r h \rho u_r$ out of the derivative and dividing by $h \rho u_r$ gives us

$$\frac{\partial u_\theta}{\partial r} + \frac{u_\theta}{r} = -\frac{f}{2} \text{sgn}(u_r) u_\theta S_D. \tag{2.4.76}$$

Using the fact that $S_D = \frac{2}{h}$ and integrating results in

$$u_\theta = \frac{c}{r} e^{-\text{sgn}(u_r)\left(\frac{f}{h}\right) r} \tag{2.4.77}$$

where $\text{sgn}(u_r) = \pm 1$ depending on the sign of u_r, and c is the constant of integration.

Since u_r and u_θ have the same sign, we could also write this as

$$u_\theta = \frac{c}{r} e^{-\text{sgn}(u_\theta)\left(\frac{f}{h}\right) r}. \tag{2.4.78}$$

Finally, we know that

$$c = \Omega r_{tip}^2 e^{\left(\frac{f}{h}\right) r_{tip}} \tag{2.4.79}$$

because the tangential velocity is assumed to be continuous at the impeller - diffuser interface (i.e. $u_\theta = \Omega r$ at $r = r_{tip}$).

This means that Eq. 2.4.74 is an ODE purely for density ρ and can be solved numerically in the same manor as Eq. 2.4.71.

Model Results

Solving Eqs. 2.4.71 and 2.4.74 for multiple mass flows at six different impeller speeds results in the compressor characteristics shown in Fig. 2-7.

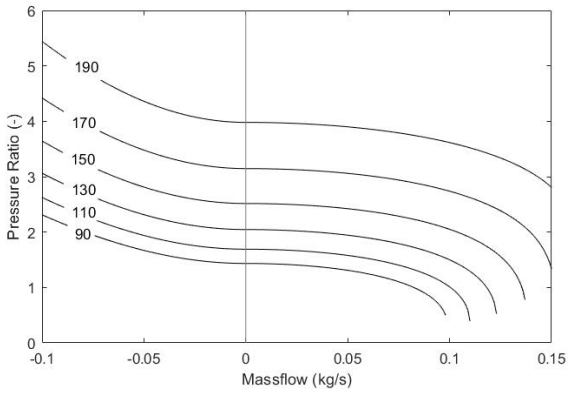

Figure 2-7: Compressor characteristics map computed by averaging the fundamental fluid equations with the inclusion of skin friction. Impeller speeds in krpm are indicated on each line.

This model is now able to capture a cubic-like shape similar to that seen in experiments (see Section 1.2.1). This means that friction plays a vital role in the operation of a compressor, and so cannot be left out of any model.

However, this model still is missing some important dynamics. Using this characteristic in the reduced order surge model developed in Section 2.2 (both the nonlinear ODEs and the Moore-Greitzer version) we only ever see stable behaviour. Figure 2-8 shows this at a low mass flow value where we would expect to see surge.

In Section 1.2.1, we saw that the characteristics observed experimentally had a local minimum at zero mass flow, rather than the point of inflection we have obtained. This

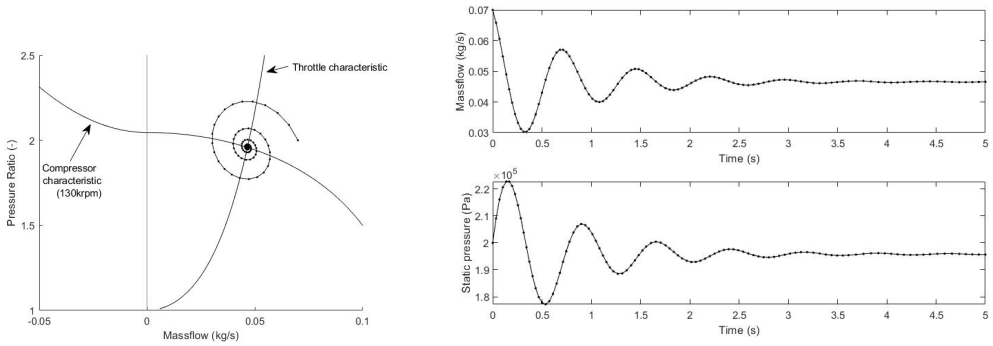

Figure 2-8: Stable operation using the Moore-Greitzer model. Left: Trajectory of compressor operation in mass flow-pressure plane. Right: Pressure and mass flow traces of compressor operation with time.

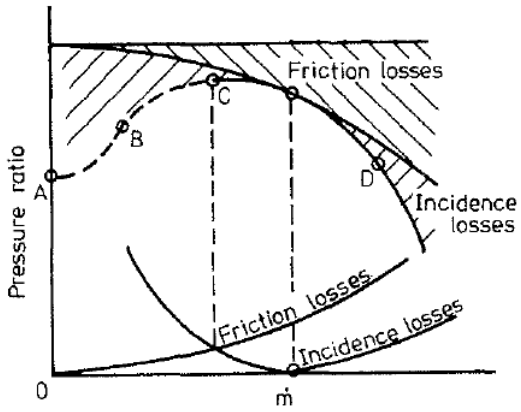

Figure 2-9: Determination of shape of compressor characteristics by looking at different losses [1]. The characteristic (A-D) is created by subtracting the loss curves shown at the bottom of the graph.

suggests that the reason our characteristic behaves stably is that it is monotonically decreasing.

Therefore, to achieve a compressor characteristic that exhibits surge behaviour, we need to include some losses that occur for small mass flow rates. According to Watson and Janota [1], the pressure drop observed at low mass flow rates are due to incidence losses (see Fig. 2-9).

2.4.3 Addition of Incidence Loss

Incidence losses occur when the flow entering the impeller does not perfectly match the blades. Figure 2-10 shows that flow entering the impeller channel at an angle larger than the blade angle can cause the flow to separate. This separation can be modelled as a blockage in the channel.

To represent this blockage we create a stall function, ξ, where $\dot{m} = \xi A \rho u_r$. This means that ξA represents the area of the channel that is available for the flow to pass through.

Suppose β is the angle of the flow entering the impeller and β_B is the impeller inlet blade angle. Then for $\beta \leq \beta_B$, we assume there are no incidence losses and so $\xi = 1$.

For $\beta > \beta_B$, we can find the stall function by considering the velocity as a function of the mass flow, i.e. $u_r(\dot{m}) = \frac{\dot{m}}{\xi A \rho}$.

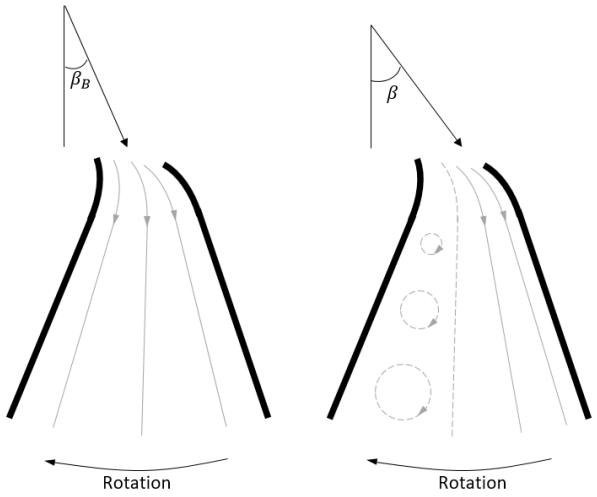

Figure 2-10: Left: Flow matches the blades perfectly, so zero incidence loss. Right: Flow enters the impeller channel at an angle $\beta > \beta_B$, so we have incidence losses. Here the flow separates and we assume the stalled flow causes a blockage in the channel.

We would like ξ to be a smooth function, therefore we will make the velocity continuously differentiable at $\beta = \beta_B$, i.e.

$$u_r(\dot{m}_B) = \frac{\dot{m}_B}{A\rho}, \tag{2.4.80}$$

$$\frac{du_r}{d\dot{m}}(\dot{m}_B) = \frac{1}{A\rho}. \tag{2.4.81}$$

Also, at zero mass flow, we would expect the velocity to be zero. So we have another condition of

$$u_r(0) = 0. \tag{2.4.82}$$

We desire a free parameter in the stall function in order to set the strength of this stall based on experimental data. Therefore, with three conditions and a free parameter, the simplest function we can use to describe the stalled velocity is a cubic:

$$u_r = a\dot{m}^3 + b\dot{m}^2 + c\dot{m} + d. \tag{2.4.83}$$

Differentiating this gives

$$\frac{du_r}{d\dot{m}} = 3a\dot{m}^2 + 2b\dot{m} + c. \tag{2.4.84}$$

Then, condition 2.4.82 immediately gives us $d = 0$, and conditions 2.4.80 and 2.4.81 gives us

$$\frac{\dot{m}_B}{A\rho} = a\dot{m}_B^3 + b\dot{m}_B^2 + c\dot{m}_B, \tag{2.4.85}$$

$$\frac{1}{A\rho} = 3a\dot{m}_B^2 + 2b\dot{m}_B + c, \tag{2.4.86}$$

respectively. Choosing a as our free parameter and solving these for b and c gives us

$$b = -2a\dot{m}_B, \tag{2.4.87}$$

$$c = \frac{1}{A\rho} + a\dot{m}_B^2. \tag{2.4.88}$$

Therefore, our stalled velocity is given by

$$u_r(\dot{m}) = a\dot{m}^3 - 2a\dot{m}_B\dot{m}^2 + \left(\frac{1}{A\rho} + a\dot{m}_B^2\right)\dot{m}. \tag{2.4.89}$$

Using the fact that $u_r = \frac{\dot{m}}{\xi A\rho}$ and rearranging for ξ results in

$$\xi(\beta) = \frac{1}{1 + \hat{a}\left(1 - \frac{\tan\beta_B}{\tan\beta}\right)^2}, \tag{2.4.90}$$

where $\hat{a} = aA\rho\dot{m}_B^2$, because

$$\frac{\dot{m}}{\dot{m}_B} = \frac{\tan\beta_B}{\tan\beta}. \tag{2.4.91}$$

Note that this doesn't change any of the ODEs in Section 2.4.2 because it only influences the definition of the constant q. Previously, $q = \frac{\dot{m}}{2\pi}$ whereas to incorporate the stalling we can change this to be

$$q = \frac{\dot{m}}{2\pi\xi(\beta)}. \tag{2.4.92}$$

The resulting compressor characteristic and its behaviour when integrated into the nonlinear reduced order surge model are presented in the paper included in the following section.

2.5 Paper 1: Modelling Axisymmetric Centrifugal Compressor Characteristics from First Principles

This declaration concerns the article entitled:			
Modeling Axisymmetric Centrifugal Compressor Characteristics from First Principles			
Publication status (tick one) **Draft manuscript** ☐ **Submitted** ☐ **In review** ☐ **Accepted** ☐ **Published** X			
Publication details (reference)	Powers, K. H., Brace, C. J., Budd, C. J., Copeland, C. D., and Milewski, P. A. (August 25, 2020). "Modeling Axisymmetric Centrifugal Compressor Characteristics from First Principles." ASME. *J. Turbomach*. September 2020; 142(9): 091010. https://doi.org/10.1115/1.4047616		
Copyright status (tick the appropriate statement) I hold the copyright for this material ☐ Copyright is retained by the publisher, but I have been given permission to replicate the material here X			
Candidate's contribution to the paper (provide details, and also indicate as a percentage)	The contribution of Katherine Powers to the paper is as follows: • Formulation of ideas (80%) with advice from supervisors • Derivation of equations for the mathematical models (90%) • Writing MATLAB code and creating of numerical simulations (100%) • Comparing numerical simulations to given experimental data, and analysing of the results (100%) • Presentation of data in journal format (100%)		
Statement from Candidate	This paper reports on original research I conducted during the period of my Higher Degree by Research candidature.		
Signed	K Hpowers	**Date**	26/02/2021

Katherine H. Powers
Department of Mathematical Sciences,
University of Bath,
Claverton Down,
Bath BA2 7AY, UK
e-mail: k.h.powers@bath.ac.uk

Chris J. Brace
Department of Mechanical Engineering,
University of Bath,
Claverton Down,
Bath BA2 7AY, UK
e-mail: c.j.brace@bath.ac.uk

Chris J. Budd
Department of Mathematical Sciences,
University of Bath,
Claverton Down,
Bath BA2 7AY, UK
e-mail: c.j.budd@bath.ac.uk

Colin D. Copeland
School of Sustainable Energy Engineering,
Simon Fraser University,
University Drive,
Surrey V3T 0N1, BC, Canada
e-mail: ccopelan@sfu.ca

Paul A. Milewski
Department of Mathematical Sciences,
University of Bath,
Claverton Down,
Bath BA2 7AY, UK
e-mail: p.a.milewski@bath.ac.uk

Modeling Axisymmetric Centrifugal Compressor Characteristics From First Principles

Turbochargers are a vital component for aiding engine manufacturers in meeting the latest emissions standards. However, their range of operation is limited for low mass flows by compressor surge. Operation in surge results in pressure and mass flow oscillations that are often damaging to the compressor and its installation. Since surge is a highly complex flow regime, full unsteady three-dimensional models are generally too computationally expensive to run. The majority of current low-dimensional surge models use a cubic compressor characteristic that needs to be fitted to experimental data. Therefore, each time a compressor is studied using these models, costly experimental testing is required. In this paper, a new technique for obtaining an axisymmetric centrifugal compressor characteristic is presented. This characteristic is built using the equations of mass, momentum, and energy from first principles in order to provide a more complete model than those currently obtained via experimental data. This approach enables us to explain the resulting cubic-like shape of the characteristic and hence to identify impeller inlet stall as a route into surge. The characteristic is used within a quasi-steady, map-based surge model in order to demonstrate its ability to predict the onset of surge while only providing geometric data as input. Validation is provided for this model by a discussion of the qualitative flow dynamics and a good fit to experimental data, especially for low impeller speeds and pressure ratios. [DOI: 10.1115/1.4047616]

Keywords: centrifugal compressors, compressor stall, surge, modeling

Introduction

There are a huge number of applications for centrifugal compressors [1]. Although the methodology presented in this paper is applicable to all centrifugal compressors (via the extension of models by, for example, Macdougal and Elder [2] who developed a one-dimensional (1D) map-based model for process plant applications), we will focus on the application to turbocharger compressors for the automotive industry.

Turbocharger compressors are normally used to increase the power output of smaller engines, so they can be used in place of larger naturally aspirated ones, making the vehicle more environmentally friendly [3]. They need a wide stable operating range, but this range is limited by surge at low mass flow rates and choke at high mass flow rates.

Surge is an instability that results in audible mass flow and pressure oscillations that would be off-putting to any driver. Moreover, these oscillations, in combination with an increase in temperature, often damage the compressor or its installation.

Surge is commonly found to be triggered by some form of stall. There are two main types of stall. The first can occur at the inlet to the impeller or a vaned diffuser and is caused by incidence. This means that, as mass flow decreases, the inlet flow angle increases and causes a separation of the flow at the blade or vane wall [4]. In the impeller, this stall can pass between neighboring channels to become a rotating stall. The second type is often seen in a vaneless diffuser and is caused by recirculation. This is where friction reduces the radial velocity of the flow near the shroud-side wall of the diffuser, reducing its spiral angle so that it is swept back into the impeller [4].

The stalling of the impeller and diffuser can occur individually or simultaneously but are not independent as stall in one component influences the behavior of stall in the other. There is extensive literature on the stall and surge behavior of compressors, for example, Refs. [5–9].

Since surge limits the amount of boost provided at low engine speeds, there is a desire to operate close to surge without entering it for prolonged periods of time. Therefore, it becomes essential to create models that can predict the location of the surge region as well as aid understanding of the flow dynamics near that region.

A very common numerical modeling approach is computational fluid dynamics (CFD). In a CFD model, a 3D domain is built in the computer, and a mesh is inserted into it. This mesh divides the domain into millions of control volumes, or cells, within which the conservation of mass, momentum, and energy equations can be solved numerically [10]. The accuracy of CFD computations has increased dramatically over the past decades due to the rapid growth in high-speed computing power. However, CFD can struggle when modeling large scale phenomena that depend on small scale effects because it is too computationally expensive to perform this direct numerical simulation with the required fineness of mesh [10]. Since surge cycles often experience local or small scale phenomena like rotating stall, recirculation, and eddies, full unsteady 3D CFD is required to completely capture the dynamics. However, the computational cost of this is not suitable for industrial needs [11].

Map-based models provide a popular alternative to CFD for modeling surge. All of these models take as an input a compressor map

Contributed by the International Gas Turbine Institute (IGTI) of ASME for publication in the JOURNAL OF TURBOMACHINERY. Manuscript received October 14, 2019; final manuscript received April 7, 2020; published online August 25, 2020. Assoc. Editor: David G. Bogard.

that has been extended beyond the surge point and into reversed flows. The speed lines on these extended compressor maps are often referred to as compressor characteristics.

Usually, these models assume that at any given time, the compressor is operating in steady-state, and so are quasi-steady in nature. There are many examples of these models in the literature for various compressor types and applications [6,12–15]. However, there has been some work on unsteady 1D models that incorporate the compressor map as a boundary condition [16,17].

The majority of these models are based on a nonlinear model by Greitzer [18]. Greitzer modeled an axial compression system by use of two actuator disks, one to represent the compressor and the other to represent the throttle valve. These are connected together by a pipe and a large plenum. The flow is considered incompressible within the pipe and to have negligible kinetic energy within the plenum. This generates a set of ordinary differential equations (ODEs) to model the behavior of flow in the compression system, for example, the Moore-Greitzer model [18,19]

$$\frac{d\Phi}{dt} = B(\psi_c - \Psi) \tag{1}$$

$$\frac{d\Psi}{dt} = \frac{1}{B}(\Phi - \psi_T^{-1}) \tag{2}$$

for nondimensional mass flow, Φ, and pressure, Ψ, where ψ_c and ψ_T are compressor and throttle characteristics, respectively.

For the throttle characteristic ψ_T, the Orifice equation [19]:

$$\psi_T = \xi_{T0} + \frac{1}{\xi_T^2}\Phi^2 \tag{3}$$

is typically used.

There have been three main approaches for obtaining the compressor characteristics. The first is through complex experimental studies, for example, Koff and Greitzer [20] proposed a cubic-like shape after experimentally testing an axial compressor in various flow regimes. The curve was reasonably straightforward to determine in backflow and steady forward flow regimes. However, when rotating stall appeared, the shape was more difficult to determine, and so transients were analyzed and an argument was made for having a smoothly varying characteristic based on the behavior of diffuser stall. This has been done more recently for small centrifugal compressors by Galindo et al. [21], also producing a cubic-like curve.

The second approach is via curve fitting and extrapolation. The most common technique is to use the cubic relation proposed by Moore and Greitzer [22], i.e.

$$\psi_c = \psi_{c_0} + H\left[1 + \frac{2}{3}\left(\frac{\Phi}{W} - 1\right) - \frac{1}{2}\left(\frac{\Phi}{W} - 1\right)^3\right] \tag{4}$$

with parameters H and W found through fitting to experimental compressor map data. However, other curve fitting techniques have been proposed, including ones involving Chebyshev polynomials in order to capture more features of the characteristics [23], and ones involving elliptic equations in order to adjust the characteristic for different settings on a variable-geometry diffuser [24].

The third is via mean-line modeling. In a mean-line model, the compressor is divided into sections over which the equations of motion and loss models are evaluated. Most of the mean-line models follow the meridional path of the compressor and typically split it into sections for the inlet, impeller, diffuser, and volute [25,26]. However, there are two-zone models that have primary and secondary flow sections within the impeller in order to account for slip [27]. The majority of these mean-line models apply empirical loss models to the sections. Typical collections of loss models for compressors can be found in Refs. [28–30]. These loss models usually have loss coefficients that need to be tuned to the particular compressor that is being studied, which makes mean-line modeling still partially reliant on data or CFD simulation.

The advantage of the purely experimental approach for finding compressor characteristics is its simplicity because reading data or evaluating polynomial-like expressions is very quick computationally. However, map-based surge models are sensitive to the shape of the compressor characteristic, so it is vital to understand this fully, and an experimental approach does not give us any insight into the reason why we get this shape of the curve. In addition, since surge is a system phenomenon, experimentally measured surge can be limited to the particular experimental setup and not, as would be desirable, any compressor installation.

The mean-line model approach can provide some understanding of the characteristic's shape because it is based in part on the physical equations of motion, and a tuned mean-line model produces some good results. However, this model usually still requires compressor specific data to tune the loss coefficients. Ideally, we would like a model that works for every type of compressor using only known information, like geometry; therefore, any parameters in the model need to be universal.

In this paper, compressor characteristics are generated through simulations of a physical model for the compressor. This physical model is derived from first principles and uses inputs solely from geometry. It has been designed to be as simple as possible while still capturing the dynamics of surge. Therefore, it contains a minimal number of parameters and has found relations for these that make them universally applicable. The strength of having a mathematically simple model is that it can be used for things like bifurcation analysis, which is a powerful tool to study the dynamics of surge as parameters, such as geometrical dimensions, are changed.

Since the model has been built from physical principles and is theoretical in nature, it gives us a new understanding of the stall and surge phenomena, which in turn will help in the design of future compressors. To the authors' knowledge, this is the first time that such a model has been created, and it makes an important step in updating the low-dimensional surge models that have remained relatively unchanged over the past 30 years. This novel approach will enable low-dimensional surge models to be a useful tool for turbocharger designers, as it will provide insight into the surge limitations of a new design while reducing the need for testing during preliminary design stages.

Equations of Motion

The key physical laws needed for deriving a model for a compressor from first principles are conservation of mass

$$\frac{\partial \rho}{\partial t} + \nabla \cdot (\rho u) = 0 \tag{5}$$

conservation of momentum in a rotating frame

$$\frac{\partial}{\partial t}(\rho u) + \nabla \cdot (\rho(u \otimes u)) + 2\rho(\Omega \times u) + \rho(\Omega \times (\Omega \times r)) = \rho g - \nabla p + \nabla \cdot \tau \tag{6}$$

and conservation of energy

$$\frac{\partial}{\partial t}(\rho E) + \nabla \cdot (\rho u E + p u) - \nabla \cdot (\tau \cdot u) = \rho \dot{Q} \tag{7}$$

In the inertial frame of reference,

$$E = \frac{|u|^2}{2} + U \tag{8}$$

where U is the specific internal energy. However, when we are in a rotating frame of reference, E becomes the relative specific energy, so

$$E + \frac{\Omega^2 r^2}{2} = \frac{|u|^2}{2} + U \tag{9}$$

to take into account the energy added to the flow by the rotation.

We also need the ideal gas law

$$p = \rho RT \tag{10}$$

and the assumption of a perfect gas so that

$$U = c_v T = \frac{1}{\gamma - 1}\frac{p}{\rho} \tag{11}$$

where c_v and γ are assumed constant.

Since we are dealing with gases, it seems reasonable to assume gravitational and viscous effects are negligible; however, we will include a term, $\boldsymbol{F}$, in the momentum equation to account for frictional losses. We will also assume that the flow is adiabatic because the time scale of heat-transfer is much longer than that of the flow velocities associated with turbochargers. Finally, we are looking for a steady-state characteristic, so we will remove the time dependence.

Model Derivation

The main components in a compressor are the impeller and the diffuser. It is easiest to consider these separately, so different simplifying assumptions can be made.

Impeller. Figure 1 shows a comparison of a typical impeller geometry to the impeller geometry, and we will assume in this model.

This simplified geometry allows us to assume that air flows through the compressor in a predominantly radial direction. Due to the straight radial blades, we can assume that $u_\theta = 0$ in the rotating frame of reference. Therefore, after writing in cylindrical polar coordinates, Eqs. (5)–(7) become

$$\frac{1}{r}\frac{\partial}{\partial r}(r\rho u_r) + \frac{\partial}{\partial x}(\rho u_x) = 0 \tag{12}$$

$$\frac{1}{r}\frac{\partial}{\partial r}(r\rho u_r^2) + \frac{\partial}{\partial x}(\rho u_r u_x) - \rho\Omega^2 r = -\frac{\partial p}{\partial r} + F_r \tag{13}$$

$$2\rho\Omega u_r = -\frac{1}{r}\frac{\partial p}{\partial \theta} + F_\theta \tag{14}$$

$$\frac{1}{r}\frac{\partial}{\partial r}(r\rho u_x u_r) + \frac{\partial}{\partial x}(\rho u_x^2) = -\frac{\partial p}{\partial x} + F_x \tag{15}$$

$$\frac{1}{r}\frac{\partial}{\partial r}(ru_r(\rho E + p)) + \frac{\partial}{\partial x}(u_x(\rho E + p)) = 0 \tag{16}$$

where

$$E = \frac{u_r^2}{2} + \frac{u_x^2}{2} + \frac{1}{\gamma - 1}\frac{p}{\rho} - \frac{\Omega^2 r^2}{2} \tag{17}$$

Defining the average of a quantity, G, by

$$\bar{G} = \frac{1}{h(r)}\int_0^{h(r)} G dx \tag{18}$$

where h is the height of the impeller blade, and using the Leibniz rule for differentiation under the integral sign, we can average Eqs. (12), (13), and (16) to get

$$\frac{1}{r}\frac{\partial}{\partial r}(rh\overline{\rho u_r}) = 0 \tag{19}$$

$$\frac{1}{r}\frac{\partial}{\partial r}(rh\overline{\rho u_r^2}) - h\bar{\rho}\Omega^2 r = -\frac{\partial}{\partial r}(h\bar{p}) + p|_h\frac{\partial h}{\partial r} + h\overline{F_r} \tag{20}$$

$$\frac{1}{r}\frac{\partial}{\partial r}(rh\overline{\rho u_r E} + rh\overline{u_r p}) = 0 \tag{21}$$

subject to no-flux boundary conditions.

At this point, further assumptions are necessary. First, we assume that we can approximate averaged products by $\overline{ab} = \bar{a}\,\bar{b}$, which requires one of the variables to not deviate much from its mean value. Second, we assume that

$$p|_h = \bar{p} \tag{22}$$

and, finally, we take $\tilde{u}_x$ as small, so

$$\bar{E} = \frac{\overline{u_r^2}}{2} - \frac{\Omega^2 r^2}{2} + \frac{1}{\gamma - 1}\frac{\bar{p}}{\bar{\rho}} \tag{23}$$

This means that a 1D model for the flow in the impeller is given by

$$\frac{1}{r}\frac{\partial}{\partial r}(rh\rho u_r) = 0 \tag{24}$$

$$\frac{1}{r}\frac{\partial}{\partial r}(rh\rho u_r^2) - h\rho\Omega^2 r = -h\frac{\partial p}{\partial r} + hF_r \tag{25}$$

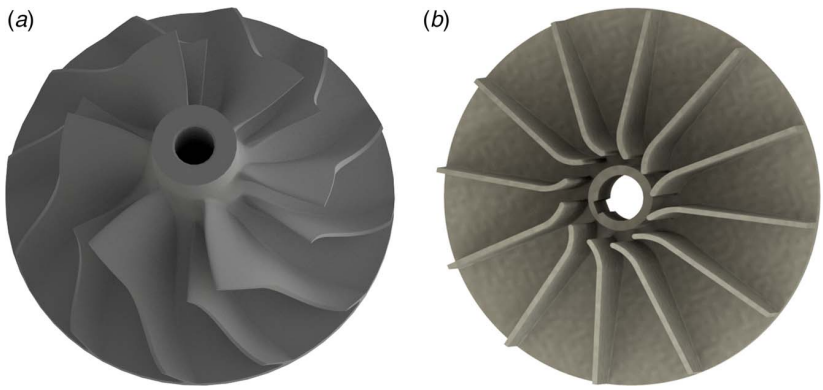

Fig. 1 (*a*) A typical impeller from a centrifugal compressor. It has backswept blades and turns the flow from the axial direction to the radial direction as it compresses. (*b*) The simplified impeller geometry used in the model derivation. Here, the flow travels radially from the center of the impeller to the outlet. It has straight radial blades but does have an inlet blade angle, so the model can account for the effects of poor inlet flow alignment.

$$\frac{1}{r}\frac{\partial}{\partial r}\left(rh\rho u_r\left(\frac{u_r^2}{2}+\frac{\gamma}{\gamma-1}\frac{p}{\rho}-\frac{\Omega^2 r^2}{2}\right)\right)=0 \tag{26}$$

where the bars have been dropped for convenience.

Diffuser. The diffuser is non-rotating, so $\Omega=0$, and we return to the inertial frame of reference. It is also assumed that the compressor has a vaneless diffuser, which allows the assumption that all variables are independent of θ.

Therefore, in this case, Eqs. (5)–(7) become

$$\frac{1}{r}\frac{\partial}{\partial r}(r\rho u_r)+\frac{\partial}{\partial x}(\rho u_x)=0 \tag{27}$$

$$\frac{1}{r}\frac{\partial}{\partial r}(r\rho u_r^2)+\frac{\partial}{\partial x}(\rho u_r u_x)-\frac{\rho u_\theta^2}{r}=-\frac{\partial p}{\partial r}+F_r \tag{28}$$

$$\frac{1}{r}\frac{\partial}{\partial r}(r\rho u_r u_\theta)+\frac{\partial}{\partial x}(\rho u_\theta u_x)+\frac{\rho u_r u_\theta}{r}=F_\theta \tag{29}$$

$$\frac{1}{r}\frac{\partial}{\partial r}(r\rho u_x u_r)+\frac{\partial}{\partial x}(\rho u_x^2)=-\frac{\partial p}{\partial x}+F_x \tag{30}$$

$$\frac{1}{r}\frac{\partial}{\partial r}(ru_r(\rho E+p))+\frac{\partial}{\partial x}(u_x(\rho E+p))=0 \tag{31}$$

where

$$E=\frac{u_r^2}{2}+\frac{u_x^2}{2}+\frac{1}{\gamma-1}\frac{p}{\rho} \tag{32}$$

Averaging Eqs. (27)–(29) and (31) subject to no-flux conditions as before, gives

$$\frac{1}{r}\frac{\partial}{\partial r}(rh\overline{\rho u_r})=0 \tag{33}$$

$$\frac{1}{r}\frac{\partial}{\partial r}(rh\overline{\rho u_r^2})-\frac{h\overline{\rho u_\theta^2}}{r}=-h\frac{\partial \bar{p}}{\partial r}+h\overline{F_r} \tag{34}$$

$$\frac{1}{r}\frac{\partial}{\partial r}(rh\overline{\rho u_r u_\theta})+\frac{h\overline{\rho u_r u_\theta}}{r}=h\overline{F_\theta} \tag{35}$$

$$\frac{1}{r}\frac{\partial}{\partial r}(rh\overline{\rho u_r E}+rh\overline{u_r p})=0 \tag{36}$$

Therefore, using the same assumptions as we did for the impeller, so that $\overline{ab}=\bar{a}\,\bar{b}$ and

$$\bar{E}=\frac{\overline{u_r^2}}{2}+\frac{\overline{u_\theta^2}}{2}+\frac{1}{\gamma-1}\frac{\bar{p}}{\bar{\rho}} \tag{37}$$

we get the following system of equations for the diffuser (after dropping the bars):

$$\frac{1}{r}\frac{\partial}{\partial r}(rh\rho u_r)=0 \tag{38}$$

$$\frac{1}{r}\frac{\partial}{\partial r}(rh\rho u_r^2)-\frac{h\rho u_\theta^2}{r}=-h\frac{\partial p}{\partial r}+hF_r \tag{39}$$

$$\frac{1}{r}\frac{\partial}{\partial r}(rh\rho u_r u_\theta)+\frac{h\rho u_r u_\theta}{r}=hF_\theta \tag{40}$$

$$\frac{1}{r}\frac{\partial}{\partial r}\left(rh\rho u_r\left(\frac{u_r^2}{2}+\frac{u_\theta^2}{2}+\frac{\gamma}{\gamma-1}\frac{p}{\rho}\right)\right)=0 \tag{41}$$

Friction. Skin friction is the only type of frictional loss that is considered in this model. It is defined as the shear stress exerted by the fluid on the surface over which it flows [31]. Therefore, if τ_w denotes the wall shear stress

$$F=-\tau_w S \tag{42}$$

$$\Rightarrow F=-\frac{1}{2}f\rho u_r^2 S \tag{43}$$

where S denotes the total surface area of the contact faces between the walls and the fluid per unit volume, and

$$f=\frac{\tau_w}{\frac{1}{2}\rho u_r^2} \tag{44}$$

is the Fanning friction factor [32].

Therefore, in the impeller, we have

$$F_r=-\frac{1}{2}f\rho u_r^2 S_I \tag{45}$$

where

$$S_I=2\left(\frac{n_b}{2\pi r}+\frac{1}{h}\right) \tag{46}$$

and for the diffuser, we have

$$F_r=-\frac{1}{2}f\rho u_r^2 S_D \tag{47}$$

$$F_\theta=-\frac{1}{2}f\rho u_r u_\theta S_D \tag{48}$$

where

$$S_D=\frac{2}{h} \tag{49}$$

Stalling. The mass flow rate is defined as $\dot{m}=A\,\rho u_r$ for a cross-sectional area A. In the diffuser, the area is simply $A=2\pi rh$. However, in the impeller, we can get stalling at the inlet. As seen in Fig. 2, low inlet velocities lead to large flow angles, β, which result in flow separation. This region of stalled flow effectively blocks part of the channel, and so reduces the area of the channel available to the unstalled flow.

Therefore, defining the impeller area as $A=\theta rh$ for

$$\theta=\begin{cases}\dfrac{2\pi}{\left(1+\alpha\left(1-\dfrac{\tan\beta_B}{\tan\beta}\right)^2\right)} & \beta>\beta_B\\ 2\pi & \text{otherwise}\end{cases} \tag{50}$$

where β_B is the inlet blade angle of the impeller, allows us to take into account this stalling. The parameter α is used to control the strength of the stalling, for example, if A_0 is the area of the entire channel, then the maximum blockage results in an area of $(1/(1+\alpha))A_0$.

It is not uncommon to use blockage as a way to represent stalled flow regimes. Day et al. [33] developed a model for rotating stall in an axial compressor. They noted that stall cells had negligible axial velocity, whereas the unstalled regions had a higher axial velocity than expected. This led to them including a stall cell blockage parameter in their model to simulate this.

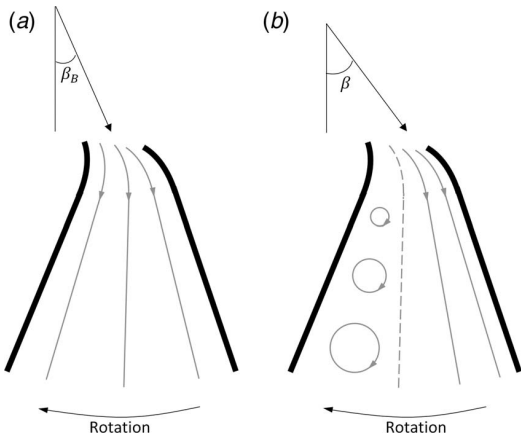

Fig. 2 Impeller channels in (*a*) unstalled and (*b*) stalled conditions. The stalled channel is caused by a low inlet radial velocity that leads to a large inlet flow angle β in comparison to the blade angle β_B. The unstalled channel is shown with an inlet flow angle that matches the blade angle β_B perfectly.

It is possible to also include diffuser stall in a similar fashion. For a vaneless diffuser, we would argue that the shroud-side area of the impeller and diffuser is blocked due to recirculation. Therefore, we could create a similar blockage formula that involves the diffuser inlet flow angle and a critical angle at which recirculation occurs. We would also be able to account for impeller backsweep in this stall model by considering its effect on the diffuser inlet angle.

If instead we were working on a vaned diffuser, we would use an area blockage argument that follows very closely to that of the impeller using the inlet diffuser flow angle and the angle of the vanes.

Numerical Implementation and Results

In order to implement this numerically, it is possible to reduce each system of ODEs for the impeller and diffuser into just one ODE for density, ρ. After rearranging, we get

$$\frac{\partial \rho}{\partial r} = \frac{-\rho q^2\left(\frac{1}{r}+\frac{1}{h}\frac{\partial h}{\partial r}\right) - \Omega^2 r^3 h^2 \rho^3 + \gamma f \rho q^2\left(\frac{n_b}{2\pi r}+\frac{1}{h}\right)}{\left(\frac{\gamma+1}{2}\right)q^2 - (\gamma-1)\left(\frac{\Omega^2 r^2}{2}+E_I\right)r^2 h^2 \rho^2} \tag{51}$$

for the impeller and

$$\frac{\partial \rho}{\partial r} = \frac{-\frac{\rho q^2}{r} - r^2 h^2 \rho^3\left(\gamma\frac{u_\theta^2}{r}+(\gamma-1)u_\theta\frac{\partial u_\theta}{\partial r}\right)+\gamma\frac{f}{h}\rho q^2}{\left(\frac{\gamma+1}{2}\right)q^2 + (\gamma-1)\left(\frac{u_\theta^2}{2}-E_D\right)r^2 h^2 \rho^2} \tag{52}$$

for the diffuser, where

$$rh\rho u_r = q = \text{const} \tag{53}$$

$$\frac{u_r^2}{2}+\frac{\gamma}{\gamma-1}\frac{p}{\rho}-\frac{\Omega^2 r^2}{2} = E_I = \text{const} \tag{54}$$

$$\frac{u_r^2}{2}+\frac{u_\theta^2}{2}+\frac{\gamma}{\gamma-1}\frac{p}{\rho} = E_D = \text{const} \tag{55}$$

$$u_\theta = \frac{\Omega r_{\text{tip}}^2}{r} e^{-(f/h)(r-r_{\text{tip}})} \tag{56}$$

Observing that

$$q = \frac{\dot{m}}{\theta} \tag{57}$$

where θ is defined as before to take into account inlet stalling, we can write

$$q = \begin{cases} \frac{\dot{m}}{2\pi}\left(1+\alpha\left(1-\frac{\tan\beta_B}{\tan\beta}\right)^2\right) & \beta > \beta_B \\ \frac{\dot{m}}{2\pi} & \text{otherwise} \end{cases} \tag{58}$$

These ODEs can be solved quickly in MATLAB using ode45 to simulate flow through the compressor in steady-state. Figure 3 shows how the properties of the flow change, as it passes through the impeller and diffuser.

We observe that the tangential velocity is increasing in the impeller with radial distance due to the fixed impeller angular speed. However, in the diffuser, there is no forced rotation, and the tangential velocity decreases due to diffusion and frictional forces.

The radial velocity is generally decreasing due to diffusion and friction. In the impeller, there is a balance between diffusion, as the channel is increasing in area, and centrifugal forces, which accelerate the flow radially. The centrifugal forces dominate at large tangential velocities, which is why the velocity begins to increase near the impeller exit.

Since we have diffusion in both the impeller and diffuser, the pressure and density rise occurs in both components.

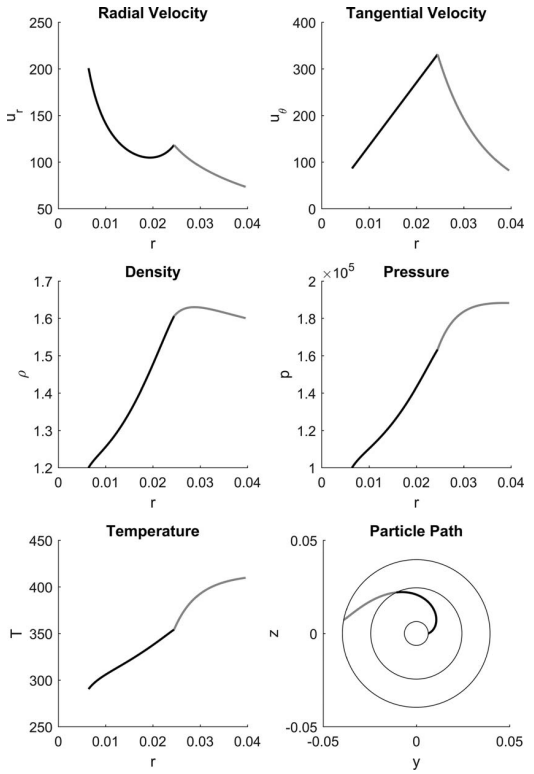

Fig. 3 Simulated gas properties as air passes through a small compressor. This shows a stable operating point, with the impeller spinning at 130 krpm and a mass flow of 0.1 kg/s. All black lines indicate that the flow is in the impeller and all gray lines indicate that the flow is in the diffuser.

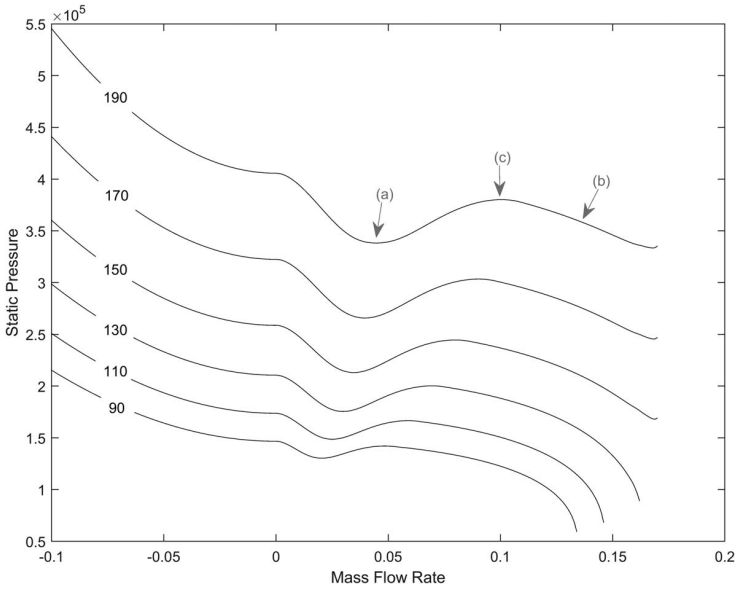

Fig. 4 Simulated static pressure compressor characteristics for six different impeller speeds, labeled on each line in krpm. The points (a) and (b) correspond to locations where stalling and friction are dominant effects, respectively. The point (c) identifies the local maximum that is used in Fig. 9.

The temperature also rises throughout the compressor because of friction. In the diffuser, friction is acting against both the radial and tangential component of velocity, whereas in the impeller, the tangential velocity is dictated by the impeller rotation and so friction only acts against the radial velocity. Therefore, we see a sharper rise in temperature in the diffuser.

The particle path shows us that the flow is traveling in an Archimedean spiral in the impeller due to the radial blades and the forced rotation. This turns into an approximately logarithmic spiral in the diffuser. If there was no friction in the diffuser, we would have a true logarithmic spiral as the path would be that of a free vortex.

Running this simulation for multiple impeller speeds and mass flows and plotting the outlet static pressure produce compressor characteristics, as seen in Fig. 4. Notice that because we also know the outlet density and velocity, we can compute the total pressure characteristic (and hence the total-to-total pressure ratio at each point).

By varying factors within the simulation, it is easy to discover why we get this cubic-like shape. The local minimum at low mass flows (Fig. 4(a)) is caused by stalling in the impeller and changes with values of the stall parameter α. The negative slope to the right of the local maximum (Fig. 4(b)) is due to friction and changes with the value of the friction factor f. Finally, in reversed flow, the compressor acts as a restrictor, and so, the characteristic has a negative slope because it follows a shape similar to that of an orifice.

Parameter Fitting. In order for the model to be predictive, relationships for the two parameters in the model, f and α, need to be determined. These relationships must only depend on the known model variables, such as mass flow or impeller speed.

We shall demonstrate this process via the use of two datasets; one for finding the relationship and the other for checking this relationship holds across different compressors. For ease, let us label these datasets as A and B. Each dataset is from an experimental study performed on the gas stand at the University of Bath and consists of a compressor map, detailing the total-to-total pressure ratio at different mass flows and impeller speeds, and surge data, including the peak static pressure oscillation amplitude for each impeller speed. Table 1 gives geometric details of the compressors associated with each dataset, where Fig. 5 can be used for reference.

Consider the friction parameter, f. Using dataset A, we can find a value for f at each impeller speed by performing a least squares fit from the model line to the compressor map data. For this, we are careful to only use the points in the dataset that are truly steady (i.e., show no form of oscillation above the normal noise level in the data) because our compressor characteristics only output steady-state compressor behavior. This provided us with a linear relationship between the friction parameter and impeller speed given by

$$f = 0.14 + 5 \times 10^{-6}\Omega \tag{59}$$

where Ω is in radians/s. To validate this relationship, we perform a least squares fit for each speed line in dataset B (again using steady points only). Figure 6 shows the linear relationship found from dataset A (crosses) alongside the desired values of f for dataset B (circles). Dataset B also appears to share the linear relationship, but the fit would be better if there was a minor shift to the intercept. Implementing this shift has no visible effect on the resulting characteristics, so the original relationship is used.

Table 1 Geometric details of the compressors used for parameter fitting and validation

	Dataset A	Dataset B
Number of blades	6 + 6	6 + 6
Hub diameter	12.8 mm	10 mm
Shroud diameter	33.5 mm	29.6 mm
Wheel tip diameter	49 mm	40 mm
Diffuser height	3.4 mm	3 mm
Diffuser length	15.1 mm	15.7 mm
Diffuser area ratio	1.6	1.8

Note: Figure 5 can be referred to for explanation of the dimensions.

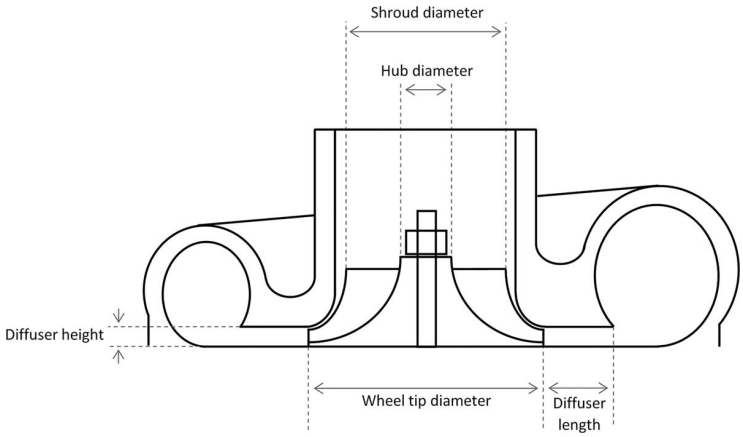

Fig. 5 Diagram indicating the dimensions given in Table 1

In reality, there would be 3D flow effects, such as eddy currents, that would add to the losses in the compressor at higher rotational speeds. These features cannot be captured by this 1D model, and so are being encompassed into the friction parameter via this relationship.

For determining the stalling parameter α, we can look at the peak static pressure amplitude observed while operating at surge for each speed line in dataset A. The left-hand-side graph in Fig. 7 shows how the value of α impacts the relationship between the observed peak surge amplitude and the impeller speed for the model. Exploiting this, we can determine that

$$\alpha = 10.3 - 1.5 \times 10^{-4}\Omega \tag{60}$$

The right-hand-side graph in Fig. 7 shows the resulting trend in the impeller speed—surge amplitude relationship, along with the surge amplitude data for dataset B. This fit is very good across the different compressors.

Quasi-Steady Model

We can now use the compressor characteristics developed above by creating a model for the flow between the compressor and a throttle valve. Ideally, we should end up with a system of ODEs similar to that of Eqs. (1) and (2).

The compressors corresponding to datasets A and B were both tested on a rig that had a pipe without a plenum connecting it to the throttle value. Therefore, using the equations of mass and momentum in the inertial frame (Eqs. (5) and (6) with $\Omega = 0$), along with the assumption of an isentropic gas

$$p = \kappa\rho^{\gamma} \tag{61}$$

allows us to obtain the following system of equations for the flow in the compression system:

$$\frac{d\dot{m}}{dt} = \frac{A}{L}(p_c(\dot{m}) - p) + \frac{\kappa^{1/\gamma}}{AL}\left(\frac{\dot{m}^2}{p_c(\dot{m})^{1/\gamma}} - \frac{\dot{m}_T(p)^2}{p^{1/\gamma}}\right) \tag{62}$$

$$\frac{dp}{dt} = \frac{\gamma\kappa^{1/\gamma}}{AL}p^{(\gamma-1)/\gamma}(\dot{m} - \dot{m}_T(p)) \tag{63}$$

where $\dot{m}_T$ is the throttle characteristic and p_c is the steady-state compressor characteristic developed within this paper.

For the throttle characteristic, we can use

$$\dot{m}_T^2(p) = \frac{2\gamma}{\gamma - 1}\left(\frac{\lambda^2 A^2 \rho\rho_{\text{amb}}}{\lambda^2\rho_{\text{amb}}^2 - \rho^2}\right)(\rho p_{\text{amb}} - \rho_{\text{amb}} p) \tag{64}$$

where λ is the fraction, the throttle is open. This has come from the steady-state forms of conservation of mass and energy (Eqs. (5) and (7)) applied to two points: one before the throttle, which has unknown density, pressure, and mass flow values, and one after the throttle, which is assumed to be at ambient conditions.

This system can then be solved numerically to identify the time-dependent behavior of the compression system. The operating point of the system is the intersection of the throttle characteristic $\dot{m}_T$ and the compressor characteristic p_c in the mass flow—static pressure plane. There are two observed behaviors with this system.

The first is steady behavior where pressure and mass flow remain constant with time. The second is oscillating behavior as shown in Fig. 8(*a*). In this case, we get a trajectory in time that tracks the negatively sloped regions of the compressor characteristic closely, traveling quickly between them. It causes oscillations in mass flow and pressure of about 6 Hz, which is good as surge typically is a low-frequency phenomena.

The dynamics of this oscillating state depends on the geometry of the pipework between the compressor and the throttle. Figures 8(*b*) and 8(*c*) show an example of what happens when the length, L, and the cross-sectional area, A, of the pipe change. The pipe length influences the frequency of the simulated oscillations because if L increases, the frequency decreases (and vice versa). The cross-sectional area has a more complex effect on the dynamics. It influences the frequency in the same way as L (larger area results in a decreased frequency and vice versa), but it has the additional

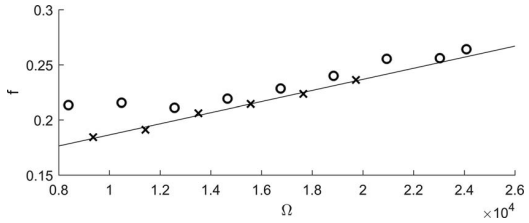

Fig. 6 Line indicating the discovered linear relationship between friction parameter, *f*, and impeller speed, Ω. The crosses are for the compressor in dataset A, and the circles are for the compressor in dataset B.

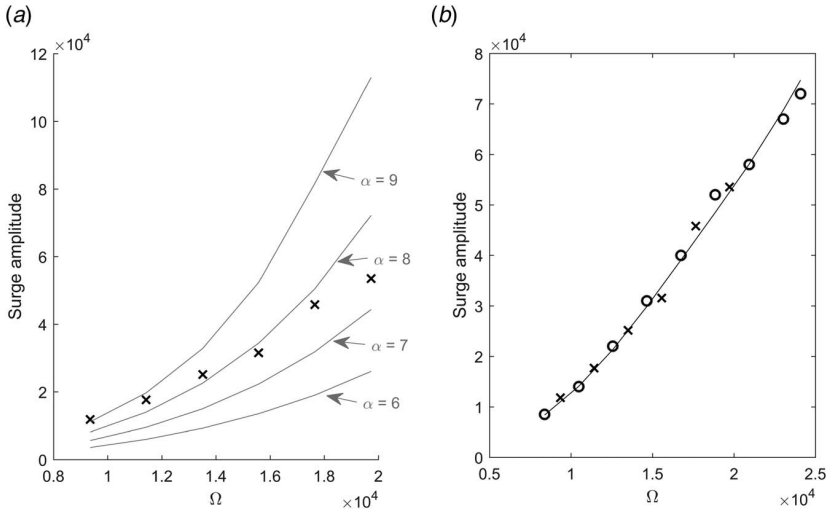

Fig. 7 (*a*) Computed relationship between impeller speed and amplitude of surge oscillations in the model for different values of the stalling parameter, α. The amplitude data from dataset A are shown as crosses for comparison. (*b*) Result when using the discovered relationship for stalling parameter α. The crosses are from dataset A, and the circles are from dataset B.

effect that as A becomes small, the shape of the limit cycle becomes smoother and does not track the compressor characteristic as close.

What is clear from all the limit cycles in Fig. 8 is that the shape of the compressor characteristic is key to the dynamics. Therefore, changing things like the inlet blade angle will alter the location of the point in which we see oscillations, i.e., our surge line. It also means that as the shape of the compressor characteristic becomes more accurate by, say, adding in a diffuser stall, we will be able to capture more of the surge dynamics.

It is good that our model can capture changes in the simulated surge dynamics for different pipe geometries and compressor characteristics because it means that it is able to simulate the testing of different compressors on different test rigs.

Model Validation. In order to evaluate our model more quantitatively, we can run this quasi-steady model at different throttle openings and compute a time average of the pressure and mass flows. This

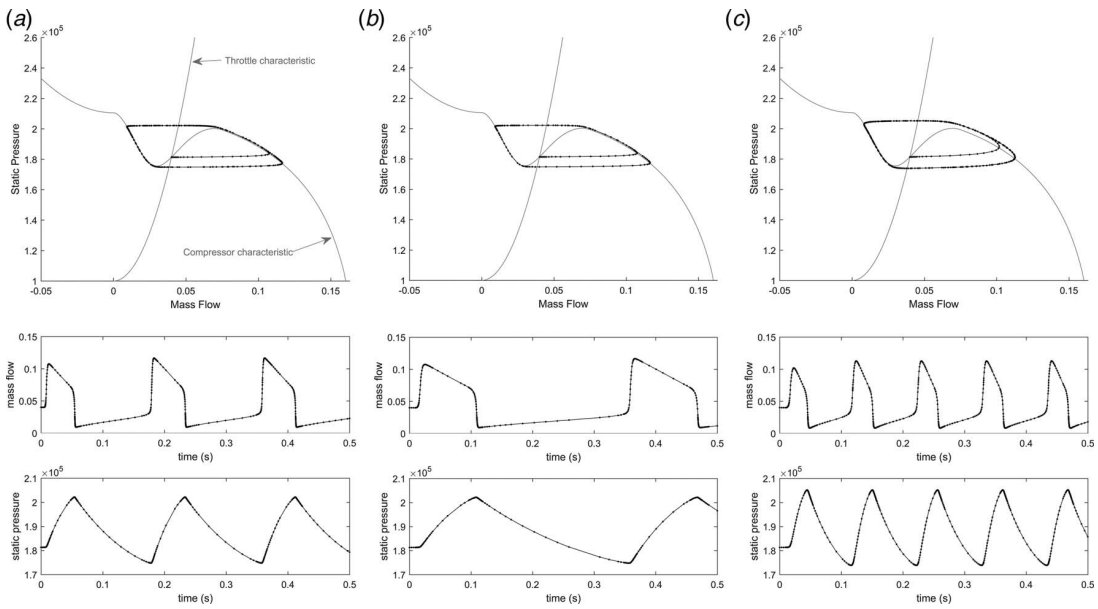

Fig. 8 Three simulated cases: (*a*) 3 m length of 3 in. diameter pipe, (*b*) 6 m length of 3 in. diameter pipe, and (*c*) 3 m length of 1.5 in. diameter pipe. For each case, the top graph is a simulated surge limit cycle in the mass flow-static pressure plane, with the compressor and throttle characteristics identified in gray, and the bottom graph is the corresponding simulated pressure and mass flow oscillations.

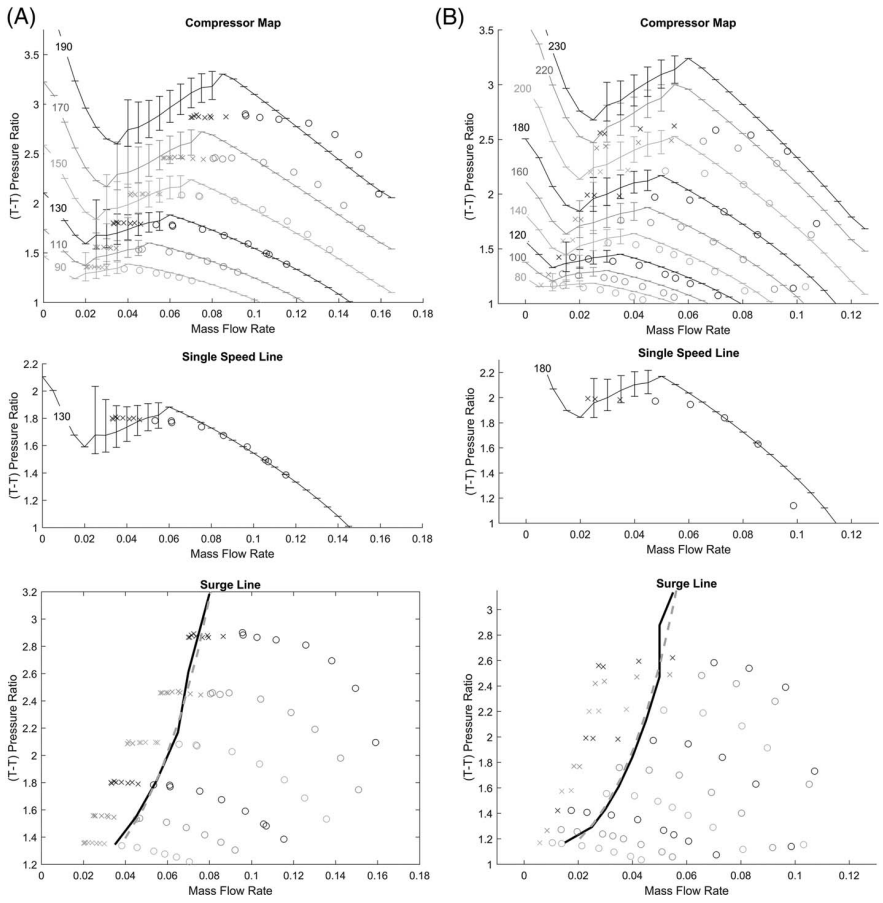

Fig. 9 Comparison between the simulated total-to-total compressor map and the data for datasets A and B. The simulated map has been plotted as lines with bars showing the max and min simulated values. The data are shown with circles if it is steady and crosses if it showed oscillations larger than the average noise level. The speed in krpm is indicated on each line. For clarity, a single speed line from the middle of the map is shown separately below. Finally, situated at the bottom, the simulated surge line is shown (in solid black) in comparison to the data. The dashed gray line shows the location of the local maximum of the compressor characteristics (Fig. 4(c)) for comparison.

can be used to produce a time-averaged compressor map, which is essentially what we get through testing. Figure 9 shows this time-averaged map with experimental data points for both datasets A and B.

We have chosen to classify the data into two categories: those that only show oscillations at the average noise level (which changes from about 100 Pa to 1000 Pa, as the impeller speed increases) are considered steady, and those that show oscillations greater than that are considered unsteady. In Fig. 9, we have plotted the steady data as circles and the unsteady data as crosses.

For the simulated compressor map, we have plotted bars that identify the range of values seen when computing the time-average solution. From this, we can see a clear line that indicates the onset of oscillations in our model. We call this the simulated surge line and have shown this with comparison to the data underneath each map.

Our simulated surge line is very close to the local maximum of the compressor characteristics (see Fig. 4(c)), which is shown with a gray dashed line in the figure. Since the gradient of the characteristic (and hence the location of local maximum and minimum) is determined by the impeller inlet stall, we can deduce that this stall is triggering our simulated compressor into surge.

We can also see that our simulated surge line is close to the point in the data where it switches from steady behavior to mild oscillation. It appears to predict an earlier surge onset for lower impeller speeds, but it is possible that this is due to the fact that distinguishing between noise and mild oscillations is difficult for these points.

At high speeds, our surge line is within the region of mild oscillation (or mild surge) and, for compressor A, is getting close to the deep surge limit (the left-most data point). This suggests that the trigger for mild surge at these points is likely to be something other than impeller inlet stall, and that it is this in combination with the impeller inlet stall that causes deep surge.

The simulated amplitude of the oscillations is increasing as mass flow decreases, which is very promising as in experiments, the oscillations typically grow toward the deep surge limit (where testing is stopped to prevent damage to the compressor). However, as mass flow is reduced, there becomes a point in our simulated map that the oscillations stop and the flow becomes stable again. This may

indeed be true because Koff and Greitzer [20] found during their experimental study of the compressor map that the flow can become stable again close to shut-off. However, we have some unsteady data points that lie in this part of our curves, so our region of stability is currently larger than is observed experimentally.

When examining the fit of the data to the simulated average total-to-total pressure ratio curves, we can see that for speeds under 200 krpm, the points follow the steady portion of the curve closely, and for speeds under 180 krpm, the time-averaged unsteady points are also a reasonable fit. From the single speed line plots, it is clear to see that, as mass flow decreases, our model predicts steady flow behavior with an increasing pressure ratio until the simulated surge line, and unsteady flow behavior with a decreasing average pressure ratio after that point. When the data approach the surge line, it seems to flatten out instead but usually remains within the simulated range of oscillation.

From the single speed line for dataset B, we can see that the model is not always able to simulate the pressure ratios for high mass flows. This is because at high mass flows, we approach the choked flow region, and the Mach number for the flow increases toward 1. Our model does not include any form of shock loss that would occur as the flow approaches the speed of sound, and so does not contain all the physics required to capture the choked flow behavior.

Above speeds of 200 krpm, the fit is not as good, meaning that our model is missing some important physical dynamics for the higher impeller speeds. Diffuser stall is a phenomenon that is usually triggered first at higher impeller speeds; therefore, incorporating this into the model is expected to improve the fit and surge dynamics at these higher speeds.

Overall, this model has been able to predict a surge line for a compressor by only considering its geometry. There are inaccuracies in the model, but we have made a choice to compromise on accuracy for the sake of having a predictive model, and these inaccuracies can be improved upon as more dynamics are added.

Summary and Conclusions

A new method for producing compressor characteristics has been presented, updating the work on low-dimensional surge models developed during the 1970s. An original steady-state compressor model was developed from the mass, momentum, and energy conservation laws, along with two factors to model friction and stalling. Creating the model this way allowed for insight into various features observed in a compressor characteristic. For example, stalling creates a local minimum and maximum in low forward mass flows. Since the location of this feature correlates to the location of the surge line in our model, we were able to identify impeller inlet stall as a route into surge.

The model equations were reduced and simplified to form ODEs that are quick to solve. If full 3D CFD was used to model flow in a compressor near surge, this highly complex problem becomes very computationally expensive. Low-dimensional surge models are a viable alternative because the need for quick evaluations outweighs the need for high accuracy, and so, it is vital that this speed of computation is maintained.

Relationships for the friction parameter and stalling parameter with impeller speed were found by comparison to test data. These relationships hold across multiple compressor geometries, allowing the model to be fully deterministic. Therefore, the model has the ability to be a predictive tool for surge limits of new compressor designs because it only needs geometric measurements as inputs.

The model showed promising results when compared with compressor map data, and is able to capture reasonably realistic surge frequencies when included in a low-dimensional surge model. It is able to identify when oscillations in mass flow and pressure are likely to appear, and is able to capture a growing amplitude in oscillations as the mass flow is further reduced.

Further work is planned to include diffuser recirculation or stall into this model. It is generally agreed that diffuser stall can trigger surge at higher impeller speeds, which will hopefully improve the accuracy of the model's surge limit.

Acknowledgment

The authors are grateful to Tomasz Duda, Stefan Tuechler, and Zheng Liu, who provided the geometry, compressor map, and surge amplitude data within this paper.

Katherine Powers is supported by a scholarship from the EPSRC Centre for Doctoral Training in Statistical Applied Mathematics at Bath (SAMBa), under the project EP/L015684/1.

Nomenclature

Mathematical Symbols

f = friction factor
g = acceleration due to gravity
h = channel height
$\dot{m}$ = mass flow
p = static pressure
q = mass flow per radian
r = radius
u = velocity
A = cross-sectional area
B = Greitzer's parameter
E = specific energy
F = friction
L = length
$\dot{Q}$ = specific heat energy
R = specific gas constant
S = surface area
T = temperature
U = specific internal energy
c_v = specific heat at constant volume
n_b = the number of impeller blades
α = stalling factor
β = flow angle
β_B = blade angle
γ = specific heat ratio
κ = isentropic constant
λ = fraction throttle is open
ξ_T = throttle parameter
ρ = density
τ = stress
Φ = nondimensional mass flow
Ψ = nondimensional pressure
Ω = angular velocity

Subscripts

amb = ambient
c = compressor
D = diffuser
I = impeller
r = radial direction
T = throttle
tip = impeller tip
x = axial direction
θ = tangential direction

References

[1] Rasmussen, P. C., and Kurz, R., 2009, "Centrifugal Compressor Applications—Upstream and Midstream," Proceedings of the 38th Turbomachinery Symposium, Texas A&M University.

[2] Macdougal, I., and Elder, R. L., 1983, "Simulation of Centrifugal Compressor Transient Performance for Process Plant Applications," J. Eng. Power, **105**(4), pp. 885–890.
[3] Stone, R., 2012, *Introduction to Internal Combustion Engines*, 4th ed., Palgrave MacMillan, Hampshire, UK.
[4] Watson, N., and Janota, M. S., 1982, *Turbocharging: The Internal Combustion Engine*, MacMillan, London.
[5] Pampreen, R. C., 1993, *Compressor Surge and Stall*, Concepts Eti, Norwich, VT.
[6] Fink, D. A., Cumpsty, N. A., and Greitzer, E. M., 1992, "Surge Dynamics in a Free-Spool Centrifugal Compressor System," ASME J. Turbomach., **114**(2), pp. 321–332.
[7] De Jager, B., 1995, "Rotating Stall and Surge Control: A Survey," Proceedings of the 34th IEEE Conference on Decision and Control, New Orleans, LA, Vol. 2, pp. 1857–1862.
[8] Longley, J. P., 1994, "A Review of Nonsteady Flow Models for Compressor Stability," ASME J. Turbomach., **116**(2), pp. 202–215.
[9] Stenning, A. H., 1980, "Rotating Stall and Surge," J. Fluid. Eng., **102**(1), pp. 14–20.
[10] Linfield, K. W., and Mudry, R. G., 2008, *Pros and Cons of CFD and Physical Flow Modeling*, Airflow Sciences Corporation, Livonia, MI.
[11] Cozzi, L., Rubechini, F., Marconcini, M., Arnone, A., Astrua, P., Schneider, A., and Silingardi, A., 2017, "Facing the Challenges in CFD Modelling of Multistage Axial Compressors," ASME Turbo Expo 2017: Turbomachinery Technical Conference and Exposition, Charlotte, NC.
[12] Arnulfi, G. L., Giannattasio, P., Giusto, C., Massardo, A. F., Micheli, D., and Pinamonti, P., 1999, "Multistage Centrifugal Compressor Surge Analysis: Part II—Numerical Simulation and Dynamic Control Parameters Evaluation," ASME J. Turbomach., **121**(2), pp. 312–320.
[13] Van Helvoirt, J., de Jager, B., Steinbuch, M., and Smeulers, J., 2004, "Stability Parameter Identification for a Centrifugal Compression System," 43rd IEEE Conference on Decision and Control, Paradise Islands, The Bahamas, Vol. 4, pp. 3400–3405.
[14] Mizuki, S., Asaga, Y., Ono, Y., and Tsujita, H., 2006, "Investigation of Surge Behavior in a Micro Centrifugal Compressor," J. Therm. Sci., **15**(2), pp. 97–102.
[15] Tamaki, H., 2008, "Effect of Piping Systems on Surge in Centrifugal Compressors," J. Mech. Sci. Technol., **2**(10), pp. 1857–1863.
[16] Galindo, J., Arnau, F. J., Tiseira, A., and Piqueras, P., 2010, "Solution of the Turbocompressor Boundary Condition for One-Dimensional Gas-Dynamic Codes," Math. Comput. Modell., **52**(7–8), pp. 1288–1297.
[17] Torregrosa, A., Arnau, F., Piqueras, P., Reyes-Belmonte, M., Knutsson, M., and Lennblad, J., 2012, "Acoustic One-Dimensional Compressor Model for Integration in a Gas-Dynamic Code," SAE 2012 World Congress & Exhibition, Detroit, MI.
[18] Greitzer, E. M., 1976, "Surge and Rotating Stall in Axial Flow Compressors—Part I: Theoretical Compression System Model," J. Eng. Power, **98**(2), pp. 190–198.
[19] Hos, C., Champneys, A., and Kullmann, L., 2003, "Bifurcation Analysis of Surge and Rotating Stall in the Moore-Greitzer Compression System," IMA J. Appl. Math., **68**(2), pp. 205–228.
[20] Koff, S. G., and Greitzer, E. M., 1984, "Stalled Flow Performance for Axial Compressors: I—Axisymmetric Characteristic," 29th International Gas Turbine Conference and Exhibit, Amsterdam, Netherlands.
[21] Galindo, J., Serrano, J. R., Climent, H., and Tiseira, A., 2008, "Experiments and Modelling of Surge in Small Centrifugal Compressor for Automotive Engines," Exp. Therm. Fluid. Sci., **32**(3), pp. 818–826.
[22] Moore, F. K., and Greitzer, E. M., 1986, "A Theory of Post-Stall Transients in Axial Compression Systems: Part I—Development of Equations," ASME J. Eng. Gas Turb. Power, **108**(1), pp. 68–76.
[23] Zagorowska, M., and Thornhill, N. F., 2017, "Compressor Map Approximation Using Chebyshev Polynomials," 25th Mediterranean Conference on Control and Automation (MED), Valletta, Malta, pp. 846–869.
[24] Li, X., Yang, C., Wang, Y., and Wang, H., 2018, "A Prediction Model of Compressor With Variable-Geometry Diffuser Based on Elliptic Equation and Partial Least Squares," R. Soc. Open Sci., **5**(1), pp. 1–19.
[25] Elder, R. L., and Gill, M. E., 1985, "A Discussion of the Factors Affecting Surge in Centrifugal Compressors," ASME J. Eng. Gas Turb. Power, **107**(2), pp. 499–506.
[26] Martin, G., Talon, V., Higelin, P., Charlet, A., and Caillol, C., 2009, "Implementing Turbomachinery Physics Into Data Map-Based Turbocharger Models," SAE Int. J. Engines, **2**(1), pp. 211–229.
[27] Japikse, D., 1996, *Centrifugal Compressor Design and Performance*, Vol. 2, Concepts Eti, White River Junction, VT.
[28] Velasquez, E. I. G., 2017, "Determination of a Suitable Set of Loss Models for Centrifugal Compressor Performance Prediction," Chinese J. Aeronaut., **30**(5), pp. 1644–1650.
[29] Oh, H. W., Yoon, E. S., and Chung, M. K., 1997, ""An Optimum Set of Loss Models for Performance Prediction of Centrifugal Compressors," Proc. Inst. Mech. Eng. Part A: J. Power Energy, **211**(4), pp. 331–338.
[30] Gong, X., and Chen, R., 2014, "Total Pressure Loss Mechanism of Centrifugal Compressors," Mech. Eng. Res., **4**(2), pp. 45–59.
[31] Burr, K. P., Akylas, T. R., and Mei, C. C., 2003, *Chapter 2: Two-Dimensional Laminar Boundary Layers*, Lecture Notes, MIT, Cambridge, MA.
[32] Winterbone, D. E., and Pearson, R. J., 2000, *Theory of Engine Manifold Design: Wave Action Methods for I.C. Engines*, Professional Engineering Publishing, London, UK.
[33] Day, I. J., Greitzer, E. M., and Cumpsty, N. A., 1978, "Prediction of Compressor Performance in Rotating Stall," J. Eng. Power, **100**(1), pp. 1–12.

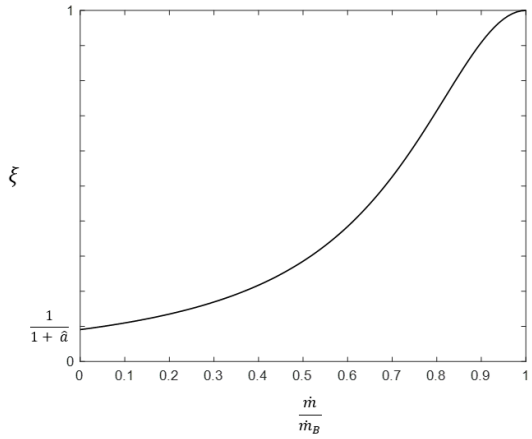

Figure 2-11: Behaviour of stall function, ξ, as mass flow decreases from stall point, $\dot{m}_B$. We have a monotonically decreasing function which takes a minimum value at $\dot{m} = 0$.

2.6 Discussion of Paper 1

As we can see in Fig. 4 of the paper, including incidence losses gives is a cubic-shaped characteristic with a minimum near zero mass flow.

All the stall function ξ does is change the effective velocity of the system. Without the stall function, the velocity was $u_r = \frac{\dot{m}}{2\pi\rho A}$ and so was linear with mass flow. Whereas, with the stall the velocity becomes

$$u_r = \frac{\dot{m}}{2\pi\xi(\dot{m})\rho A}, \quad \xi(\dot{m}) = \frac{1}{1+\hat{a}\left(1-\frac{\dot{m}}{\dot{m}_B}\right)^2}. \tag{2.6.1}$$

We can deduce from Section 2.4.2, that the pressure is monotonically decreasing with velocity (as it is monotonically decreasing with unstalled mass flow). Therefore, the local minimum we see in Paper 1, Fig. 4 must coincide with a local maximum of the velocity.

Figure 2-11 shows the behaviour of the stall function with mass flow. As mass flow decreases from the initial stall point, the stall function decreases monotonically.

Therefore, since $u_r \propto \frac{\dot{m}}{\xi(\dot{m})}$, both the numerator and denominator decrease with a reduction in mass flow. This balance of behaviours explains why the maximum velocity, and hence minimum pressure, occurs away from the $\dot{m} = 0$ axis.

Furthermore, as was shown in Paper 1, Fig. 8, this new shape of characteristic can simulate surge-like behaviour when combined with the nonlinear reduced order model presented in Section 2.2.

This surge-like behaviour coincides with the positive gradient of the compressor characteristic (between the local minimum (a) and local maximum (c) as labelled in Paper 1, Fig. 4). This positive gradient only occurs because of our inclusion of incidence losses into the model. Therefore, incidence loss and the resulting impeller inlet stall is a vital mechanism for surge.

As we can see from Paper 1, Fig. 8, the mass flow oscillations stay positive for all time. Therefore this is technically classed as mild surge. However, the simulated amplitudes of oscillation imply this should be deep surge. This means that the current stall function may not be using the correct assumptions.

2.6.1 Improvement of Stall Function

From Paper 1, Fig. 8, it appears that the intercept value is too high for our limit cycles to enter the negative flow regime. The limit cycle appears to retain an almost constant pressure from the local maximum until it intersects the characteristic just before the axis. If the intercept value was lower, then it's possible for the limit cycle to enter the negative mass flow region before intersecting the characteristic.

This implies that we may have had the wrong condition at $\dot{m} = 0$. Since $\dot{m} = 2\pi\xi A\rho u_r$, we assumed that $\dot{m} = 0$ results in $u_r = 0$. However, there is the possibility that $\xi = 0$ instead. This would mean that at zero flow, incidence losses are at a maximum as the entire impeller channel has stalled. This agrees with the suggestion from Watson and Janota [1] shown in Fig. 2-9 where the incidence losses increase monotonically from the optimal case of flow angle matching the blade angle.

In Section 2.4.3 we derived the form of the stall function using

$$\frac{\dot{m}}{\xi A\rho} = u_r(\dot{m}) = a\dot{m}^3 + b\dot{m}^2 + c\dot{m} + d. \tag{2.6.2}$$

By no longer requiring $u_r = 0$ at $\dot{m} = 0$, we do not assume $d = 0$, but the other

conditions:

$$\frac{\dot{m}_B}{A\rho} = a\dot{m}_B^3 + b\dot{m}_B^2 + c\dot{m}_B + d, \tag{2.6.3}$$

$$\frac{1}{A\rho} = 3a\dot{m}_B^2 + 2b\dot{m}_B + c, \tag{2.6.4}$$

remain valid. As before, we can solve this system for b and c to give

$$b = -2a\dot{m}_B - \frac{d}{\dot{m}_B^2}, \tag{2.6.5}$$

$$c = \frac{1}{A\rho} + a\dot{m}_B^2 - \frac{2d}{\dot{m}_B}. \tag{2.6.6}$$

Substituting these into Eq. 2.6.2 and rearranging for ξ results in

$$\xi = \frac{1}{\hat{a}\left(\frac{\dot{m}}{\dot{m}_B}\right)^2 - \left(2\hat{a} + \hat{d}\right)\frac{\dot{m}}{\dot{m}_B} + \left(1 + \hat{a} - 2\hat{d}\right) + \hat{d}\left(\frac{\dot{m}_B}{\dot{m}}\right)} \tag{2.6.7}$$

where $\hat{a} = aA\rho\dot{m}_B^2$ and $\hat{d} = d\left(\frac{A\rho}{\dot{m}_B}\right)$. From this we can see that $\xi \to 0$ as $\dot{m} \to 0$ provided $d \neq 0$, and so we have a relatively free choice of d.

If the behaviour of the stall function dominates the behaviour of the velocity, we know that the stall function decreasing results in an increase of velocity. Since the channel being fully stalled is a maximum condition, it makes sense that the velocity is also at a maximum condition here. Therefore, we will assume

$$\frac{du_r}{d\dot{m}}(0) = 0, \tag{2.6.8}$$

which is equivalent to choosing $\hat{d} = \frac{1+\hat{a}}{2}$.

Therefore, the resulting stall function becomes

$$\xi = \frac{1}{\frac{1}{2}\left(\frac{\tan\beta}{\tan\beta_B} + \frac{\tan\beta}{\tan\beta_B}\right) + \hat{a}\left(1 + \frac{1}{2}\frac{\tan\beta}{\tan\beta_B}\right)\left(\frac{\tan\beta_B}{\tan\beta} - 1\right)^2} \tag{2.6.9}$$

A full derivation of this can be found in Section 3.2 (Paper 2, Appendix A). As we can see from Fig. 2-12, this new assumption has not dramatically changed the shape of the stall function. It appears very similar to the original, but now satisfies the $\xi(0) = 0$ condition as desired.

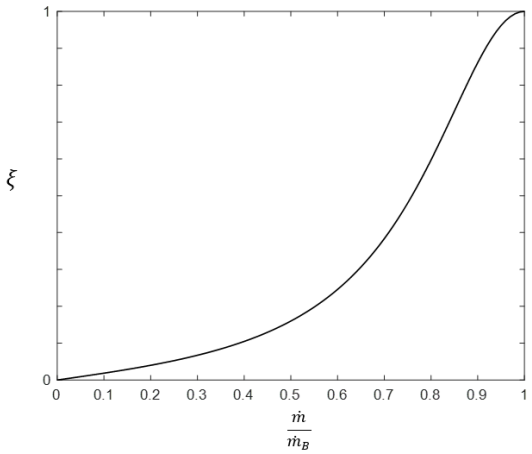

Figure 2-12: Behaviour of revised stall function, ξ, as mass flow decreases from stall point, $\dot{m}_B$. We have a monotonically decreasing function which satisfies $\xi(0) = 0$.

Figure 2-13 shows the compressor characteristics if we use this new stall function. We observe that we have a discontinuity at zero flow. This is problematic because it is unclear how we should define the compressor characteristic at $\dot{m} = 0$. Furthermore, numerical software for solving ODEs can have problems resolving discontinuities so special care would need to be taken around this point. (See Gear and Osterby [58] for a discussion of solving ODEs with discontinuities.)

To understand why we have a discontinuity, recall (from Eq.2.4.69 and 2.4.72) that we

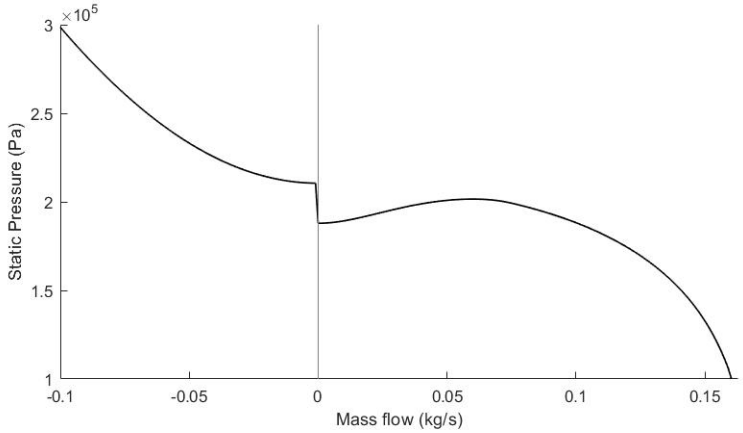

Figure 2-13: Resulting compressor characteristic for new stall function. A discontinuity occurs at $\dot{m} = 0$ due to a jump in velocity at this point.

have

$$p = \frac{\gamma - 1}{\gamma}\left(E_I\rho - \frac{\rho u_r^2}{2} + \frac{\rho\Omega^2 r^2}{2}\right) \tag{2.6.10}$$

$$p = \frac{\gamma - 1}{\gamma}\left(E_D\rho - \frac{\rho u_r^2}{2} - \frac{u_\theta^2}{2}\right) \tag{2.6.11}$$

in the impeller and diffuser respectively.

The new stall function implies that at $\dot{m} = 0$ we have a velocity $u_r \neq 0$ as $\xi = 0$. However, in reverse flow we have no stall function and so $u_r = 0$ at zero flow. This jump in velocity explains the jump in pressure.

As we saw in Section 1.2.1, all the previously proposed compressor characteristics have been smooth with no discontinuities. If we believe this to hold for our characteristic, then that means energy is lost in some way in the reverse flow regime so that E_I and E_D can balance the jump in velocity at zero flow.

Therefore, it is worth taking a more detailed look into the behaviour of flow travelling in the reversed direction through the compressor. This is the topic of the next chapter.

2.7 Conclusions

In this chapter, we have derived a reduced order model for compressor surge, along with a throttle and compressor characteristic.

Through the derivation of the steady-state compressor characteristic, we have learned that friction and incidence losses are key dynamics in order to achieve realistic simulations of a compressor.

Since we have developed loss functions to incorporate the dynamics of friction and impeller inlet stall, the resulting model depends on two parameters that control the strength of these losses. In order for this model to be fully predictive, universal relations need to be found for these parameters. Paper 1 found some relations that are promising, however due to limits of the amount of available data, we cannot conclude these relations will hold universally across a variety of compressor sizes.

In Paper 1, we also observed that our model may be too simplistic to predict the surge line accurately for all impeller speeds. We saw that our model was predicting surge onset at lower mass flows than the experimental data suggested for the higher impeller

speeds, and deduced that the inclusion of diffuser recirculation may be needed.

We also noticed that our current model was only capturing mild surge dynamics as the mass flows remained positive for all times, despite the pressure oscillations having amplitudes reminiscent of deep surge.

We have proposed an alternative stall function that assumes the impeller channels are fully stalled at zero flow. This gives a more promising shape of characteristic for $\dot{m} > 0$. However, it results in a discontinuity at $\dot{m} = 0$ and so we concluded that a more detailed look into reverse flow was required.

Chapter 3

Reverse Flow Region in Compressor Characteristics

As we discovered in Section 2.6.1, it is important to consider the dynamics of flow travelling backwards through the compressor. This is an area of research that tends to be overlooked, but it is important as the shape of the characteristic for $\dot{m} < 0$ will influence the behaviour of deep surge cycles.

3.1 Reverse Flow Model Development

From now on, we will construct the compressor characteristic by two separate models. The first will be the model developed in the previous chapter, with the new stall function suggested in Section 2.6.1, for positive mass flows. The second we will develop in this chapter and will be for negative mass flows.

Figure 3-1 shows how the model developed in Section 2.5 modelled reversed flow. These are plots with radius so they need to be read from right to left (as the flow is travelling from the diffuser outlet to the impeller inlet).

There are two main points to note. Firstly, the direction of flow in the diffuser does not follow the shape of the volute. Instead it is in the same direction as positive flow. Secondly, the tangential velocity is increasing monotonically until it matches the speed of the impeller at the impeller-diffuser interface.

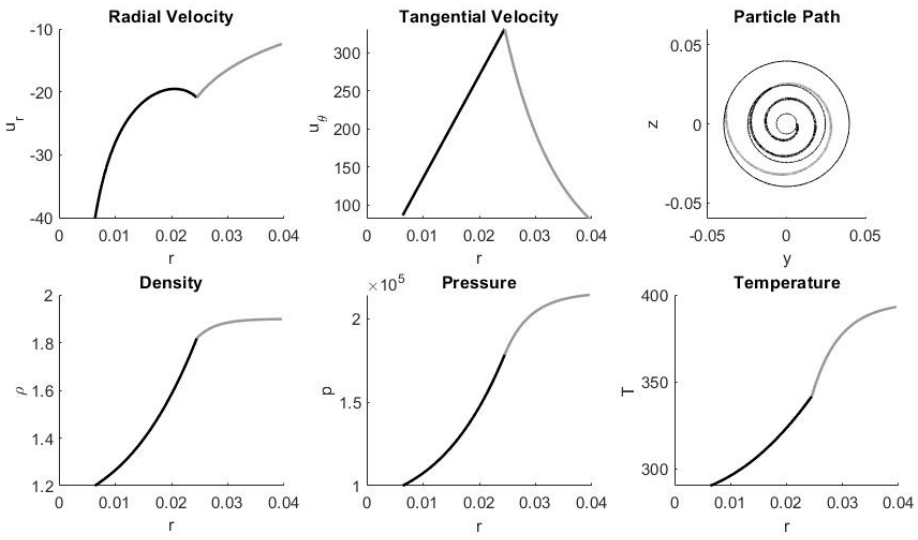

Figure 3-1: Properties of flow at a $\dot{m} = -0.02$kg/s for the model developed in Section 2.5. Black lines denote flow in the impeller and grey lines denote flow in the diffuser.

These two points suggest the behaviour of reversed flow simulated by this model is more reminiscent of a local flow recirculation. Figure 3-2(a) illustrates this.

Suppose the global flow is travelling forwards through the compressor, but some trajectories cannot escape the diffuser or volute, and so recirculate. The blue lines show the forward flow trajectory. Once this portion of air get sucked back into the diffuser (grey line), it is being hit by other forward flowing trajectories and hence will be accelerated to match their speed (assuming no losses due to the collision of air particles). Since the forward flowing air is faster nearer the impeller, the recirculated air is being accelerated continually as it travels inwards. Finally, once it enters the impeller (black line) it is swept up by the impeller blades.

This theory is problematic for a number of reasons. Firstly, there are flaws to the physics. If air particles are colliding we would expect frictional losses, and hence a rise in temperature. Also, the centrifugal force of the impeller and the forward travelling particles would be driving the recirculated particles out of the impeller and diffuser again, so it is unlikely this recirculated air would ever reach the inlet.

Furthermore, we are looking for the flow dynamics of a global flow reversal. This is where the pressure is so high at the volute outlet that it drives the air towards the impeller. This is the case illustrated in Fig. 3-2(b).

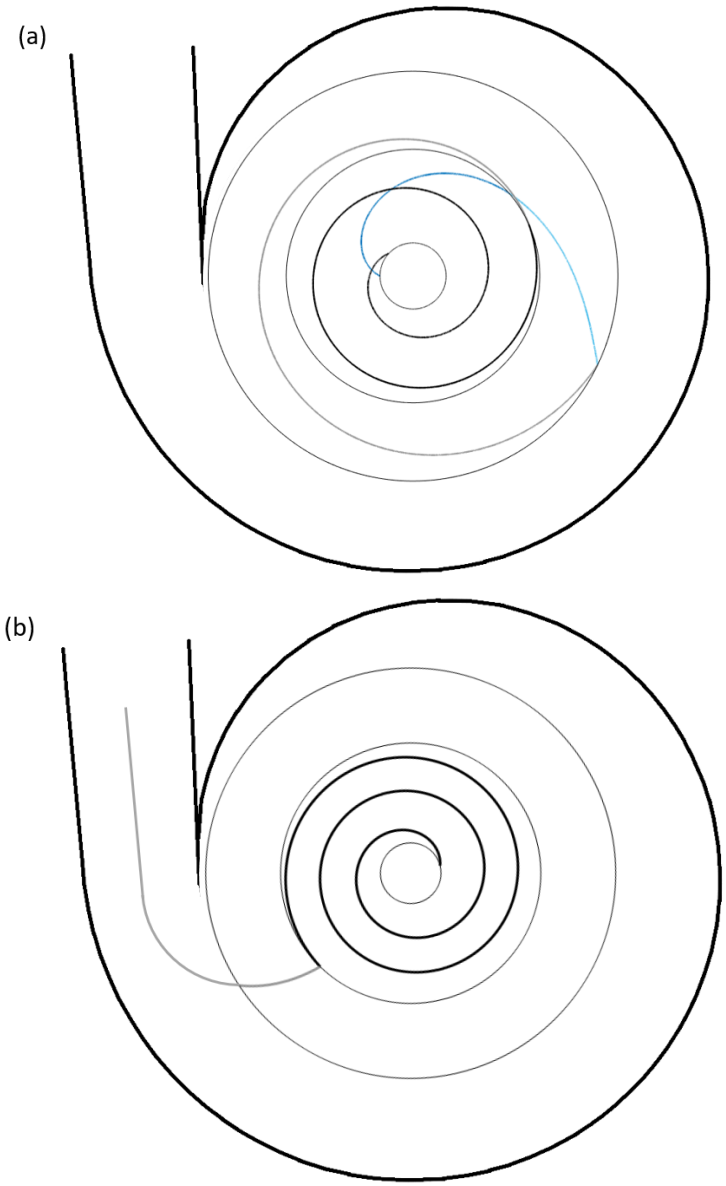

Figure 3-2: (a) Reverse flow behaviour suggested by model developed in Section 2.5. The blue trajectory is a forward flow simulation, and the grey/black trajectory shows what happens if this then reverses. (b) Flow behaviour we expect to see for a global flow reversal.

In order to simulate this global flow reversal, a different boundary condition needs to be used for tangential velocity. The previous model assumed that the tangential velocity at the impeller-diffuser interface would be equal to that of the rotating impeller, but this need not be the case. Instead we will look for a boundary condition that depends on the shape of the volute so we know at what angle the flow would enter the diffuser.

Moreover, noticing that we expect there to be a large a jump in tangential velocity at the impeller-diffuser interface, we can expect shear losses to play an important role for reverse flow. These shear losses would provide a way to balance the pressure drop at $\dot{m} = 0$ seen in forward flow due to the new stall function (presented in Section 2.6.1).

The paper in the next section derives a new model for reversed flow, including the two main changes suggested above. It also presents the resulting compressor characteristics and compares them with experimental data for the reversed flow regime.

3.2 Paper 2: Development and Validation of a Model for Centrifugal Compressors in Reversed Flow Regimes

This declaration concerns the article entitled:			
Development and Validation of a Model for Centrifugal Compressors in Reversed Flow Regimes			
Publication status (tick one) **Draft manuscript** ☐ **Submitted** ☐ **In review** ☐ **Accepted** ☐ **Published** X			
Publication details (reference)	Powers, K., Kennedy, I., Brace, C., Milewski P., and Copeland, C. (January 11, 2021) "Development and Validation of a Model for Centrifugal Compressors in Reversed Flow Regimes." *Proceedings of the ASME Turbo Expo 2020: Turbomachinery Technical Conference and Exposition*. ASME. https://doi.org/10.1115/GT2020-16005		
Copyright status (tick the appropriate statement) I hold the copyright for this material ☐ Copyright is retained by the publisher, but I have been given permission to replicate the material here X			
Candidate's contribution to the paper (provide details, and also indicate as a percentage)	The contribution of Katherine Powers to the paper is as follows: • Formulation of ideas (90%) with advice from supervising authors • Derivation of equations for the mathematical models (90%) • Participation in design and implementation of experiments (40%) • Writing MATLAB code and creating of numerical simulations (100%) • Comparing numerical simulations to given experimental data, and analysing of the results (100%) • Presentation of data in journal format (90%)		
Statement from Candidate	This paper reports on original research I conducted during the period of my Higher Degree by Research candidature.		
Signed	KHlaces	**Date**	26/02/2021

Proceedings of ASME Turbo Expo 2020
Turbomachinery Technical Conference and Exposition
GT2020
June 22-26, 2020, London, England

GT2020-16005

DEVELOPMENT AND VALIDATION OF A MODEL FOR CENTRIFUGAL COMPRESSORS IN REVERSED FLOW REGIMES

Katherine H. Powers, Ian J. Kennedy, Chris J. Brace, Paul A. Milewski, Colin D. Copeland
University of Bath
Claverton Down, Bath, BA2 7AY. UK
Email: k.h.powers@bath.ac.uk

ABSTRACT

Turbochargers are widely used to help reduce the environmental impact of automotive engines. However, a limiting factor for turbochargers is compressor surge. Surge is an instability that induces pressure and flow oscillations that often damages the turbocharger and its installation.

Most predictions of the surge limit are based on low-order models, such as the Moore-Greitzer model. These models tend to rely on a characteristic curve for the compressor created by extrapolating the constant speed lines of a steady-state compressor map into the negative mass flow region. However, there is little validation of these assumptions in the public literature.

In this paper, we develop further the first-principles model for a compressor characteristic presented in Powers et al. [1], with a particular emphasis on reverse flow. We then perform experiments using a 58mm diameter centrifugal compressor provided by Cummins Turbo Technologies, where we feed air in the reverse direction though the compressor while the impeller is spinning in the forwards direction in order to obtain data in the negative mass flow region of the compressor map.

This demonstrated experimentally that there is a stable operating region in the reverse flow regime. The recorded data showed a good match with the theoretical model developed in this paper. We also identified a change in characteristic behaviour as the impeller speed is increased which, to the authors knowledge, has not been observed in any previously published experimental work.

NOMENCLATURE

A	Cross-sectional area
$\hat{a}$	Stalling factor
B	Greitzer's parameter
det	Determinant
E	Specific energy
f	Friction factor
F	Skin friction
$\mathbf{g}$	Acceleration due to gravity
h	Channel height
J	Jacobian
L	Length
$\dot{m}$	Mass flow
n_b	Number of impeller blades
p	Static pressure
$\dot{Q}$	Heat transfer
q	Mass flow per radian
R	Specific gas constant
S	Surface area per unit volume
T	Temperature
tr	Trace
u	Velocity
β	Flow angle
β_B	Blade angle
δ	Thickness of shear layer
γ	Specific heat ratio
κ	Isentropic constant
λ	Second viscosity coefficient
μ	Dynamic viscosity

ν Parameter for shear loss
ξ Stall parameter
ξ_T Throttle parameter
ρ Density
τ Stress
Φ Nondimensional mass flow
Ψ Nondimensional pressure
Ω Angular velocity

Subscripts:
c Compressor
D Diffuser
I Impeller
r Radial direction
s Stalled flow
T Throttle
u Unstalled flow
x Differentiation w.r.t. x
y Differentiation w.r.t. y
θ Tangential direction

Abbreviations:
ODE Ordinary differential equation

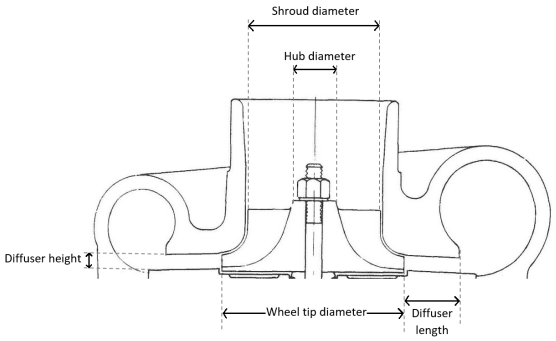

FIGURE 1. DIAGRAM INDICATING THE DIMENSIONS GIVEN IN TABLE 1 [1, 2].

INTRODUCTION

Turbochargers are components that use energy from engine exhaust gases to compress air prior to entering the engine. Using compressed air means there is more oxygen per unit volume in the engine cylinders, so more fuel can be burnt to increase the power output of that size of engine. Often turbochargers are used in combination with a downsized engine because smaller engines are more environmentally friendly. [2, 3]

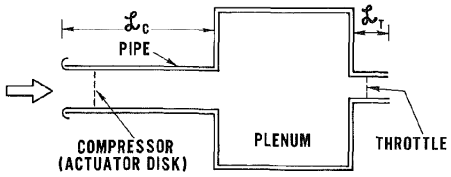

FIGURE 2. SCHEMATIC OF THE COMPRESSION SYSTEM THAT GREITZER BASED HIS MODEL OF SURGE ON [10].

With increasingly strict emissions regulations, the performance and efficiency of turbochargers is becoming a primary concern for manufacturers. For automotive turbochargers to perform effectively, they require a wide range of mass flows in which they can operate stably. However, this range is limited by compressor surge at low mass flows.

During operation at low mass flow rates, it is possible for a system level flow reversal to occur. When this happens, the average flow reverses direction and travels from the high pressure region at the compressor outlet to the low pressure region at the inlet. This flow reversal results in a drop in pressure at the compressor outlet, and so creates a condition that allows the flow to travel in the forward direction again. This oscillation in mass flow and pressure is termed surge [2]. Surge is an aerodynamic instability that is not only loud and off-putting to drivers, but is often damaging to the compressor and its installation.

Map based models are a popular method for predicting surge. These models use a function to describe the steady state behaviour of a compressor, usually from extending a compressor map beyond the surge point into negative mass flows. There are many examples of these in the literature [4–9]. The majority of these are based on a model by Greitzer [10] and Moore [11]. This model consisted of a compressor linked to a throttle via a pipe and a plenum (see Fig. 2).

The Moore-Greitzer model [10–12] can be written as a system of ODEs to represent the pressure and mass flow in the pipework between the compressor and the throttle:

$$\frac{d\Phi}{dt} = B(\psi_c - \Psi) \tag{1}$$

$$\frac{d\Psi}{dt} = \frac{1}{B}(\Phi - \psi_T^{-1}) \tag{2}$$

where Φ and Ψ are the nondimensional mass flow and pressure respectively. The term ψ_T represents the pressure drop over the throttle. Typically the orifice equation

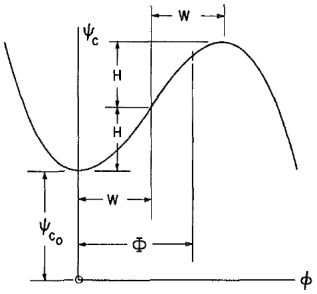

FIGURE 3. CUBIC FUNCTION AND ITS PARAMETERISATION THAT MOORE AND GREITZER USED AS A COMPRESSOR CHARACTERISTIC [11].

$$\psi_T = \xi_{T0} + \frac{1}{\xi_T^2}\Phi^2, \tag{3}$$

[12] is used.

The term ψ_c is the compressor characteristic, which represents the pressure rise over the compressor in steady-state conditions. This characteristic is difficult to determine. Koff and Greitzer [13] performed an experimental study on an axial compressor to determine its shape. They discovered that it was approximately cubic, so Moore and Greitzer [11] proposed using a cubic polynomial with parameters that can be fitted to compressor map data, i.e.

$$\psi_c = \psi_{c_0} + H\left[1 + \frac{2}{3}\left(\frac{\Phi}{W} - 1\right) - \frac{1}{2}\left(\frac{\Phi}{W} - 1\right)^3\right] \tag{4}$$

where the parameters are explained in Fig. 3. In 2008, Galindo et al. [14] did a similar experimental study for a small centrifugal compressor, also producing a cubic-like curve.

Since the compressor map data is contained within the positive mass flow region, using a cubic effectively extrapolates the trend into the negative flow region, meaning error can easily be induced here.

There have been some more theoretical approaches to determine the compressor characteristic. The majority of those seen in the literature have involved mean-line or lumped parameter modelling, e.g. [15–17], but recently Powers et al. [1] developed a model from first principles. However, there is little evidence to validate these compressor characteristics in the reverse flow regime.

The reverse flow region is important because it contributes to the behaviour of the flow during deep surge cycles. Therefore, understanding the physics in the reversed flow region better could help us understand the nature of surge cycles and help mitigate their damaging behaviour.

Also, a more accurate representation of reverse flow will improve the accuracy of surge models. Surge models are vital for turbocharger and engine designers because they need to understand the operating regimes of the turbocharger and, more specifically, the limits in which they can operate safely.

The aim of this paper is to perform a more detailed study into the reversed flow region of the compressor characteristic. Firstly, we will further develop the model presented by Powers et al. [1], taking more care over the reversed flow region. Then we will perform experiments using a 58mm compressor in order to map this region and look at how the characteristic shape changes over different operating regimes. Finally, we will compare the experimental results to physical models for compressor characteristics, focusing in particular on the model developed here.

MATHEMATICAL MODEL

Powers et al. [1] developed a model for the compressor characteristics starting from the fundamental equations for conservation of mass, momentum (in a rotating frame) and energy:

$$\frac{\partial \rho}{\partial t} + \nabla\cdot(\rho\mathbf{u}) = 0, \tag{5}$$

$$\tfrac{\partial}{\partial t}(\rho\mathbf{u}) + \nabla\cdot(\rho(\mathbf{u}\otimes\mathbf{u})) + 2\rho(\boldsymbol{\Omega}\times\mathbf{u}) + \rho(\boldsymbol{\Omega}\times(\boldsymbol{\Omega}\times\mathbf{r})) = \rho\mathbf{g} - \nabla p + \nabla\cdot\tau, \tag{6}$$

$$\frac{\partial}{\partial t}(\rho E) + \nabla\cdot(\rho\mathbf{u}E + p\mathbf{u}) - \nabla\cdot(\tau\cdot\mathbf{u}) = \rho\dot{Q} \tag{7}$$

respectively, along with the ideal gas law $p = \rho RT$ and the assumption of a perfect gas (so the specific heat ratio, γ, is assumed constant).

This was reduced to a system of 1D ODEs in the radial direction by assuming:

(i) radial impeller blades, so $u_\theta = 0$ in the rotating frame, and
(ii) a vaneless diffuser with axisymmetric flow, so $\frac{\partial}{\partial\theta} = 0$,

and then averaging over the axial direction.

The resulting ODEs for the impeller were

$$\frac{1}{r}\frac{\partial}{\partial r}(rh\rho u_r) = 0, \tag{8}$$

$$\frac{1}{r}\frac{\partial}{\partial r}(rh\rho u_r^2) - h\rho\Omega^2 r = -h\frac{\partial p}{\partial r} + hF_r, \tag{9}$$

$$\frac{1}{r}\frac{\partial}{\partial r}\left(rh\rho u_r\left(\frac{u_r^2}{2} + \frac{\gamma}{\gamma-1}\frac{p}{\rho} - \frac{\Omega^2 r^2}{2}\right)\right) = 0, \tag{10}$$

and for the diffuser were

$$\frac{1}{r}\frac{\partial}{\partial r}(rh\rho u_r) = 0, \tag{11}$$

$$\frac{1}{r}\frac{\partial}{\partial r}(rh\rho u_r^2) - \frac{h\rho u_\theta^2}{r} = -h\frac{\partial p}{\partial r} + hF_r, \tag{12}$$

$$\frac{1}{r}\frac{\partial}{\partial r}(rh\rho u_r u_\theta) + \frac{h\rho u_r u_\theta}{r} = hF_\theta, \tag{13}$$

$$\frac{1}{r}\frac{\partial}{\partial r}\left(rh\rho u_r\left(\frac{u_r^2}{2} + \frac{u_\theta^2}{2} + \frac{\gamma}{\gamma-1}\frac{p}{\rho}\right)\right) = 0, \tag{14}$$

where

$$F_r = \frac{f}{2}\rho u_r^2 S \tag{15}$$

$$F_\theta = \frac{f}{2}\rho u_r u_\theta S \tag{16}$$

represent skin friction.

A relationship for the friction parameter was found from performing a least squares fit to data:

$$f = 0.14 + 5\times 10^{-6}\Omega. \tag{17}$$

This was validated against different compressor geometries to show its potential as a universal relationship.

Powers et al. [1] also created a stall function to take into account how the compressor responds to incidence losses and any resulting local recirculation. We have deviated from their work and propose a new stall function, ξ.

Writing

$$\dot{m} = \xi A\rho u_r, \tag{18}$$

we see that ξA represents the area of the channel that is not blocked due to stall. Therefore, at $\xi = 1$ the flow is not stalled and at $\xi = 0$ the flow is completely stalled.

We shall assume that, like Powers et al., when the flow stalls, the velocity is continuous with a continuous gradient. However, instead of forcing the unstalled flow velocity to be zero at zero mass flow, we shall assume that the velocity of the unstalled flow increases with stalling and will be a maximum when the system is fully stalled.

It may sound counter-intuitive to allow a non-zero velocity for the unstalled portion of the flow when the average flow is zero. However, let subscripts u and s denote unstalled and stalled portions respectively, then

$$\dot{m} = A_s\rho u_s \overset{0}{\cancel{}} + \overset{0}{\cancel{A_u}}\rho u_u = 0. \tag{19}$$

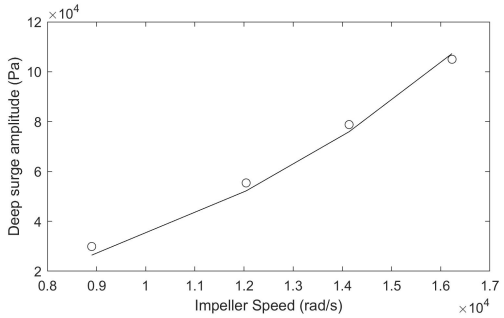

FIGURE 4. RELATIONSHIP BETWEEN IMPELLER SPEED AND DEEP SURGE AMPLITUDE FOR STALL PARAMETER $\hat{a} = 1.7$. TEST DATA INDICATED AS CIRCLES HAS BEEN ADDED FOR COMPARISON.

This shows us that at $\dot{m} = 0$, all of the flow is stalled and so have an average velocity of zero, and none of the flow is unstalled so it is a valid to have a non-zero velocity at that point.

These assumptions result in

$$\xi = \frac{1}{\frac{1}{2}\left(\frac{\tan\beta_B}{\tan\beta} + \frac{\tan\beta}{\tan\beta_B}\right) + \hat{a}\left(1 + \frac{1}{2}\frac{\tan\beta}{\tan\beta_B}\right)\left(\frac{\tan\beta_B}{\tan\beta} - 1\right)^2}, \tag{20}$$

where $\hat{a}$ is the parameter that controls the level of stalling (see Appendix A for full derivation).

Since this is a different function to the stall parameter from Powers et al. we cannot use their correlation. Surge tests were performed using the same turbocharger as in the reverse flow tests below. Using the amplitude of the pressure oscillations during a deep surge cycle, we determined that $\hat{a} = 1.7$ for this compressor (see Fig. 4). Unlike Powers et al. this is not a universal relation and so further work is needed to develop a relationship for the stall parameter so the model developed can remain predictive.

The stall function created by Powers et al. [1] had a local minimum in the positive flow region, which implied that the flow would recover from surge and be stable at a low enough forward mass flow. However, this new function effectively shifts the local minimum in the characteristic so that it is at zero mass flow, meaning that, once the flow is surging, it will continue to surge as the mass flow is reduced to zero, and only once the flow is reversed will it stabilise.

Reverse flow

We shall now make a few small changes to this model to make it suitable for the reverse flow case. First, it is important to

note that Powers et al. [1] changed the sign of the friction parameter for negative mass flows, even though this wasn't explicitly stated, because friction will always oppose motion. Therefore, for reverse flow the ODEs are

$$\frac{1}{r}\frac{\partial}{\partial r}(rh\rho u_r) = 0 \tag{21}$$

$$\frac{1}{r}\frac{\partial}{\partial r}(rh\rho u_r^2) - h\rho\Omega^2 r = -h\frac{\partial p}{\partial r} + hf\rho u_r^2\left(\frac{1}{h} + \frac{n_b}{2\pi r}\right) \tag{22}$$

$$\frac{1}{r}\frac{\partial}{\partial r}\left(rh\rho u_r\left(\frac{u_r^2}{2} + \frac{\gamma}{\gamma-1}\frac{p}{\rho} - \frac{\Omega^2 r^2}{2}\right)\right) = 0 \tag{23}$$

for the impeller and

$$\frac{1}{r}\frac{\partial}{\partial r}(rh\rho u_r) = 0 \tag{24}$$

$$\frac{1}{r}\frac{\partial}{\partial r}(rh\rho u_r^2) - \frac{h\rho u_\theta^2}{r} = -h\frac{\partial p}{\partial r} + h\frac{f}{h}\rho u_r^2 \tag{25}$$

$$\frac{1}{r}\frac{\partial}{\partial r}(rh\rho u_r u_\theta) + \frac{h\rho u_r u_\theta}{r} = h\frac{f}{h}u_r u_\theta \tag{26}$$

$$\frac{1}{r}\frac{\partial}{\partial r}\left(rh\rho u_r\left(\frac{u_r^2}{2} + \frac{u_\theta^2}{2} + \frac{\gamma}{\gamma-1}\frac{p}{\rho}\right)\right) = 0 \tag{27}$$

for the diffuser.

The main changes we suggest are related to the boundary conditions. Powers et al. used the same conditions as forward flow, i.e. having a known mass flow, ambient pressure, and ambient density at the impeller inlet, but these will be unrealistic for the reversed flow regime.

In reality, the density of the air exiting the impeller inlet need not be the same as ambient air. Instead we can use the condition that the temperature of the air being fed into the compressor (i.e. at the diffuser outlet) is constant. This now means we have to solve a boundary value problem, which can be done via the shooting method.

Another condition we need to provide is the value for the tangential velocity entering the diffuser, $u_{\theta D}$. The absolute velocity in the volute is given by

$$u = \sqrt{u_r^2 + u_\theta^2}. \tag{28}$$

In forward flow, the volute is designed purely to collect the air around the diffuser. The area increase in the volute is to account for the increase in mass being added to the volute as this happens, therefore the properties of the gas in the volute, e.g. velocity and density, are reasonably constant. Therefore, it seems reasonable to assume that the velocity and density are unchanged in the volute in reverse flow conditions too, and so $\rho = \text{const.}$ and

$$u = \sqrt{u_{rD}^2 + u_{\theta D}^2}. \tag{29}$$

We know that, from Eqn. 24, the mass flow at the outermost radius of the diffuser is given by

$$\dot{m} = 2\pi r_D h_D \rho u_{rD} = A_D \rho u_{rD}. \tag{30}$$

We also know at the critical area of the volute, A^*, all of the mass has been collected and will pass through this area with velocity u. Therefore,

$$\dot{m} = A^* \rho u. \tag{31}$$

Equating these gives us

$$u = \frac{A_D}{A^*}u_{rD} \tag{32}$$

$$\implies u_{rD}^2 + u_{\theta D}^2 = \left(\frac{A_D}{A^*}\right)^2 u_{rD}^2 \tag{33}$$

$$\implies u_{\theta D}^2 = \left[\left(\frac{A_D}{A^*}\right)^2 - 1\right] u_{rD}^2 \tag{34}$$

$$\implies u_{\theta D} = u_{rD}\sqrt{\left(\frac{A_D}{A^*}\right)^2 - 1}. \tag{35}$$

For the geometry of the compressor used for testing in the following sections, this gives us a flow angle into the diffuser from the volute of

$$\theta = \tan^{-1}\left(\frac{u_{\theta D}}{u_{rD}}\right) = \tan^{-1}\left(\sqrt{\left(\frac{A_D}{A^*}\right)^2 - 1}\right) = 39.3^o. \tag{36}$$

However, it is interesting to note that the resulting pressure simulated in the reverse flow case is not very sensitive to this angle. Changing the angle between 20^o to 60^o resulted in a maximum difference of 5%.

The final change we suggest is the need to account for shear losses as we go from the diffuser to the impeller. We are considering flow reversal in the situation where the impeller still rotates in the conventional direction but the air is travelling from the volute backwards through the compressor (see left-hand diagram of Fig. 5). This will result in a shear layer at the impeller-diffuser interface because of a huge change in tangential velocity. The

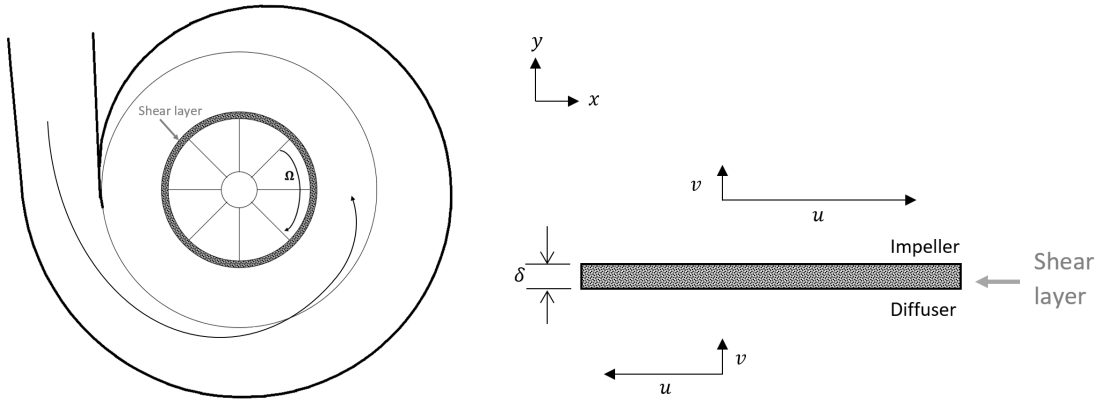

FIGURE 5. SHEAR LAYER OF THICKNESS δ AT THE IMPELLER-DIFFUSER INTERFACE DURING REVERSE FLOW IN STANDARD GEOMETRY (LEFT) AND AN *x*-*y* CO-ORDINATE SYSTEM (RIGHT).

air not only changes direction but is accelerated to the large rotational speed of the impeller in a very short radial distance. This will result in a large amount of viscous dissipation, which was considered small and so neglected during the derivation of the ODEs for the impeller and diffuser.

To see what happens over this shear layer, let's consider the impeller-diffuser interface in the *x*-*y* coordinate system shown in Fig. 5. In this case, we can assume that all variables are independent of x. This means that conservation of mass, momentum and energy become

$$(\rho v)_y = 0 \tag{37}$$

$$\rho v u_y = -p_x + \mu u_{yy} \tag{38}$$

$$\rho v v_y = -p_y + \mu v_{yy} \tag{39}$$

$$\rho v e_y = -p v_y + \lambda v_y^2 + \mu u_y^2 + 2\mu v_y^2 \tag{40}$$

respectively, where subscripts have been used to denote differentiation [18]. Let's assume that the flow across the shear layer is incompressible, so conservation of mass leads to $v_y = 0$. Then conservation of energy becomes

$$\rho v \frac{\partial e}{\partial y} = \mu \left(\frac{\partial u}{\partial y}\right)^2 \tag{41}$$

$$\implies \frac{\rho v}{\gamma - 1} \frac{\partial}{\partial y}\left(\frac{p}{\rho}\right) = \mu \left(\frac{\partial u}{\partial y}\right)^2 \tag{42}$$

$$\implies \frac{v}{\gamma - 1} \frac{\partial p}{\partial y} = \mu \left(\frac{\partial u}{\partial y}\right)^2. \tag{43}$$

We can approximate these derivatives by assuming the shear layer has a thickness δ to give,

$$\frac{v}{\gamma - 1} \frac{\Delta p}{\delta} = \mu \left(\frac{\Delta u}{\delta}\right)^2 \tag{44}$$

$$\implies \Delta p = \frac{\mu(\gamma - 1)}{v\delta} (\Delta u)^2. \tag{45}$$

Therefore, returning to previous notation we have a pressure jump of

$$p_I = p_D - \nu (u_{\theta I} - u_{\theta D})^2, \tag{46}$$

at the impeller-diffuser interface, where

$$\nu = \frac{\mu(\gamma - 1)}{u_r \delta} \tag{47}$$

is our shear loss parameter.

For the model presented here, we will assume that the parameter ν is always finite. For this to be the case, $u_r \neq 0$ and so some form of transport always occurs across the impeller-diffuser interface. We believe this is a reasonable assumption because, due to turbulent flow, we would expect some flux across the boundary even when the average mass flow is zero. However, there is scope for further research into the form of this shear loss.

To determine ν we will assume that the width of the shear layer δ is such that there is continuity in static pressure at zero mass flow between the forward flow and reverse flow models.

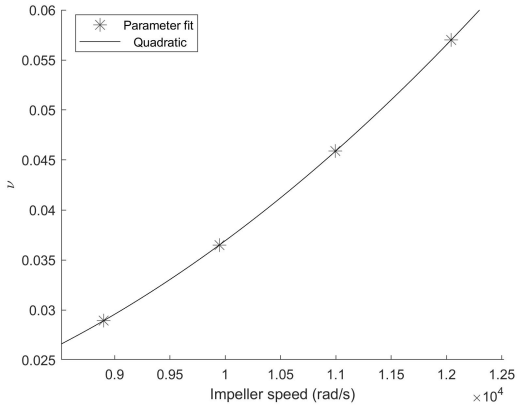

FIGURE 6. RELATIONSHIP FOR SHEAR PARAMETER WITH IMPELLER SPEED. THE POINTS IDENTIFY THE PARAMETER VALUE OBTAINED WHERE THE STATIC PRESSURE AT ZERO FLOW IN THE FORWARD FLOW MODEL AND REVERSE FLOW MODEL ARE EQUATED.

This tells us

$$\nu \propto u_\theta^2 \tag{48}$$

(see Fig. 6), which makes sense because it is likely that shear losses increase with the turbulent kinetic energy of the system.

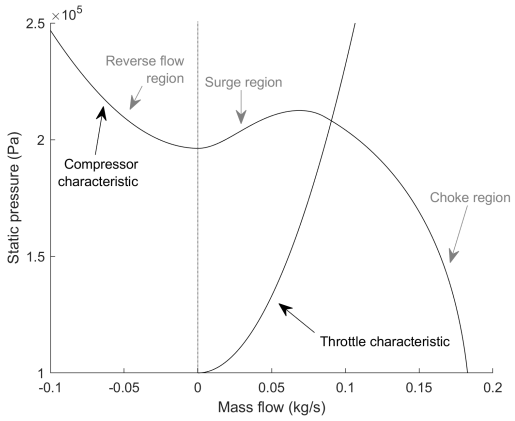

FIGURE 7. IMPROVED COMPRESSOR CHARACTERISTIC FROM FIRST PRINCIPLES. THE THROTTLE CHARACTERISTIC FROM POWERS ET AL. [1] IS ALSO SHOWN.

All of the above modifications gives us the compressor characteristic shown in Fig. 7.

Quasi-steady model

These compressor characteristics can be used within quasi-steady models for surge. For example, Powers et al. [1] developed the following model:

$$\frac{d\dot{m}}{dt} = \frac{A}{L}(p_c(\dot{m}) - p) + \frac{\kappa^{\frac{1}{\gamma}}}{AL}\left(\frac{\dot{m}^2}{p_c(\dot{m})^{\frac{1}{\gamma}}} - \frac{\dot{m}_T(p)^2}{p^{\frac{1}{\gamma}}}\right), \tag{49}$$

$$\frac{dp}{dt} = \frac{\gamma\kappa^{\frac{1}{\gamma}}}{AL} p^{\frac{\gamma-1}{\gamma}}(\dot{m} - \dot{m}_T(p)), \tag{50}$$

where $\dot{m}_T$ is the throttle characteristic and p_c is the steady-state compressor characteristic.

It is important to understand that the compressor characteristic, though important, is not the only ingredient needed to understand the surge phenomenon. We know that surge is a system level phenomenon and so depends on the geometry of the test rig pipework, but it is only here in the quasi-steady model that this comes into play. In this case, the terms A and L are the cross-sectional area and length of the pipework between the turbocharger and the throttle valve, but it is possible to adopt quasi-steady models that take into account inlet geometry as well.

PROCEDURE

To validate this model a turbocharger with dimensions given in Table 1 was tested using the gas stand facilities at the University of Bath.

In the facility, compressed air was supplied through two separate electrically heated flow paths. Gate valves were used to

TABLE 1. GEOMETRIC DETAILS OF THE COMPRESSOR USED FOR TESTING. FIGURE 1 CAN BE REFERRED TO FOR EXPLANATION OF THE DIMENSIONS.

Number of blades	$6+6$
Hub diameter	13.5 mm
Shroud diameter	41 mm
Wheel tip diameter	58 mm
Diffuser height	3.15 mm
Diffuser length	16.7 mm
Diffuser area ratio	2.48
Critical area of housing	7 cm^2

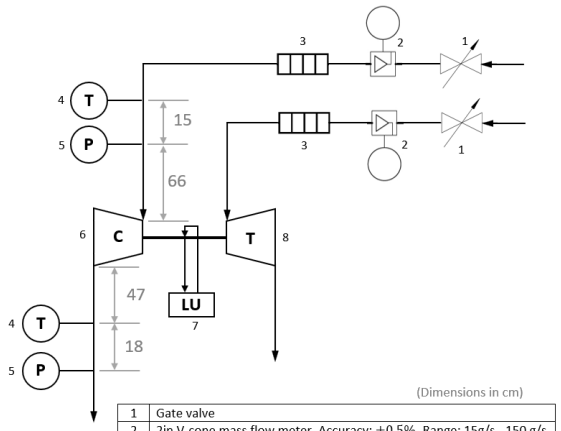

1	Gate valve
2	2in V-cone mass flow meter. Accuracy: ±0.5%. Range: 15g/s - 150 g/s
3	Variable power electric heater
4	PRT temperature sensor. Accuracy: $\pm(0.15 + 0.002\,T)°C$
5	Pneumatically averaged pressor sensor. Accuracy: ±560 Pa
6	Turbocharger compressor
7	Turbocharger lubrication unit
8	Turbocharger turbine

FIGURE 8. SCHEMATIC OF THE GAS STAND USED TO TEST THE COMPRESSORS.

control the flow. One flow was used to drive the turbine and was in the conventional direction, entering at the turbine inlet. This was the predominant means of controlling the speed of the turbocharger. The other compressed air stream was fed in the reverse flow direction through the compressor, entering at the compressor outlet. See Fig. 8 for a schematic of the test rig set-up.

To run the experiment, air was let into the turbine side to drive the rotor. The valve feeding air to the compressor outlet remained closed so there was no air going through the compressor side. This led to surging behaviour with an audible pulsating flow. The turbine speed was limited to approximately 20,000 rpm so not to cause damage to the compressor.

Compressed air was then fed into the compressor side in the reverse direction by opening the valve. This stopped the surging behaviour and stabilised the flow.

The turbine speed was then increased to the desired values. The compressor side valve was adjusted to keep the flow in the stable backflow regime throughout the testing. At fixed speeds, the compressor side mass flow was slowly increased from 15g/s to 80g/s to map out the reversed flow characteristic. This was repeated multiple times and for multiple different speeds.

A high-frequency pressure measurement was recorded to check the steadiness of the flow. Since the flow was found to be steady, measurements were taken at 10Hz of the mass flow, temperature and pressure on the compressor side. A V-cone was used to measure the mass flow, PRTs for the temperature, and pneumatically averaged pressure transducers for static and total pressure measurements. The locations and accuracy of these measurements are indicated in Fig. 8.

RESULTS AND DISCUSSION

The first interesting observation was that the flow was surging when the valve feeding air into the compressor was fully closed. A snapshot of this is shown in Fig. 9. Therefore, it is highly probable that the flow dynamics are continually unsteady between zero flow and the surge line in forward flow. Combining this with the fact that the flow dynamics at negative mass flows was observed to be steady, shows us that a switch of stability has to occur at zero mass flow. Therefore, this supports our new stall function with a local minimum at zero flow.

The next important result to recognise is that the flow is steady in the reverse flow region. Consider the Moore-Greitzer model (Eqns. 1 & 2) [12]:

$$\frac{d\Phi}{dt} = B(\psi_c - \Psi) = f(\Phi,\Psi), \tag{51}$$

$$\frac{d\Psi}{dt} = \frac{1}{B}(\Phi - \psi_T^{-1}) = g(\Phi,\Psi). \tag{52}$$

Computing the Jacobian, J, allows us to determine regions of stability for this model:

$$J = \begin{bmatrix} \frac{df}{d\Phi} & \frac{df}{d\Psi} \\ \frac{dg}{d\Phi} & \frac{dg}{d\Psi} \end{bmatrix} = \begin{bmatrix} B\frac{d\psi_c}{d\Phi} & -B \\ \frac{1}{B} & -\frac{1}{B}\left(\frac{d\psi_T}{d\Phi}\right)^{-1} \end{bmatrix}. \tag{53}$$

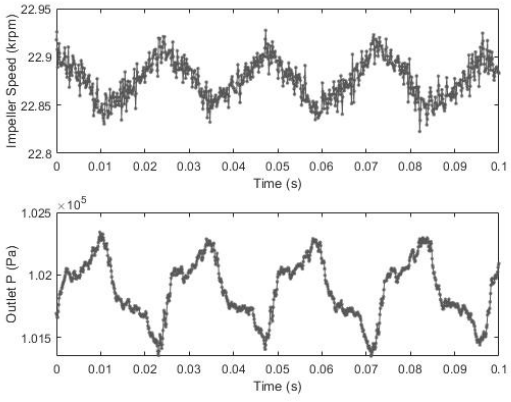

FIGURE 9. SURGING BEHAVIOUR OF THE COMPRESSOR WHEN OPERATING AT ZERO MASS FLOW.

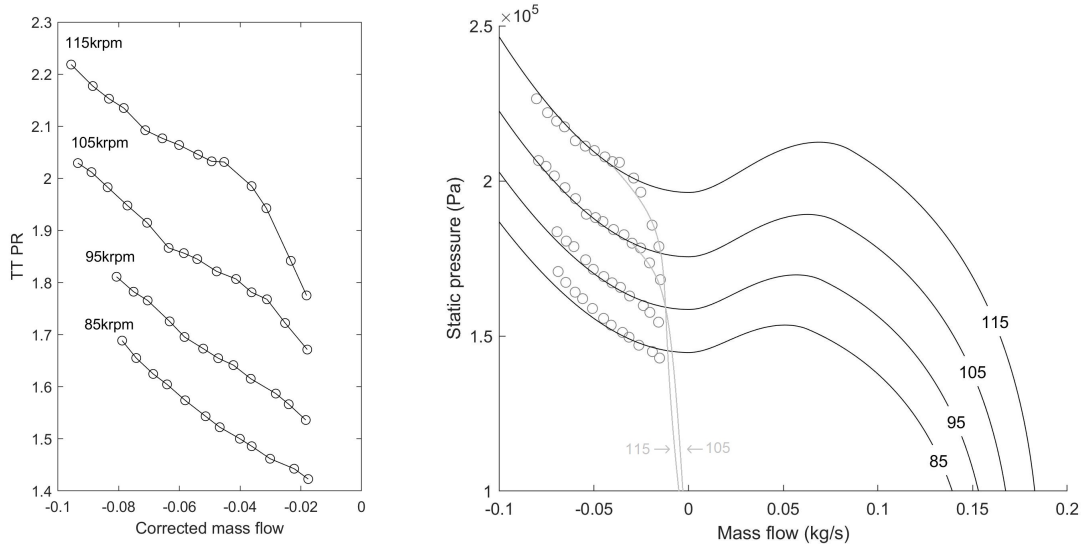

FIGURE 10. RECORDED COMPRESSOR MAPPINGS IN NEGATIVE MASS FLOW REGION AT DIFFERENT IMPELLER SPEEDS. LEFT SHOWS THE RAW DATA AND THE RIGHT SHOWS A COMPARISON BETWEEN THE DATA AND THE MODEL. THEORETICAL ASYMPTOTES FOR THE DATA HAVE BEEN ADDED IN GREY TO THE RIGHT HAND PLOT. THE SPEEDS INDICATED ON EACH LINE ARE IN KRPM.

The system is stable if $\det J > 0$ and $\mathrm{tr}J < 0$ [19]. In our case,

$$\det J = 1 - \frac{d\psi_c}{d\Phi}\left(\frac{d\psi_T}{d\Phi}\right)^{-1}, \tag{54}$$

$$\mathrm{tr}J = B\frac{d\psi_c}{d\Phi} - \frac{1}{B}\left(\frac{d\psi_T}{d\Phi}\right)^{-1}. \tag{55}$$

The surge models in literature all have a throttle characteristic with a positive gradient (see Fig. 7). Also, as most models are based on the cubic characteristic of Moore and Greitzer (Eqn. 4) they tend to assume a negative gradient of the compressor characteristic. The model we developed above also has this feature of a negative slope in the reverse flow region.

This means that

$$\frac{d\psi_T}{d\Phi} > 0 > \frac{d\psi_c}{d\Phi} \tag{56}$$

$$\implies \frac{d\psi_c}{d\Phi}\left(\frac{d\psi_T}{d\Phi}\right)^{-1} < 1 \tag{57}$$

$$\implies \det J > 0 \tag{58}$$

and

$$\frac{d\psi_T}{d\Phi} > 0, \frac{d\psi_c}{d\Phi} < 0 \tag{59}$$

$$\implies \mathrm{tr}J = B\frac{d\psi_c}{d\Phi} - \frac{1}{B}\left(\frac{d\psi_T}{d\Phi}\right)^{-1} < 0 \tag{60}$$

so having a negative gradient of the compressor characteristic results in a mathematically stable system and hence steady flow. So observing experimentally stable flow supports compressor characteristics having a negative gradient in the negative mass flow region.

The left-hand plot of Fig. 10 shows the raw test data obtained in the pressure-mass flow plane at different impeller speeds. The right-hand plot shows how this data compares to the model developed in the previous sections. We can see that we achieve a good quantitative fit to our model for all points, except the near-zero points at higher impeller speeds.

The 85krpm and 95krpm speed lines also have a good qualitative fit because they share the same quadratic-like shape that our model predicts. Therefore, the model we developed above must capture the predominant physics going on in reverse flow.

Looking closely at the raw data, we can see a gradual change in shape of the reverse flow characteristic as the impeller speed

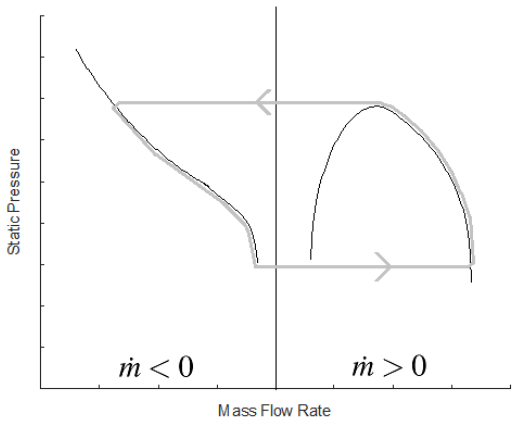

FIGURE 11. POSSIBLE DEEP SURGE TRAJECTORY FOR HIGH IMPELLER SPEEDS.

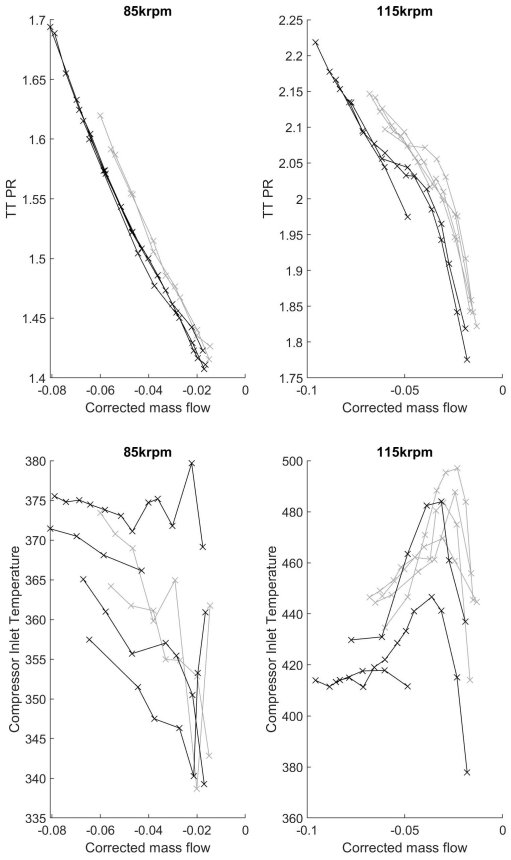

FIGURE 12. REPEATED RUNS OF TESTING FOR DIFFERENT IMPELLER SPEEDS. TWO IDENTICAL COMPRESSORS WERE TESTED (ONE SHOWN IN GREY AND ONE IN BLACK). THERE ARE NATURAL VARIATIONS IN THE PRODUCT WHICH RESULT IN A SHIFT, BUT THE CHANGE IN CHARACTERISTIC SHAPE IS VISIBLE IN BOTH. THE TEMPERATURE (IN K) FOR EACH OF THESE IS SHOWN IN THE PLOTS UNDERNEATH.

increases. We can see that, for 105krpm and 115krpm, the data points appear to be tending to a vertical asymptote close to zero flow. These possible asymptotes have been added in grey to the right-hand plot in Fig. 10. This is the first time something like this has been recorded in literature.

We note here that the V-cone used to measure the mass flow was within the measurement range but reaching the lower limit at which we would see $\pm 0.5\%$ accuracy. However, the pressure sensor will still be accurate in this range so the characteristic shapes observed are valid with some possible variation in the location of this vertical asymptote.

This asymptote suggests that, at high impeller speeds, there is a minimum reverse mass flow required to overcome the operation of the compressor in steady state. This is effectively a rotor head because pressure is created due to the rotation of the impeller. This rotor head will be larger for higher rotational speeds. This explains why the theoretical asymptote for 115krpm crosses 1bar pressure at a larger negative flow rate than 105krpm: a higher fluid momentum is required to overcome the rotor head.

It is possible that a different form of the shear loss to Eqns. 46-47 would allow the model to capture this asymptotic behaviour. For example, we assumed ν to be finite but relaxing this assumption would allow for the possibility of asymptotes developing near zero flow.

Having this vertical asymptote at near-zero mass flow would likely cause the deep surge cycles to have large pressure amplitudes since the trajectories of surge cycles tend to track the mathematically stable regions of the compressor characteristic closely (see e.g. [1,10,12]). Therefore, the trajectory tracking the reverse flow part of this observed compressor characteristic will include transient dynamics passing through near atmospheric pressure values, as shown in Fig. 11. This large amplitude pressure oscillation would explain why surge cycles can be far more violent at higher speeds than lower ones.

Being able to model this reverse flow phenomenon is really important because modelling is the first step in the management of a system. From there it might be possible to optimise the system to reduce the violence of deep surge cycles.

Figure 12 shows multiple runs overlayed for the 85krpm

and 115 krpm speed lines, the temperature at each of these runs is shown below them. These runs were performed on different days, with the test cell starting cold and starting warm. For low impeller speeds the repeatability was good. However, the variability in the repeats increased with impeller speed.

From looking at the plots of temperature, we believe that this is not the cause of the variability. There is a large variability in the temperature of the points at both speeds, but only minimal change in the repeat runs for 85krpm. If it were the temperature, we would expect to see the variability in both 85krpm and 115krpm.

During testing, we noticed that the main cause of variation seemed to be the starting condition. We usually started at low mass flows and swept gradually upwards to larger ones, but starting part way up this sweep gave us different results initially. This could mean that either (i) the system itself is sensitive, or (ii) the two types of dynamics creating the change in characteristic shape are interacting or can be observed at the same mass flow dependent on the starting conditions.

It is interesting to note that the highest temperatures recorded for 115krpm coincide with the points at which we get this transition from the quadratic-like shape to the asymptotic behaviour. Therefore, any physical phenomenon that causes this transition appears to result in a large rise in temperature.

We tested two identical turbochargers during these reversed flow experiments and we have plotted the results from both on Fig. 12. There is standard manufacturing variability between the two turbochargers, but it is interesting to note that both turbochargers observed this change in characteristic shape with impeller speed.

We would have liked to obtain results at higher impeller speeds. However, pushing the turbine to higher speeds while maintaining the reversed flow conditions in the impeller leads to catastrophic failure of the turbocharger (see Fig. 13). We also decided not to test at larger negative mass flows due to the risk of causing a failure, because the temperature of the system was reaching values over 200^{o}C.

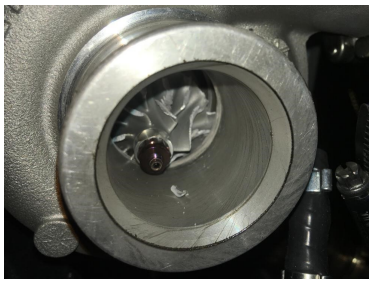

FIGURE 13. TURBOCHARGER FAILURE AS A RESULT OF TESTING AT 135 KRPM.

CONCLUSIONS

The majority of surge models for turbochargers rely on a steady-state compressor characteristic that is extrapolated into the reverse flow region. We have conducted experiments to measure the characteristic in the region of negative mass flows. We have shown that the flow operates stably in this case, which provides supporting evidence for the models like the Moore-Greizter model.

We further developed the model by Powers et al. [1], taking care of the dynamics and boundary conditions that hold in reversed flow conditions. We suggested a new stall function that results in a characteristic with a local minimum at zero flow, and have provided supporting experimental evidence for this.

We experimentally identified a change in characteristic shape as the impeller speed increases. This is the first time such a change has been recorded, and it suggests that the physical dynamics of the flow change at high impeller speeds at near-zero flow.

The model in the reverse flow regime showed excellent agreement to the experimental data. However, the model doesn't currently capture the change in characteristic shape. This phenomenon is likely to be caused by a rotor head, and further work is planned to incorporate this into the mathematical model by using a different form of shear loss at the impeller-diffuser interface.

ACKNOWLEDGMENT

The authors very are grateful to Cummins Turbo Technologies for their continued support of this work and, particularly, for providing the turbochargers used for carrying out this test work.

Katherine Powers is supported by a scholarship from the EPSRC Centre for Doctoral Training in Statistical Applied Mathematics at Bath (SAMBa), under the project EP/L015684/1.

REFERENCES

[1] Powers, K. H., Brace, C. J., Budd, C. J., Copeland, C. D., and Milewski, P. A. "Modelling axisymmetric centrifugal compressor characteristics from first principles". In ASME Turbo Expo 2019: Turbomachinery Technical Conference and Exposition, American Society of Mechanical Engineers Digital Collection.

[2] Watson, N., and Janota, M. S., 1982. *Turbocharging: The internal combustion engine*. MacMillan.

[3] Stone, R., 2012. *Introduction to internal combustion engines*, 4 ed. Palgrave MacMillan.

[4] Emmons, H. W., Pearson, C. E., and Grant, H. P., 1955. "Compressor surge and stall propagation, traks". ASME.

[5] Fink, D. A., Cumpsty, N. A., and Greitzer, E. M., 1992. "Surge dynamics in a free-spool centrifugal compressor system". *Journal of Turbomachinery,* ***114***, pp. 321– 332.

[6] Arnulfi, G. L., Giannattasio, P., Giusto, C., Massardo, A. F., Micheli, D., and Pinamonti, P., 1999. "Multistage centrifugal compressor surge analysis: Part II - Numerical simulation and dynamic control parameters evaluation". *Journal of Turbomachinery,* ***121***(2), pp. 312–320.

[7] Van Helvoirt, J., de Jager, B., Steinbuch, M., and Smeulers, J., 2004. "Stability parameter identification for a centrifugal compression system". In Decision and Control, 2004. CDC. 43rd IEEE Conference on, Vol. 4, IEEE, pp. 3400–3405.

[8] Mizuki, S., Asaga, Y., Ono, Y., and Tsujita, H., 2006. "Investigation of surge behavior in a micro centrifugal compressor". *Journal of Thermal Science,* ***15***(2), p. 97.

[9] Bozza, F., and De Bellis, V., 2011. "Map-based and 1d simulation of a turbocharger compressor in surging operation". *SAE International Journal of Engines,* ***4***(2), pp. 2418–2433.

[10] Greitzer, E. M., 1976. "Surge and rotating stall in axial flow compressors - Part I: Theoretical compression system model". *Journal of Engineering for Power,* ***98***(2), pp. 190–198.

[11] Moore, F. K., and Greitzer, E. M., 1986. "A theory of post-stall transients in axial compression systems: Part I - Development of equations". *Journal of Engineering for Gas Turbines and Power,* ***108***(1), pp. 68–76.

[12] Hős, C., Champneys, A., and Kullmann, L., 2003. "Bifurcation analysis of surge and rotating stall in the Moore–Greitzer compression system". *IMA Journal of Applied Mathematics,* ***68***(2), pp. 205–228.

[13] Koff, S. G., and Greitzer, E. M., 1984. "Stalled flow performance for axial compressors: I - Axisymmetric characteristic". In 29th International Gas Turbine Conference and Exhibit, Vol. 1, American Society of Mechanical Engineers.

[14] Galindo, J., Serrano, J., Climent, H., and Tiseira, A., 2008. "Experiments and modelling of surge in small centrifugal compressor for automotive engines". *Experimental Thermal and Fluid Science,* ***32***(3), pp. 818–826.

[15] Japikse, D., 1996. *Centrifugal compressor design and performance*, Vol. 2. Concepts Eti White River Junction, VT.

[16] Martin, G., Talon, V., Higelin, P., Charlet, A., and Caillol, C., 2009. "Implementing turbomachinery physics into data map-based turbocharger models". *SAE International Journal of Engines,* ***2***(1), pp. 211–229.

[17] Elder, R. L., and Gill, M. E., 1985. "A discussion of the factors affecting surge in centrifugal compressors". *Journal of Engineering for Gas Turbines and Power,* ***107***, pp. 499–506.

[18] Currie, I. G., 2016. *Fundamental mechanics of fluids*. CRC press.

[19] Arrowsmith, D. K., and Place, C. M., 1990. *An introduction to dynamical systems*. Cambridge university press.

Appendix A: Derivation of Impeller Stall Function

When impeller inlet stall occurs, we assume this causes a blockage within the channel (see Fig. 14). To represent this blockage we create a stall function, ξ, where $\dot{m} = \xi A \rho u_r$. This means that ξA represents the area of the channel that is not blocked due to the stall, and so is the area that is available for the flow to pass through.

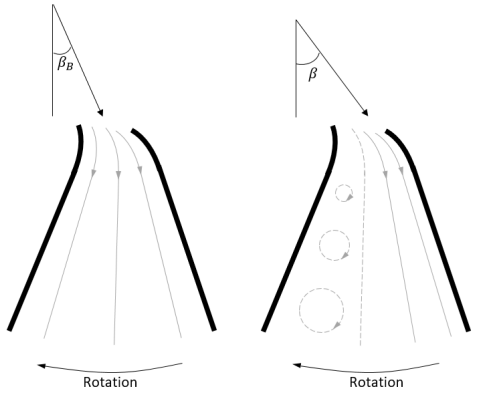

FIGURE 14. IMPELLER CHANNELS IN UNSTALLED (LEFT) AND STALLED (RIGHT) CONDITIONS [1].

If β is the angle of the flow entering the impeller, and β_B is the impeller inlet blade angle, then we assume stall occurs in the impeller only for $\beta > \beta_B$ and is smoothly increasing in severity until a maximum at zero flow. This implies that $\xi = 1$ when $\beta = \beta_B$ and $\xi = 0$ when $\dot{m} = 0$ (i.e. the entire channel is blocked due to stall, so the effective area is zero).

We can find the stall function by considering the velocity as a function of the mass flow, i.e. $u_r(\dot{m}) = \frac{\dot{m}}{\xi A \rho}$. For ξ to result in a smooth function, we assume that at $\beta = \beta_B$

$$u_r(\dot{m}_B) = \frac{\dot{m}_B}{A\rho}, \tag{61}$$

$$\frac{du_r}{d\dot{m}}(\dot{m}_B) = \frac{1}{A\rho}. \tag{62}$$

For the velocity to reach a maximum at zero flow, we get that

$$\frac{du_r}{d\dot{m}}(0) = 0. \tag{63}$$

We desire a free parameter in the stall function in order to set the strength of this stall based on experimental data. Therefore,

with three conditions and a free parameter, the simplest function we can use to describe the stalled velocity is a cubic:

$$u_r = a\dot{m}^3 + b\dot{m}^2 + c\dot{m} + d. \tag{64}$$

Differentiating this gives

$$\frac{du_r}{d\dot{m}} = 3a\dot{m}^2 + 2b\dot{m} + c. \tag{65}$$

Therefore, Eqn. 63 leads to $c = 0$ and Eqn. 62 gives us

$$3a\dot{m}_B^2 + 2b\dot{m}_B = \frac{1}{A\rho} \tag{66}$$

$$\implies b = \frac{1}{2A\rho\dot{m}_B} - \frac{3}{2}a\dot{m}_B. \tag{67}$$

Finally, Eqn. 61 gives us

$$a\dot{m}_B^3 + \left(\frac{1}{2A\rho\dot{m}_B} - \frac{3}{2}a\dot{m}_B\right)\dot{m}_B^2 + d = \frac{\dot{m}_B}{A\rho} \tag{68}$$

$$\implies d = \frac{\dot{m}_B}{2A\rho} + \frac{a}{2}\dot{m}_B^3. \tag{69}$$

Therefore, the stalled velocity has the form

$$u_r(\dot{m}) = a\dot{m}^3 + \left(\tfrac{1}{2A\rho\dot{m}_B} - \tfrac{3}{2}a\dot{m}_B\right)\dot{m}^2 + \left(\tfrac{\dot{m}_B}{2A\rho} + \tfrac{a}{2}\dot{m}_B^3\right) \tag{70}$$

$$\implies \tfrac{\dot{m}}{A\rho\xi} = a\dot{m}^3 + \left(\tfrac{1}{2A\rho\dot{m}_B} - \tfrac{3}{2}a\dot{m}_B\right)\dot{m}^2 + \left(\tfrac{\dot{m}_B}{2A\rho} + \tfrac{a}{2}\dot{m}_B^3\right) \tag{71}$$

$$\implies \tfrac{1}{\xi} = (aA\rho\dot{m}_B^2)\tfrac{\dot{m}^2}{\dot{m}_B^2} + \left(\tfrac{\dot{m}}{2\dot{m}_B} - \tfrac{3}{2}(aA\rho\dot{m}_B^2)\tfrac{\dot{m}}{\dot{m}_B}\right) + \left(\tfrac{\dot{m}_B}{2\dot{m}} + \tfrac{(aA\rho\dot{m}_B^2)}{2}\tfrac{\dot{m}_B}{\dot{m}}\right). \tag{72}$$

Let $\hat{a} = aA\rho\dot{m}_B^2$, then

$$\frac{1}{\xi} = \hat{a}\frac{\dot{m}^2}{\dot{m}_B^2} + \left(\frac{1}{2} - \frac{3}{2}\hat{a}\right)\frac{\dot{m}}{\dot{m}_B} + \left(\frac{1}{2} + \frac{1}{2}\hat{a}\right)\frac{\dot{m}_B}{\dot{m}} \tag{73}$$

$$\implies \tfrac{1}{\xi} = \tfrac{1}{2}\left(\tfrac{\dot{m}}{\dot{m}_B} + \tfrac{\dot{m}_B}{\dot{m}}\right) + \hat{a}\left(1 + \tfrac{1}{2}\tfrac{\dot{m}_B}{\dot{m}}\right)\left(\tfrac{\dot{m}}{\dot{m}_B} - 1\right)^2. \tag{74}$$

Finally notice that

$$\frac{\dot{m}}{\dot{m}_B} = \frac{A\rho u_r}{A\rho u_r^B} = \frac{u_r}{\Omega r}\frac{\Omega r}{u_r^B} = \frac{\tan\beta_B}{\tan\beta}, \tag{75}$$

so the stall function becomes

$$\xi = \frac{1}{\frac{1}{2}\left(\frac{\tan\beta_B}{\tan\beta} + \frac{\tan\beta}{\tan\beta_B}\right) + \hat{a}\left(1 + \frac{1}{2}\frac{\tan\beta}{\tan\beta_B}\right)\left(\frac{\tan\beta_B}{\tan\beta} - 1\right)^2}. \tag{76}$$

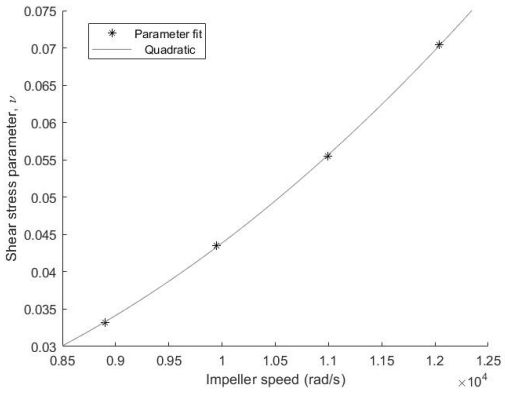

Figure 3-3: (Corrected) Relationship for shear parameter with impeller speed. The points identify the parameter value obtained assuming continuous static pressure at $\dot{m} = 0$. This follows a quadratic trend, implying shear losses are proportional to turbulent kinetic energy.

3.2.1 Paper 2 Addendum

Please note that there is a sign error in Eq. 46, this should read

$$p_I = p_D + \nu(u_{\theta I} - u_{\theta D})^2. \tag{3.2.1}$$

.

Also, there was a computational error in the parameter fitting for the shear loss shown in Fig. 6. Figure 3-3 shows the correct values. These values are slightly larger than the ones presented in the paper, but the trend is still the same so does not affect the results or conclusions of the paper.

3.3 Discussion of Paper 2

Figure 3-4 shows the flow properties for the new reversed flow model. We now observe the behaviour we would expect for a global flow reversal.

Again, these plots need to be read from right to left as the flow is travelling from large radii to small radii. The flow now enters the diffuser at an angle determined by the shape of the volute. Therefore, at the impeller-diffuser interface the tangential velocity changes from a small negative value to a large positive value as contact is made with

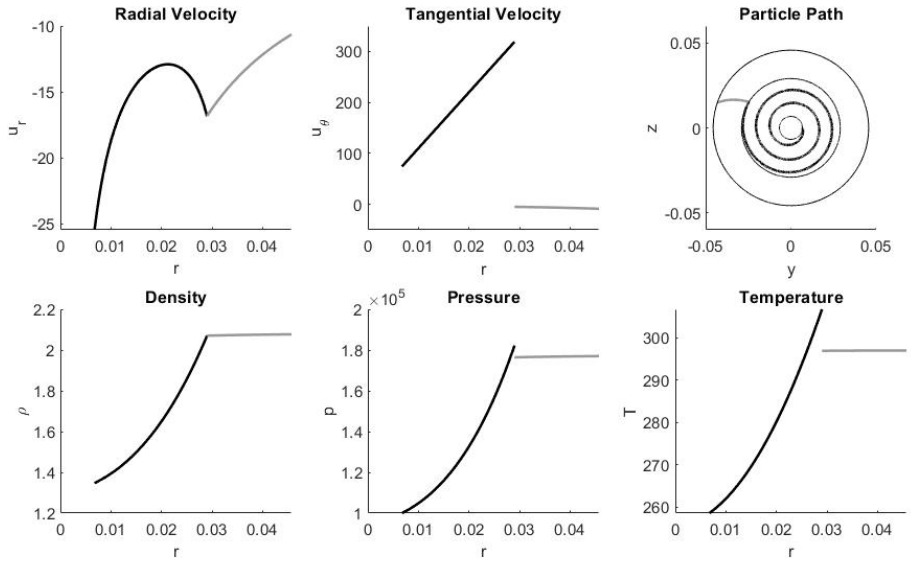

Figure 3-4: Properties of flow at a $\dot{m} = -0.02$kg/s for the model developed in Section 3.2. Black lines denote flow in the impeller and grey lines denote flow in the diffuser.

the impeller blades.

There is also a shear layer that acts instantaneously at the impeller-diffuser interface. The shear losses produce extra heat, which is why there is a sudden rise in temperature. There is also a jump in pressure because the flow satisfies the state equation $p = \rho RT$.

One of the interesting things about the reversed flow regime, is that it is stable despite being an off-design condition with complex flow dynamics.

Figure 3-5 shows our model simulating the experimental reversed flow testing performed in Paper 2. For a typical surge experiment, the throttle valve would exit into ambient air, and so the intercept of the throttle curve is approximately 1 bar. However, since we are feeding compressed air into the compressor outlet, this is equivalent to having a very high pressure at the outlet of the throttle valve. Therefore, the throttle characteristic has shifted vertically to account for this.

We can see that this system is stable because the trajectory moves to the operating point (the intersection between the compressor and throttle characteristic) and stays there for all time.

In Paper 2, we showed that the mathematical stability of the system depended on the gradient of the compressor and throttle characteristics. However, the mathematical

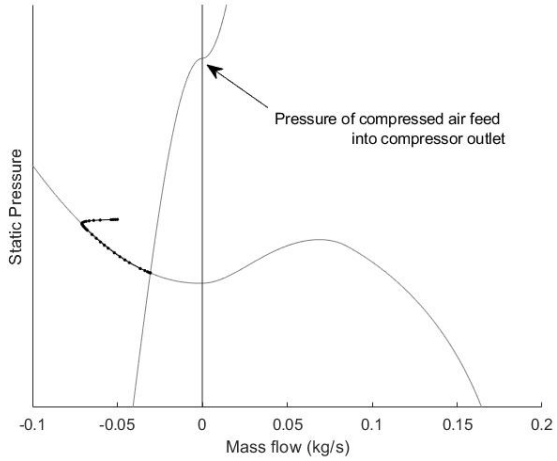

Figure 3-5: Simulation of stable reverse flow: the trajectory tends towards the stable operating point and stays there for all time. The throttle characteristic has an intercept value equal to that of the compressed air feed used to supply the compressor outlet.

stability does not take into account the stress being applied to the components of the turbocharger. Thus, despite the system being mathematically stable, it is often not possible to operate in this region because the stress applied to the shaft connecting the compressor impeller and the turbine rotor is enough to cause failure.

The other interesting result is the potential for asymptotic behaviour occurring for higher speeds. This is the first time such behaviour has been observed. However, experimentally measuring the reverse-flow region of the compressor characteristic is a very uncommon process, so there is little data available for comparison.

As discussed in Section 1.2.1, Galindo et al. [31] performed this experiment but for a much smaller centrifugal compressor. We saw in Fig. 1-11 that they measured cubic-shaped characteristics. However, looking closely at the spread of data points, the smallest measured negative mass flow point is further from $\dot{m} = 0$ for higher speeds. This suggests that Galindo et al. also had difficulty obtaining points close to $\dot{m} = 0$ for higher impeller speeds. So there is some support for there being a minimum negative mass flow required to overcome the centrifugal force of the impeller.

However, this asymptotic behaviour may not be fundamentally caused by the shape of the compressor characteristic, and be more of a system level phenomenon.

3.4 Conclusions

In this chapter we have derived a model for flow travelling in the reverse direction through a centrifugal compressor. We recognised that the model in Section 2.5 treated flow reversal in a way that is similar to local flow recirculation, but we were after the properties of the compressor for when global flow reversal occurred.

We created a new boundary condition for tangential velocity, based on the geometry of the volute. We also incorporated a shear layer at the impeller-diffuser interface.

We combined this new reverse flow model with the forward flow model from Section 2.5 using the new form of stall function developed in Section 2.6.1. This has resulted in a cubic-shaped compressor characteristic with a local minimum at zero flow. This characteristic is very similar in shape to those commonly used in literature (see Section 1.2.1) but has the advantage of being made from first-principles.

We also discovered possible asymptotic behaviour in the negative flow regime while undertaking experimental work. This could mean the compressor characteristic itself should contain an asymptote, or that there is some system level phenomenon that changes the behaviour of simulations for low mass flows.

The assumption that our compressor characteristic is continuous at zero flow is actively included in the model developed in Section 3.2 via the choice of the shear loss parameter ν. Therefore, it is possible to develop a model for the compressor with a different assumption, which would allow asymptotes to occur.

However, having a continuous curve means we do not have to deal with discontinuous ODEs while simulating surge. Furthermore, the majority of centrifugal compressor characteristics proposed in literature are smooth. Therefore, for the next chapter, we will continue to use this assumption.

Chapter 4

Surge Model with Quintic-shaped Compressor Characteristics and Spatial Effects

As discussed in Section 2.5, we believe that including diffuser recirculation into the model for the compressor characteristic may improve the prediction of the surge limit for higher impeller speeds. Hence, the main focus of this chapter is on including this into our reduced surge model, and evaluating its performance in comparison to experimental data.

In order to get a realistic comparison to experimental data, we need to model the experimental test rig in space and time so we can simulate the behaviour of mass flow and pressure at locations equivalent to the sensor locations. Therefore, this will require us to solve a Partial Differential Equation (PDE) system.

4.1 PDE Form of the Reduced Surge Model

Recall that, in Section 2.2, we derived two PDEs (Eqs. 2.2.38 and 2.2.39) that simulated the mass flow and pressure of any constant-area, frictionless pipe. These were

$$\frac{\partial p}{\partial t} = -\frac{\gamma \kappa^{\frac{1}{\gamma}}}{A} p^{\frac{\gamma-1}{\gamma}} \frac{\partial \dot{m}}{\partial x}, \tag{4.1.1}$$

$$\frac{\partial \dot{m}}{\partial t} = -A\frac{\partial p}{\partial x} - \frac{\kappa^{\frac{1}{\gamma}}}{A}\frac{\partial}{\partial x}\left(\frac{\dot{m}^2}{p^{\frac{1}{\gamma}}}\right). \tag{4.1.2}$$

One way to solve these PDEs is by the Method of Lines (see for example [59]), where a discretisation to the x variable is applied. This results in a system of ODEs for mass flow and pressure at every point in the spacial discretisation. These ODEs can then be solved numerically as before using Runga-Kutta methods.

Suppose we have a regular grid of K points in the x direction, with grid spacing Δx. Applying a centred difference discretisation to our PDEs results in

$$\frac{\partial p_j}{\partial t} = \frac{\gamma \kappa^{\frac{1}{\gamma}}}{A} p_j^{\frac{\gamma-1}{\gamma}} \frac{\dot{m}_{j-1} - \dot{m}_{j+1}}{2\Delta x}, \tag{4.1.3}$$

$$\frac{\partial \dot{m}_j}{\partial t} = A\frac{p_{j-1} - p_{j+1}}{2\Delta x} + \frac{\kappa^{\frac{1}{\gamma}}}{A}\frac{1}{2\Delta x}\left(\frac{\dot{m}_{j-1}^2}{p_{j-1}^{\frac{1}{\gamma}}} - \frac{\dot{m}_{j+1}^2}{p_{j+1}^{\frac{1}{\gamma}}}\right), \tag{4.1.4}$$

for $j = 2, ..., K-1$. To compute $\frac{\partial \dot{m}_j}{\partial t}$ and $\frac{\partial p_j}{\partial t}$ at $j = 1$ and $j = K$ we would use first order differences, for example,

$$\frac{\partial p_1}{\partial t} = \frac{\gamma \kappa^{\frac{1}{\gamma}}}{A} p_1^{\frac{\gamma-1}{\gamma}} \frac{\dot{m}_1 - \dot{m}_2}{\Delta x}, \tag{4.1.5}$$

so we do not require values from outside the domain.

Notice that Eq. 4.1.3 states that p only depends on the neighbouring grid points through $\dot{m}$. Similarly, Eq. 4.1.4 states that the linear contribution to $\dot{m}$ depends on p only at its neighbours. Therefore, it makes sense to set up a staggered grid to numerically solve these PDEs.

Suppose K is even, and we have boundary conditions for p_1 and $\dot{m}_K$. Then solving on a staggered grid would work by solving Eq. 4.1.3 for p on $j = 2, 4, ..., K$ and Eq. 4.1.4 for $\dot{m}$ on $j = 1, 3, ..., K-1$. To be able to compute Eq. 4.1.4, the values of $\dot{m}$ on $j = 2, 4, ..., K-2$ are found by linearly interpolating the neighbouring points.

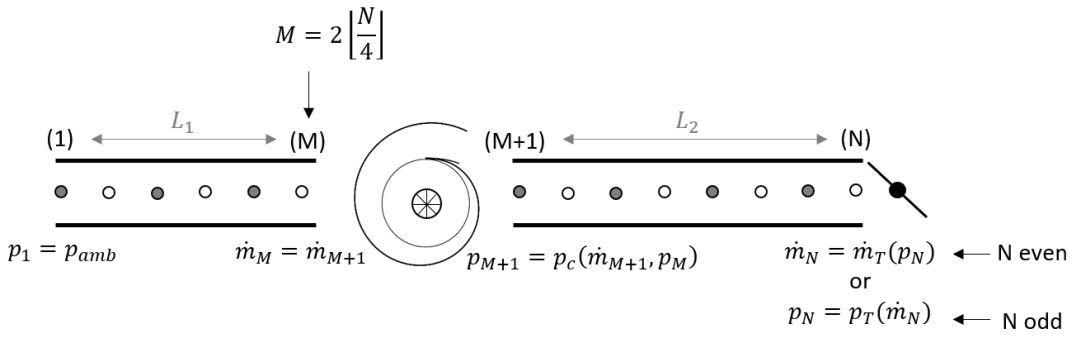

Figure 4-1: Model set up for simulating surge behaviour. Both the inlet and outlet pipes are modelled using the specified boundary conditions. The numerical solution is computed on a staggered grid: white points indicate locations where the pressure PDE is solved and grey points indicate where the mass flow PDE is solved.

The specification of boundary conditions informs us of whether we require K to be odd or even, and which of Eq. 4.1.3 or 4.1.4 are solved on the even or odd grid points. Table 4.1 summaries this.

Figure 4-1 shows a simple schematic of the test facility we used to experimentally record surge behaviour. Measurements we taken at locations both in the inlet pipe and outlet pipe to the compressor, so we need to model both pipes.

Suppose the inlet pipe is from $j = 1, .., M$ and the outlet pipe is from $j = M+1, ..., N$. In the test facility, the inlet pipe was open to the room, and so we can set the boundary condition as $p_1 = p_{amb}$. We also know that the compressor sits between M and $M+1$, meaning that

$$p_{M+1} = p_c(\dot{m}_{M+1}, p_M), \tag{4.1.6}$$

where p_c is the steady-state compressor characteristic. We could use this expression to set a constraint on either p_{M+1}, p_M or $\dot{m}_{M+1}$.

Boundary conditions	K	Eq. 4.1.3	Eq. 4.1.4
p_1 and $\dot{m}_K$	Even	$j = 2, 4, ..., K$	$j = 1, 3, ..., K-1$
p_1 and p_K	Odd	$j = 2, 4, ..., K-1$	$j = 1, 3, ..., K$
$\dot{m}_1$ and p_K	Even	$j = 1, 3, ..., K-1$	$j = 2, 4, ..., K$
$\dot{m}_1$ and $\dot{m}_K$	Odd	$j = 1, 3, ..., K$	$j = 2, 4, ..., K-1$

Table 4.1: Requirements on number of points, K, in the discretisation, as well as which equations are solved on which grid points, for each possible pair of boundary conditions.

Notice that, if we picked an arbitrary p_{M+1} (for a given p_M), we could identify multiple $\dot{m}_M$ that would result in this pressure. Therefore, it is best that we do not invert this function, and so use this condition to set p_{M+1}.

Furthermore, to allow the compressor to operate freely, we wish to keep $\dot{m}_{M+1}$ and p_M as free variables so the boundary condition we specify at M has to be a restriction on $\dot{m}_M$. We know that a compressor operating in steady-state has a constant mass flow across it. Therefore, we can set $\dot{m}_M = \dot{m}_{M+1}$.

Finally, at N, we have the throttle and so

$$\dot{m}_N = \dot{m}_T(p_N) \tag{4.1.7}$$

holds. The throttle characteristic is a bijection (i.e. each mass flow maps to a unique pressure and vice versa), and so it does not matter whether this boundary condition is used to constrain mass flow or pressure.

Referring to Tab. 4.1, these boundary conditions require Eq. 4.1.3 (Eq. 4.1.4) to be solved on even (resp. odd) grid points for both pipes. We also have the requirement that M is even, but N can be any integer due to the flexibility of condition 4.1.7.

Another advantage of using a staggered grid is that this system can be related to previously mentioned ODE systems. Suppose we do not have the inlet pipe, so $M = 0$ and $p_M = p_{amb}$. Then if we set $N = 3$, $\Delta x = \frac{1}{2}L_2$ we get

$$\frac{\partial \dot{m}_1}{\partial t} = \frac{2A}{L_2}(p_c(\dot{m}_1) - p_2) + \frac{2\kappa^{\frac{1}{\gamma}}}{AL_2}\left(\frac{\dot{m}_1^2}{p_c(\dot{m}_1)^{\frac{1}{\gamma}}} - \frac{(\dot{m}_1 + \dot{m}_3)^2}{4p_2^{\frac{1}{\gamma}}}\right), \tag{4.1.8}$$

$$\frac{\partial p_2}{\partial t} = \frac{\gamma\kappa^{\frac{1}{\gamma}}}{AL_2}p_2^{\frac{\gamma-1}{\gamma}}(\dot{m}_1 - \dot{m}_3), \tag{4.1.9}$$

$$\frac{\partial \dot{m}_3}{\partial t} = \frac{2A}{L_2}(p_2 - p_T(\dot{m}_3)) + \frac{2\kappa^{\frac{1}{\gamma}}}{AL_2}\left(\frac{(\dot{m}_1 + \dot{m}_3)^2}{4p_2^{\frac{1}{\gamma}}} - \frac{\dot{m}_3^2}{p_T(\dot{m}_3)^{\frac{1}{\gamma}}}\right), \tag{4.1.10}$$

which are equivalent to the ODEs in Greitzer's 1976 paper [17], once the nonlinearity

is removed (see Eqs. 1.2.7 - 1.2.9). Furthermore, taking $N = 2$, $\Delta x = L_2$ we get

$$\frac{\partial \dot{m}_1}{\partial t} = \frac{A}{L_2}(p_c(\dot{m}_1) - p_2) + \frac{\kappa^{\frac{1}{\gamma}}}{AL_2}\left(\frac{\dot{m}_1^2}{p_c(\dot{m}_1)^{\frac{1}{\gamma}}} - \frac{\dot{m}_T(p_2)^2}{p_2^{\frac{1}{\gamma}}}\right), \tag{4.1.11}$$

$$\frac{\partial p_2}{\partial t} = \frac{\gamma\kappa^{\frac{1}{\gamma}}}{AL_2} p_2^{\frac{\gamma-1}{\gamma}} (\dot{m}_1 - \dot{m}_T(p_2)). \tag{4.1.12}$$

which is identical to the ODE form of the reduced order surge model developed in Section 2.2.

4.2 Compressor Characteristic with Diffuser Recirculation

Diffuser recirculation is a local flow reversal within the compressor. The air close to the stationary housing that covers the rotating impeller can leak between impeller channels and usually exits the impeller more tangentially than the bulk flow. At high impeller rotational speeds, and low mass flows, this flow can become so tangential that it can't escape from the diffuser and gets swept back into the impeller.

Similarly to impeller incidence, this can be modelled as a blockage. Therefore, we define a stall function of the form (Eq. 2.6.9) to represent this blockage, i.e.

$$\eta = \frac{1}{\frac{1}{2}\left(\frac{\tan\alpha}{\tan\alpha^*} + \frac{\tan\alpha}{\tan\alpha^*}\right) + \hat{b}\left(1 + \frac{1}{2}\frac{\tan\alpha}{\tan\alpha^*}\right)\left(\frac{\tan\alpha^*}{\tan\alpha} - 1\right)^2}, \tag{4.2.1}$$

where α is angle of the bulk flow entering the diffuser, and α^* is the angle of the bulk flow at which this flow recirculation initialises. Notice that η restricts the area in the axial direction, whereas the stall due to impeller incidence losses, $\xi(\beta)$, restricts the area in the tangential direction.

The main difficulty with including diffuser recirculation into the model is the interaction between the two stall functions, ξ and η. Since the flow in the impeller will impact the flow in the diffuser, it is clear that impeller stall will affect the amount of diffuser stall. However, the impact of diffuser recirculation on the impeller inlet flow angle is not obvious. Therefore, for simplicity, we will only assume a one-way interaction. Figure 4-2 shows how this one-way interaction can be implemented.

In this case, the impeller inlet stall is determined, and the impeller is run with this

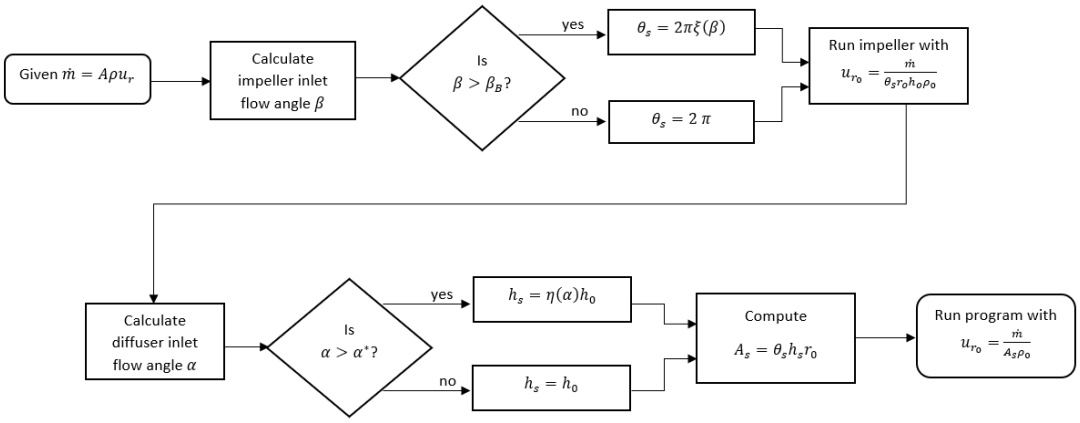

Figure 4-2: Flow chart showing how both impeller inlet stall and diffuser stall are implemented in the steady-state model for the compressor. Impeller incidence has the ability to affect diffuser recirculation, but not vice versa. Subscript 0 denotes an initial value.

stalled area to determine the flow angle into the diffuser. The diffuser stall is then determined and the stalled area recomputed to account for this. The entire system (both impeller and diffuser) are then run with this stalled area A_s to simulate the dynamics.

It is possible to allow the diffuser stall to impact the impeller inlet angle and iteratively solve to find the stalled area, but this would add extra complexity and computation time.

The paper in the next section presents the resulting compressor characteristics once diffuser recirculation is incorporated into the model. It considers how to define the critical angle α^*, and the stall factor $\hat{b}$. It also extends the compressor model to include some effects of the volute in order to improve the choked-flow properties.

Finally, the paper looks at simulated dynamics of the entire compression system when this characteristic is incorporated into the PDE model above, and compares these to experimental data.

4.3 Paper 3: A New First-principles Model to Predict Incipient and Deep Surge for a Centrifugal Compressor

<table>
<tr><th colspan="5">This declaration concerns the article entitled:</th></tr>
<tr><td colspan="5">A New First-Principles Model to Predict Incipient and Deep Surge for a Centrifugal Compressor</td></tr>
<tr><td colspan="5">Publication status (tick one)
Draft manuscript [ ] Submitted [X] In review [ ] Accepted [ ] Published [ ]</td></tr>
<tr><td>Publication details (reference)</td><td colspan="4">Powers, K., Kennedy, I., Archer, J., Eynon, P., Horsley, J., Brace, C., Copeland, C., and Milewski, P. (2021) “A New First-Principles Model to Predict Incipient and Deep Surge for a Centrifugal Compressor.” Journal of Energy (Submitted)</td></tr>
<tr><td colspan="5">Copyright status (tick the appropriate statement)
I hold the copyright for this material [X] Copyright is retained by the publisher, but I have been given permission to replicate the material here [ ]</td></tr>
<tr><td>Candidate’s contribution to the paper (provide details, and also indicate as a percentage)</td><td colspan="4">The contribution of Katherine Powers to the paper is as follows:
Formulation of ideas (90%) with advice from supervising authors
Derivation of equations for the mathematical models (90%)
Participation in design and implementation of experiments (40%)
Writing MATLAB code and creating of numerical simulations (100%)
Comparing numerical simulations to given experimental data, and analysing of the results (100%)
Presentation of data in journal format (100%)</td></tr>
<tr><td>Statement from Candidate</td><td colspan="4">This paper reports on original research I conducted during the period of my Higher Degree by Research candidature.</td></tr>
<tr><td>Signed</td><td colspan="2">  </td><td>Date</td><td>26/02/2021</td></tr>
</table>

A New First-principles Model to Predict Incipient and Deep Surge for a Centrifugal Compressor

Katherine Powers[a,1], Ian Kennedy[b], Jamie Archer[c], Paul Eynon[c], John Horsley[c], Chris Brace[b], Colin Copeland[d], Paul Milewski[a]

[a]*Department of Mathematical Sciences, University of Bath, Claverton Down, Bath, BA2 7AY, UK*
[b]*Department of Mechanical Engineering, University of Bath, Claverton Down, Bath, BA2 7AY, UK*
[c]*Cummins Turbo Technologies, St Andrew's Road, Huddersfield, HD1 6RA, UK*
[d]*School of Sustainable Energy Engineering, Simon Fraser University, 5118 - 10285 University Drive, Surrey, V3T 0N1, BC, Canada*

Abstract

Centrifugal compressors are used in many applications, including micro-gas turbines, automotive turbochargers, and air-conditioning. Compressor surge is an instability that occurs at low flow rates that is often damaging to the compressor and its installation. In particular, the incipient surge regime is known to produce noise characteristics that cause problems with customer acceptance. It is therefore important to be able to predict both incipient and deep surge onset which has historically only been possible to assess experimentally.

Powers et al. [1, 2] have developed a model for the compressor characteristic from first-principles so that surge could be predicted without the reliance on costly testing. In this paper, we will extend their work to include diffuser recirculation and show a new quintic-like shape for the compressor characteristic that is able to differentiate between incipient and deep surge.

We will then use this model to simulate the surge behaviour observed on a test rig. We develop a model that allows variations in both space and time to capture the wave dynamics in the pipework. We explore how the system evolves from stable operation, through incipient surge, into deep surge. This model is validated via experiment conducted at the University of Bath.

[1]Please address all correspondence to this author. Email: k.h.powers@bath.ac.uk

Preprint submitted to Elsevier *24th February 2021*

The potential of this model to predict both surge regimes will allow engineers to better design centrifugal compressors, and match them to particular applications to avoid problematic surge behaviour, in advance of experimental tests.

Keywords: Surge, Centrifugal/Radial Compressors, Compressible Fluids, Reduced order modelling, Ordinary Differential Equations

---

Nomenclature

A	Cross-sectional area
$\hat{a}$	Impeller inlet stall parameter
B	Greitzer's parameter
$\hat{b}$	Diffuser stall parameter
c	Speed of sound
E	Specific energy
F	Friction function
f	Friction coefficient
f_q	Frequency
g	Acceleration due to gravity
h	Channel height
L	Length
$\dot{m}$	Mass flow
$\hat{\dot{m}}$	Effective mass flow
n_b	Number of impeller blades
ODE	Ordinary differential equation
p	Pressure
q	Mass flow per radian
$\dot{Q}$	Heat flux
R	Specific gas constant
r	Radius
S	Surface area per unit volume
s	Distance
t	Time
T	Temperature
u	Velocity
x	Distance
α	Wheel exit flow angle
α^*	Critical wheel exit flow angle
α_B	Impeller backsweep angle
β	Impeller inlet flow angle
β_B	Impeller inlet blade angle
γ	Specific heat ratio
Δx	Grid spacing
η	Diffuser stall function
κ	Isentropic constant
λ	Throttle setting
ν	Shear loss parameter
ξ	Impeller inlet stall function
ξ_T	Throttle parameters
ρ	Density
τ	Deviatoric stress tensor
Φ	Nondimensional mass flow
Ψ	Nondimensional pressure
Ω	Angular rotation

Subscripts/superscripts:

amb Ambient	T Throttle
c Compressor	*tip* Impeller wheel tip
D Diffuser	V Volute
I Impeller	θ Tangential direction
r Radial direction	$*$ Critical

1. Introduction

Centrifugal compressors have wide range of applications because compressed air is such an important commodity. Compressed air is an important medium for energy transfer in many processes, from pneumatics, to vehicle propulsion and breaks, to refrigeration. In this paper, we will discuss the centrifugal compressor in the context of automotive turbochargers, but the methodology presented is applicable to many more uses.

Nowadays most road vehicles have downsized turbocharged engines. There is a drive to reduce pollutants, especially greenhouse gasses, and downsized engines are more environmentally friendly [3]. It is the turbocharger that allows us to use downsized engines because they increase the power output of that engine making it comparable to the previously used larger naturally aspirated engines [4].

Surge is an aerodynamic instability that exists when operating the turbocharger compressor at low mass flows [4]. Therefore, surge limits the compressor operating regime and hence limits the amount of boost provided at low engine speeds. As a result, being able to predict the onset of surge is vital for engine manufacturers.

Surge causes oscillations in mass flow and pressure. There are different classes of surge. When the oscillations in mass flow are large enough that actual flow reversal is seen, this is called deep surge [5]. Operating in deep surge often causes damage to the impeller blades within the compressor because the oscillations unbalance the machinery and results in contact between the blades and the housing. The temperature rises significantly as a result of oscillating flow and can sometimes causes connections between the compressor and its installation to fail.

However, when mass flow and pressure oscillations are observed but the flow always remains travelling in the forward direction, this is classed as incipient surge [5]. This form of surge is less damaging, but is still very

noisy. This causes problems with customer acceptance because the sound would be off-putting to any driver. Furthermore, the pressure oscillations may influence downstream component performance.

Models for the compressor surge have been around since the 50s [6]. The first such model was proposed by Huppert and Benser in 1953 [7], closely followed by Emmons et al. in 1955 [8], both of whom used lumped parameter models. However, nearly all models are based on the work by Greitzer in 1976 [9] where he developed a quasi-steady model for surge that incorporated a characteristic for the compressor and throttle. In its most basic form, this can be written as

$$\frac{d\Phi}{dt} = B(\psi_c - \Psi), \tag{1}$$

$$\frac{d\Psi}{dt} = \frac{1}{B}(\Phi - \psi_T^{-1}), \tag{2}$$

where Φ and Ψ are nondimensional mass flow and pressure respectively, and ψ_c and ψ_T are the compressor and throttle characteristics [10, 9]. It is generally agreed that the orifice equation is a good approximation for the steady-state behaviour of the throttle

$$\psi_T = \xi_{T0} + \frac{1}{\xi_T^2}\Phi^2, \tag{3}$$

[10]. However, the steady-state behaviour of the compressor is more complex and so a characteristic is more complicated to determine.

It was Koff and Greitzer [11] who performed the first experimental study to determine the shape of the compressor characteristic. They observed a cubic-like shape, which lead to Moore and Greitzer [12] proposing the use of a cubic which can be fitted to experimental data,

$$\psi_c = \psi_{c_0} + H\left[1 + \frac{2}{3}\left(\frac{\Phi}{W} - 1\right) - \frac{1}{2}\left(\frac{\Phi}{W} - 1\right)^3\right], \tag{4}$$

where ψ_{c_0}, H and W are parameters that are found via fitting to compressor map data. The study by Koff and Greitzer was done using an axial compressor, but a more recent study by Galindo et al. [13] of a small centrifugal compressor came to the same conclusion of a cubic-like shape.

Since then, there have been some theoretical approaches to finding the compressor characteristic. The majority of these use a meanline modelling

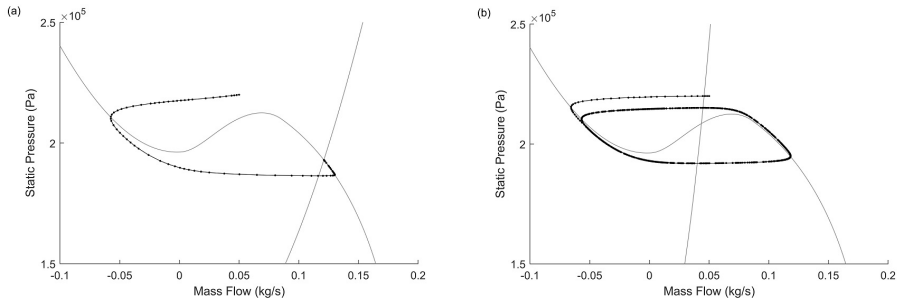

Figure 1: The only two possible behaviours of cubic-like compressor characteristic in quasi-steady model: stable (a) and limit cycle involving reversed flow (b). These simulations use the model from Powers et al. [2].

approach where the compressor is broken down into sections and the equations of motion are applied across these along with multiple loss models [14, 15, 16]. In 2019, Powers et al. [1] developed a model from first principles with a minimal number of parameters so that the surge limit could be predicted. All of these models also result in a cubic-like shape for the characteristic.

However, this cubic-like shape is only able to capture deep surge oscillations. The quasi-steady system with a cubic characteristic is either stable, or a limit cycle which involves flow reversal (see Fig. 1). Therefore, the a cubic shaped characteristic cannot be capturing all of the dynamics near surge because we know that incipient surge exists, and it is equally important to capture in a model.

When testing turbochargers to find their surge limit, it can be the case that incipient surge is observed but if you push through this the system stabilises again before deep surge occurs. This quietening period doesn't always occur, and it can make it difficult for turbocharger manufacturers to define the location of their surge limit. This unknown behaviour makes it difficult to predict how a turbocharger will respond once it is introduced into a vehicle system. So understanding the physics could have a significant impact on how manufacturers interpret the surge characteristics observed through testing on a gas stand.

The aim of this paper is to create an improved model for the flow near and in surge conditions, including incipient surge. We will extend the model by Powers et al. [1, 2] to include diffuser recirculation. Then, we will develop a model of the test rig to simulate surge in this system and validate this via

experimental data.

2. Mathematical Model for Compressor Characteristics

In 2019, Powers et al. [1] developed a compressor characteristic from first principles. The fundamental equations for air flow through a compressor are conservation of mass, momentum (in a rotating frame) and energy:

$$\frac{\partial \rho}{\partial t} + \nabla \cdot (\rho \mathbf{u}) = 0, \tag{5}$$

$$\tfrac{\partial}{\partial t}(\rho \mathbf{u}) + \nabla \cdot (\rho(\mathbf{u} \otimes \mathbf{u})) + 2\rho(\mathbf{\Omega} \times \mathbf{u}) + \rho(\mathbf{\Omega} \times (\mathbf{\Omega} \times \mathbf{r})) = \rho \mathbf{g} - \nabla p + \nabla \cdot \tau, \tag{6}$$

$$\frac{\partial}{\partial t}(\rho E) + \nabla \cdot (\rho \mathbf{u} E + p\mathbf{u}) - \nabla \cdot (\tau \cdot \mathbf{u}) = \rho \dot{Q} \tag{7}$$

respectively. Powers et al. assumed:

(i) An ideal gas: $p = \rho R T$,

(ii) A perfect gas: specific heat ratio $\gamma = \text{const.}$,

(iii) Radial impeller blades: $u_\theta = 0$ in the rotating frame,

(iv) Vaneless diffuser with axisymmetric flow: $\frac{\partial}{\partial \theta} = 0$,

(v) Small variations in axial direction: $\int ab\,dx \approx \int a\,dx \int b\,dx$,

so that the fundamental equations could be reduced to a system of 1D ODEs in the radial direction.

The ODEs they obtained for the impeller are

$$\frac{1}{r}\frac{\partial}{\partial r}(r h \rho u_r) = 0, \tag{8}$$

$$\frac{1}{r}\frac{\partial}{\partial r}(r h \rho u_r^2) - h\rho\Omega^2 r = -h\frac{\partial p}{\partial r} + hF_r, \tag{9}$$

$$\frac{1}{r}\frac{\partial}{\partial r}\left(r h \rho u_r \left(\frac{u_r^2}{2} + \frac{\gamma}{\gamma - 1}\frac{p}{\rho} - \frac{\Omega^2 r^2}{2}\right)\right) = 0, \tag{10}$$

and for the diffuser are

$$\frac{1}{r}\frac{\partial}{\partial r}(rh\rho u_r) = 0, \tag{11}$$

$$\frac{1}{r}\frac{\partial}{\partial r}(rh\rho u_r^2) - \frac{h\rho u_\theta^2}{r} = -h\frac{\partial p}{\partial r} + hF_r, \tag{12}$$

$$\frac{1}{r}\frac{\partial}{\partial r}(rh\rho u_r u_\theta) + \frac{h\rho u_r u_\theta}{r} = hF_\theta, \tag{13}$$

$$\frac{1}{r}\frac{\partial}{\partial r}\left(rh\rho u_r\left(\frac{u_r^2}{2} + \frac{u_\theta^2}{2} + \frac{\gamma}{\gamma-1}\frac{p}{\rho}\right)\right) = 0, \tag{14}$$

where

$$F_r = \frac{f}{2}\rho u_r^2 S \tag{15}$$

$$F_\theta = \frac{f}{2}\rho u_r u_\theta S \tag{16}$$

represents skin friction.

In 2020, Powers et al. [2] developed this further. They suggested a stall function of

$$\xi = \frac{1}{\frac{1}{2}\left(\frac{\tan\beta_B}{\tan\beta} + \frac{\tan\beta}{\tan\beta_B}\right) + \hat{a}\left(1 + \frac{1}{2}\frac{\tan\beta}{\tan\beta_B}\right)\left(\frac{\tan\beta_B}{\tan\beta} - 1\right)^2}, \tag{17}$$

to take into account incidence losses. This works by writing $\dot{m} = \xi A\rho u_r$ so that ξA represents the area of the impeller channel that is not blocked due to stall (see Fig. 2). Therefore, when the flow angle β is equal to the blade angle β_B, $\xi = 1$ and there is no stalling. However, as $\beta \to 90^o$, $\xi \to 0$ and the channel becomes fully stalled.

The authors also looked in depth at the reverse flow part of this characteristic. In this case, air is travelling from the volute through to the impeller inlet but the impeller wheel is still rotating in the forward direction as this is controlled by the turbine. In this case, the angle at which air enters from the volute into the diffuser has to be specified, and Powers et al. [2] argued that this should be

$$\theta = \tan^{-1}\left(\frac{u_{\theta D}}{u_{rD}}\right) = \tan^{-1}\left(\sqrt{\left(\frac{A_D}{A^*}\right)^2 - 1}\right) \tag{18}$$

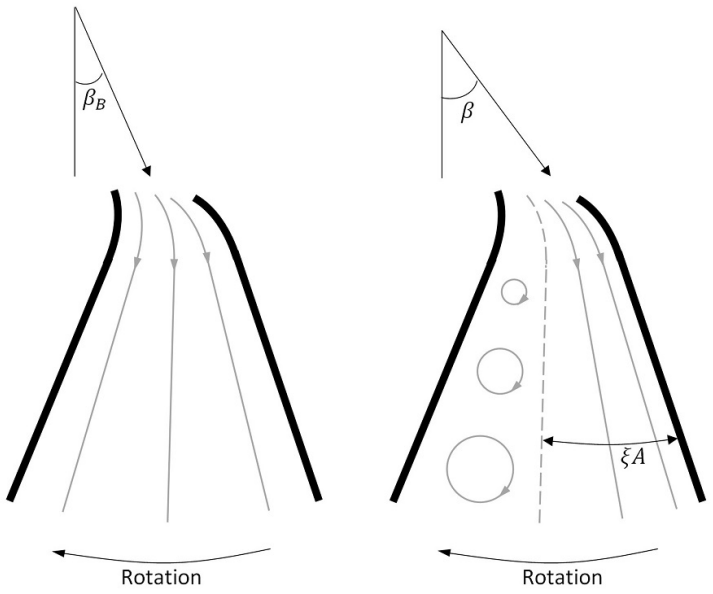

Figure 2: Flow dynamics in an impeller channel with blade angle β_B. Left: The flow enters at angle $\beta = \beta_B$, and the channel has no stall. Right: The flow enters at angle $\beta > \beta_B$ and we have stall that effectively blocks the channel. The flow can only travel through an area of ξA.

from geometry considerations. Here, $A_D = 2\pi rh$ is the cross-sectional area of the diffuser and A^* is the critical area of the housing.

Another important addition for the reverse flow case is the existence of a shear layer between the diffuser and the impeller. When the air comes into contact with the impeller it is suddenly accelerated in the opposite direction, and so there is a large change in tangential velocity in a short radial distance. The shear layer causes a loss in pressure due to viscous dissipation. Powers et al. [2] decided to use an instantaneous loss at the interface,

$$p_I = p_D + \nu(u_{\theta I} - u_{\theta D})^2, \tag{19}$$

where the shear loss parameter ν was found by assuming the characteristic is continuous at zero flow.

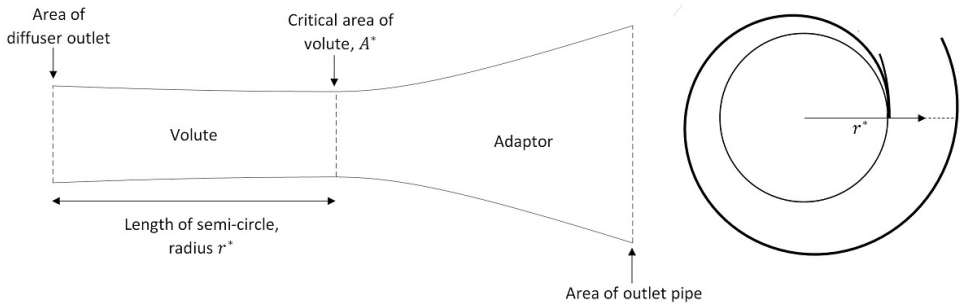

Figure 3: Left: Volute and adaptor included in compressor model. Right: Traditional volute identifying the critical radius, r^*.

2.1. Additional model improvements

The first improvement we make is to add a model for the volute and adaptor to the outlet pipe.

We choose to model the volute by assuming it is a simple pipe which instantly contains all the air rather than collecting it as it curves round the diffuser (see Fig. 3). We quadratically reduce the area until we reach the critical area of the volute, and then quadratically increase the area until we reach the area of the outlet pipe. Using quadratic functions allows the gradient at the critical area to equal to zero for both the volute and adaptor sections of the pipe, meaning the area is continuously differentiable from the diffuser outlet to the pipe.

The ODEs for this volute-adaptor model are given by

$$\frac{\partial}{\partial s}(A\rho u) = 0, \tag{20}$$

$$\frac{\partial}{\partial s}(A\rho u^2) = -A\frac{\partial p}{\partial s} - \frac{A}{2} f \rho u^2 S, \tag{21}$$

$$\frac{\partial}{\partial s}\left(A\rho u\left(\frac{u^2}{2} + \frac{\gamma}{\gamma - 1}\frac{p}{\rho}\right)\right) = 0, \tag{22}$$

where s is the distance down the pipe, $u = \sqrt{u_r^2 + u_\theta^2}$ is the velocity of fluid going down the pipe, A is the cross-sectional area as described above, and S is the surface area per unit volume.

The crucial part of this addition is that it allows us to take the critical area of the housing into account. This has improved the choke region of the compressor characteristic significantly because, in reality, the flow often chokes in the housing, especially for high impeller speeds.

Another improvement we made was to capture some of the effects of backswept blades into the model. In order to keep the impeller ODEs simple and efficient to solve, we wish to keep the assumption of radial blades within the impeller. However, we can easily take into account the effect backsweep has on the angle at which the flow exits the impeller into the diffuser by

$$u_\theta\big|_{tip} = \Omega r_{tip} - u_r\big|_{tip} \tan(\alpha_B) \tag{23}$$

where α_B is the backsweep angle.

Since the flow angle into the diffuser effects how long flow remains in the diffuser, this addition is able to capture some of the pressure drop backswept blades cause. It will also allow us the capture how backsweep affects the stability of the system when considering diffuser recirculation in the next section.

2.2. Diffuser Recirculation

Diffuser recirculation occurs when air exits the impeller in a predominantly tangential direction. When this happens, some of the air does not escape from the diffuser, and instead gets drawn back into the impeller. Due to leakage flow over the top of the blades, the air exiting the impeller at the shroud-side is usually more tangential than the main flow. Therefore, the recirculation usually occurs here.

This can be accounted for by considering the recirculation as a blockage, in a similar way to the impeller inlet stall developed by Powers et al. [1, 2]. This idea is shown in Fig. 4.

In reality, the exit angle of the flow depends on the axial height. Therefore, the critical angle for stall in the diffuser will be the angle at which the main body of the flow has to exit for the shroud-side portion of the flow to recirculate. To get an estimate for this angle, we looked at CFD simulations for four different compressors near surge (as this is where diffuser stall is likely to occur). The results are shown in Fig. 5. This shows us that the critical angle is likely to be in the range of 70^o to 75^o. In literature, this angle is often given between 75^o and 85^o [17, 18]. Therefore, we shall use 75^o for our critical angle.

Since we are treating diffuser recirculation as a blockage, we can develop a stall function in the exactly same way as Powers et al. [2]. This gives us a function,

$$\eta = \frac{1}{\frac{1}{2}\left(\frac{\tan\alpha^*}{\tan\alpha} + \frac{\tan\alpha}{\tan\alpha^*}\right) + \hat{b}\left(1 + \frac{1}{2}\frac{\tan\alpha}{\tan\alpha*}\right)\left(\frac{\tan\alpha^*}{\tan\alpha} - 1\right)^2}, \tag{24}$$

where α is the flow angle and α^* is the critical angle. As with impeller inlet stall, we have $\eta = 1$ implies no stall and $\eta \to 0$ when the recirculation blocks the entire channel.

It's important to notice that, since we have two forms of stalling that effectively restrict the area inside the compressor, there will be interactions between the two. There is a natural impact of the impeller stall on the diffuser stall because impeller inlet stall will influence the impeller exit velocity, and hence angle α. However, the impact of the diffuser stall on the impeller is not obvious. Here we assume for simplicity that it doesn't affect the angle of the incoming flow and so the impeller stall is unaffected by the diffuser stalling.

2.3. Parameter fittings

With these additions to the compressor model, we now have three unknown parameters: (i) f the friction coefficient, (ii) $\hat{a}$ the stall factor for impeller inlet stall, and (iii) $\hat{b}$ the stall factor for diffuser recirculation.

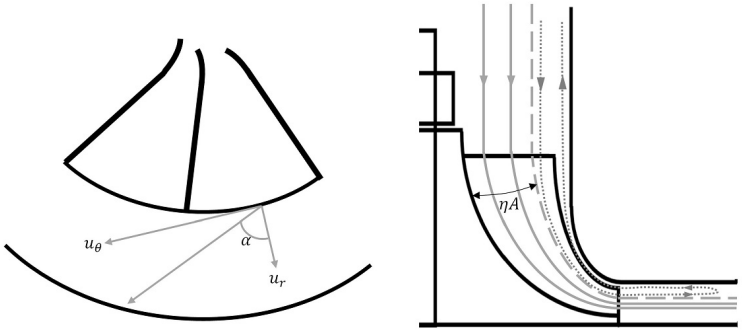

Figure 4: Diffuser stall causing shroud-side recirculation due to air exiting the impeller at an angle greater than a critical angle $\alpha > \alpha^*$. The recirculation effectively causes a blockage: ηA is the effective area available to the flow.

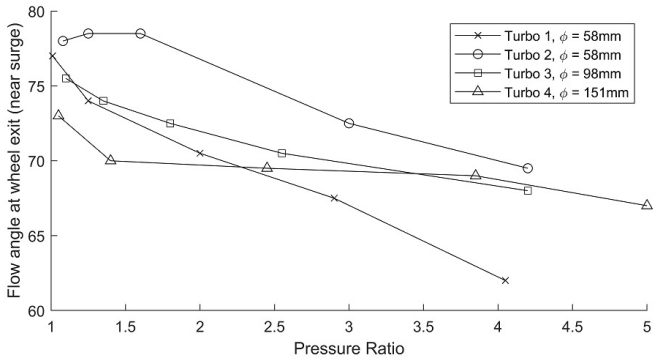

Figure 5: CFD data of the average flow angle at the wheel exit close to the surge limit for four different turbochargers, the tip diameter of which are included in the legend. Each compressor was run at five different impeller speeds - the higher speeds correspond to the points with higher pressure ratio.

For friction, Powers et al. [1, 2] showed that there existed a linear relationship between the friction factor and the impeller speed. This is because 3D losses that are more prominent for higher speeds cannot be captured by our 1D model, and so are being encompassed into the friction factor. For our model, we will use

$$f = 0.013 + 1.15 \times 10^{-5}\Omega. \tag{25}$$

This was found by comparing our model to experimental data for steady points.

For impeller inlet stall, Powers et al. [2] showed that a constant stall factor was able to capture the behaviour. Similarly, in this paper we use a constant factor of $\hat{a} = 5$. This value was calculated by comparing our model with the amplitude of deep surge oscillations observed in experiments.

Finally, for diffuser recirculation, we have tuned the stall parameter by comparing our model with the amplitude of incipient surge oscillations from experimental data. See Table 1 for the results. Here, we did not find a relationship that can be explained physically, which means that the real-life system is more complex than our model predicts. For example, our assumption that the critical angle α^* is constant with impeller speed and it's just the flow angle that changes could be too simplistic. Figure 5 suggests that the critical angle could decrease with impeller speed, meaning that stalling occurs earlier (so $\hat{b}$ is larger)for higher impeller speeds.

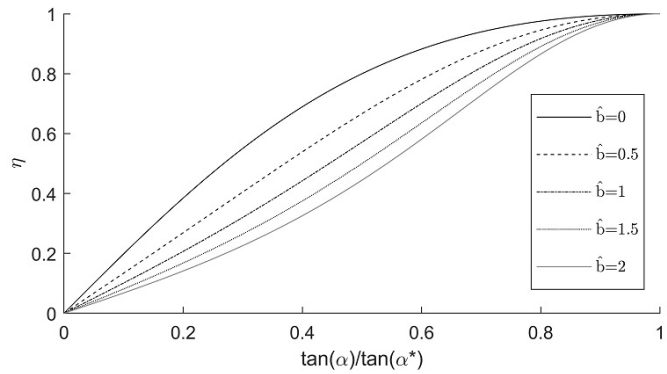

Figure 6: The variation in the diffuser stall function, η, with stall factor $\hat{b}$.

Moreover, the computed values for $\hat{b}$ only span a small range of the possible values, and they only has a small effect on the stall function. Figure 6 shows how the stall function changes with $\hat{b}$. It only affects the gradient, i.e. whether stall initially occurs quickly and then slows, or is initially slow and speeds up.

Universal relations need to be found to make this compressor model fully predictive. This can be done by regression analysis on a large dataset from a wide range of turbochargers. However, due to a limit of resources available to the authors, this is out of scope for this paper.

Table 1: Tuned values for diffuser recirculation stall factor $\hat{b}$.

Ω	$\hat{b}$
85 krpm	0
115 krpm	0.5
135 krpm	1.6
155 krpm	1.2

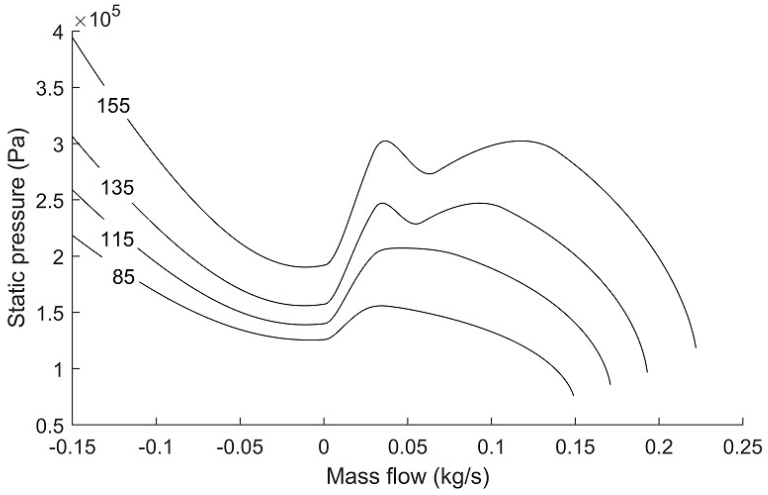

Figure 7: Resulting compressor characteristics when both impeller stall and diffuser recirculation are included. The impeller speeds in krpm are labelled on each line.

2.4. Resulting characteristic

Similarly to Powers et al. [1, 2], we can reduce the above systems of equations to the following ODEs:

$$\text{Impeller:} \quad \frac{\partial \rho}{\partial r} = \frac{-\rho q^2 \left(\frac{1}{r} + \frac{1}{h}\frac{\partial h}{\partial r}\right) - \gamma \Omega^2 r^3 h^2 \rho^3 + \gamma f \rho q^2 \left(\frac{n_b}{2\pi r} + \frac{1}{h}\right)}{\left(\frac{\gamma+1}{2}\right) q^2 - (\gamma - 1) E_I r^2 h^2 \rho^2}, \tag{26}$$

$$\text{Diffuser:} \quad \frac{\partial \rho}{\partial r} = \frac{-\frac{\rho q^2}{r} - r^2 h^2 \rho^3 \left(\gamma \frac{u_\theta^2}{r} + (\gamma - 1) u_\theta \frac{\partial u_\theta}{\partial r}\right) + \gamma \frac{f}{h} \rho q^2}{\left(\frac{\gamma+1}{2}\right) q^2 + (\gamma - 1) \left(\frac{u_\theta^2}{2} - E_D\right) r^2 h^2 \rho^2}, \tag{27}$$

$$\text{Volute:} \quad \frac{\partial \rho}{\partial s} = \frac{\dot{m}^2 \rho f S - 2\rho \dot{m}^2 \frac{dA}{ds}}{(3 - \gamma)\dot{m}^2 - 2(\gamma - 1) E_V \rho^2 A^2}, \tag{28}$$

where

$$E_I = \frac{u_r^2}{2} + \frac{\gamma}{\gamma - 1}\frac{p}{\rho} = \text{const.}, \tag{29}$$

$$E_D = \frac{u_r^2}{2} + \frac{u_\theta^2}{2} + \frac{\gamma}{\gamma - 1}\frac{p}{\rho} = \text{const.}, \tag{30}$$

$$u_\theta = \frac{\Omega r_{\text{tip}}^2}{r} e^{-\frac{f}{h}\left(r - r_{\text{tip}}\right)}, \tag{31}$$

$$E_V = \frac{u^2}{2} + \frac{\gamma}{\gamma - 1}\frac{p}{\rho} = \text{const.}, \tag{32}$$

and $q = \frac{\dot{m}}{2\pi}$ is mass flow per radian.

The stalling is taken into account through calculating $\dot{m}$ and q. Notice that only the effective mass flow, $\hat{\dot{m}} = \xi\eta A\rho u$, is known, so the stall functions are included in the above equations via

$$\dot{m} = \frac{\hat{\dot{m}}}{\xi\eta} \quad \text{and} \quad q = \frac{\hat{\dot{m}}}{2\pi\xi\eta}.$$

Figure 7 shows the new compressor characteristics. By including diffuser stall we get a quintic-like curve for higher impeller speeds instead of the well-known cubic-like characteristics.

This occurs because, for the high impeller speeds, the diffuser stall is triggered first and we get a drop in pressure. Then, when the mass flow is reduced further, the impeller inlet also stalls which has the effect of initially reducing the diffuser stall and the pressure starts to recover. This is because the impeller stall causes an increase in the radial velocity component, which means the air exits the impeller straighter and so lessens the amount of diffuser recirculation. As the mass flow is reduced further still, this recovery stops and the pressure drops quickly as both the impeller and diffuser stall are having a negative impact on the compressor.

The lower impeller speeds still have a cubic-like shape because diffuser recirculation has a minimal, if any, effect on them. Diffuser recirculation is a lot stronger for high rotational speeds because the air exiting the wheel will have a much larger tangential component. Therefore, the pressure drop seen for the lower speeds is caused predominantly by impeller inlet stall.

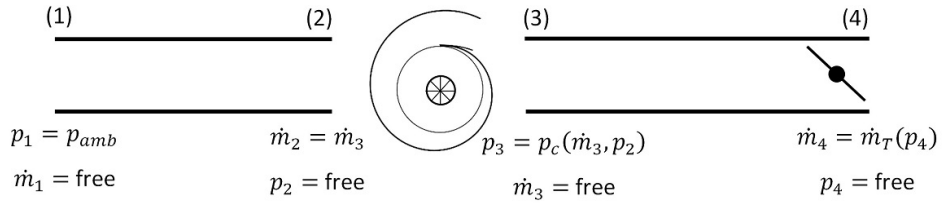

Figure 8: Schematic for mathematical test rig model. It is composed of an inlet and outlet pipe for the compressor. There is also a throttle valve at the exit of the outlet pipe. The boundary conditions used for the two pipes are also shown.

3. Mathematical Model for Test Rig

Surge is a system level phenomenon. Therefore, to study this behaviour we need to model the system around the compressor as well as the compressor itself. Since we will validate this model by comparing it to experimental data gathered on a test rig, we shall create a model consisting of straight inlet and outlet pipes, with a throttle valve on exit. See Fig. 8 for details.

The fluid in these pipes will obey the standard conservation of mass (Eq. 5) and conservation of momentum (Eq. 6) equations. We shall assume that we have an isentropic flow in the pipes, i.e. $p = \kappa\rho^\gamma$, to replace the conservation of energy equation. Written in 1D for mass flow and pressure, with direction along the pipe denoted by x, this gives:

$$\frac{\partial p}{\partial t} + \frac{\gamma\kappa^{\frac{1}{\gamma}}}{A} p^{\frac{\gamma-1}{\gamma}} \frac{\partial \dot{m}}{\partial x} = 0, \tag{33}$$

$$\frac{\partial \dot{m}}{\partial t} + A\frac{\partial p}{\partial x} + \frac{\kappa^{\frac{1}{\gamma}}}{A}\frac{\partial}{\partial x}\left(\frac{\dot{m}^2}{p^{\frac{1}{\gamma}}}\right) + \frac{fS\kappa^{\frac{1}{\gamma}}}{2A}\frac{\dot{m}^2}{p^{\frac{1}{\gamma}}} = 0, \tag{34}$$

where f is a friction factor. Although, f is part of a skin friction term, this term will encompass the losses due to dissipation. The flow on exit from the compressor will be more turbulent than the air prior to it and so we expect there to be more dissipation losses in the outlet pipe. Therefore, we shall use $f = 0.05$ in the inlet pipe and $f = 0.1$ in the outlet pipe.

In order to reduce this to a system of ODEs that can be solved within MATLAB, we use a centred-difference discretisation in x. Therefore, for a

location x_j within the pipes, and grid spacing Δx, we have:

$$\frac{\partial p_j}{\partial t} = \frac{\gamma \kappa^{\frac{1}{\gamma}}}{A} p_j^{\frac{\gamma-1}{\gamma}} \frac{\dot{m}_{j-1} - \dot{m}_{j+1}}{2\Delta x}, \tag{35}$$

$$\frac{\partial \dot{m}_j}{\partial t} = A \frac{p_{j-1} - p_{j+1}}{2\Delta x} + \frac{\kappa^{\frac{1}{\gamma}}}{A} \frac{1}{2\Delta x} \left(\frac{\dot{m}_{j-1}^2}{p_{j-1}^{\frac{1}{\gamma}}} - \frac{\dot{m}_{j+1}^2}{p_{j+1}^{\frac{1}{\gamma}}} \right) - \frac{f S \kappa^{\frac{1}{\gamma}}}{2A} \frac{\dot{m}_j^2}{p_j^{\frac{1}{\gamma}}}. \tag{36}$$

At each end point of the pipe, we cannot use central differences because it would require a point outside of the domain of the pipe. Therefore, we use a first-order difference instead. We also need to specify boundary conditions for each end of the pipes. Figure 8 shows the boundary conditions we use.

For the inlet pipe we have a fixed ambient pressure at (1) because this pipe is left open to the room. At (2), we have a constraint that the mass flux into the compressor must be the same as that leaving the compressor at point (3).

For the outlet pipe, we apply the compressor characteristic developed in Section 2 at (3), which requires both the mass flux through the compressor as well as the inlet pressure to compute the outlet pressure. Finally, we apply the throttle characteristic at (4). We use the same throttle characteristic as Powers et al. [1] but assume constant density for simplicity, namely:

$$\dot{m} = \mathrm{sgn}(p - p_{amb}) \sqrt{\frac{2\gamma}{\gamma - 1} \rho_{amb} A^2 \frac{\lambda^2}{1 - \lambda^2} |p - p_{amb}|}. \tag{37}$$

where λ is the fraction the throttle is open, and $\mathrm{sgn}(x) = \frac{x}{|x|}$ returns the sign of variable x.

4. Experiments

To provide some validation for this model, we tested a turbocharger using the gas stand facilities at the University of Bath. The turbocharger tested had dimensions given in Table 2, and the layout of the test facility is shown in Fig. 9.

For the turbine section, compressed air was supplied through electrically heated flow paths and gate valves were used to control the flow. For the compressor section, the inlet pipe was left open so the compressor could draw air in freely from the test cell room. The amount of flow passing through the compressor was controlled by a gate valve in the outlet pipe.

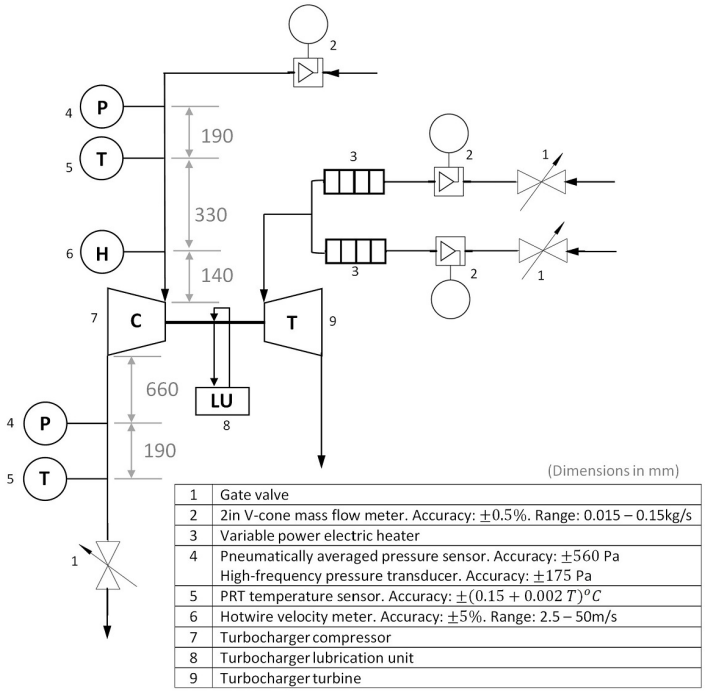

1	Gate valve
2	2in V-cone mass flow meter. Accuracy: $\pm 0.5\%$. Range: 0.015 – 0.15kg/s
3	Variable power electric heater
4	Pneumatically averaged pressure sensor. Accuracy: ± 560 Pa High-frequency pressure transducer. Accuracy: ± 175 Pa
5	PRT temperature sensor. Accuracy: $\pm(0.15 + 0.002\,T)^oC$
6	Hotwire velocity meter. Accuracy: $\pm 5\%$. Range: 2.5 – 50m/s
7	Turbocharger compressor
8	Turbocharger lubrication unit
9	Turbocharger turbine

Figure 9: Layout of gas-stand test facility at the University of Bath. The table lists the components with their measurement accuracy where applicable.

To run the experiment, the compressor outlet pipe valve was opened fully to ensure the turbocharger would initially operate in a non-surge region.

Table 2: Geometric details of the tested compressor.

Number of blades	$6 + 6$
Hub diameter	13.5 mm
Shroud diameter	41 mm
Wheel tip diameter	58 mm
Diffuser height	3.15 mm
Diffuser area ratio	2.48

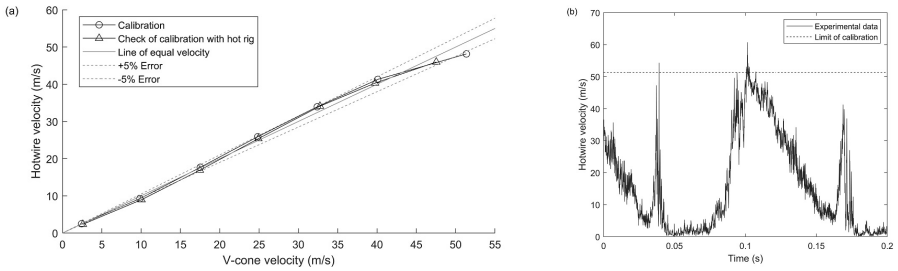

Figure 10: (a) Calibration of hotwire sensor to V-cone velocities. A check of the calibration was also done with a hot rig. The line where points would lie if the two sensors agreed, along with ±5% error, is shown in grey. (b) Experimental data that contains the highest velocities (155krpm deep surge operating point) and the calibration limit. A very small portion of the data lies outside the calibration and so will have lower accuracy. However, this will have minimal impact on the overall result.

Then hot, compressed air was let into the turbine side to drive the rotor. Once the desired rotor speed was reached, the compressor outlet valve was shut gradually while adjusting the turbine-side valves in order to keep the rotor speed constant.

The manufacturer supplied compressor map was used as a guide to identify a near surge location. Starting from this point, high-frequency pressure and flow velocity signals were recorded approximately every 0.002kg/s as the compressor outlet valve was closed until the compressor entered deep surge. This was repeated for four different rotor speeds.

A hotwire was used to measure the velocity (and hence, with measured

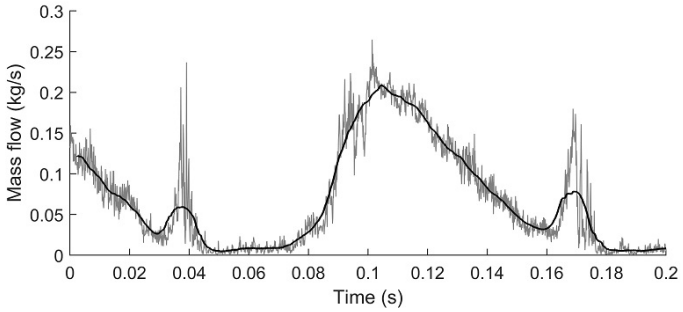

Figure 11: Grey: Original mass flow data using hotwire sensor. Black: Smoothed signal using a 100-point moving average.

density and cross-sectional area values, calculate the mass flow) close to the compressor inlet at a frequency of 10kHz, and pressure transducers were used to measure the pressure in the inlet and outlet pipes, also at 10 kHz. Measurements were also recorded at 10Hz for pressure, temperature, and mass flow using pneumatically averaged pressure sensors, PRTs, and a V-cone respectively. The location and accuracy of these sensors are shown in Fig. 9.

During set-up, the hotwire needed to be calibrated. Therefore, measurements from the V-cone were assumed to be the true velocities so this data could be used to calibrate the sensor. Since the hotwire is sensitive to temperature, the calibration points were checked again once the rig was hot. Figure 10 shows the results. We get a good match between the hot-rig data and the initial calibration, and all results remain within a 5% error band. We have a larger error at higher velocities, but the only time such high velocities were observed was for the 155krpm deep surge point. As seen in Fig. 10(b), only a small portion of the peak of this surge pulse is affected, meaning the overall accuracy of the signal is still good.

The hotwire sensor was very sensitive and picked up high-frequency turbulent flow variations. Since we are more interested in the behaviour of the bulk flow, we smoothed the signal using a 100-point moving average (see Fig. 11). The pressure signals seemed reasonable, so we used the original output signals to compare to model simulations.

5. Results

5.1. Surge Lines

For turbocharger and engine manufacturers, it is extremely useful to be able to predict the on-set of both incipient and deep surge for a compressor. Therefore, the first comparison we make between our mathematical model and the experimental data are the surge lines. Figure 12 shows the results.

The surge lines for our mathematical model were simple to determine by identifying the smallest operating point required to observe incipient or deep surge oscillations in the simulated dynamics. However, a difficulty arises when we observe a region where the dynamics follow a combination of incipient surge cycles and deep surge cycles, as it is not clear whether to class this region as incipient or as deep surge. Therefore we have identified the onset to all three regions in Fig. 12. (See Section 5.4 for more details on the three regions.)

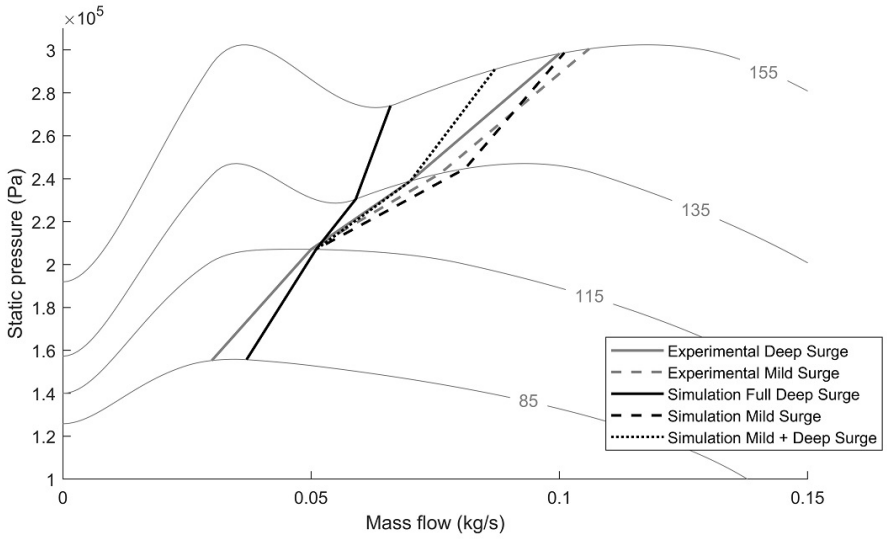

Figure 12: A comparison to the model predicted surge lines (black) and the surge lines from experimental data (grey). The impeller speeds (in krpm) are labelled on each compressor characteristic.

To determine the surge line for the data, we needed to identify the mass flow of the operating point, i.e. the average mass flow going through the throttle. We decided to use the V-cone measurements for this as being further from the compressor, it shouldn't be influenced as much by the instantaneous flow dynamics.

For steady operation, the V-cone mass flow gives us the operating point, and for incipient surge, the oscillations are relatively small so the average mass flow is close to the operating point. However, for deep surge, the mass flow oscillations vary a lot and are often far from the operating point. Furthermore, the V-cone sensor cannot distinguish between forward and reverse flow as it only identifies the magnitude of the flow, meaning that taking a direct average of this sensor would not be appropriate.

All we know for certain is that the operating point will have a smaller mass flow than the previous operating point, and so we chose to use a mass flow that was approx. 0.002kg/s smaller than the previous one. For example, for the 155krpm speed line, steady operation was observed for 0.174kg/s through to 0.118kg/s. Mild surge was first observed when the flow was re-

duced further from 0.118kg/s and registered an average flow of 0.106kg/s. Mild surge continued to register through to an average flow of 0.102kg/s. Reducing the flow further resulted in deep surge oscillations which registered an average flow of 0.109kg/s. Since we know the deep surge was observed after a reduction in flow from the previous mild surge point, we chose the location of the deep surge line to be at a mass flow of 0.1kg/s.

Comparing the incipient surge lines, we see a good match throughout. We correctly predict that there is no incipient surge for the lowest two speeds, and we can predict the onset of incipient surge to within 5% for the top two speeds.

Notice that the existence of simulated incipient surge dynamics coincides with quintic-shaped characteristics (not cubic-shaped ones). This implies that incipient surge is caused by the interaction of impeller inlet stall and diffuser recirculation. Since this is the first time a quintic-like characteristic has been captured by any model of a centrifugal compressor, it is the first time anyone has suggested a reason for the observed behaviour of incipient surge.

Looking at the experimental deep surge line, we can see that is it much closer to the point at which we simulate a mix of deep and incipient surge, rather than the point at which we simulate full deep surge. This makes sense because it is possible for the experimental noise to tip the system from switching between incipient and deep surge cycles into solely deep surge cycles, and so this mixed region becomes deep surge.

Moreover, since most compressor mappings are performed in a way to prevent damage occurring, they are likely to back off at the first sign of deep surge irrespective of whether this is mixed with incipient oscillations. Therefore, it is likely that most compressor designers would classify this mixed surge region as deep surge because large pressure oscillations occur.

Therefore, assuming the mixed surge region is classified as deep surge, we get a good prediction for the deep surge line as well. We predict deep surge onset slightly early for low speeds and slightly late for high speeds, but the error has stayed within 20%.

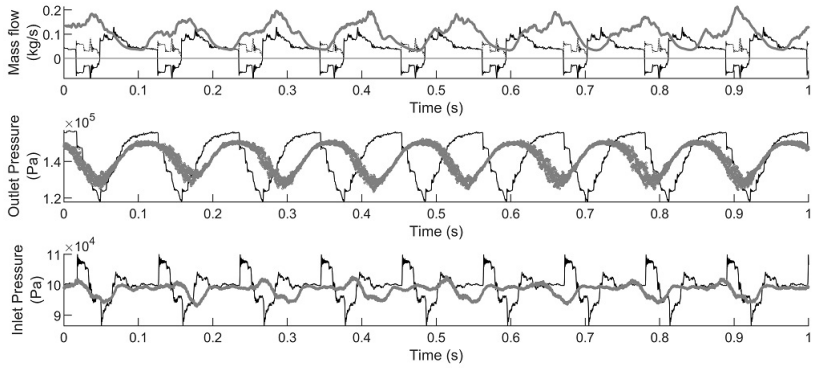

(a) 85krpm

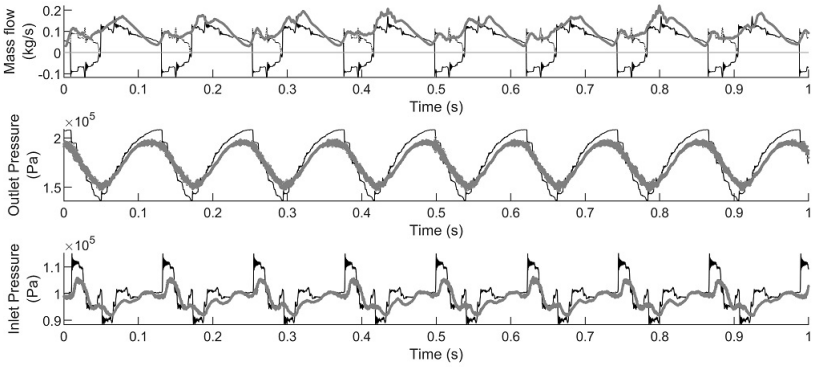

(b) 115krpm

Figure 13: Comparison of deep surge between model (black) and experimental data (grey) for different impeller speeds.The hotwire sensor only records magnitude and not direction, so the absolute value of the simulated mass flow is shown as a dotted line for comparison to this.

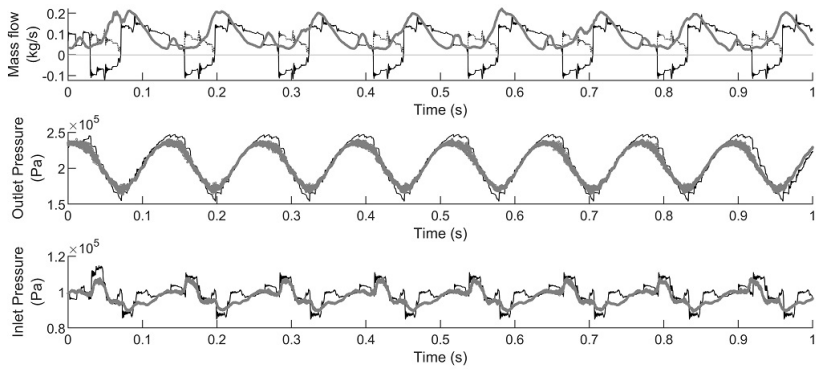

(c) 135krpm

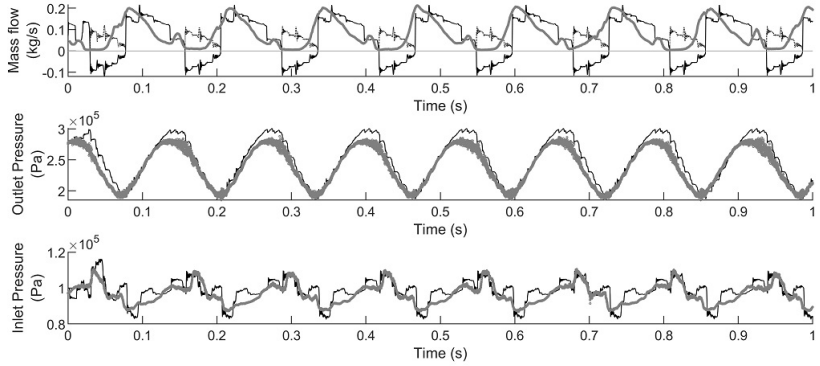

(d) 155krpm

Figure 13: Comparison of deep surge between model (black) and experimental data (grey) for different impeller speeds [cont.]. The hotwire sensor only records magnitude and not direction, so the absolute value of the simulated mass flow is shown as a dotted line for comparison to this.

5.2. Deep surge

As seen above there is a difference between the simulated full deep surge line and the observed deep surge line in experimental data. Here, we put aside this shift and directly compare a deep surge simulation to the deep surge time-resolved data for that speed line, e.g. for 155krpm, we compare a simulation for $\dot{m} = 0.066$kg/s to data at $\dot{m} \approx 0.1$kg/s. The results are shown in Fig. 13.

Case (a), which is for the 85krpm speed line, has a miss-match with oscillation frequency. The simulation predicts a 9Hz oscillation, whereas the observed data has a 8Hz oscillation. The qualitative agreement between the two signals is still good, and the rest of the speeds (cases (b)-(d)) have a remarkable fit between the simulation and the data.

If we consider the simulation of outlet pressure for the four cases, we can observe a small change in shape for the signal: it appears to becomes smoother, more rounded, as speed increases. The experimental data appears to keep a smooth, almost sinusoidal, shape for all speeds. However, there is a very close fit between the two and it is possible that damping associated with the pressure sensor itself could stop experimental data picking up sharp features.

The mathematical simulation gives us some insight into why we observe oscillating flow in the outlet pipe. We can identify that the peak pressure occurs just before the flow reverses, so the compressor is causing the pressure to continually rise until there is so much pressure in the outlet pipe to cause a flow reversal. The pressure then drops quite rapidly and becomes a minimum while the flow has reversed.

The inlet pressure simulation has a great resemblance to the observed data. We are able to pick out the peaks and troughs of the signal very clearly. Again, the mathematical model can give us some understanding of the signal shape. The peak inlet pressure occurs when we have flow reversal, so high pressure air has travelled backwards through the compressor and caused a pressure rise in the inlet pipe. The trough occurs just as the flow returns to the forward direction. This causes a rapid change in mass flow as the compressor suddenly draws in a lot of air from the inlet pipe and so generates a low pressure here.

The mass flow signal plots are slightly more complicated to understand. The hotwire could only detect the magnitude of the flow, not the direction, so can't differentiate between forward and reverse flow. Therefore, we added the

plot $|\dot{m}|$ for the simulated flow as a dotted line in order to compare with the data collected. Looking at case (b), with impeller speed 115krpm, gives the best comparison between the simulation and the data. It follows the dotted line very closely, and so the data was able to identify both the forward and reverse flow signals. For all cases, the data and simulation are a good match for the forward flow peaks. However, for case (d) the hotwire did not appear to pick up the reverse flow and so shows as near zero during this period.

5.3. Incipient surge

We now do a similar comparison for incipient surge. The results are shown in Fig. 14.

This time, for both cases we have a miss-match of oscillation frequency. The data has an oscillation of approximately 12Hz, whereas our model predicts a frequency of 13Hz instead. This is still very good because we are able to simulate surge behaviour within a frequency of the expected order of magnitude.

Overall, the fits are not as good as for the deep surge cases, but our model is still able to capture a remarkable amount of the features seen in the data. For example, for mass flow, we are able to pick out a signal with the correct amplitude and even pick out the double-peak or trough that is observed in the data.

For the outlet pressure, our simulation has a higher average pressure and a slightly larger amplitude than observed in the data. However, the shape of the signal is very triangular which agrees with the shape of the data signal.

Finally, for the inlet pressure, our model seems to be predicting a higher peak inlet pressure for both signals and, as with the outlet pressure, seems to have a higher average pressure. However, we are still able to capture a significant amount of the signal shape, especially for case (b).

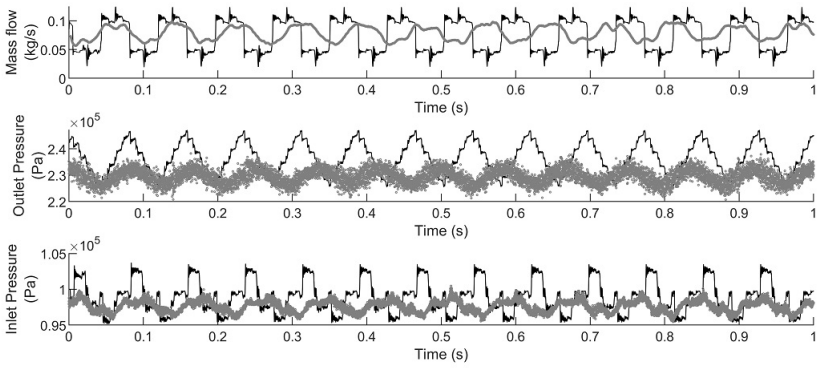

(a) 135krpm

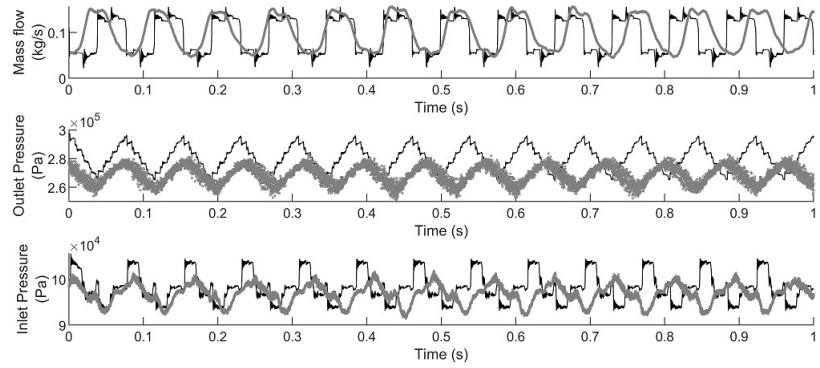

(b) 155krpm

Figure 14: Comparison of incipient surge between model (black) and experimental data (grey) for different impeller speeds.

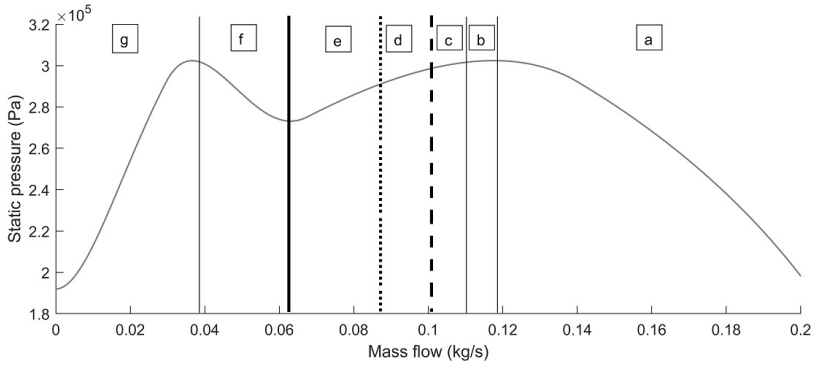

(1) 155krpm compressor characteristic

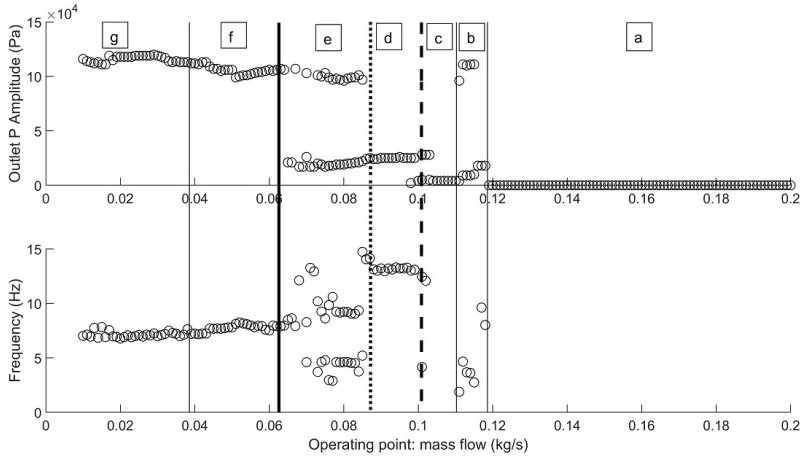

(2) Simulated amplitudes and frequencies of pressure oscillations for an initial condition far from the operating point

Figure 15: Detailed look at the 155krpm speed line. Sections a-g highlight different modes of operation observed for our mathematical model.The location of the fully-deep surge line is shown by a thick solid line, the mixed mild-deep surge line by a thick dotted line, and incipient surge by a thick dashed line.

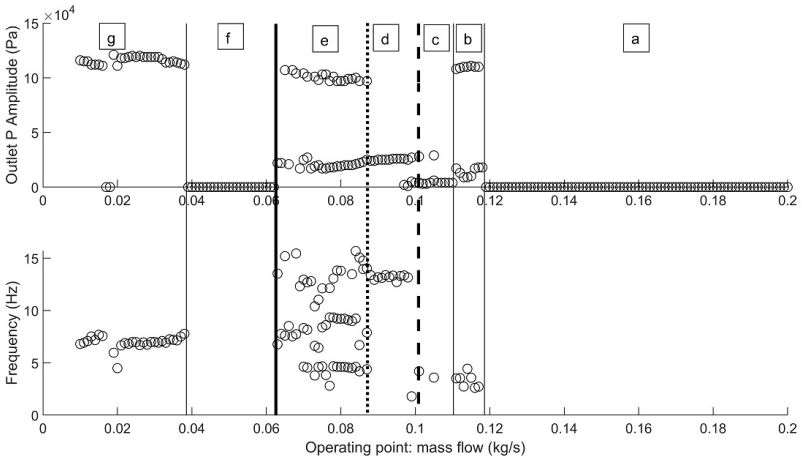

(3) Simulated amplitudes and frequencies of pressure oscillations for an initial condition close to the operating point

Figure 15: Detailed look at the 155krpm speed line (cont.). Sections a-g highlight different modes of operation observed for our mathematical model.The location of the fully-deep surge line is shown by a thick solid line, the mixed mild-deep surge line by a thick dotted line, and incipient surge by a thick dashed line.

5.4. Transition from steady to deep surge

In this section, we take a detailed look at the mathematical model we've developed for the top speed line, 155krpm, in order to show the simulated behaviours our model predicts as the compressor is operated in and around surge. Figure 15 shows the compressor characteristic and a summary of the behaviours observed. Each plot has been divided into sections where different behaviours occur.

The behaviour observed in section (a) is completely stable. We do not see any oscillation for any of the operating points within this region, which is why the amplitude is shown as zero and there is no frequency data. This is the normal operating region for the compressor.

In section (b), we observe resonant behaviour. The length of the outlet pipe is $L = 1.86$m, and the speed of sound (based on the average pressure) is $c = 397$m/s. Therefore, the resonant frequency of the outlet pipe is approximately

$$f_q = \frac{c}{4L} = 53Hz. \tag{38}$$

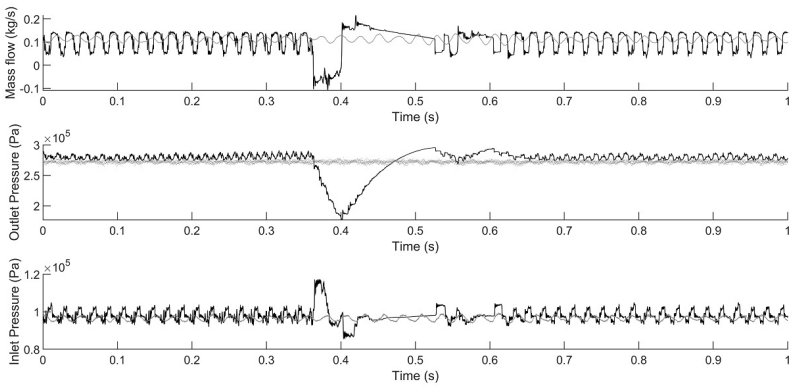

Figure 16: Resonance observed in simulation (black) and experimental data (grey). This corresponds to section (b) of Fig. 15.

Figure 16 shows the simulated results at this point, along with a comparison to experimental data. Our simulation shows a small amplitude oscillation with a frequency of approximately 50Hz. This oscillation causes our simulation to jump into deep surge cycles every now and again, which is why a deep surge amplitude is observed in Fig. 15 for this section. The observed data shows that the system is indeed oscillating at a very small amplitude, but unlike the simulation, this doesn't trigger a deep surge cycle. The data has a frequency in the same order of magnitude as the simulation, but at approximately 40Hz instead of 50Hz.

In section (c), we have less resonance and are stable again. The incipient surge line separates section (c) from section (d), where mild surge behaviour is observed and we get the oscillations as shown in Fig. 14(b).

The region of incipient surge is not large and we soon reach the mixed surge line and enter section (e). The dynamics here follow a combination of incipient surge cycles and deep surge cycles. For example, Fig. 17 shows the flow tracking one incipient cycle, then one deep cycle, repeatedly. This section ends with the full deep surge line.

The combination of incipient and deep cycles changes throughout section (e) as we transition from incipient surge to full deep surge. Therefore, near the mixed surge line it is possible to see a combination with more incipient cycles than deep cycles, whereas the opposite holds near the deep surge line.

Section (f) is the only section where the behaviour depends on the initial

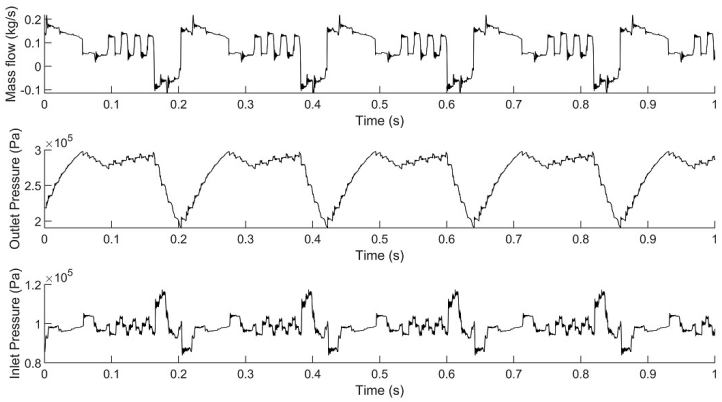

Figure 17: Simulated mass flow and pressure for the transition period between incipient and deep surge.This corresponds to section (e) of Fig. 15.

condition of the simulation. We have two possible behaviours in this region. The first is full deep surge as seen in Fig. 15(2), and the second is steady behaviour as seen in Fig. 15(3).

We can plot these two behaviours in the mass flow - pressure plane (see Fig. 18) to get a better understanding of what is happening. This shows us that there is a region (shaded grey) close to the operating point (the intersection between throttle and compressor characteristics) that if we start the simulation within we will see stable behaviour. Outside of this region, we will observe deep surge.

Having two possible dynamics occur at the same operating point can cause some really interesting behaviour. If region (f) is observed as stable, it effectively moves the deep surge line to the beginning of section (g). Therefore, it explains why quiet periods can occur between incipient and deep surge.

Figure 19 show some experimental data from Cummins Turbo Technologies where this quiet period is observed. However, it is not always observed and sometimes repeat tests will give different answers, which can cause difficulties when trying to determine the deep surge limit. This is the first time that this observed behaviour has been predicted and explained by surge modelling. Furthermore, being aware of the existence of two possible behaviours in region (f) is of key importance as it will help designers to determine more

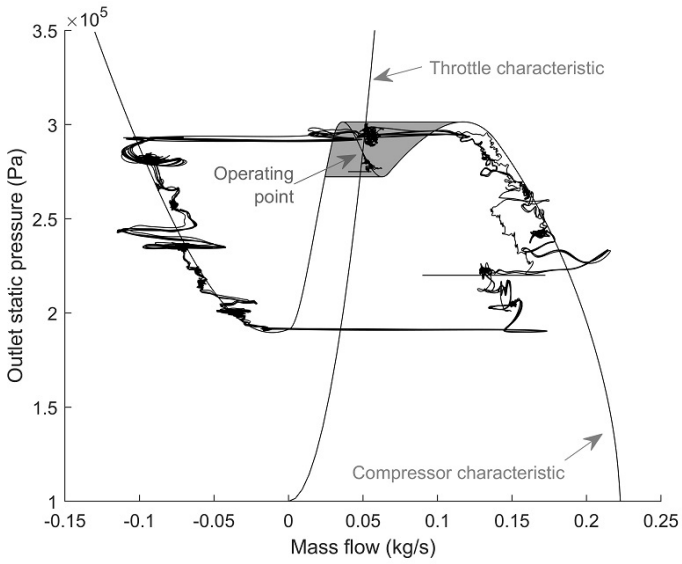

Figure 18: Stable operation and deep surge limit cycle observed for the same throttle setting in the mass flow-pressure plane (corresponding to section (f) of Fig. 15). The domain of attraction for stable operation is shown in grey. Using an initial condition for the simulation outside of this region results in deep surge.

accurate surge limits with more confidence.

It is interesting to note that region (f) corresponds to the local region of negative gradient in the compressor characteristic (see Fig. 15(1)), which is the result of the interaction between diffuser recirculation and impeller inlet stall. Therefore, this suggests that having both forms of stall present in the system and working against one another, could actually result in stabilised operation.

Finally, for section (g), we only observe deep surge behaviour and get oscillations as shown in Fig. 13(d).

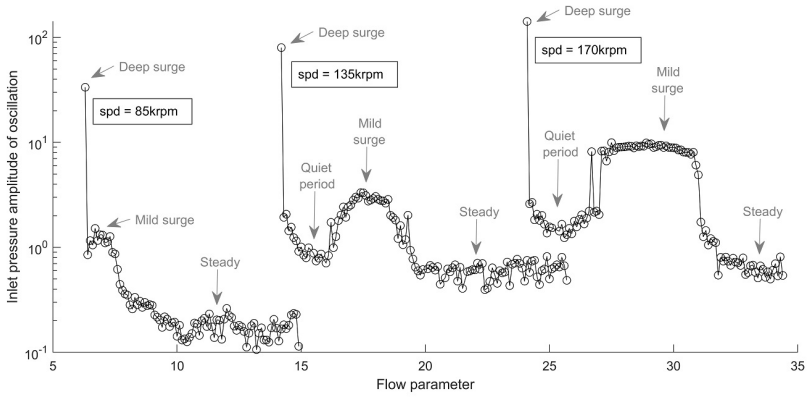

Figure 19: Experimental data showing the amplitude of inlet pressure oscillations decrease between incipient and deep surge, implying a quiet period exists.

6. Conclusions

We have further developed the first-principles model for a centrifugal compressor by Powers et al. [1, 2]. This new model is able to capture the dynamics of both incipient and deep surge, which is very important for engineers when designing and matching a compressor to an engine. This has been done by including both impeller inlet stall and diffuser recirculation. The interaction between these two phenomena results in a quintic-like compressor characteristic for high impeller speeds.

This is the first time any model has been able to capture both classes of surge, and thus, the first time an explanation for the existence of mild surge has be suggested. We have proposed that incipient surge is caused by the interaction between impeller inlet stall and diffuser recirculation.

The benefit of a first-principles model is that it can be used to predict the performance of a compressor solely on geometric data and a minimal number of parameters. In this paper, we have three parameters f, $\hat{a}$, and $\hat{b}$, that need universal relations to be found in order for this model to be fully predictive. This was out of scope for this project, but would be useful future work.

However, it is positive that we only need to calibrate three constants in order to get a good agreement to experimental results. The commonly used meanline modelling approach typically has multiple loss models and associated loss parameters that require fitting to data (for example, [19] has 9 loss models), which not only make the calibration process more difficult

but also reduces the models predictive ability as it has a higher dependence on experimental or CFD data.

We then developed a non-linear test-rig model in which we can use the compressor characteristics developed in this paper, and this was validated via experiments conducted at the University of Bath.

We have shown a great fit between simulation and data for incipient and deep surge oscillations, for all impeller speeds. We are able to capture a lot of the details in the experimental data signals for mass flow and pressure. There is some minor miss-match with frequency of $\pm$1Hz, but the oscillation frequency always remains in the correct order of magnitude.

At low impeller speeds, diffuser recirculation is not triggered and we return to the cubic-like shape of compressor characteristic commonly seen in literature. Since incipient surge is only simulated with the quintic-like shape, we do not simulate mild surge for the lower speeds. This agrees with the data, as incipient surge was only observed for high impeller rotational speeds.

We have shown the range of behaviours that can be simulated by our test rig model for the 155krpm speed line. We were able to capture resonance, incipient surge, transitions between mild and deep surge, deep surge, and the potential for a quiet period between incipient and deep surge.

Observing that our model can simulate both stable operation and deep surge for the same throttle setting, helps to explain the quietening phenomenon where a stable region is sometimes observed between incipient and deep surge operation. The behaviour of the mathematical model in this region depends on the initial conditions given to it, which explains why repeated experiments can result in observing different surge behaviour for this region.

This model has huge potential for helping centrifugal compressor manufacturers. The mathematical models have a great predictive ability and are able to capture the dynamics observed in and around surge to remarkable detail. Also, by extending the test-rig model to a model of an engine, it is possible to use the compressor characteristics to predict the on-engine performance of a compressor and the location of the surge limits for that pipework.

Furthermore, this is the first time incipient surge and the potential for a quiet periods have been predicted in a model. This has allowed us to propose explanations for the existence of such phenomena where one did not exist before.

Acknowledgements

Katherine Powers is supported by a scholarship from the EPSRC Centre for Doctoral Training in Statistical Applied Mathematics at Bath (SAMBa), under the project EP/L015684/1.

References

[1] K. H. Powers, C. J. Brace, C. J. Budd, C. D. Copeland, P. A. Milewski, Modeling axisymmetric centrifugal compressor characteristics from first principles, Journal of Turbomachinery 142 (9) (2020) 091010(11 pages).

[2] K. H. Powers, I. J. Kennedy, C. J. Brace, P. A. Milewski, C. D. Copeland, Development and validation of a model for centrifugal compressors in reversed flow regimes, in: ASME Turbo Expo 2020: Turbomachinery Technical Conference and Exposition, American Society of Mechanical Engineers Digital Collection, 2020.

[3] R. Stone, Introduction to internal combustion engines, 4th Edition, Palgrave MacMillan, 2012.

[4] N. Watson, M. S. Janota, Turbocharging: The internal combustion engine, MacMillan, 1982.

[5] D. A. Fink, Surge dynamics and unsteady flow in centrifugal compressors, Ph.D. thesis, Massachusetts Institute of Technology (1988).

[6] I. Day, Stall, surge, and 75 years of research, Journal of Turbomachinery 138 (1) (2016) 011001.

[7] M. C. Huppert, W. Benser, Some stall and surge phenomena in axial-flow compressors, Journal of the Aeronautical Sciences 20 (12) (1953) 835–845.

[8] H. Emmons, C. Pearson, H. Grant, Compressor surge and stall propagation, Trans. of the ASME 77 (4) (1955) 455–467.

[9] E. M. Greitzer, Surge and rotating stall in axial flow compressors - Part I: Theoretical compression system model, Journal of Engineering for Power 98 (2) (1976) 190–198.

[10] C. Hős, A. Champneys, L. Kullmann, Bifurcation analysis of surge and rotating stall in the Moore–Greitzer compression system, IMA Journal of Applied Mathematics 68 (2) (2003) 205–228.

[11] S. G. Koff, E. M. Greitzer, Stalled flow performance for axial compressors: I - Axisymmetric characteristic, in: 29th International Gas Turbine Conference and Exhibit, Vol. 1, American Society of Mechanical Engineers, 1984.

[12] F. K. Moore, E. M. Greitzer, A theory of post-stall transients in axial compression systems: Part I - Development of equations, Journal of Engineering for Gas Turbines and Power 108 (1) (1986) 68–76.

[13] J. Galindo, J. Serrano, H. Climent, A. Tiseira, Experiments and modelling of surge in small centrifugal compressor for automotive engines, Experimental Thermal and Fluid Science 32 (3) (2008) 818–826.

[14] R. L. Elder, M. E. Gill, A discussion of the factors affecting surge in centrifugal compressors, Journal of Engineering for Gas Turbines and Power 107 (1985) 499–506.

[15] G. Martin, V. Talon, P. Higelin, A. Charlet, C. Caillol, Implementing turbomachinery physics into data map-based turbocharger models, SAE International Journal of Engines 2 (1) (2009) 211–229.

[16] D. Japikse, Centrifugal compressor design and performance, Vol. 2, Concepts Eti White River Junction, VT, 1996.

[17] E. Sundström, M. Mihăescu, M. Giachi, E. Belardini, V. Michelassi, Analysis of vaneless diffuser stall instability in a centrifugal compressor, International Journal of Turbomachinery, Propulsion and Power 2 (4) (2017) 19.

[18] A. N. Abdelhamid, Analysis of rotating stall in vaneless diffusers of centrifugal compressors, in: ASME 1980 International Gas Turbine Conference and Products Show, ASME, 1980.

[19] H. W. Oh, E. S. Yoon, M. Chung, An optimum set of loss models for performance prediction of centrifugal compressors, Proceedings of the Institution of Mechanical Engineers, Part A: Journal of Power and Energy 211 (4) (1997) 331–338.

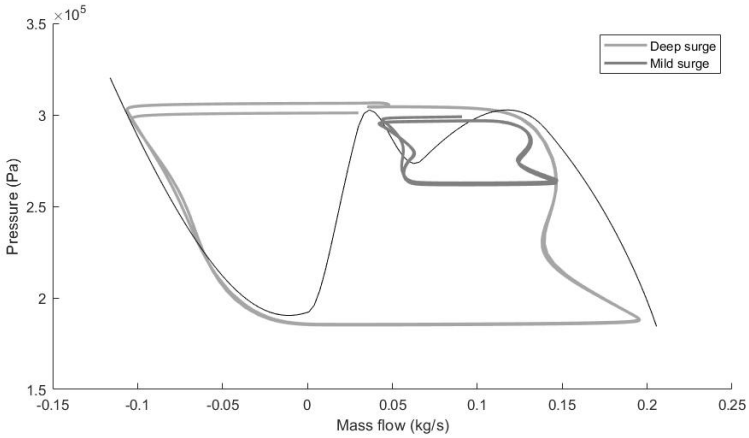

Figure 4-3: Mild and deep surge dynamics shown in the mass flow - pressure plane. They track different branches of the compressor characteristic, meaning a quintic-like shape is required for both behaviours to exist. This simulation was run with $N = 4$ discrete points.

4.4 Discussion of Paper 3

As can be seen in Fig. 7 of the paper, the inclusion of diffuser stall has resulted in a quintic-shaped characteristic for the higher impeller speeds. This is the first time this shape has been suggested for compressor characteristics. It is significant because it is the existence of multiple maxima that allow both mild and deep surge cycles to be simulated.

As can be seen in Fig. 4-3, mild surge cycles track the compressor characteristic around the first ($\dot{m} \neq 0$) local minimum, whereas deep surge cycles tack the characteristic around the minimum at $\dot{m} = 0$. Note that the trajectories do not follow the compressor characteristic as closely as seen in Paper 1 (see Section 2.5) because of the influence of the inlet pipe.

Unlike the model in Section 2.5, the surge lines do not coincide precisely with the maxima of the compressor characteristics (see Paper 3, Fig. 12). The mild surge line is relatively close to the first (or, for low impeller speeds, only) maxima of the characteristics, but deep surge cycles can be observed well before the $\dot{m} \neq 0$ local minimum. So the stability is dependent on something other than the sign of the compressor characteristic gradient.

However, there is a good agreement between the experimental and simulated surge lines, so our model shows a good predictive ability.

In the paper, the PDEs for the compression system (Eqs. 33 and 34) have an additional term to the ones we derived in Section 4.1. This is because, on programming Eqs. 4.1.1-4.1.2, we observed high-frequency growing oscillations that are often found in numerical solutions to PDEs. To remove these unphysical oscillations, we needed to incorporate some form of damping.

Therefore, we chose to include some viscous dissipation into the model. Recall from Section 2.1, that the fundamental equations of motion with stresses and viscous dissipation are

$$\frac{\partial \rho}{\partial t} + \nabla \cdot (\rho \mathbf{u}) = 0, \tag{4.4.1}$$

$$\frac{\partial}{\partial t}(\rho \mathbf{u}) + \nabla \cdot (\rho(\mathbf{u} \otimes \mathbf{u})) = -\nabla p + \nabla \cdot \tau, \tag{4.4.2}$$

$$\frac{\partial}{\partial t}(\rho E) + \nabla \cdot (\rho \mathbf{u} E + p\mathbf{u}) - \nabla \cdot (\tau \cdot \mathbf{u}) = 0. \tag{4.4.3}$$

Recall also that viscous dissipation can be decomposed into two parts

$$\nabla \cdot (\tau \cdot \mathbf{u}) = \mathbf{u} \cdot (\nabla \cdot \tau) - \tau : \nabla \mathbf{u}. \tag{4.4.4}$$

By assuming $\tau : \nabla \mathbf{u} = 0$ and just including dissipation in the form of the first term, we can retain the isentropic flow assumption.

To see this, notice that subtracting conservation of momentum dotted with $\mathbf{u}$ from the conservation of energy will cause the $\mathbf{u} \cdot (\nabla \cdot \tau)$ terms to cancel so we can follow the same procedure as in Section 2.2 (Eqs. 2.2.6 - 2.2.11) to obtain the isentropic relation $p = \kappa \rho^{\gamma}$.

When modelling the steady-state behaviour of the compressor, we have chosen to model $\nabla \cdot \tau$ as a friction term, F. Therefore, to be consistent with this approach, so we decided to include a viscous dissipation term of

$$\nabla \cdot (\tau \cdot \mathbf{u}) = \mathbf{u} \cdot (\nabla \cdot \tau) = \frac{f}{2} \rho |\mathbf{u}|^3 S, \tag{4.4.5}$$

which resulted in Eqs. 33 and 34 in the paper.

The simulation results of this PDE model with dissipation have a remarkable fit to the experimental data. This is especially true for simulating deep surge (Paper 3, Fig. 13) where we are able to capture the shapes of the mass flow, outlet pressure, and inlet pressure traces to considerable detail.

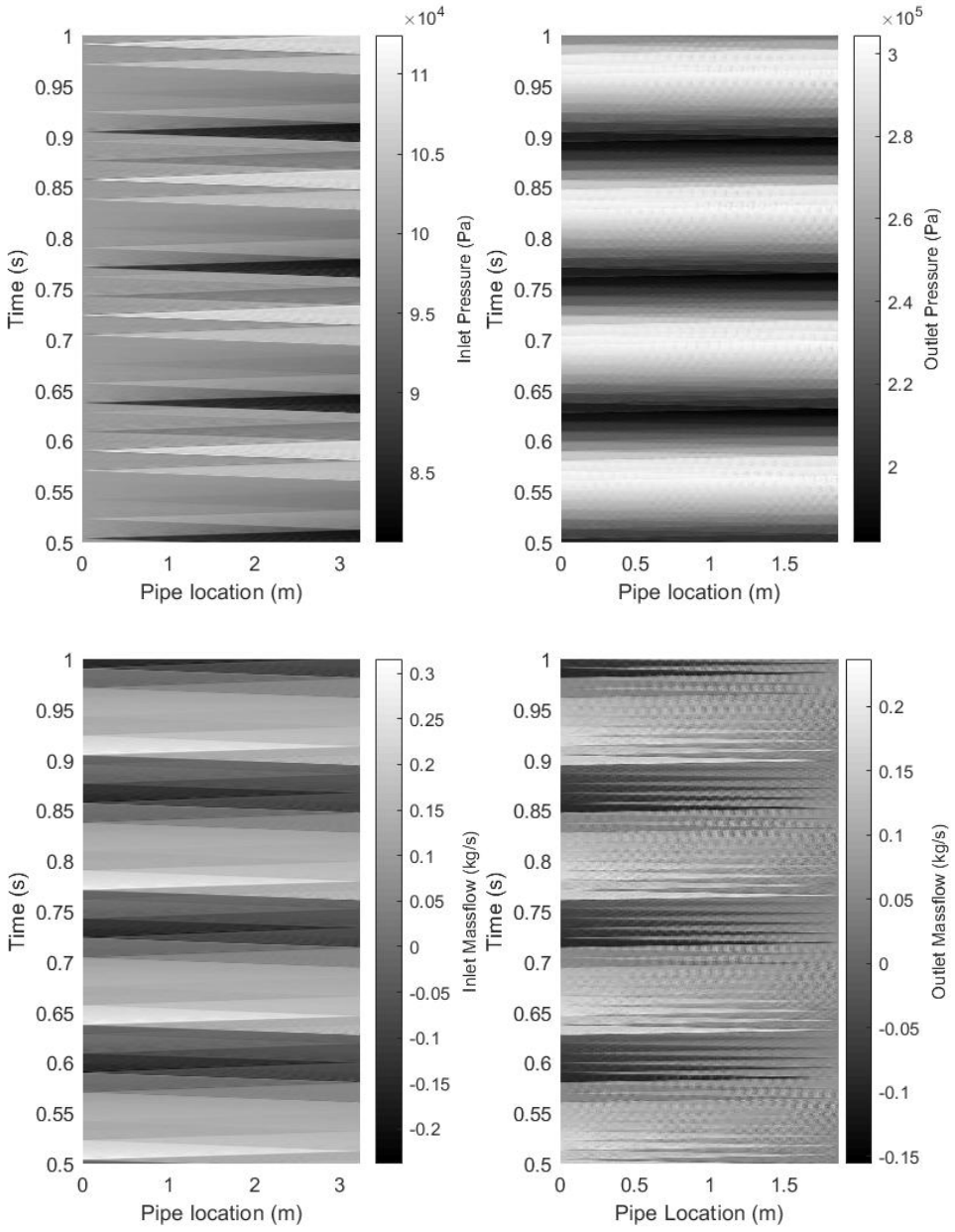

Figure 4-4: Pressure and mass flow dynamics with time at all locations within the inlet and outlet pipes.

Moreover, the advantage of having a model that has both a time and spacial dimension, is that we can capture the wave dynamics within the pipework. Figure 4-4, shows how the pressure and mass flow at all spatial locations within the pipework vary with time.

Here, we can see a series of triangles. These are waves travelling from one end of the pipe to the other at the speed of sound, a. We can see from this that the period of a surge oscillation is an integer multiple of the time it takes for these waves to travel, i.e. $\frac{L}{a}$, where L is the length of the pipe.

To try and understand the period (and hence frequency) of the simulated surge oscillations, consider the simple case where $N = 4$ and the system is a linearised, so

$$\frac{\partial \dot{m}_1}{\partial t} = \frac{A}{L_1}(p_{amb} - p_2), \tag{4.4.6}$$

$$\frac{\partial p_2}{\partial t} = \frac{a_1^2}{AL_1}(\dot{m}_1 - \dot{m}_3), \tag{4.4.7}$$

$$\frac{\partial \dot{m}_3}{\partial t} = \frac{A}{L_2}(p_c(\dot{m}_3) - p_4), \tag{4.4.8}$$

$$\frac{\partial p_4}{\partial t} = \frac{a_2^2}{AL_2}(\dot{m}_3 - \dot{m}_T(p_4)), \tag{4.4.9}$$

where a_1, a_2 are constant values for speed of sound for the inlet and outlet pipes depending on the average of p_2 and p_4 respectively.

As seen in Fig. 4-5(a), fast and slow dynamics are observed when plotting inlet mass flow against outlet pressure. The slow dynamics occur when the trajectory follows the compressor characteristic closely, and the fast dynamics occur when the trajectory switches from one branch of the compressor characteristic to another.

Thus, a reasonable approximation for the period of oscillation is the sum of the time taken for the slow dynamics (i.e. $T_\uparrow$ and $T_\downarrow$ in Fig. 4-5(b)). The slow dynamics occur when the change in mass flow is small and so Eqs. 4.4.7 and 4.4.9 dominate. Eliminating $\dot{m}_3$ in these gives:

$$\frac{d}{dt}\left(p_4 + \frac{a_2^2 L_1}{a_1^2 L_2} p_2\right) = \frac{a_2^2}{AL_2}(\dot{m}_1 - \dot{m}_T(p_4)). \tag{4.4.10}$$

We can get an approximation to $T_\uparrow$ by replacing the mass flow values with their average

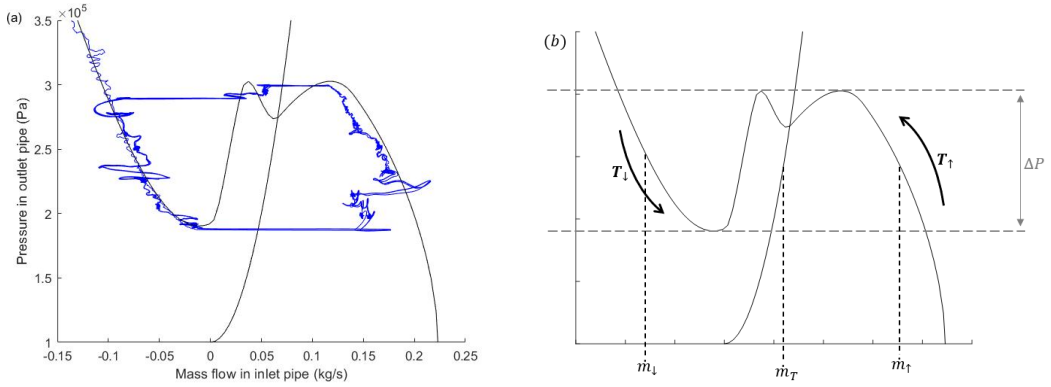

Figure 4-5: (a) Deep surge trajectory in the mass flow - pressure plane. The dynamics is very fast when moving between branches of the compressor characteristic. (b) Diagram used to find an approximation for the period of surge oscillation.

($\dot{m}_\uparrow$ and $\dot{m}_T$ in Fig. 4-5(b)), and approximating the derivative. This gives

$$\frac{\Delta P + \frac{a_2^2 L_1}{a_1^2 L_2}\Delta P_{in}}{T_\uparrow} \approx \frac{a_2^2}{AL_2}(\dot{m}_\uparrow - \dot{m}_T), \tag{4.4.11}$$

and so, on rearranging for $T_\uparrow$, we have

$$T_\uparrow \approx \left(\frac{AL_2\Delta P}{a_2^2} + \frac{AL_1\Delta P_{in}}{a_1^2}\right)\frac{1}{\dot{m}_\uparrow - \dot{m}_T} \tag{4.4.12}$$

where ΔP is the change in outlet pressure shown in Fig. 4-5(b), and ΔP_{in} is the change in inlet pressure. This is typically a lot smaller than ΔP (e.g. Fig. 4-4 shows us $\Delta P \approx 1$bar and $\Delta P_{in} \approx 0.4$bar), but will still impact the period of oscillation.

Similarly, for $T_\downarrow$ we have

$$T_\downarrow \approx -\left(\frac{AL_2\Delta P}{a_2^2} + \frac{AL_1\Delta P_{in}}{a_1^2}\right)\frac{1}{\dot{m}_\downarrow - \dot{m}_T}. \tag{4.4.13}$$

Therefore, combining these for the period $T \approx T_\uparrow + T_\downarrow$ results in

$$T \approx \frac{(\dot{m}_\uparrow - \dot{m}_\downarrow)}{(\dot{m}_\uparrow - \dot{m}_T)(\dot{m}_T - \dot{m}_\downarrow)}\left(\frac{A\Delta P}{a_2}\frac{L_2}{a_2} + \frac{A\Delta P_{in}}{a_1}\frac{L_1}{a_1}\right). \tag{4.4.14}$$

Notice that $\frac{L_1}{a_1}$ and $\frac{L_2}{a_2}$ are the lengths of time it takes for information to travel down the inlet and outlet pipes respectively. Therefore, the true period is likely to be an integer linear combination of these that is the close to the above approximation.

Furthermore, assuming there is no inlet pipe (and hence $\Delta P_{in} = 0$) will result in a smaller period (higher frequency). So the inlet pipework actually lowers the observed frequency of oscillation, and explains why models without the inlet pipework can struggle to match the observed surge dynamics.

This relation also tells us that the larger the surge amplitude, both in pressure, ΔP, and mass flow, $\Delta\dot{m} = \dot{m}_{\uparrow} - \dot{m}_{\downarrow}$, results in a longer period (as hence lower frequency). This agrees with the observation of mild surge having a higher frequency than deep surge.

Also, this relation tells us that an increase in pipe cross-sectional area, or length, will result in a longer period (lower frequency). This agrees with what we saw in Section 2.5.

Finally, notice that we can approximate the change dynamic pressure $\frac{1}{2}\Delta(\rho u^2)$ by

$$\frac{1}{2}\Delta(\rho u)\bar{u} = \frac{1}{2}\frac{\Delta\dot{m}}{A}\bar{u}, \tag{4.4.15}$$

where $\bar{u}$ is the average velocity in the pipe. Therefore, we could write the period as

$$T \approx \frac{1}{2\overline{\Delta\dot{m}_T}^2}\left(\frac{1}{\mathrm{Ma}_2}\frac{\Delta P}{\frac{1}{2}\Delta(\rho u^2)}\frac{L_2}{a_2} + \frac{1}{\mathrm{Ma}_1}\frac{\Delta P_{in}}{\frac{1}{2}\Delta(\rho u_{in}^2)}\frac{L_1}{a_1}\right) \tag{4.4.16}$$

where

$$\overline{\Delta\dot{m}_T} = \sqrt{\left(\frac{\dot{m}_{\uparrow} - \dot{m}_T}{\dot{m}_{\uparrow} - \dot{m}_{\downarrow}}\right)\left(\frac{\dot{m}_T - \dot{m}_{\downarrow}}{\dot{m}_{\uparrow} - \dot{m}_{\downarrow}}\right)} \tag{4.4.17}$$

is the geometric mean of the distance between $\dot{m}_{\uparrow}$, $\dot{m}_{\downarrow}$ and the throttle mass flow. Therefore, we can expect the period of oscillation to be impacted by the throttle setting, the Mach number in both pipes, and the ratio of static to dynamic pressure in each pipe.

These approximations show us that the frequency of observed compressor surge is a complex process that is influenced by many variables. Therefore, it is not surprising that our model cannot always accurately predict the frequency of oscillation observed in experimental measurements of surge.

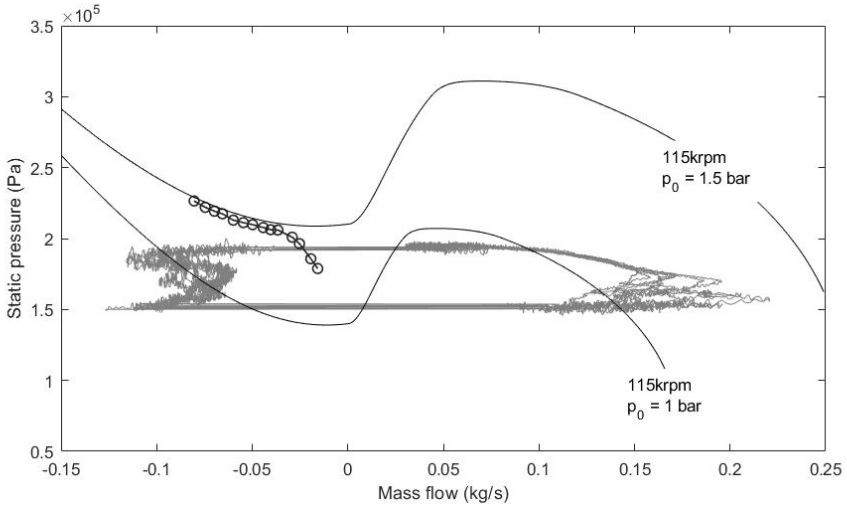

Figure 4-6: Reverse flow test data (black circles) shown with simulated compressor characteristic with inlet pressure (p_0) of 1.5bar. Also, surge test data (grey) shown with characteristic with inlet pressure 1bar. All experimental data was collected for impeller speed of 115krpm.

4.4.1 Return to Reverse Flow

The compressor tested in this paper is the same as that used for the reverse flow tests in Paper 2 (see Section 3.2). Figure 4-6 shows the resulting experimental deep surge cycle alongside the reverse flow test for the impeller speed of 115krpm.

Since the data and our simulated mass flows were closely aligned, we used the sign of our simulated mass flow to distinguish between forward flowing and backward flowing air in the data.

Recall that, during the reverse flow tests, compressed air was being fed into the compressor outlet. Therefore, in this experiment, the air exiting the impeller inlet was compressed air and only dispersed to ambient pressure once it exited the compressor inlet pipe. Therefore, the compressor inlet pressure for the reverse-flow tests was higher than ambient.

Here we can see that the surge cycle appears to track the compressor characteristic, and so does not track the asymptotic branch of the reverse flow test. Thus, the behaviour as proposed in Paper 2, Fig. 11 appears unlikely.

This behaviour supports the assumption made in Section 3.2, and in this chapter, that

we have a continuous compressor characteristic. It also suggests that the asymptotic behaviour seen in the reversed flow tests is likely to be linked to the behaviour of the system as a whole. For example, as seen in Fig. 3-5, the throttle characteristic has a very steep gradient, and so the behaviour could be explained if the system switches from following the compressor characteristic to following the throttle characteristic for small negative mass flows.

4.5 Conclusions

In this chapter we have further developed the steady-state compressor characteristic so that it includes diffuser recirculation. This has resulted in a quintic-shaped characteristic that has the ability to capture both mild and deep surge.

We also used the PDE form of the reduced order surge model created in Section 2.2 and solved this over a staggered grid. The staggered grid formulation provided us with a simple way to transform between the PDEs and the ODE system used in the previous two chapters.

We get excellent agreement to experimental data for mass flow and pressure traces at a variety of different impeller speeds. We have some difficulty in accurately predicting the correct frequency of oscillation. However, after a more detailed look into what affects the period of a surge oscillation, it is clear that this is sensitive to many factors and so it is unsurprising that a simple reduced model would have difficulty capturing this.

We also see a good ability of the model to predict the onset of both mild and deep surge. This implies that our reduced order model now contains the most important dynamics to simulate this physical phenomena.

We have seen that the addition of inlet pipework has some interesting effects on the simulated dynamics. Figure 4-3 shows us that the trajectories do not follow the compressor characteristic as closely when the inlet pipe is modelled. The inlet pipe also reduces the simulated frequency of oscillation.

Another thing to note is that, while exploring the effect inlet pressure has on the compressor characteristics, the following relation was discovered:

$$p_{M+1} = p_c\left(\left[\frac{p_{amb}}{p_M}\right]\dot{m}_{M+1}, p_{amb}\right)\frac{p_M}{p_{amb}}. \tag{4.5.1}$$

Since this was discovered by simulation, mathematical investigation is needed to validate this result. However, this result is interesting because it means that the compressor characteristic ODEs only need to be computed using ambient inlet pressure. This would help with computational efficiency of the PDE model presented in the paper, as the compressor characteristic ODEs need not been solved each time the p_c boundary condition is implemented.

Finally, we compared the results from the surge tests conducted in this Section 4.3 to the reverse flow test in Section 3.2. Since the surge results have such a good fit while using a continuous characteristic, it appears likely that the deviation of the reverse flow tests from the characteristic is related to a system level phenomenon, rather than the shape of the characteristic itself.

Now we have developed a model which captures the dynamics of surge with good results, we can start to dig deeper into the mathematical properties of the model itself. In particular, looking into conditions for the switch of stability is vital information when trying to predict the location of surge limits.

Chapter 5

Stability Analysis of Surge Model

In all three papers (Sections 2.5, 3.2 and 4.3) we have observed that the stability of the system appears to be dependent on the gradient of the compressor characteristic. In particular, when the gradient of the compressor characteristic is negative, the system appears to always be stable.

In order to understand this dependence further, we can perform more formal stability analysis on our surge model.

5.1 Selected Model for Analysis

We wish to analyse a system which captures the main dynamics of surge, but is simple enough that the analytical calculations are manageable. Therefore, we shall return to the ODE model developed in Section 2.2:

$$\frac{d\dot{m}}{dt} = \frac{A}{L}(p_c(\dot{m}) - p) + \frac{\kappa^{\frac{1}{\gamma}}}{AL}\left(\frac{\dot{m}^2}{p_c(\dot{m})^{\frac{1}{\gamma}}} - \frac{\dot{m}_T(p)^2}{p^{\frac{1}{\gamma}}}\right) \equiv f(\dot{m}, p), \tag{5.1.1}$$

$$\frac{dp}{dt} = \frac{\gamma\kappa^{\frac{1}{\gamma}}}{AL}p^{\frac{\gamma-1}{\gamma}}(\dot{m} - \dot{m}_T(p)) \equiv g(\dot{m}, p). \tag{5.1.2}$$

The results from analysing this model will still be applicable to the PDE model in Section 4.1 since this is the case where $N = 2$ and we have no inlet pipe.

As noted in Section 4.4, the inlet pipe does influence the behaviour of the system, and

is therefore likely to have some influence on the system stability. However, surge is still observed in the case with no inlet pipe and so we should be able to identify the key variables which control the onset of surge instabilities without including this in the stability analysis.

For the compressor characteristic, we shall use the model developed in Section 4.3 as this will enable us to understand both mild surge and deep surge stability.

For the throttle characteristic, we shall use an incompressible version of that developed in Section 2.3, i.e.

$$\dot{m}_T = \text{sgn}(p - p_{amb})\sqrt{\frac{2\gamma}{\gamma - 1}A^2\rho_{amb}\frac{\mu^2}{1-\mu^2}|p - p_{amb}|}, \tag{5.1.3}$$

to make analytical computations involving this simpler. For our analysis, we shall only consider $p > p_{amb}$ as this means the compressor is functioning as expected and generating pressure within the pipework. Therefore this can be written as

$$\dot{m}_T = (\sigma f(\mu)(p - p_{amb}))^{\frac{1}{2}} \tag{5.1.4}$$

for a constant

$$\sigma = \frac{2\gamma}{\gamma - 1}A^2\rho_{amb}, \tag{5.1.5}$$

and function

$$f(\mu) = \frac{\mu^2}{1-\mu^2}, \tag{5.1.6}$$

where μ is the throttle parameter.

We have observed that by closing the throttle, we can see a switch of stability that corresponds to the onset of surge. Therefore, we wish to understand how our system changes with the behaviour of the parameter μ.

Let $\mathbf{x} = (\dot{m}, p)^T$ and $\mathbf{F}(\cdot) = (f(\cdot), g(\cdot))^T$. Then our system can be written as $\dot{\mathbf{x}} = \mathbf{F}(\mathbf{x})$ where $\dot{\mathbf{x}}$ denotes differentiation with respect to t.

5.2 Equilibrium Points

The first step in stability analysis is finding the equilibrium (or stationary) points of the system. These are points which remain unchanged by the differential equations, so

if the system was given an initial condition of an equilibrium point, it would remain there for all time.

Let $\mathbf{x}^*$ be an equilibrium point. Then $\dot{\mathbf{x}}^* = \mathbf{F}(\mathbf{x}^*) = 0$, which implies $f(\dot{m}^*, p^*) = g(\dot{m}^*, p^*) = 0$.

For our system, if $g(\dot{m}, p) = 0$ then either $p = 0$ or $\dot{m} = \dot{m}_T(p)$.

Now, $p = 0$ is outside our domain of interest as $p_{amb} > 0$. However, there is no equilibrium point here as $f \to \infty$ as $p \to 0$ because, from Eq. 5.1.4, we have

$$\frac{\dot{m}_T^2}{p^{\frac{1}{\gamma}}} = \sigma f(\mu) \left(p^{\frac{\gamma-1}{\gamma}} - \frac{p_{amb}}{p^{\frac{1}{\gamma}}} \right) \to -\infty \tag{5.2.1}$$

as $p \to 0$.

If $\dot{m} = \dot{m}_T(p)$, then $f(\dot{m}, p) = 0$ when

$$\frac{A}{L}(p_c(\dot{m}) - p) + \frac{\dot{m}^2 \kappa^{\frac{1}{\gamma}}}{AL} \left(\frac{1}{p_c(\dot{m})^{\frac{1}{\gamma}}} - \frac{1}{p^{\frac{1}{\gamma}}} \right) = 0, \tag{5.2.2}$$

which is true when $p = p_c(\dot{m})$.

Therefore, the system has an equilibrium point at $(\dot{m}^*, p^*)$ where $\dot{m}^* = \dot{m}_T(p^*)$ and $p^* = p_c(\dot{m}^*)$.

As seen in previous chapters, the intersection between the compressor characteristic and the throttle characteristic is the operating point of the compression system. Therefore, this tells us the operating point is an equilibrium point. This makes sense because when the system is stable it tends to the operating point, and once there it remains there for all time.

The next step is therefore to determine when this equilibrium is stable, which would mean the compression system operates in a stable manner.

5.3 Linear Stability Analysis

To determine the stability of an equilibrium point, we want to study the behaviour of nearby points, i.e. $\mathbf{x} = \mathbf{x}^* + \mathbf{y}$ for small $\mathbf{y}$. Differentiating gives $\dot{\mathbf{x}} = \dot{\mathbf{y}}$ and

$$\dot{\mathbf{x}} = \mathbf{F}(\mathbf{x}^* + \mathbf{y}) = \cancelto{0}{\mathbf{F}(\mathbf{x}^*)} + D\mathbf{F}(\mathbf{x}^*)\mathbf{y} + \mathcal{O}(|\mathbf{y}|^2) \tag{5.3.1}$$

by Taylor expanding around $\mathbf{x}^*$, where the matrix of partial derivatives, $D\mathbf{F}$, is termed the Jacobian [60]. Therefore, studying the linear system

$$\dot{\mathbf{y}} = D\mathbf{F}(\mathbf{x}^*)\mathbf{y} \tag{5.3.2}$$

will give us a reasonable idea of the behaviour of $\mathbf{y} = \mathbf{x} - \mathbf{x}^*$ [60].

In the case of a non-singular Jacobian, the solution of Eq. 5.3.2 is

$$\mathbf{y}(t) = \sum_{i=1}^{n} \mathbf{y}_i e^{\lambda_i t}, \tag{5.3.3}$$

where $(\lambda_i, \mathbf{y}_i)$ are eigenvalue - eigenvector pairs of the system. This tells us that, in the direction of eigenvector $\mathbf{y}_i$, the solution is either growing or shrinking exponentially dependent on the sign of λ_i [61]. Therefore:

- If all eigenvalues have negative real part, $\mathbf{y} \to 0$, and so $\mathbf{x} \to \mathbf{x}^*$ and the equilibrium point is stable.

- If all eigenvalues have positive real part, $\mathbf{y} \to \infty$, so $\mathbf{x}$ grows away from $\mathbf{x}^*$ and the equilibrium point is unstable.

- If we have a mix of positive and negative real parts, $\mathbf{y}$ will shrink exponentially in some directions and grow exponentially in others. This is called a saddle point, and the equilibrium point is unstable.

Moreover, if the eigenvalue has a non-zero imaginary part, the behaviour is oscillatory in nature [61]. So we will have growing or shrinking spiral behaviour.

5.3.1 Computing the Jacobian

For our case, denote the Jacobian by J, then

$$J^* = \left(\begin{array}{cc} \frac{\partial f}{\partial \dot{m}} & \frac{\partial f}{\partial p} \\ \frac{\partial g}{\partial \dot{m}} & \frac{\partial g}{\partial p} \end{array} \right) \Bigg|_{(\dot{m}^*, p^*)}. \tag{5.3.4}$$

Differentiating Eqs. 5.1.1 and 5.1.2 gives

$$\frac{\partial f}{\partial \dot{m}} = \frac{A}{L}\frac{dp_c}{d\dot{m}} + \frac{\kappa^{\frac{1}{\gamma}}}{AL}\left(\frac{2\dot{m}}{p_c(\dot{m})^{\frac{1}{\gamma}}} - \frac{\dot{m}^2}{\gamma p_c(\dot{m})^{\frac{\gamma+1}{\gamma}}}\frac{dp_c}{d\dot{m}} \right), \tag{5.3.5}$$

$$\frac{\partial f}{\partial p} = -\frac{A}{L} - \frac{\kappa^{\frac{1}{\gamma}}}{AL}\left(\frac{2\dot{m}_T(p)}{p^{\frac{1}{\gamma}}}\frac{d\dot{m}_T}{dp} + \frac{\dot{m}_T(p)^2}{\gamma p^{\frac{\gamma+1}{\gamma}}} \right), \tag{5.3.6}$$

$$\frac{\partial g}{\partial \dot{m}} = \frac{\gamma\kappa^{\frac{1}{\gamma}}}{AL} p^{\frac{\gamma-1}{\gamma}}, \tag{5.3.7}$$

$$\frac{\partial g}{\partial p} = \frac{\gamma\kappa^{\frac{1}{\gamma}}}{AL}\left(\frac{\gamma-1}{\gamma}\frac{(\dot{m} - \dot{m}_T(p))}{p^{\frac{1}{\gamma}}} - p^{\frac{\gamma-1}{\gamma}}\frac{d\dot{m}_T}{dp} \right), \tag{5.3.8}$$

so evaluating at $(\dot{m}^*, p^*)$ results in

$$\left(\frac{\partial f}{\partial \dot{m}}\right)^* = \left(\frac{A}{L} - \frac{\kappa^{\frac{1}{\gamma}}}{\gamma AL}\frac{\dot{m}^{*2}}{p^{*\frac{\gamma+1}{\gamma}}} \right)\frac{dp_c}{d\dot{m}}(\dot{m}^*) + \frac{2\kappa^{\frac{1}{\gamma}}}{AL}\frac{\dot{m}^*}{p^{*\frac{1}{\gamma}}}, \tag{5.3.9}$$

$$\left(\frac{\partial f}{\partial p}\right)^* = -\frac{2\kappa^{\frac{1}{\gamma}}}{AL}\frac{\dot{m}^*}{p^{*\frac{1}{\gamma}}}\frac{d\dot{m}_T}{dp}(p^*) - \left(\frac{A}{L} - \frac{\kappa^{\frac{1}{\gamma}}}{\gamma AL}\frac{\dot{m}^{*2}}{p^{*\frac{\gamma+1}{\gamma}}} \right), \tag{5.3.10}$$

$$\left(\frac{\partial g}{\partial \dot{m}}\right)^* = \frac{\gamma\kappa^{\frac{1}{\gamma}}}{AL} p^{*\frac{\gamma-1}{\gamma}}, \tag{5.3.11}$$

$$\left(\frac{\partial g}{\partial p}\right)^* = -\frac{\gamma\kappa^{\frac{1}{\gamma}}}{AL} p^{*\frac{\gamma-1}{\gamma}}\frac{d\dot{m}_T}{dp}(p^*). \tag{5.3.12}$$

In Section 2.2, we determined that the system was isentropic so $p = \kappa\rho^\gamma$ (see Eq. 2.2.37). We can also write $a^2 = \frac{\gamma p}{\rho}$ due to Eq. 2.2.47, and $u = \frac{\dot{m}}{A\rho}$ by definition of mass flow rate. Therefore, the above can be simplified to get

$$\left(\frac{\partial f}{\partial \dot{m}}\right)^* = \frac{A}{L}\left(1 - \frac{u^{*2}}{a^{*2}} \right)\frac{dp_c}{d\dot{m}}(\dot{m}^*) + \frac{2u^*}{L}, \tag{5.3.13}$$

$$\left(\frac{\partial f}{\partial p}\right)^* = -\frac{2u^*}{L}\frac{d\dot{m}_T}{dp}(p^*) - \frac{A}{L}\left(1 - \frac{u^{*2}}{a^{*2}}\right), \tag{5.3.14}$$

$$\left(\frac{\partial g}{\partial \dot{m}}\right)^* = \frac{a^{*2}}{AL}, \tag{5.3.15}$$

$$\left(\frac{\partial g}{\partial p}\right)^* = -\frac{a^{*2}}{AL}\frac{d\dot{m}_T}{dp}(p^*). \tag{5.3.16}$$

5.3.2 Determinant-Trace Argument

Since this is a 2D system, we can use the determinant and trace of J^* to give us stability criteria. Consider the matrix

$$A = \begin{pmatrix} a & b \\ c & d \end{pmatrix}. \tag{5.3.17}$$

The eigenvalues are solutions of the characteristic polynomial

$$0 = \det(A - \lambda I) = \begin{vmatrix} a-\lambda & b \\ c & d-\lambda \end{vmatrix} = \lambda^2 - (\mathrm{tr}A)\lambda + \det A, \tag{5.3.18}$$

where $\mathrm{tr}A = a + d$ and $\det A = ad - bc$, are the trace and determinant, respectively.

Let λ_1 and λ_2 be the eigenvalues, then

$$\lambda_{1,2} = \frac{\mathrm{tr}A \pm \sqrt{\mathrm{tr}A^2 - 4\det A}}{2}. \tag{5.3.19}$$

We can also get from this that $\lambda_1 + \lambda_2 = \mathrm{tr}A$ and $\lambda_1\lambda_2 = \det A$ [61].

From this we know:

- $\det A < 0$ means the eigenvalues have opposite signs and we have a saddle.
- $\det A > 0$ and $\mathrm{tr}A < 0$ means the eigenvalues have negative real part and we have stability.
- $\det A > 0$ and $\mathrm{tr}A > 0$ means the eigenvalues have positive real part and the system is unstable.
- $4\det A > \mathrm{tr}A^2$ means we have complex eigenvalues and observe either stable or unstable oscillatory behaviour.

This is summarised in Fig. 5-1.

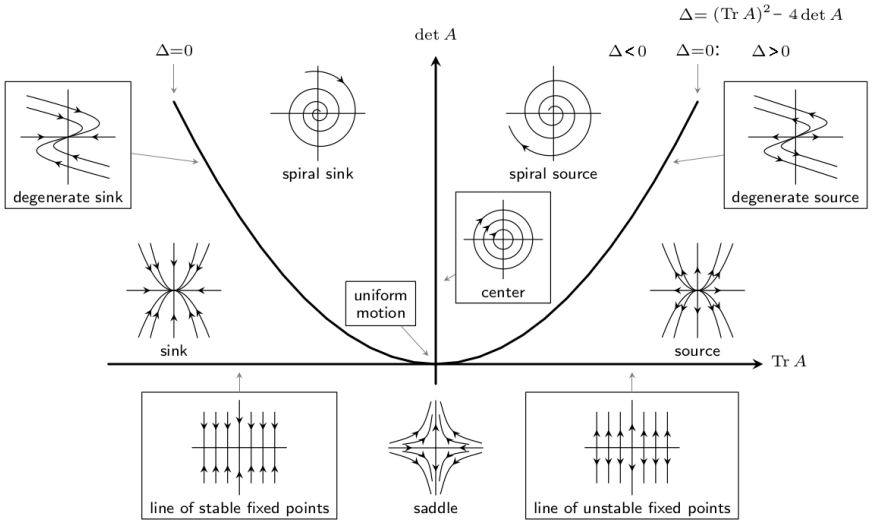

Figure 5-1: Stability of an equilibrium point in the det$A$ - tr$A$ plane, where A is the corresponding Jacobian [62].

For our Jacobian, the determinant is given by

$$\det J^* = \frac{1}{L^2}(a^{*2} - u^{*2})\left(1 - \frac{dp_c}{d\dot{m}}(\dot{m}^*)\frac{d\dot{m}_T}{dp}(p^*)\right), \tag{5.3.20}$$

and the trace is

$$\mathrm{tr} J^* = \frac{A}{L}\left(1 - \frac{u^{*2}}{a^{*2}}\right)\frac{dp_c}{d\dot{m}}(\dot{m}^*) + \frac{2u^*}{L} - \frac{a^{*2}}{AL}\frac{d\dot{m}_T}{dp}(p^*). \tag{5.3.21}$$

We can see from this that the gradient of both the compressor and throttle characteristic will play an important role in the stability of the system. Therefore, we will now look for relations in terms of the gradient of the compressor characteristic, $\frac{dp_c}{d\dot{m}}$, and the gradient of the throttle characteristic,

$$\frac{dp_T}{d\dot{m}} = \left(\frac{d\dot{m}_T}{dp}\right)^{-1}, \tag{5.3.22}$$

with the mass flow as the dependent variable. This is because we usually plot characteristics with mass flow on the x-axis and pressure on the y-axis, so the gradients are easier to understand in this form.

Suppose we have subsonic flow (i.e. $u^* < a^*$), then we have stable behaviour when

$\det J^* > 0$ and $\mathrm{tr} J^* < 0$, which means

$$\frac{dp_T}{d\dot{m}}(\dot{m}^*) > \frac{dp_c}{d\dot{m}}(\dot{m}^*) \tag{5.3.23}$$

and

$$\frac{dp_T}{d\dot{m}}(\dot{m}^*) < \frac{a^{*2}}{A^2\left(1-\frac{u^{*2}}{a^{*2}}\right)\frac{dp_c}{d\dot{m}}(\dot{m}^*) + 2Au^*} \tag{5.3.24}$$

respectively.

Similarly, for supersonic flow, stable behaviour occurs if

$$\frac{dp_T}{d\dot{m}}(\dot{m}^*) < \frac{dp_c}{d\dot{m}}(\dot{m}^*) \tag{5.3.25}$$

and

$$\frac{dp_T}{d\dot{m}}(\dot{m}^*) < \frac{a^{*2}}{2Au^* - A^2\left(\frac{u^{*2}}{a^{*2}}-1\right)\frac{dp_c}{d\dot{m}}(\dot{m}^*)}. \tag{5.3.26}$$

Finally, we can classify the behaviour as a stable focus if, in addition, $4\det J^* > (\mathrm{tr} J^*)^2$ holds.

Using the fact that $(a+b)^2 = (a-b)^2 + 4ab$, we can write

$$(\mathrm{tr} J^*)^2 = \left(\frac{A}{L}\left(1-\frac{u^{*2}}{a^{*2}}\right)\frac{dp_c}{d\dot{m}} - \left[\frac{2u^*}{L} - \frac{a^{*2}}{AL}\frac{d\dot{m}_T}{dp}\right]\right)^2 + \frac{4}{L^2}(a^{*2}-u^{*2})\left[\frac{2Au^*}{a^{*2}}\frac{dp_c}{d\dot{m}} - \frac{dp_c}{d\dot{m}}\frac{d\dot{m}_T}{dp}\right]. \tag{5.3.27}$$

Therefore, $4\det J^* > (\mathrm{tr} J^*)^2$ can be written as

$$\frac{4}{L^2}(a^{*2}-u^{*2})\left(1-\frac{2Au^*}{a^{*2}}\frac{dp_c}{d\dot{m}}\right) > \left(\frac{A}{L}\left(1-\frac{u^{*2}}{a^{*2}}\right)\frac{dp_c}{d\dot{m}} - \frac{2u^*}{L} + \frac{a^{*2}}{AL}\frac{d\dot{m}_T}{dp}\right)^2. \tag{5.3.28}$$

Taking square-roots gives us that either of the following hold:

$$\frac{A}{L}\left(1-\frac{u^{*2}}{a^{*2}}\right)\frac{dp_c}{d\dot{m}} - \frac{2u^*}{L} + \frac{a^{*2}}{AL}\frac{d\dot{m}_T}{dp} > -\sqrt{\frac{4}{L^2}(a^{*2}-u^{*2})\left(1-\frac{2Au^*}{a^{*2}}\frac{dp_c}{d\dot{m}}\right)} \tag{5.3.29}$$

$$\frac{A}{L}\left(1-\frac{u^{*2}}{a^{*2}}\right)\frac{dp_c}{d\dot{m}} - \frac{2u^*}{L} + \frac{a^{*2}}{AL}\frac{d\dot{m}_T}{dp} < \sqrt{\frac{4}{L^2}(a^{*2}-u^{*2})\left(1-\frac{2Au^*}{a^{*2}}\frac{dp_c}{d\dot{m}}\right)}. \tag{5.3.30}$$

Therefore, on rearranging for the throttle gradient, we have either of

$$\frac{dp_T}{d\dot{m}}(\dot{m}^*) > \frac{a^{*2}}{2Au^* - A^2\left(1-\frac{u^{*2}}{a^{*2}}\right)\frac{dp_c}{d\dot{m}} + 2A\sqrt{(a^{*2}-u^{*2})\left(1-\frac{2Au^*}{a^{*2}}\frac{dp_c}{d\dot{m}}\right)}}, \tag{5.3.31}$$

$$\frac{dp_T}{d\dot{m}}(\dot{m}^*) < \frac{a^{*2}}{2Au^* - A^2\left(1-\frac{u^{*2}}{a^{*2}}\right)\frac{dp_c}{d\dot{m}} - 2A\sqrt{(a^{*2}-u^{*2})\left(1-\frac{2Au^*}{a^{*2}}\frac{dp_c}{d\dot{m}}\right)}}, \tag{5.3.32}$$

hold if we observe a focus.

5.3.3 Results

All of the stability criteria depends on three things: (i) the gradient of the throttle characteristic, (ii) the gradient of the compressor characteristic, and (iii) the velocity of the flow in comparison to the speed of sound.

Figure 5-2 shows how the stability of the system depends on the gradient of the characteristics. The plots were constructed assuming u^* and a^* were constant, but the cases of subsonic and supersonic flow are considered separately.

For subsonic regimes, a negative gradient of the compressor characteristic is almost always stable, and surge (unstable focus/node) occurs mostly in the positive gradient region. This is why in Section 2.5 we observed that the switch of stability coincided with the maximum of the compressor characteristic.

However, our analysis also tells us that, for shallow throttle characteristic gradients, the switch of stability will occur after the maxima. At higher impeller speeds, the surge limit occurs at a higher positive mass flow value. Therefore, the gradient of the throttle characteristic intersecting this point will be shallower than those at lower speeds. This means we expect surge to occur after the maxima for higher speeds.

Moreover, our analysis tells us the opposite also holds true, i.e. that at lower impeller speeds the onset of surge can be observed before the maximum of the compressor characteristic.

For supersonic regimes, we can see that the system is only stable if the compressor characteristic has a positive gradient. We are only likely to see supersonic flows in the compression system if we are operating the compressor in choke (i.e. sonic flows are occurring within the compressor). However, the gradient of the compressor character-

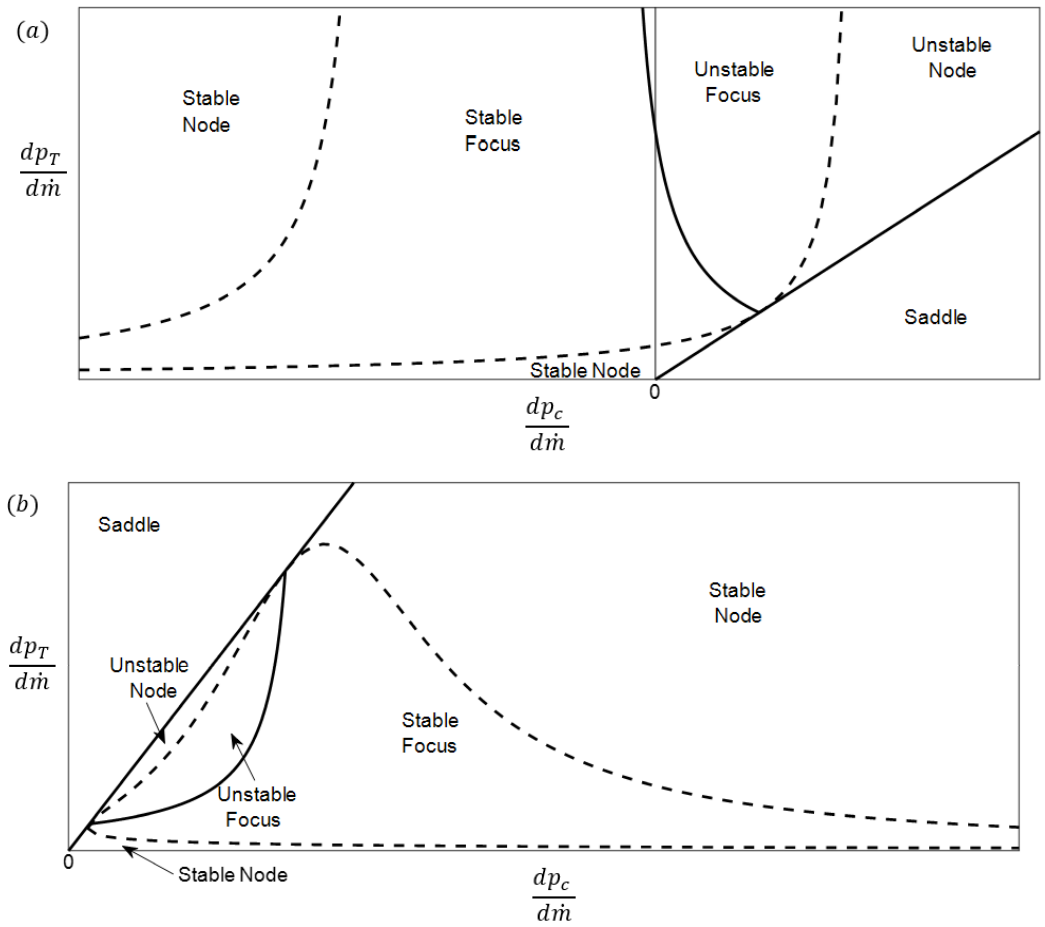

Figure 5-2: Stability analysis as the gradient of throttle and compressor characteristics vary, for constant u^*, a^* values. (a) shows the subsonic case ($u^* < a^*$), and (b) the supersonic case ($u^* > a^*$).

istic tends to negative infinity when operating in choke (see Fig. 1-6 and Fig. 4-5, for example). Therefore, we would observe a saddle.

5.4 Hopf Bifurcation

In Fig. 5-2, we can see that the stability of the system switches from stable to unstable through the $\mathrm{tr}J^* = 0$ line. When the system is unstable, we observe surge and so we expect stable limit cycles to be present in this region.

One way in which limit cycles appear in the system is through a Hopf bifurcation. This is when an equilibrium point switches its stability at the point where a periodic solution comes into existence. There is a theorem that can be used to prove the existence of Hopf bifurcations (see, e.g. [63]).

Theorem 5.1. *Hopf Bifurcation Theorem*
Consider the planar system $\dot{\mathbf{x}} = \mathbf{F}_\mu(\mathbf{x})$, written in component form as

$$\begin{aligned} \dot{x} &= f_\mu(x, y), \\ \dot{y} &= g_\mu(x, y), \end{aligned}$$

where μ is a parameter. Suppose $\exists \mathbf{x}^*$ such that $\mathbf{F}(\mathbf{x}^*) = 0$ and denote the eigenvalues of the Jacobian $D\mathbf{F}_\mu(\mathbf{x}^*)$ by

$$\lambda_\pm = \alpha(\mu) \pm i\beta(\mu).$$

Suppose further that $\exists \mu^*$ such that

1. *Non-hyperbolicity condition: $\alpha(\mu^*) = 0, \beta(\mu^*) = \omega \neq 0$, where $sgn(\omega) = sgn(g_x)$.*
2. *Transversality condition: $\left.\frac{d\alpha}{d\mu}\right|_{\mu^*} = d_H \neq 0$.*
3. *Genericity condition: When the system is written in the form*

$$\begin{pmatrix} x \\ y \end{pmatrix} = \begin{pmatrix} 0 & -\omega \\ \omega & 0 \end{pmatrix} \begin{pmatrix} x \\ y \end{pmatrix} + \begin{pmatrix} \hat{f}(x, y) \\ \hat{g}(x, y) \end{pmatrix}$$

we have that $a_H \neq 0$, where $a_H = \frac{1}{16}(\hat{f}_{xxx} + \hat{f}_{xyy} + \hat{g}_{xxy} + \hat{g}_{yyy}) + \frac{1}{16\omega}(\hat{f}_{xy}(\hat{f}_{xx} + \hat{f}_{yy}) - \hat{g}_{xy}(\hat{g}_{xx} + \hat{g}_{yy}) - \hat{f}_{xx}\hat{g}_{xx} + \hat{f}_{yy}\hat{g}_{yy})$.

where the notation

$$f_{xy} = \left.\frac{\partial^2 f_\mu}{\partial x \partial y}\right|_{\mu^*} (\mathbf{x}^*)$$

has been used.

Then:

- *a unique curve of periodic solutions bifurcates from* $\mathbf{x}^*$ *into the region* $\mu > \mu^*$ *(*$\mu < \mu^*$*) if* $a_H d_H < 0$ *(resp.* $a_H d_H > 0$*).*
- $\mathbf{x}^*$ *is a stable fixed point for* $\mu > \mu^*$ *(*$\mu < \mu^*$*) and an unstable fixed point for* $\mu < \mu^*$ *(*$\mu > \mu^*$*) if* $d_H < 0$ *(resp.* $d_H > 0$*).*
- *the periodic solutions have opposite stability to* $\mathbf{x}^*$ *on the side of* $\mu = \mu^*$ *where they exist.*

Furthermore, the amplitude of the periodic orbits grows like $\sqrt{-\frac{d_H}{a_H}(\mu - \mu^*)}$ *whilst their periods tend to* $\frac{2\pi}{|\omega|}$ *as* $|\mu| \to \mu^*$*.*

We will use this theorem to look for the existence of Hopf bifurcations for our system as the parameter in the throttle characteristic, μ, varies.

5.4.1 Non-hyperbolicity

For the non-hyperbolicity condition of Theorem 5.1, recall that the eigenvalues of the system are

$$\lambda_{1,2} = \frac{\mathrm{tr}J^* \pm \sqrt{(\mathrm{tr}J^*)^2 - 4\mathrm{det}J^*}}{2}. \tag{5.4.1}$$

and so we require $\mathrm{tr}J^* = 0$ and $\mathrm{det}J^* > 0$.

From Eq. 5.3.21, $\mathrm{tr}J^* = 0$ gives us

$$\frac{d\dot{m}_T}{dp}(p^*) = \frac{A^2}{a^{*2}}\left(1 - \frac{u^{*2}}{a^{*2}}\right)\frac{dp_c}{d\dot{m}}(\dot{m}^*) + 2A\frac{u^*}{a^{*2}}. \tag{5.4.2}$$

Substituting this into Eq. 5.3.20 and simplifying, we get

$$\mathrm{det}J^* = \left(\frac{a^*}{L}\right)^2 - \left(\frac{A}{L}\left(1 - \frac{u^{*2}}{a^{*2}}\right)\frac{dp_c}{d\dot{m}} + \frac{u^*}{L}\right)^2. \tag{5.4.3}$$

The non-hyperbolicity condition is satisfied provided this is greater than zero, i.e.

$$\left(\frac{A}{L}\left(1 - \mathrm{Ma}^2\right)\frac{dp_c}{d\dot{m}} + \frac{u^*}{L}\right)^2 < \left(\frac{a^*}{L}\right)^2, \tag{5.4.4}$$

which, on rearranging for the compressor characteristic gradient, becomes

$$-\frac{a^*}{A(1-\mathrm{Ma})} < \frac{dp_c}{d\dot{m}} < \frac{a^*}{A(1+\mathrm{Ma})} \tag{5.4.5}$$

where $\mathrm{Ma} = \frac{u^*}{a^*}$ is the Mach number.

5.4.2 Transversality

For the transversality condition, we require the derivative of $\mathrm{tr}J^*$ with respect to the throttle parameter μ to be non-zero at the point where Eq. 5.4.2 holds.

In terms of $\dot{m}^* = \dot{m}_T(p^*)$ and p^*, we have

$$\mathrm{tr}J^* = \left(\frac{A}{L} - \frac{\kappa^{\frac{1}{\gamma}}}{\gamma AL}\frac{\dot{m}^{*2}}{{p^*}^{\frac{\gamma+1}{\gamma}}}\right)\frac{dp_c}{d\dot{m}}(\dot{m}^*) + \frac{2\kappa^{\frac{1}{\gamma}}}{AL}\frac{\dot{m}^*}{{p^*}^{\frac{1}{\gamma}}} - \frac{\gamma\kappa^{\frac{1}{\gamma}}}{AL}{p^*}^{\frac{\gamma-1}{\gamma}}\frac{d\dot{m}_T}{dp}(p^*). \tag{5.4.6}$$

Using the fact that the only variable depending on μ is $\dot{m}_T$, we can differentiate this to get

$$\begin{aligned}\frac{d}{d\mu}(\mathrm{tr}J^*) = &-\frac{2\kappa^{\frac{1}{\gamma}}}{\gamma AL}\frac{\dot{m}_T}{{p^*}^{\frac{\gamma+1}{\gamma}}}\frac{d\dot{m}_T}{d\mu}\frac{dp_c}{d\dot{m}} + \left(\frac{A}{L} - \frac{\kappa^{\frac{1}{\gamma}}}{\gamma AL}\frac{\dot{m}_T^2}{{p^*}^{\frac{\gamma+1}{\gamma}}}\right)\frac{d^2p_c}{d\dot{m}^2}\frac{d\dot{m}_T}{d\mu} \\ &+ \frac{2\kappa^{\frac{1}{\gamma}}}{AL}\frac{1}{{p^*}^{\frac{1}{\gamma}}}\frac{d\dot{m}_T}{d\mu} - \frac{\gamma\kappa^{\frac{1}{\gamma}}}{AL}{p^*}^{\frac{\gamma-1}{\gamma}}\frac{d}{d\mu}\left(\frac{d\dot{m}_T}{dp}\right).\end{aligned} \tag{5.4.7}$$

Recall from Eq. 5.1.4 that $\dot{m}_T = (\sigma f(\mu)(p - p_{amb}))^{\frac{1}{2}}$ for a constant σ and function $f(\mu) = (\mu^{-2} - 1)^{-1}$. Therefore, we can use the fact that

$$f'(\mu) = 2\mu^{-3}(\mu^{-2} - 1)^{-2} = \frac{2}{\mu(1-\mu^2)}f(\mu), \tag{5.4.8}$$

to determine

$$\frac{d\dot{m}_T}{d\mu} = \frac{1}{2}\sigma(p - p_{amb})f'(\mu)(\sigma f(\mu)(p - p_{amb}))^{-\frac{1}{2}} = \frac{\dot{m}_T}{\mu(1-\mu^2)}. \tag{5.4.9}$$

Similarly, differentiating

$$\frac{d\dot{m}_T}{dp} = \frac{1}{2}\sigma f(\mu)\left(\sigma f(\mu)(p - p_{amb})\right)^{-\frac{1}{2}} \tag{5.4.10}$$

with respect to μ and using the relation for $f'(\mu)$ gives us

$$\frac{d}{d\mu}\left(\frac{d\dot{m}_T}{dp}\right) = \frac{1}{\mu(1-\mu^2)}\frac{d\dot{m}_T}{dp}. \tag{5.4.11}$$

Substituting these into Eq. 5.4.7 and grouping terms results in

$$\frac{d}{d\mu}(\mathrm{tr}J^*) = \frac{\mathrm{tr}J^*}{\mu(1-\mu^2)} - \frac{1}{\mu(1-\mu^2)}\left[\frac{A}{L} + \frac{\kappa^{\frac{1}{\gamma}}}{\gamma AL}\frac{\dot{m}^{*2}}{p^{*\frac{\gamma+1}{\gamma}}}\right]\frac{dp_c}{d\dot{m}} + \left(\frac{A}{L} - \frac{\kappa^{\frac{1}{\gamma}}}{\gamma AL}\frac{\dot{m}^{*2}}{p^{*\frac{\gamma+1}{\gamma}}}\right)\frac{\dot{m}^*}{\mu(1-\mu^2)}\frac{d^2p_c}{d\dot{m}^2}. \tag{5.4.12}$$

Therefore, evaluating this at μ^* (the critical value of μ for which $\mathrm{tr}J^* = 0$), and writing this back in terms of u^* and a^*, we have

$$d_H = \frac{1}{\mu^*(1-\mu^{*2})}\left[\frac{A}{L}\left(1 - \frac{u^{*2}}{a^{*2}}\right)\dot{m}^*\frac{d^2p_c}{d\dot{m}^2} - \frac{A}{L}\left(1 + \frac{u^{*2}}{a^{*2}}\right)\frac{dp_c}{d\dot{m}}\right]. \tag{5.4.13}$$

Thus, the transversality condition of $d_H \neq 0$ holds provided the compressor characteristic does not have a point of inflection.

5.4.3 Genericity

Let us write $\dot{m} = x$ and $p = y$. The Taylor expansion of $\dot{x} = f(x,y)$ and $\dot{y} = g(x,y)$ are

$$\dot{x} = f^*_x x + f^*_y y + \tfrac{1}{2}f^*_{xx}x^2 + f^*_{xy}xy + \tfrac{1}{2}f^*_{yy}y^2 + \tfrac{1}{6}f^*_{xxx}x^3 + \tfrac{1}{2}f^*_{xxy}x^2y + \tfrac{1}{2}f^*_{xyy}xy^2 + \tfrac{1}{6}f^*_{yyy}y^3, \tag{5.4.14}$$

$$\dot{y} = g^*_x x + g^*_y y + \tfrac{1}{2}g^*_{xx}x^2 + g^*_{xy}xy + \tfrac{1}{2}g^*_{yy}y^2 + \tfrac{1}{6}g^*_{xxx}x^3 + \tfrac{1}{2}g^*_{xxy}x^2y + \tfrac{1}{2}g^*_{xyy}xy^2 + \tfrac{1}{6}g^*_{yyy}y^3, \tag{5.4.15}$$

where the subscript x or y denotes differentiation with respect to that variable, and $*$ denotes evaluation at the equilibrium point $\mathbf{x}^*$ and critical parameter value μ^*.

From Eq. 5.3.5 or 5.3.6 we can see that $f_{xy} = 0$, and thus $f_{xyy} = f_{xxy} = 0$. Similarly Eq. 5.3.7 gives us $g_{xx} = 0$, and so $g_{xxx} = g_{xxy} = 0$. Finally, from the non-hyperbolicity condition we know $\mathrm{tr}J^* = 0$, which means $f^*_x = -g^*_y$. This means Eqs. 5.4.14 and 5.4.15 can be reduced to

$$\dot{x} = -g^*_y x + f^*_y y + \frac{1}{2}f^*_{xx}x^2 + \frac{1}{2}f^*_{yy}y^2 + \frac{1}{6}f^*_{xxx}x^3 + \frac{1}{6}f^*_{yyy}y^3, \tag{5.4.16}$$

$$\dot{y} = g^*_x x + g^*_y y + g^*_{xy}xy + \frac{1}{2}g^*_{yy}y^2 + \frac{1}{2}g^*_{xyy}xy^2 + \frac{1}{6}g^*_{yyy}y^3. \tag{5.4.17}$$

We also know from the non-hyperbolicity condition that, at $\mathrm{tr}J^* = 0$ the eigenvalues are given by

$$\lambda_{1,2} = \pm\sqrt{\det J^*}\ \ i = \pm\sqrt{-g_y^{*2} - f_y^* g_x^*}\ \ i, \tag{5.4.18}$$

so we have $\omega = \sqrt{-g_y^{*2} - f_y^* g_x^*}$.

Since,

$$-\frac{1}{\omega f_y^*}\begin{pmatrix} g_y^* & -f_y^* \\ -\omega & 0 \end{pmatrix}\begin{pmatrix} -g_y^* & f_y^* \\ g_x^* & g_y^* \end{pmatrix}\begin{pmatrix} 0 & f_y^* \\ \omega & g_y^* \end{pmatrix} = \begin{pmatrix} 0 & -\omega \\ \omega & 0 \end{pmatrix},$$

we can change variables to $(u, v)^T$ where

$$\begin{pmatrix} x \\ y \end{pmatrix} = \begin{pmatrix} 0 & f_y^* \\ \omega & g_y^* \end{pmatrix}\begin{pmatrix} u \\ v \end{pmatrix} \tag{5.4.19}$$

and can write our system in the form

$$\begin{pmatrix} \dot{u} \\ \dot{v} \end{pmatrix} = \begin{pmatrix} 0 & -\omega \\ \omega & 0 \end{pmatrix}\begin{pmatrix} u \\ v \end{pmatrix} + \begin{pmatrix} \hat{f}(u,v) \\ \hat{g}(u,v) \end{pmatrix}, \tag{5.4.20}$$

where

$$\begin{aligned}\hat{f}(u,v) = {} & g_{xy}^* f_y^* uv + \frac{g_y^* f_y^*}{2\omega}(2g_{xy}^* - f_{xx}^*)v^2 + \frac{(g_{yy}^* f_y^* - fyy^* g_y^*)}{2\omega f_y^*}(\omega u + g_y^* v)^2 \\ & + \frac{g_{xyy}^* f_y^*}{2\omega}(\omega u + g_y^* v)^2 v - \frac{f_{xxx}^* g_y^* (f_y^*)^2}{6\omega}v^3 + \frac{(g_{yy}^* f_y^* - fyy^* g_y^*)}{6\omega f_y^*}(\omega u + g_y^* v)^3\end{aligned} \tag{5.4.21}$$

$$\hat{g}(u,v) = \frac{f_{xx}^* f_y^*}{2}v^2 + \frac{f_{yy}^*}{2f_y^*}(\omega u + g_y^* v)^2 + \frac{f_{yyy}^*}{6f_y^*}(\omega u + g_y^* v)^3 + \frac{f_{xxx}^*(f_y^*)^2}{6}v^3 \tag{5.4.22}$$

Therefore, after differentiation and evaluating at $(u, v)^T = (0, 0)^T$, the genericity condition becomes

$$\begin{aligned}a_H = {} & \frac{f_y^*}{16}[2g_{xyy}^* g_y^* + f_{xxx}^* f_y^* - g_{yyy}^* g_x^*] + \frac{f_y^*}{16\omega^2}[(f_{yy}^* g_x^* + g_{xy}^* f_y^*)(f_{xx}^* g_y^* + g_{xy}^* g_y^* - g_{yy}^* g_x^*) \\ & + g_y^* f_y^* \left((g_{xy}^*)^2 - (f_{xx}^*)^2\right) + g_{yy}^* g_y^* (2g_{xy}^* g_y^* - g_{yy}^* g_x^*)].\end{aligned} \tag{5.4.23}$$

By differentiating our system (Eqs. 5.1.1 and 5.1.2) and evaluating at the equilibrium

point $\mathbf{x}^*$, we get

$$f_y^* = \frac{A}{L}(1-\mathrm{Ma}^2)\frac{dp_c}{d\dot{m}} + \frac{2u^*}{L} \tag{5.4.24}$$

$$g_x^* = \frac{a^*}{AL} \tag{5.4.25}$$

$$g_y^* = -\frac{a^*}{AL}\frac{d\dot{m}_T}{dp} \tag{5.4.26}$$

$$f_{xx}^* = \frac{A}{L}(1-\mathrm{Ma}^2)\frac{d^2p_c}{d\dot{m}^2} + \frac{A}{L}\frac{\gamma+1}{\gamma}\frac{\mathrm{Ma}^2}{p^*}\left(\frac{dp_c}{d\dot{m}}\right)^2 - 4\frac{A}{L}\frac{\mathrm{Ma}^2}{\dot{m}^*}\frac{dp_c}{d\dot{m}} + \frac{2u^*}{L\dot{m}^*} \tag{5.4.27}$$

$$f_{yy}^* = -\frac{2u^*}{L}\frac{d^2\dot{m}_T}{dp^2} - \frac{2u^*}{L\dot{m}^*}\left(\frac{d\dot{m}_T}{dp}\right)^2 + \frac{\gamma+1}{\gamma}\frac{A}{L}\frac{\mathrm{Ma}^2}{p^*} \tag{5.4.28}$$

$$g_{xy}^* = \frac{(\gamma-1)u^*}{\dot{m}^*L} \tag{5.4.29}$$

$$g_{yy}^* = -\frac{2(\gamma-1)u^*}{L\dot{m}^*}\frac{d\dot{m}_T}{dp} - \frac{a^{*2}}{AL}\frac{d^2\dot{m}_T}{dp^2} \tag{5.4.30}$$

$$\begin{aligned} f_{xxx}^* = {} & \frac{A}{L}(1-\mathrm{Ma}^2)\frac{d^3p_c}{d\dot{m}^3} + 3\frac{A}{L}\frac{\gamma+1}{\gamma}\frac{\mathrm{Ma}^2}{p^*}\frac{d^2p_c}{d\dot{m}^2}\frac{dp_c}{d\dot{m}} - 6\frac{A}{L}\frac{\mathrm{Ma}^2}{\dot{m}^*}\frac{d^2p_c}{d\dot{m}^2} \\ & - \frac{(2\gamma+1)(\gamma+1)}{\gamma^2}\frac{A}{L}\frac{\mathrm{Ma}^2}{p^{*2}}\left(\frac{dp_c}{d\dot{m}}\right)^3 + 6\frac{\gamma+1}{\gamma}\frac{A}{L}\frac{Ma^2}{\dot{m}^*p^*}\left(\frac{dp_c}{d\dot{m}}\right)^2 - 6\frac{A}{L}\frac{\mathrm{Ma}^2}{\dot{m}^{*2}}\frac{dp_c}{d\dot{m}} \end{aligned} \tag{5.4.31}$$

$$g_{xyy}^* = -(\gamma-1)\frac{A}{L}\frac{\mathrm{Ma}^2}{\dot{m}^{*2}} \tag{5.4.32}$$

$$g_{yyy}^* = -\frac{a^{*2}}{AL}\frac{d^3\dot{m}_T}{dp^3} - \frac{3(\gamma-1)u^*}{L\dot{m}^*}\frac{d^2\dot{m}_T}{dp^2} + 3(\gamma-1)\frac{A}{L}\frac{\mathrm{Ma}^2}{\dot{m}^{*2}}\frac{d\dot{m}_T}{dp}. \tag{5.4.33}$$

Therefore, the genericity condition of $a_H \neq 0$ is satisfied provided $\mathrm{Ma} \neq 1$,

$$\frac{dp_c}{d\dot{m}} \neq -\frac{2u^*}{A(1-\mathrm{Ma}^2)}, \tag{5.4.34}$$

and we do not have any hyperflex points (i.e. points where at least the first three derivatives are zero) in either characteristic.

5.4.4 Results

The above calculations tell us that Hopf bifurcations exist in our model when

1. $\frac{dp_c}{d\dot{m}} > -\frac{a^*}{A(1-\mathrm{Ma})}$, $\frac{dp_c}{d\dot{m}} \neq -\frac{2u^*}{A(1-\mathrm{Ma}^2)}$ and $\frac{dp_c}{d\dot{m}} < \frac{a^*}{A(1+\mathrm{Ma})}$,
2. $p_c(\dot{m})$ does not have a point of inflection,
3. Neither $p_c(\dot{m})$ nor $\dot{m}_T(p)$ have hyperflex points,
4. The flow is not sonic ($\mathrm{Ma} \neq 1$).

The resulting Hopf bifurcation is supercritical (subcritical) when the periodic orbit generated at this bifurcation point is stable (resp. unstable). Since a_H changes sign dependent on the derivatives of the compressor and throttle characteristics, we have the potential to observe both subcritical and supercritical Hopf bifurcations in our system.

5.5 Interpretation of Results

We will now look at the stability of our system for our specific compressor and throttle characteristics in the mass flow - pressure plane. We shall consider mass flow values between 0.005kg/s and 0.14kg/s, and pressure values between 1.25bar and 2.3bar.

The first thing we need to determine is whether the flow in the compression system is subsonic or supersonic. This will tell us which of the analyses in Fig. 5-2 applies. Figure 5-3 shows the Mach number within the area we are considering. This is well below one, so we are dealing with subsonic flow.

Next, we need to compute the first three derivatives for the compressor and throttle characteristics at each point in the plane.

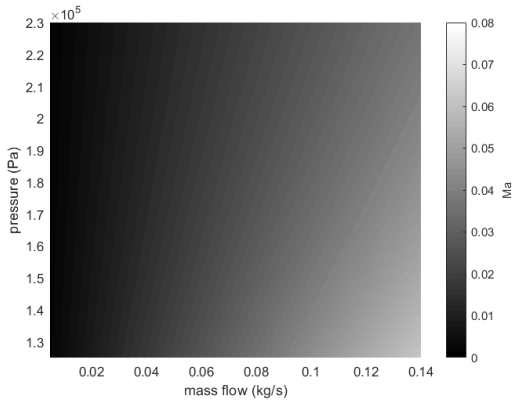

Figure 5-3: Mach number at each point in the mass flow - pressure plane.

Consider the throttle characteristic

$$\dot{m} = \dot{m}_T(p, \mu) = \sqrt{\sigma f(\mu)(p - p_{amb})}. \tag{5.5.1}$$

We can directly calculate the derivatives of the throttle characteristic for different values of pressure and throttle parameter, i.e.

$$\frac{\partial^i \dot{m}_T}{\partial p^i}(p, \mu), \quad \text{for } i = 1, 2, 3. \tag{5.5.2}$$

However, we require the value of the gradient in terms of mass flow and pressure. Therefore, we have to invert the throttle characteristic to find

$$\mu = \dot{m}_T^{-1}(\dot{m}, p). \tag{5.5.3}$$

Similarly, we can numerically compute the derivatives of the compressor characteristic for different mass flow and impeller speed values, i.e.

$$\frac{\partial^i p_c}{\partial \dot{m}^i}(\dot{m}, \Omega), \quad \text{for } i = 1, 2, 3. \tag{5.5.4}$$

Therefore, we have to compute the inverse

$$\Omega = p_c^{-1}(\dot{m}, p) \tag{5.5.5}$$

in order to calculate the derivates at points in the mass flow - pressure plane.

Since the inverses of the two characteristics are unknown, we numerically invert them on a grid in the mass flow - pressure plane. This inversion process is the main source of numerical error in the following analysis.

Having computed the derivatives, we can now compute $\det J^*$ and $\mathrm{tr} J^*$ in order to check the linear stability criteria. Figure 5-4 shows the results. Notice that $\det J^* > 0$ everywhere, so we do not observe saddle points.

This also means that $\mathrm{tr} J^*$ is the only function that determines the stability of the system. Whenever $\mathrm{tr} J^* < 0$ the system is stable and $\mathrm{tr} J^* > 0$ the system is unstable. Therefore, using Eq. 5.3.21 to compute $\mathrm{tr} J^* = 0$ is a quick way to determine the location of the surge limit.

Also, since $\det J^* > 0$, we know that whenever $\mathrm{tr} J^* = 0$ we get a Hopf bifurcation. In

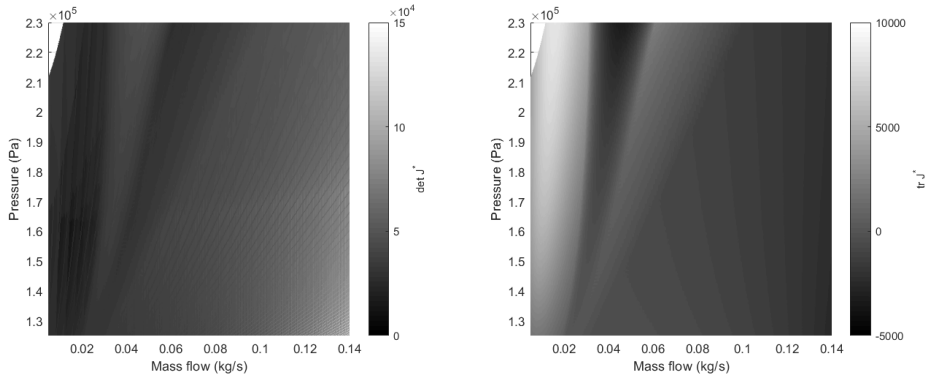

Figure 5-4: Surface plots of the determinant (left) and trace (right) of the Jacobian in the mass flow - pressure plane, wherever the gradients of characteristics are defined.

order to determine the form of these bifurcations, we need to compute parameters d_H and a_H at the $\mathrm{tr}J^* = 0$ lines.

The shaded region in Fig. 5-5 shows the area in the mass flow - pressure plane where $d_H < 0$, and the three black lines identify where $\mathrm{tr}J^* = 0$. Notice that we do not get clean lines or edges of the shaded regions because of the numerical error introduced by inverting the characteristics on a grid. However, starting from high mass flow rates, we can identify that the first line occurs in the $d_H < 0$ region, the second in $d_H > 0$ and the third in $d_H < 0$. This means that the middle Hopf bifurcation is in the opposite direction to the other two.

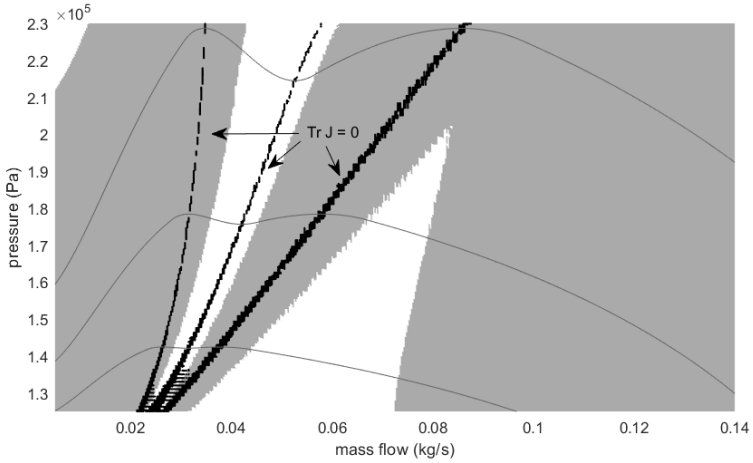

Figure 5-5: Region (grey) in mass flow - pressure plane where $d_H < 0$. Lines indicating where $\mathrm{tr}J^* = 0$ are added in black.

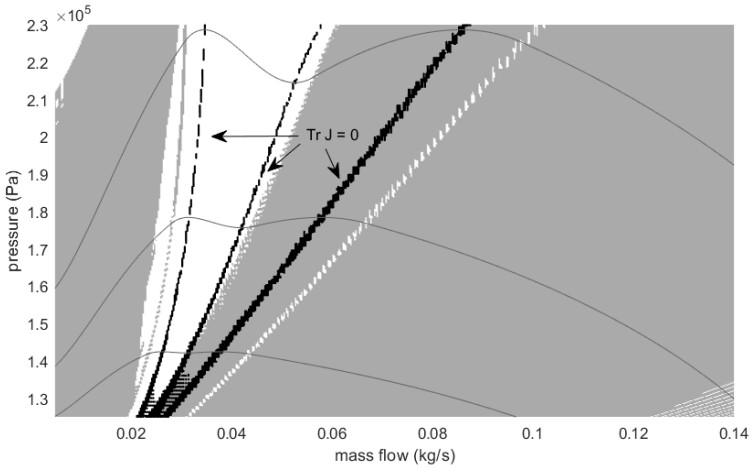

Figure 5-6: Region (grey) in mass flow - pressure plane where $a_H < 0$. Lines indicating where $\mathrm{tr}J^* = 0$ are added in black.

Figure 5-6 shows a similar plot but for parameter a_H. This shows us, again starting from high mass flows, that the first $\mathrm{tr}J^* = 0$ line occurs in the $a_H < 0$ region, but the following two occur in $a_H > 0$ region.

This means that we have one supercritical and two subcritical Hopf bifurcations. Figure 5-7 shows the resulting bifurcations as the throttle parameter μ changes. The line of zero amplitude shows the stability of the equilibrium point. We can see the switch in stability at each $\mathrm{tr}J^* = 0$ point.

For large μ, the equilibrium point is stable and the system is steady. As the throttle is gradually shut (μ decreasing), we see stable limit cycles and the system is unsteady.

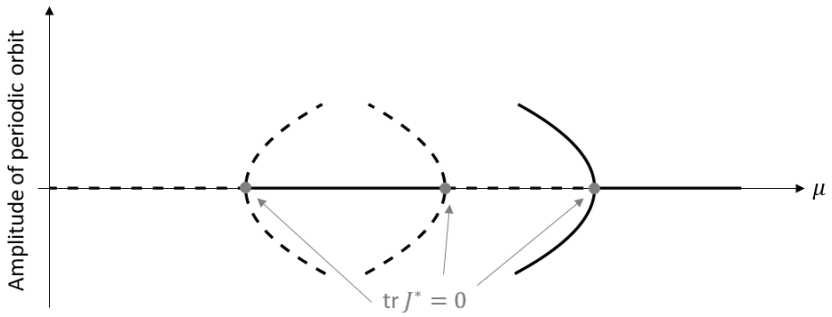

Figure 5-7: Bifurcation diagram showing three Hopf bifurcations as the throttle parameter μ changes. A stable (unstable) equilibrium point or period orbit is show with a solid (resp. dashed) line.

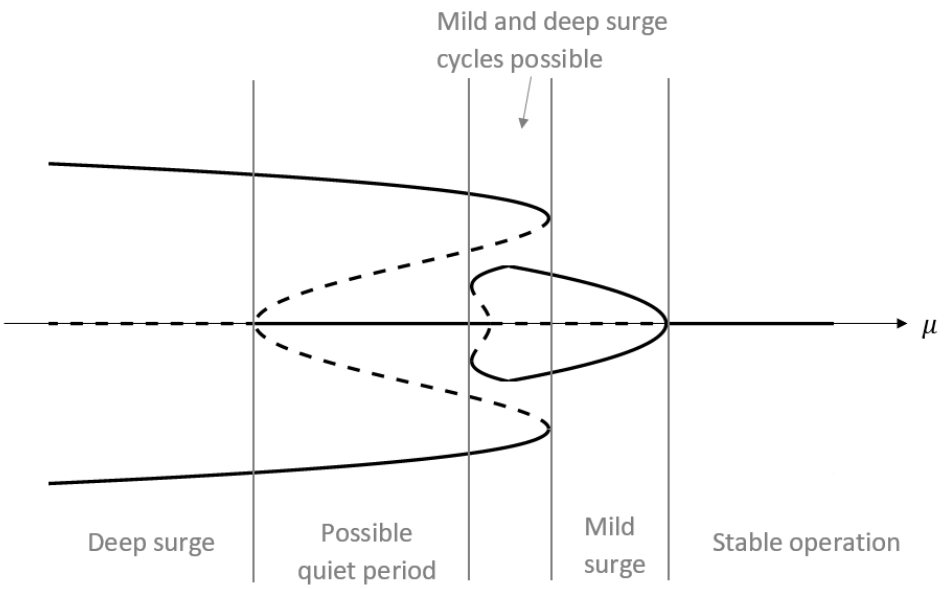

Figure 5-8: Suggested global bifurcation diagram for our system based on evidence from numerical simulation.

As we reduce μ further, we have unstable limit cycles. We would need to look at a global picture to fully understand the behaviour of the system at this point.

Figure 5-8 shows an estimate of a global bifurcation diagram. Here we are predicting saddle node bifurcations from the unstable Hopf bifurcations that result in stable period orbits.

These stable periodic orbits do not have to grow with the bifurcation parameter μ, so can explain why deep surge appears to be a fixed amplitude oscillation. Our estimate for the location of these saddle nodes was deduced by studying Paper 3, Fig. 15 (Section 4.3).

This simulation showed us that we had a region of mild surge, followed by a region where a combination of mild and deep surge limit cycles were observed. This implies that a large amplitude periodic orbit (relating to deep surge) could be observed within the first region where the equilibrium point becomes unstable. It also implies that there must be a relatively small basin of attraction for both stable periodic orbits as we can jump between them within a single simulation.

Paper 3, Fig. 15 then showed us that we have region where the simulation is either stable, or a large amplitude periodic orbit, depending on the initial condition. So

again, we must have two stable behaviours. The unstable periodic orbit separates these two stable behaviours. Since there is a larger distance between the stable and unstable behaviour, it explains why the system does not jump between these two stable behaviours within a simulation. It would require a larger deviation between calculated points than that caused by numerically solving the ODEs or PDEs.

Finally, Paper 3 Fig. 15 observes a region where the only stable behaviour is a large amplitude periodic orbit corresponding to deep surge. We observe this after the final (smallest μ) bifurcation point.

Further investigation is needed in order to verify this global bifurcation picture. One possibility would be to use a numerical continuation software, like AUTO [64].

Another area needing further investigation is the effect of including an inlet pipe into the system. As seen in Fig. 5-5 or 5-6, the $\mathrm{tr}J^* = 0$ lines coincide with the turning points of the compressor characteristic. This location of the surge line agrees with what we observed in Section 2.5, when we had no inlet pipe. However, in Section 4.3, we observed that the surge limits were further to the left than this. Therefore, performing stability analysis on the system of 4 ODEs that take into account the inlet pipe may produce different criteria for the location of the surge lines.

5.6 Conclusions

In this chapter we analysed the mathematical stability of our reduced order surge model. We discovered that the operating point of the system is an equilibrium point, and so the stability of the compression system depends on the stability of that equilibrium.

We performed linear stability analysis and discovered that the gradient of the compressor and throttle characteristics were key factors in determining the stability. We also noticed that the stability of the system changes dramatically if the flow in the pipework is supersonic instead of subsonic.

Furthermore, we discovered that Hopf bifurcations exist whenever the trace of our Jacobian is zero. For our compressor and throttle characteristics, we discovered that we get three successive Hopf bifurcations: one supercritical and two subcritical.

We proposed a global bifurcation diagram based on our analysis and numerical simulations of our model. This proposes an explanation for the multiple stable phenomena

observed in simulations (e.g. a stable equilibrium and stable limit cycle), and suggests they are separated by an unstable limit cycle generated from a Hopf bifurcation.

A similar analysis was conducted by Hös et al. [28] for a linearised system. In their work, the Mach number of the fluid did not appear in calculations, meaning the switch of stability due to sonic flow only occurs due to the nonlinearity in our model.

They obtained a similar stability analysis picture to Fig. 5-2(a), but with the $\mathrm{tr}J^* = 0$ line entirely in the region of positive compressor gradient. Therefore, using a linearised system may predict the onset of surge later than observed experimentally for lower impeller speeds.

Furthermore, they used a cubic polynomial for the compressor characteristic, and this resulted in one Hopf bifurcation. The stability of the resulting periodic orbit depended on the parameter for the intercept of the throttle characteristic, which we know relates to the value of ambient pressure.

For low impeller speeds where we observe a cubic-shaped, rather than quintic-shaped, characteristic, we observe a single supercritical Hopf bifurcation. This is similar to the results in Hös et al. [28] for smaller values of their intercept parameter.

Finally, we noted that it would be useful to undertake further work into the global bifurcations occurring of our model, and on a stability analysis for a model that incorporates an inlet pipe.

Chapter 6

Conclusions

The work undertaken in this thesis was motivated by the problem of identifying surge limits in radial compressors, with a particular emphasis on automotive turbochargers.

In Chapter 2, we developed a reduced order model for a compression system that included a compressor and a throttle valve. We then developed steady-state throttle and compressor characteristics to be incorporated into the reduced order surge model. All models were developed using averaging to reduce the dimension of the 3D fundamental equations of motion.

We also included two more empirical loss functions into the compressor characteristic to take into account friction and incidence losses. These introduced two parameters into the model that need universal relations in order for the model to be fully predictive.

In Chapter 3, we looked in more detail at the behaviour of air when it is travelling backwards through the compressor. We developed a model for reverse flow that took into account shear losses at the interface between the impeller and the diffuser. The shear loss parameter was calibrated by assuming the compressor characteristic is continuous.

During experimental validation of the reversed flow model, the resulting data appeared to imply the existence of an asymptote near zero mass flow as we approach from $\dot{m} < 0$. However, the surge study carried out in Chapter 4 shows that an asymptote is unlikely to exist in a characteristic and so this behaviour was more likely caused by a system level phenomenon.

In Chapter 4, we included a further loss function into the compressor model relating to diffuser recirculation. This resulted in a new shape of compressor characteristic never

derived before in literature. Combining this characteristic with the reduced order model for surge allowed us to capture both mild and deep surge oscillations, as well as phenomena like an observed mid-surge quiet period.

We also used the PDE form of the reduced order surge model and solved this numerically using a staggered grid method. This allowed us to capture wave dynamics in the compression system pipework.

Furthermore, we modelled a compression system with both an inlet and outlet pipe in order to compare to experimental data. This gave us insight into the role the inlet pipe has on the system, including frequency, and stability (when comparing to results in Chapter 5).

Finally, in Chapter 5, we performed stability analysis on our model to mathematically determine the location of the surge limit. We discovered that the gradients of the compressor and throttle characteristics were key for determining stability.

We also discovered that we observe Hopf bifurcations whenever we have a switch in stability. We obtain both supercritical and subcritical Hopf bifurcations, and have suggested a global bifurcation diagram that would explain the simulated dynamics observed from our model.

6.1 Key Insights

Throughout this research project, we have learned many things about the dynamics of surge and the key physical phenomena involved. We list the key points below.

1. Friction is needed to simulate operation of a radial compressor.
   We derived the steady-state compressor characteristic by starting with the simplest possible dynamics, and included additional physical phenomena based on the results. In the isentropic formulation we discovered that the simulated compressor generated more pressure for higher flow rates, whereas the opposite holds true in experiments. It was only with the addition of friction that we were able to simulate realistic behaviour of a compressor.

2. Incidence loss is a key phenomenon for simulating surge.
   Similarly to point 1, we observed that a model with friction but no other losses could not simulate unsteady behaviour reminiscent of surge. With the inclusion

of incidence losses, we observed the existence of limit cycles. Once we had the stall function tending to zero as the flow tends to zero, we were able to relate these limit cycles to deep surge cycles.

3. Shear losses are important for reverse flow conditions.
   We studied flow travelling in the reverse direction through a radial compressor. We noticed that there is a large jump in tangential velocity at the impeller - diffuser interface that would cause losses. This explained why we were observing higher than expected pressure values at small negative mass flow rates. By including this loss, we were able to regain a continuous compressor characteristic that could simulate deep surge cycles.

4. Diffuser recirculation is vital for observing mild surge.
   We noticed that for high impeller rotational speeds, we were not capturing the location of surge onset as well as for lower speeds. This prompted us to add diffuser recirculation into the steady-state compressor characteristic model. We used the same form of the stall function as with incidence losses, and this resulted in a characteristic with two local minima, instead of just one. Having this extra minima allowed our reduced order surge model to simulate two different limit cycles, and we related each cycle to mild or deep surge depending on the amplitude of oscillation. This was the first time any model had been able to capture and explain the existence of both mild and deep surge.

5. Mid-surge quiet period is explained by interaction between the two types of stall.
   We observed that our model simulated a region of stable operation after mild surge had been triggered but prior to a deep surge cycle. This area typically coincided with a region of negative gradient for the compressor characteristic. This negative gradient is caused by the interaction between impeller inlet stall (caused by incidence losses) and diffuser stall (caused by local flow recirculation). Diffuser stall is triggered first and causes a pressure drop. When impeller stall was triggered, this straightened the flow entering the diffuser and so reduced the pressure drop caused by diffuser stall. This recovery of pressure causes the negative gradient in that region of the compressor characteristic.

6. Stability is dependent on Mach number and gradients of characteristic curves.
   We performed mathematical stability analysis on the reduced order surge model. Using the fact that the operating point of the system is an equilibrium, we calculated the Jacobian matrix at this point to understand the linear stability of the system. By considering the determinant and trace of the Jacobian, we were able

to identify relations for when the system switches stability that depended only on the Mach number and the gradients of the compressor and throttle characteristics.

7. Hopf bifurcations exist in the system.
   Using the Hopf bifurcation theorem, we were able to identify the existence of Hopf bifurcations whenever the system changed stability. This is where a periodic orbit comes into existence at the bifurcation point. We identified that, for characteristics with two minima, we observed three Hopf bifurcations. The first of which is supercritical, i.e. the resulting periodic orbit is stable, and the remaining two are subcritical.

8. Simulated behaviour is explained by the existence of multiple stable attractors.
   Using the results of the stability analysis, and understanding from simulations of the model, we were able to propose a global bifurcation diagram. This suggested that a saddle node bifurcation occurs for both of the unstable periodic orbits generated by subcritical Hopf bifurcations. This saddle node bifurcation would lead to a stable limit cycle of larger amplitude. The co-existence of this limit cycle with other stable attractors, such as a stable periodic orbit or equilibrium point, explains why simulations can observe multiple behaviours depending on initial conditions of the system.

6.2 Future Work

While undertaking this work, we encountered areas of research that would be interesting to pursue but lack of resources or time prevented us from doing so.

The first of these is finding universal relations for the three unknown parameters in the steady-state model for the compressor. These were the friction factor and the two stall parameters. To do this, a large amount of data would be required across a diverse range of radial compressors.

Consider the friction factor. This can be determined by performing a least squares fit between compressor map data and each individual speed line of the compressor. The fitted friction factor values can then be compared to independent variables, like impeller speed, impeller wheel size, and critical area of the housing, to find any relations. For example, in Section 2.5, we discovered that the friction factor increased linearly with impeller speed.

Using statistical regression, like the Generalised Additive Model approach described in Section 1.2.2, we can formalise this and find relations for parameters in cases where the interactions between independent variables are important.

The second area to explore is the form of the stall functions used for impeller incidence and diffuser recirculation. In Section 2.6.1 we had a free choice of the parameter d provided it was non-zero. Therefore, exploring different possibilities for d, and its effect on the resulting compressor characteristic and surge dynamics, would be interesting and may allow us to capture the surge limit to higher accuracy.

Moreover, in Section 4.3 the fitted value for the diffuser stall parameter was not constant and did not appear to have a relationship to independent variables (like impeller speed) that could be explained physically. It would be useful to explore the form of the stall function in this case because it is possible that it is not capturing the physical dynamics of diffuser recirculation. For example, we identified that the critical angle at which local flow reversal occurs, α^*, may need a model itself as it is a complex phenomena that could depend on many factors of the flow.

The final area to explore in relation to the compressor characteristic is the effect of inlet pressure. As discovered in Section 4.5, changing the inlet pressure appears to cause a simple shift and stretch of the characteristics at ambient pressure. Formally deriving this relation would help us understand exactly how the inlet pipe influences the compressor system.

Furthermore, knowing the exact form of this relation would help us to incorporate the effect of the inlet pipe into the stability analysis conducted in Chapter 5. For example, if we understand how the inlet pressure varies with mass flow, and know the effect this has on the compressor characteristic, we could use

$$\frac{dp_c}{d\dot{m}}(\dot{m}, p_0) = \frac{\partial p_c}{\partial \dot{m}} + \frac{\partial p_c}{\partial p_0}\frac{dp_0}{d\dot{m}} \tag{6.2.1}$$

in the derived formulae to understand the effect inlet pressure has on the location of the surge line.

There are other ways in which we could incorporate the effect of the inlet pipe into the dynamical systems theory and stability analysis performed in Chapter 5. One way would be to analyse the 4D system found by the PDE form of the reduced order surge model with N=4 (see Section 4.1). This would result in a 4x4 matrix for the Jacobian, and therefore make the analytical formulae far more complex and difficult to derive. It

is likely that numerical computation would be the most efficient way forward in this case.

Another approach is to perform dynamical systems analysis on a discrete-time map. Consider the linearised PDEs for flow in a pipe,

$$\frac{\partial p}{\partial t} + \frac{a^2}{A}\frac{\partial \dot{m}}{\partial x} = 0, \tag{6.2.2}$$

$$\frac{\partial \dot{m}}{\partial t} + A\frac{\partial p}{\partial x} = 0. \tag{6.2.3}$$

If we change variables to

$$v_+ = p + \frac{a}{A}\dot{m}, \tag{6.2.4}$$

$$v_- = p - \frac{a}{A}\dot{m} \tag{6.2.5}$$

then

$$\frac{dv_+}{dt}(x,t) = 0 \qquad \text{on} \quad \frac{dx}{dt} = a, \tag{6.2.6}$$

$$\frac{dv_-}{dt}(x,t) = 0 \qquad \text{on} \quad \frac{dx}{dt} = -a. \tag{6.2.7}$$

This means that a map can be found for the pressure and mass flow at different locations in the pipe. Fig. 6-1 shows how this works for the pressure at the midpoint of the outlet pipe. Here the difference in time between p_n and p_{n+1} is $\frac{L_2}{a}$.

The boundary conditions allow the inclusion of the effects of the inlet pipe, and the fact we have no averaging over the length of the pipe means wave dynamics will still occur in this system.

Another area to explore is the behaviour of the reversed-flow tests at low mass flow rates (see Section 3.2). The results from the experiments seemed to suggest that the compressor characteristic had an asymptote near zero flow for high impeller speeds. However, the surge tests for the same compressor (conducted in Section 4.3) imply that this asymptotic behaviour is more likely due to a system level phenomenon.

It would be very interesting to repeat the reverse flow tests with the focus of understanding this behaviour. It would also be interesting if the behaviour could be captured by modelling the reverse flow experimental procedure in a similar manner to our PDE form of the surge model in Section 4.3. A new form of the throttle characteristic would probably have to be developed in order to capture the true behaviour of high pressure

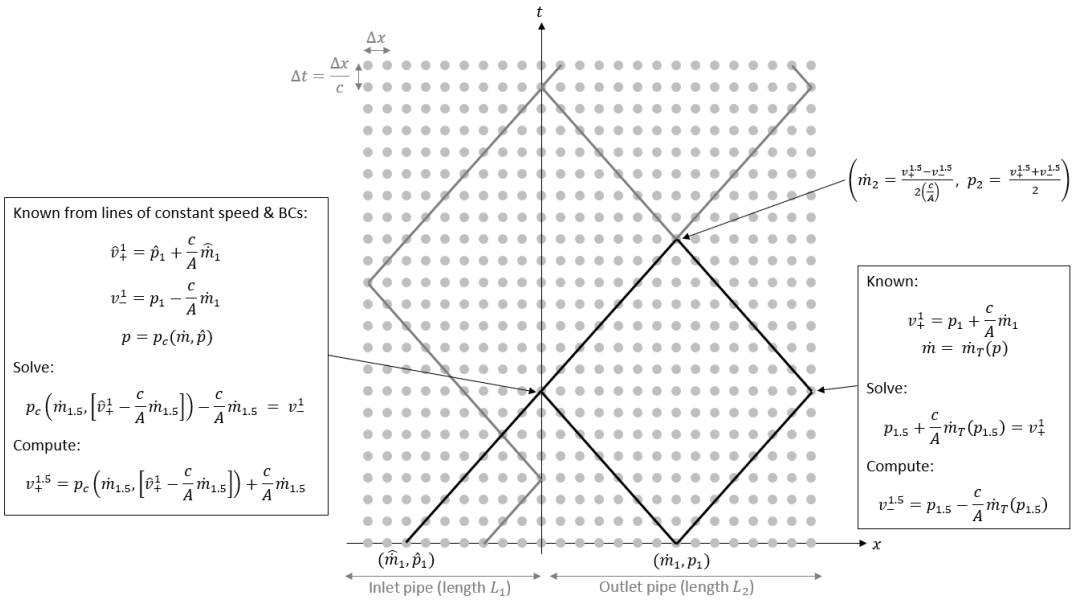

Figure 6-1: Derivation of a map between mass flow and pressure at time 0 and time $\frac{L_2}{c}$ where c is the speed of sound. The derivation uses the fact that $v, \hat{v}$ are constant on lines of constant speed c.

air being forced into the outlet of the compressor.

The final three suggestions for future work are ways in which the work presented here could be taken forward to help answer other open questions in this field. The first is related to simulating and capturing dynamics observed in rotating stall.

Rotating stall occurs when the stall in the impeller channel influences the inlet angle of the flow entering neighbouring channels. Therefore, in order to capture its dynamics it would be possible to couple multiple versions of our compressor impeller channel model together. With careful consideration of the boundary conditions allowing flow from one channel to influence the neighbouring ones, it may be possible to simulate rotating stall and understand important factors in what causes and maintains it.

The second is related to capturing on-engine dynamics near the surge limit. Surge is a system level phenomenon and so depends on the shape and size of its installation pipework. It would be possible to extend the PDE form of the reduced order surge model that was designed to match results on a steady gas stand to that of an engine inlet manifold. This would require capturing the wave dynamics throughout the inlet manifold for example, those caused by opening and closing of valves.

In doing this, it might be possible to predict the surge limit for specific on-engine applications. This would remove the need for an estimated surge margin on compressor maps which takes into account the uncertainty of how a compressor will operate when installed for a particular application, rather than the gas stand there the map was initially generated.

The last is looking into a way to control or mitigate surge behaviour. Once a global bifurcation analysis has been performed, it would be possible to identify domains of attraction of stable behaviour and use this insight to design control strategies. These strategies are likely to involve mechanisms for flow management that could prevent or quickly respond to the existence of surge-like behaviour in a system.

References

[1] N. Watson and M. S. Janota, *Turbocharging: The internal combustion engine*. MacMillan, 1982.

[2] R. Stone, *Introduction to internal combustion engines*. Palgrave MacMillan, 4 ed., 2012.

[3] "Turbocharger history." http://www.cummins.ru/en/components/turbo-technologies/turbocharger-history. [Online], Accessed 07/12/2020.

[4] "Turbocharger history." http://www.turbo-tec.eu/uk/turbocharger-history/. [Online], Accessed 07/12/2020.

[5] "Axial compressors." http://turbomachinery.mandieselturbo.com/products/compressors/axial. [Online], Accessed 19/01/2018.

[6] "Turbocharger." https://en.wikipedia.org/wiki/Turbocharger. [Online], Accessed 03/08/2016.

[7] "Axial compressor." https://en.wikipedia.org/wiki/Axial_compressor. [Online], Accessed 19/01/2018.

[8] "Centrifugal compressor." https://en.wikipedia.org/wiki/Centrifugal_compressor. [Online], Accessed 03/08/2016.

[9] T. Puiu, "This is what 109,000 horsepower looks like." https://www.zmescience.com/science/biggest-most-poweful-engine-world/, 2019. [Online], Accessed 07/12/2020.

[10] "Broadest turbo range." https://www.garrettmotion.com/turbocharger-technology/how-a-turbo-works/broadest-turbo-range/. [Online], Accessed 07/12/2020.

[11] "Turbocharger specs." https://turbochargerspecs.blogspot.com/2013/03/garrett-gt06-gt0632sz-32-trim-80-hp.html, 2013. [Online], Accessed 07/12/2020.

[12] "History." http://www.turbos.bwauto.com/en/products/turbochargerHistory.aspx#:~:text=The%20real%20breakthrough%20in%20passenger,VW%20Golf%20Turbodiesel%20in%201981. [Online], Accessed 07/12/2020.

[13] D. for Transport, "Vehicle licensing statistics: 2019 quarter 1 (jan-mar)." https://assets.publishing.service.gov.uk/government/uploads/system/uploads/attachment_data/file/812253/vehicle-licensing-statistics-january-to-march-2019.pdf. [Online], Accessed 07/12/2020.

[14] "Synthetic fuels/audi e-fuels." https://www.audi-mediacenter.com/en/audi-e-fuels-243. [Online], Accessed 07/12/2020.

[15] B. Roy and A. M. Pradeep, "Turbomachinery aerodynamics." http://nptel.ac.in/courses/101101058/downloads/Lec-31ppts.pdf. [Online], Accessed 03/08/2016.

[16] M. Stewart, *Surface Production Operations*. Gulf Professional Publishing, Boston, 2019.

[17] E. M. Greitzer, "Surge and rotating stall in axial flow compressors - Part I: Theoretical compression system model," *Journal of Engineering for Power*, vol. 98, no. 2, pp. 190–198, 1976.

[18] D. A. Fink, *Surge Dynamics and Unsteady Flow in Centrifugal Compressors*. PhD thesis, Massachusetts Institute of Technology, 1988.

[19] D. A. Fink, N. A. Cumpsty, and E. M. Greitzer, "Surge dynamics in a free-spool centrifugal compressor system," *Journal of Turbomachinery*, vol. 114, pp. 321– 332, 1992.

[20] R. L. Elder and M. E. Gill, "A discussion of the factors affecting surge in centrifugal compressors," *Journal of Engineering for Gas Turbines and Power*, vol. 107, pp. 499–506, 1985.

[21] K. Chan, A. Ordys, K. Volkov, and O. Duran, "Comparison of engine simulation software for development of control system," *Modelling and Simulation in Engineering*, vol. 2013, 2013.

[22] I. Gamma Technologies, "Gt-power engine simulation software." `https://www.gtisoft.com/gt-suite-applications/propulsion-systems/gt-power-engine-simulation-software/`. [Online], Accessed 17/01/2021.

[23] O. Vítek, J. Macek, and M. Polášek, "New approach to turbocharger optimization using 1-d simulation tools," tech. rep., SAE Technical Paper, 2006.

[24] I. Gamma Technologies, "Gt-suite engine performance tutorials." `https://mycourses.aalto.fi/pluginfile.php/637426/mod_folder/content/0/Engine_Performance-tutorials.pdf`. [Online], Accessed 17/01/2021.

[25] A. Rose, *Application of a Continuously Variable Transmission to Engine Boosting and Exhaust Energy Recovery Systems*. PhD thesis, University of Bath, 2013.

[26] I. Day, "Stall, surge, and 75 years of research," *Journal of Turbomachinery*, vol. 138, no. 1, p. 011001, 2016.

[27] G. L. Arnulfi, P. Giannattasio, C. Giusto, A. F. Massardo, D. Micheli, and P. Pinamonti, "Multistage centrifugal compressor surge analysis: Part II - Numerical simulation and dynamic control parameters evaluation," *Journal of Turbomachinery*, vol. 121, no. 2, pp. 312–320, 1999.

[28] C. Hős, A. Champneys, and L. Kullmann, "Bifurcation analysis of surge and rotating stall in the Moore–Greitzer compression system," *IMA Journal of Applied Mathematics*, vol. 68, no. 2, pp. 205–228, 2003.

[29] H. Tamaki, "Effect of piping systems on surge in centrifugal compressors," *Journal of Mechanical Science and Technology*, vol. 22, no. 10, pp. 1857–1863, 2008.

[30] S. G. Koff and E. M. Greitzer, "Stalled flow performance for axial compressors: I - Axisymmetric characteristic," in *29th International Gas Turbine Conference and Exhibit*, vol. 1, American Society of Mechanical Engineers, 1984.

[31] J. Galindo, J. Serrano, H. Climent, and A. Tiseira, "Experiments and modelling of surge in small centrifugal compressor for automotive engines," *Experimental Thermal and Fluid Science*, vol. 32, no. 3, pp. 818–826, 2008.

[32] F. K. Moore and E. M. Greitzer, "A theory of post-stall transients in axial compression systems: Part I - Development of equations," *Journal of Engineering for Gas Turbines and Power*, vol. 108, no. 1, pp. 68–76, 1986.

[33] M. Zagorowska and N. Thornhill, "Compressor map approximation using chebyshev polynomials," 2017.

[34] X. Li, C. Yang, Y. Wang, and H. Wang, "A prediction model of compressor with variable-geometry diffuser based on elliptic equation and partial least squares," *Royal Society open science*, vol. 5, no. 1, p. 171468, 2018.

[35] G. Martin, V. Talon, P. Higelin, A. Charlet, and C. Caillol, "Implementing turbomachinery physics into data map-based turbocharger models," *SAE International Journal of Engines*, vol. 2, no. 1, pp. 211–229, 2009.

[36] D. Japikse, *Centrifugal compressor design and performance*, vol. 2. Concepts Eti White River Junction, VT, 1996.

[37] E. I. G. VELáSQUEZ, "Determination of a suitable set of loss models for centrifugal compressor performance prediction," *Chinese Journal of Aeronautics*, vol. 30, no. 5, pp. 1644–1650, 2017.

[38] H. W. Oh, E. S. Yoon, and M. Chung, "An optimum set of loss models for performance prediction of centrifugal compressors," *Proceedings of the Institution of Mechanical Engineers, Part A: Journal of Power and Energy*, vol. 211, no. 4, pp. 331–338, 1997.

[39] X. Gong and R. Chen, "Total pressure loss mechanism of centrifugal compressors," *Mechanical engineering research*, vol. 4, no. 2, p. 45, 2014.

[40] K. W. Linfield and R. G. Mudry, "Pros and cons of cfd and physical flow modeling," *Airflow Sciences Corporation*, 2008.

[41] P. Fischer, "Introduction to galerkin methods." `http://fischerp.cs.illinois.edu/tam470/refs/galerkin2.pdf`. [Online], Accessed 22/12/2020.

[42] J. Ratz, S. Leichtfuß, M. Beck, H.-P. Schiffer, and F. Fröhlig, "Surge margin optimization of centrifugal compressors using a new objective function based on local flow parameters," *International Journal of Turbomachinery, Propulsion and Power*, vol. 4, no. 4, p. 42, 2019.

[43] A. D. Muradova, "The spectral method and numerical continuation algorithm for the von kármán problem with postbuckling behaviour of solutions," *Advances in Computational Mathematics*, vol. 29, no. 2, pp. 179–206, 2008.

[44] I. Lomtev and G. E. Karniadakis, "A discontinuous galerkin method for the navier–stokes equations," *International journal for numerical methods in fluids*, vol. 29, no. 5, pp. 587–603, 1999.

[45] S. N. Wood, *Generalized additive models: an introduction with R*. CRC press, 2017.

[46] J. A. Sanders, F. Verhulst, and J. Murdock, *Averaging methods in nonlinear dynamical systems*, vol. 59. Springer, 2007.

[47] H. Steinrück, *Asymptotic methods in fluid mechanics: Survey and recent advances*, vol. 523. Springer Science & Business Media, 2012.

[48] J. Hateley, "The lorenz system." `http://web.math.ucsb.edu/~jhateley/paper/lorenz.pdf`. [Online], Accessed 17/01/2021.

[49] D. John and J. Anderson, "Computational fluid dynamics: the basics with applications," *P. Perback, International ed., Published*, 1995.

[50] "B5.4 waves & compressible flow." `https://www0.maths.ox.ac.uk/system/files/coursematerial/2015/3080/19/wcf.pdf`. [Online], Accessed 19/07/2016.

[51] D. J. Acheson, *Elementary fluid dynamics*. Oxford University Press, 1990.

[52] R. Von Mises, H. Geiringer, and G. S. S. Ludford, *Mathematical theory of compressible fluid flow*. Courier Corporation, 1958.

[53] E. M. Greitzer, C. S. Tan, and M. B. Graf, *Internal flow: concepts and applications*. Cambridge University Press, 2004.

[54] P. R. N. Childs, *Rotating Flow*. Elsevier Inc., 2011.

[55] H. Stewart, "The energy equation for a viscous compressible fluid," *Proceedings of the National Academy of Sciences*, vol. 28, pp. 161–164, 1942.

[56] K. P. Burr, T. R. Akylas, and C. C. Mei, "Chapter 2: Two-dimensional laminar boundary layers." `http://web.mit.edu/fluids-modules/www/highspeed_flows/ver2/bl_Chap2.pdf`. [Online], Accessed 27/03/2017.

[57] D. E. Winterbone and R. J. Pearson, *Theory of engine manifold design: Wave action methods for IC engines*. Professional Engineering Publishing, 2000.

[58] C. W. Gear and O. Osterby, "Solving ordinary differential equations with discontinuities," *ACM Transactions on Mathematical Software (TOMS)*, vol. 10, no. 1, pp. 23–44, 1984.

[59] A. V. Wouwer, P. Saucez, and C. Vilas, *Simulation of Ode/Pde Models with MATLAB®, OCTAVE and SCILAB: Scientific and Engineering Applications*. Springer, 2014.

[60] S. Wiggins, *Introduction to applied nonlinear dynamical systems and chaos*, vol. 2. Springer Science & Business Media, 2003.

[61] G. Layek, *An introduction to dynamical systems and chaos*. Springer, 2015.

[62] "Stability theory." `https://en.wikipedia.org/wiki/Stability_theory`. [Online], Accessed 03/02/2021.

[63] J. Guckenheimer and P. Holmes, *Nonlinear oscillations, dynamical systems, and bifurcations of vector fields*, vol. 42. Springer Science & Business Media, 2013.

[64] "Auto software for continuation and bifurcation problems in ordinary differential equations." `http://cmvl.cs.concordia.ca/auto/`. [Online], Accessed 17/02/2021.